



nanomaterials

Special Issue Reprint

Functionalized Nanostructures for Novel Energy Storage Systems

Edited by
Wilhelm Pfleging

[mdpi.com/journal/nanomaterials](https://www.mdpi.com/journal/nanomaterials)



Functionalized Nanostructures for Novel Energy Storage Systems

Functionalized Nanostructures for Novel Energy Storage Systems

Guest Editor

Wilhelm Pfleging



Basel • Beijing • Wuhan • Barcelona • Belgrade • Novi Sad • Cluj • Manchester

Guest Editor

Wilhelm Pfleging
Institute for Applied Materials
(IAM-AWP)
Karlsruhe Institute of
Technology
Karlsruhe
Germany

Editorial Office

MDPI AG
Grosspeteranlage 5
4052 Basel, Switzerland

This is a reprint of the Special Issue, published open access by the journal *Nanomaterials* (ISSN 2079-4991), freely accessible at: https://www.mdpi.com/journal/nanomaterials/special_issues/energy_nano.

For citation purposes, cite each article independently as indicated on the article page online and as indicated below:

Lastname, A.A.; Lastname, B.B. Article Title. <i>Journal Name</i> Year , Volume Number, Page Range.
--

ISBN 978-3-7258-4569-9 (Hbk)

ISBN 978-3-7258-4570-5 (PDF)

<https://doi.org/10.3390/books978-3-7258-4570-5>

Cover image courtesy of Wilhelm Pfleging
Laser Ablation of Electrode

© 2025 by the authors. Articles in this book are Open Access and distributed under the Creative Commons Attribution (CC BY) license. The book as a whole is distributed by MDPI under the terms and conditions of the Creative Commons Attribution-NonCommercial-NoDerivs (CC BY-NC-ND) license (<https://creativecommons.org/licenses/by-nc-nd/4.0/>).

Contents

About the Editor	vii
Preface	ix
Werner Bauer, Marcus Müller, Luca Schneider, Marcel Häringer, Nicole Bohn, Joachim R. Binder, et al. Using Hierarchically Structured, Nanoporous Particles as Building Blocks for NCM111 Cathodes Reprinted from: <i>Nanomaterials</i> 2024 , <i>14</i> , 134, https://doi.org/10.3390/nano14020134	1
Zelai Song, Penghui Zhu, Wilhelm Pfleging and Jiyu Sun Electrochemical Performance of Thick-Film $\text{Li}(\text{Ni}_{0.6}\text{Mn}_{0.2}\text{Co}_{0.2})\text{O}_2$ Cathode with Hierarchic Structures and Laser Ablation Reprinted from: <i>Nanomaterials</i> 2021 , <i>11</i> , 2962, https://doi.org/10.3390/nano11112962	19
Penghui Zhu, Jiahao Han and Wilhelm Pfleging Characterization and Laser Structuring of Aqueous Processed $\text{Li}(\text{Ni}_{0.6}\text{Mn}_{0.2}\text{Co}_{0.2})\text{O}_2$ Thick-Film Cathodes for Lithium-Ion Batteries Reprinted from: <i>Nanomaterials</i> 2021 , <i>11</i> , 1840, https://doi.org/10.3390/nano11071840	35
Minh Xuan Tran, Peter Smyrek, Jihun Park, Wilhelm Pfleging and Joong Kee Lee Ultrafast-Laser Micro-Structuring of $\text{LiNi}_{0.8}\text{Mn}_{0.1}\text{Co}_{0.1}\text{O}_2$ Cathode for High-Rate Capability of Three-Dimensional Li-ion Batteries Reprinted from: <i>Nanomaterials</i> 2022 , <i>12</i> , 3897, https://doi.org/10.3390/nano12213897	54
Lukas Neidhart, Katja Fröhlich, Nicolas Eshraghi, Damian Cupid, Franz Winter and Marcus Jahn Aqueous Manufacturing of Defect-Free Thick Multi-Layer NMC811 Electrodes Reprinted from: <i>Nanomaterials</i> 2022 , <i>12</i> , 317, https://doi.org/10.3390/nano12030317	64
Lukas Schweighofer, Bernd Eschelmüller, Katja Fröhlich, Wilhelm Pfleging and Franz Pichler Modelling and Optimisation of Laser-Structured Battery Electrodes Reprinted from: <i>Nanomaterials</i> 2022 , <i>12</i> , 1574, https://doi.org/10.3390/nano12091574	79
Alexandra Meyer, Fabian Ball and Wilhelm Pfleging The Effect of Silicon Grade and Electrode Architecture on the Performance of Advanced Anodes for Next Generation Lithium-Ion Cells Reprinted from: <i>Nanomaterials</i> 2021 , <i>11</i> , 3448, https://doi.org/10.3390/nano11123448	96
Yijing Zheng, Danni Yin, Hans Jürgen Seifert and Wilhelm Pfleging Investigation of Fast-Charging and Degradation Processes in 3D Silicon–Graphite Anodes Reprinted from: <i>Nanomaterials</i> 2022 , <i>12</i> , 140, https://doi.org/10.3390/nano12010140	122
Vo Pham Hoang Huy, Il Tae Kim and Jaehyun Hur Gallium-Telluride-Based Composite as Promising Lithium Storage Material Reprinted from: <i>Nanomaterials</i> 2022 , <i>12</i> , 3362, https://doi.org/10.3390/nano12193362	141
Hun-Seung Jeong and Byung-Joo Kim Effects of Nickel Impregnation on the Catalytic Removal of Nitric Oxide by Polyimide-Based Activated Carbon Fibers Reprinted from: <i>Nanomaterials</i> 2023 , <i>13</i> , 2297, https://doi.org/10.3390/nano13162297	157

Po-Chih Yang, Yu-Xuan Ting, Siyong Gu, Yasser Ashraf Gandomi, Jianlin Li and Chien-Te Hsieh

Effect of Solvent on Fluorescence Emission from Polyethylene Glycol-Coated Graphene Quantum Dots under Blue Light Illumination

Reprinted from: *Nanomaterials* **2021**, *11*, 1383, <https://doi.org/10.3390/nano11061383> **170**

About the Editor

Wilhelm Pfleging

Wilhelm Pfleging is the head of the Laser Materials Processing Group at the Institute of Applied Materials (IAM-AWP) at the Karlsruhe Institute of Technology (KIT) and a Professor of laser technology. Thanks to his extensive experience in laser technology, materials processing, materials science, and battery technology, Prof. Pfleging has established himself as a leading expert in these fields. He is particularly interested in the laser-assisted micro- and nano-structuring of battery materials, battery manufacturing processes, ultrashort pulse laser technology, and laser-assisted plasma spectroscopy for advanced energy storage systems. Prof. Pfleging is actively involved in several cutting-edge research projects, including developing laser-structured thick-film electrodes for high-performance lithium-ion batteries and innovating 3D electrode design methods. He has made significant contributions to the scientific community and has published over 200 peer-reviewed articles. He also serves on the editorial boards of renowned journals such as *Batteries*, *Nanomaterials*, and the *International Journal of Extreme Manufacturing*. He currently teaches and supervises young researchers, supervises dissertations, and gives lectures on laser-assisted methods and energy storage materials. His dedication to advancing laser technology and energy storage systems continues to drive innovation in sustainable energy solutions.

Preface

The Special Issue “Functionalized Nanostructures for Novel Energy Storage Systems” represents a significant contribution to the field of energy storage, showcasing eleven innovative studies that explore the transformative potential of nanostructures in addressing critical challenges in lithium-ion batteries and related systems. This collection highlights advancements in material design, manufacturing processes, and optimization techniques, offering a multidisciplinary perspective on the future of energy storage technologies.

The motivation behind this Special Issue is rooted in the global need for energy storage solutions that are efficient, durable, and environmentally sustainable. As renewable energy sources become increasingly established, the demand for high-performance energy storage systems continues to grow. Functionalized nanostructures offer a promising pathway to overcome limitations in current technologies, enabling improved ion transport, mechanical stability, and scalability for commercial applications. By focusing on these cutting-edge innovations, the authors aim to provide application-relevant insights that can drive the development of next-generation systems.

The manuscripts featured in this Special Issue cover a diverse range of topics, including the use of hierarchically structured nanoporous particles in cathodes, the optimization of laser-structured electrodes, and the development of novel anode materials such as gallium-telluride-based composites. Other studies explore environmentally friendly manufacturing processes, such as aqueous processing, and investigate the catalytic applications of nanomaterials for environmental technologies. Each contribution emphasizes the importance of functionalized nanostructures in enhancing energy storage performance, durability, and sustainability.

This Special Issue is designed to serve as a valuable resource for a wide audience, including researchers, engineers, industry professionals, and students who are engaged in the development of advanced energy storage systems. It provides a platform for the dissemination of cutting-edge research, promotes interdisciplinary collaboration, and inspires new ideas. By addressing key challenges and presenting innovative solutions, this collection aims to accelerate the transition toward sustainable energy technologies.

The contributing authors are sincerely thanked for their dedication and expertise, which have made this Special Issue a significant contribution to the field. Their work not only advances scientific understanding but also provides practical insights that can advance the development of commercial energy storage systems. Special thanks are also extended to the editorial team and reviewers for their invaluable support in ensuring the quality and relevance of the published manuscripts.

As the world moves toward a more sustainable future, the insights and advancements presented in this Special Issue will undoubtedly play a crucial role in shaping the next generation of energy storage technologies. It is hoped that this collection will inspire researchers and practitioners to explore the high potential of functionalized nanostructures and contribute to the development of innovative solutions that address the growing demand for efficient and sustainable energy storage systems.

Wilhelm Pfleging

Guest Editor



Article

Using Hierarchically Structured, Nanoporous Particles as Building Blocks for NCM111 Cathodes

Werner Bauer ^{1,*}, Marcus Müller ¹, Luca Schneider ¹, Marcel Häring ¹, Nicole Bohn ¹, Joachim R. Binder ¹, Julian Klemens ², Philip Scharfer ², Wilhelm Schabel ² and Helmut Ehrenberg ¹

¹ Institute for Applied Materials (IAM), Karlsruhe Institute of Technology (KIT), Hermann-von-Helmholtz-Platz 1, 76344 Eggenstein-Leopoldshafen, Germany; helmut.ehrenberg@kit.edu (H.E.)

² Thin Film Technology (TFT), Karlsruhe Institute of Technology (KIT), Straße am Forum 7, 76131 Karlsruhe, Germany; wilhelm.schabel@kit.edu (W.S.)

* Correspondence: werner.bauer@kit.edu; Tel.: +49-721-608-22990

Abstract: Nanoparticles have many advantages as active materials, such as a short diffusion length, low charge transfer resistance, or a reduced probability of cracking. However, their low packing density makes them unsuitable for commercial battery applications. Hierarchically structured microparticles are synthesized from nanoscale primary particles by targeted aggregation. Due to their open accessible porosity, they retain the advantages of nanomaterials but can be packed much more densely. However, the intrinsic porosity of the secondary particles leads to limitations in processing properties and increases the overall porosity of the electrode, which must be balanced against the improved rate stability and increased lifetime. This is demonstrated for an established cathode material for lithium-ion batteries ($\text{LiNi}_{0.33}\text{Co}_{0.33}\text{Mn}_{0.33}\text{O}_2$, NCM111). For active materials with low electrical or ionic conductivity, especially post-lithium systems, hierarchically structured particles are often the only way to produce competitive electrodes.

Keywords: battery; lithium-ion battery; active material; cathode; porosity; nanomaterial

1. Introduction

A standard lithium-ion battery electrode consists of a particulate active material, conductivity enhancing components such as carbon black or graphite, and a polymer binder that holds all the particles together and attaches them to the metal current collector. The active materials play a central role in this concept, acting as a source and sink for the lithium ions to provide the desired capacity for energy storage. The theoretical capacity of the battery is determined by the chemical composition and the crystalline phase of the active material. However, the size, crystalline structure, and morphology of the particles also play important roles in the practical capacity. This is mainly because the diffusion of the ions in the active materials in the solid state is much slower than the transport rates in a liquid electrolyte. To improve the performance of the cells, various tailor-made structures have been developed [1], such as preferentially oriented crystals within the particles [2], nanobrick morphology [3], one-dimensional hierarchical microrods [4], and hierarchically structured particles [5–8].

Especially for high power densities, it is advantageous to use small particles that keep the diffusion distance in the solid state short and allow the lithium ions to enter the electrolyte as quickly as possible. Rapid ion transport reduces the occurrence of overvoltage at higher current densities. As a result, the cutoff voltage is reached later, resulting in a higher charge or discharge capacity compared to large active material particles. Although the larger specific surface area of smaller particles must not improve the rate performance by increasing the contact area between the electrolyte and the active material [9], it can multiply the contact points to the conductive carbon network. This improves the electrical connection, especially for active materials with low electronic conductivity. In addition,

the mechanical integrity of active materials is known to improve with decreasing primary particle size. The stresses that occur during cycling accumulate in larger particles, making nano-sized active materials less susceptible to cracking than their macro-sized polycrystalline counterparts [10]. All these arguments support the use of nanoscale active electrode materials. In contrast, most active materials are commercially offered as dense, compact, and equiaxed particles in the 5–10 μm size range, ignoring the advantages of nanoparticles.

The main advantage of micron-sized active materials is the improved electrode packing, which enables high energy density at the cell level, while nanomaterials have a significantly lower loading. This is due to the need to add conductive additives and binders, otherwise the electrical conductivity or mechanical stability of the electrode is not suitable for battery applications. Carbon black, as the main conductive additive, typically has an average particle size in the nanoscale. In TEM studies, primary particle diameters are found to be less than 50 nm [11]. However, the primary particles form highly sintered aggregates with average sizes of 100–300 nm, which cannot be further disaggregated even by intensive mixing [12]. If the size of the active materials is of the same order of magnitude, the formation of a conductive microstructure is significantly hindered. Percolation theory can be used to describe this phenomenon [13]. It explains why the carbon black content must be 16 vol% or more for similarly sized particles, because only then will the statistically distributed carbon black particles form a percolation structure that ensures sufficient electrical connection of the active material particles to the current collector. On the other hand, if the active materials have a significantly larger particle size than the carbon black, the volume already occupied by the active material leads to directed percolation due to the localization and denser packing of the carbon black particles in the pores. As a result, the percolation threshold is lowered, and high electrode conductivity is achieved at lower carbon black levels. A particularly low percolation threshold is possible when there is a two-dimensional distribution in which the carbon black particles occupy only the surface of the active materials. In addition, if the carbon black and active material particles are the same size in the nanoscale, the number of particles increases massively. This also increases the amount of binder required to crosslink the particles. While nanoscale active materials require the addition of more than 20% *w/w* binder and conductive carbon black, the quantity of inactive components can be reduced to less than 5% *w/w* for common particle sizes of about 10 μm . The significantly higher active material content results in a higher energy density and explains why nanomaterials have not yet been widely used on an industrial scale.

2. Hierarchically Structured Electrode Materials

Active materials with an easily accessible, nanoscale pore structure are an attractive approach to make the positive properties of nanomaterials available with microscopic particles or to achieve higher packing densities even when using nanomaterials [14]. For this purpose, the nanoparticles are agglomerated into microscopic granules. They are then thermally solidified by forming sinter bridges to produce particles that are stable enough to be processed into electrodes and cells analogous to conventional active materials. However, the sintering process must be limited to preserve the open pore structure of the agglomerates and nanoscale dimensions of the primary particles. This allows the electrolyte to fill the open pores and accelerate ion transport through the pore channels. In this state, the nanoporous particles form a hierarchical structure of interparticular and intragranular pores in the electrode (Figure 1), giving the materials their name.

The granulation step can produce both single-phase materials and composite materials. These composites can include an electrically conductive phase, allowing for the creation of active material powders with low electrical conductivity at high packing densities, which would otherwise only work at the nanoscale. This makes nanocomposites a prerequisite for certain materials to have commercial potential in batteries (also see chapter 7).

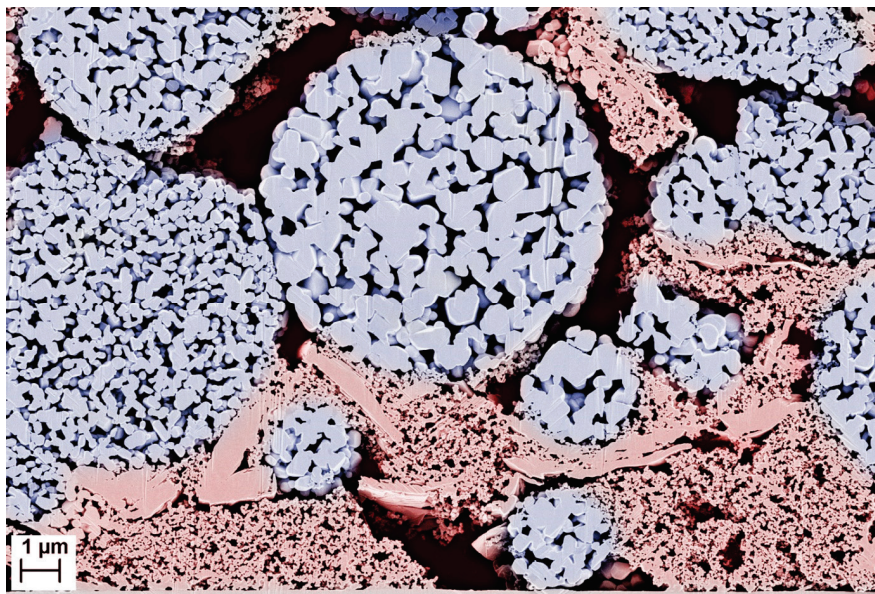


Figure 1. SEM cross-section through a hierarchically structured NCM111 cathode with regions of interparticulate (red) and intragranular (blue) porosity. Interparticulate pores are partially filled by binder-stabilized domains of the conductive additives carbon black and graphite.

Hierarchically structured materials can be prepared in two ways (Figure 2). In the top-down approach, a commercial electrode material with a micron particle size is wet-milled down to the nanoscale. Agitator bead mills have proven to be very efficient in achieving high particle fineness even at high throughputs. The addition of a dispersing agent helps to stabilize the resulting fines against re-agglomeration. The grinding suspension can be used directly in a spray dryer for the granulation step without intermittent drying process [6]. The alternative bottom-up approach starts with a precursor solution of acetates, carbonates, gluconates, or other salts of the desired cations [12]. The use of water as a solvent allows for a cheaper and more environmentally friendly synthesis. The nanoparticles are also precipitated from this solution by spray drying. The most elegant way is to combine the precipitation step with the subsequent granulation step and perform both processes in a single pass in the spray dryer [13]. However, this is only feasible for single-phase materials, while for composites it is necessary to separate the precipitation and granulation steps. The size of the granules can be adjusted from a few microns to over 30 μm by changing the speed of the impeller. This makes it possible to cover the entire range in which active materials are commonly used. Granulation is followed by a calcination step in which the precipitated granules are thermally treated in a furnace. This process removes unwanted phases and precursor residues, and heals mechanical damage caused by milling. The thermal treatment also induces the formation of the sinter necks between the primary particles, which increase the mechanical stability and electronic conductivity of the granules.

The bottom-up approach offers greater freedom in composition and morphological design, as a variety of precipitation reactions can be used. It also allows the synthesis of active materials that are not commercially available. It is the more economical approach because it does not require the costly milling step. The top-down approach is particularly interesting from a scientific point of view, as it allows a direct comparison of the properties of the dense starting material and the porous granules. In this paper, the processing behavior and electrode properties of dense and porous particles with similar sizes and chemical compositions are investigated for $\text{LiNi}_{0.33}\text{Co}_{0.33}\text{Mn}_{0.33}\text{O}_2$ (NCM111) using a top-down approach. NCM111 is less sensitive to moisture than NCM materials with higher nickel contents. This reduces the likelihood that the particle properties will be differently affected by reactions with the environment.

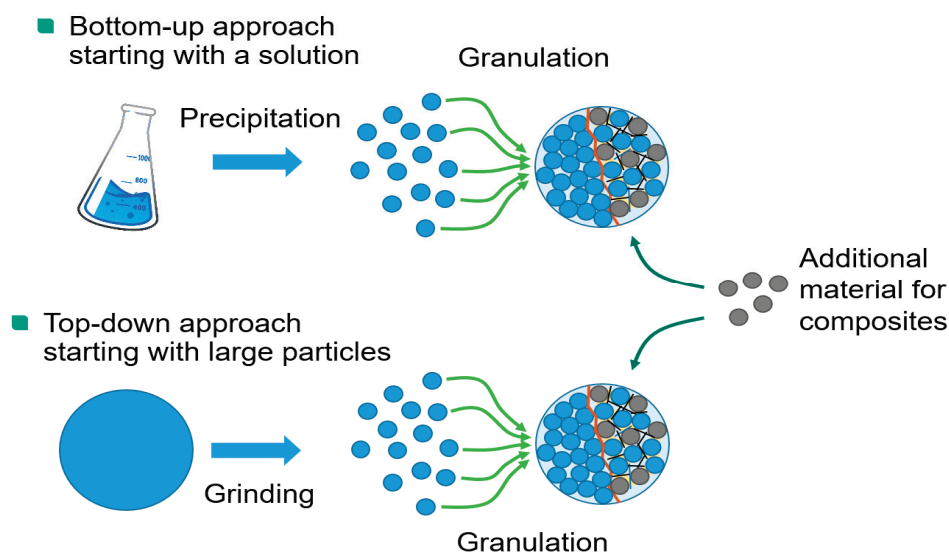


Figure 2. Schematic preparation of hierarchically structured cathode materials by a bottom-up versus a top-down approach.

3. Experimental

3.1. Material Synthesis

For the top-down approach, $\text{LiNi}_{0.33}\text{Co}_{0.33}\text{Mn}_{0.33}\text{O}_2$ (NCM111) powder (NM-3100, Toda Kogyo Corp., Tokio, Japan) was suspended in deionized water with a dispersant (Darvan 821A, R.T. Vanderbilt, Norwalk, CT, USA) and milled in an agitator bead mill (LabStar LS1, Netzsch GmbH, Selb, Germany) with ZrO_2 beads (0.1 mm or 0.2 mm diameter) at 3000 rpm for 1 h. The suspension was then spray-dried (MobileMinor spray dryer, GEA AG, Düsseldorf, Germany) with adjusted impeller speed to receive granules with nearly the same diameter as the original material. The spray-dried NCM111 granules were calcined at temperatures between 700 and 1000 °C for 5 h under air to yield a hierarchically structured cathode material.

The size of the secondary particles was determined via laser diffraction (Horiba LA950, Retsch GmbH, Haan, Germany), surface area through N_2 adsorption with evaluation by Brunauer-Emmett-Teller (BET) theory (Gemini VII 2390, Micromeritics Instruments Corporation, Norcross, GA, USA), and granule porosity and pore size distribution were measured by mercury intrusion porosimetry (CEI Pascal 1.05, ThermoElectron S.p.A., Milan, Italy).

3.2. Electrode Manufacturing and Testing

Cathodes for coin cells were prepared by mixing the hierarchically structured NCM111, a PVDF binder (KYNAR Powerflex LBG-1, Arkema, Lyon, France), and carbon black (C-ENERGY Super C65, Imerys Graphite & Carbon, Bironico, Switzerland) with a magnetic stirrer in an 8:1:1 ratio in NMP and manually doctor-blading the slurry at a 200 μm gap height on an aluminum current collector. The foils were dried overnight at 80 °C and processed to half cells without calendaring.

For pouch cells, NCM111 (as received or processed in the top-down approach) was mixed with C65 carbon black, graphite (C-ENERGY KS6L, Imerys Graphite & Carbon, Bironico, Switzerland), and PVDF (Solef 5130, Solvay S.A., Bollate, Italy) in N-methyl-2-pyrrolidone (NMP, Carl Roth GmbH, Karlsruhe, Germany) using a dissolver mixer (Dispermat SN-10, VMA Getzmann GmbH, Reichshof, Germany) for 1 h at 1000 rpm, at a 100:4:4:4 ratio and a solid content of 50.5% *w/w*. The preparation of the electrodes was performed on aluminum foil (20 μm , Schlenk SE, Roth, Germany) using a roll-to-roll coater (KTFS, Mathis AG, Oberhasli, Switzerland) with a knife coating device and two integrated convection-drying stages set to 80 and 120 °C, respectively. Drying time was less than 10 min. Compaction of the electrodes was performed in a heated calender

(Saueressig GLK 200, Matthews Europe GmbH, Vreden, Germany) at 50 °C. Alternatively, a waterborne route was prepared with sodium carboxy methylcellulose, (CMC, CRT2000 PA, IFF Inc., Bomlitz, Germany) and a fluorine acrylic copolymer latex (TRD202A, JSR Micro NV., Leuven, Belgium) in a 1:1 ratio instead of the PVDF binder. The CMC solution was added at the beginning of the mixing process, whereas the latex binder was added 5 min before the end of mixing at 500 rpm. Drying temperatures for the aqueous route were 40 °C and 80 °C.

Drying experiments of the cathodes were carried out as a discontinuous process. The aluminum foil was attached to a temperature-controlled plate. The coating was applied with a doctor blade (ZUA 2000.60, Zehntner GmbH, Sissach, Switzerland) and immediately the coating was moved under the drying nozzles of an impingement dryer. For homogeneous drying, the coating is periodically moved under the dryer until the electrode was dry.

The viscosity of the slurries was measured by a rotation viscometer (Physica MCR 101, Anton Paar GmbH, Graz, Austria) in a plate–plate configuration with a 25 mm diameter at 25 °C. The gap size was fixed at 500 µm. Before the frequency-dependent oscillation test, an amplitude sweep was performed to determine the linear viscoelastic range.

A 90° peel test, based on DIN EN 28510-1, was carried out for the measurement of the adhesion strength (10 N load cell, Zwick). Strips of the dried cathodes (17 mm in width, 60 mm in length) were attached with the coated side to an adhesive strip. The sample was pressed for 2 s at a load of 200 kg and then peeled off at a constant speed of 600 mm/min. The resulting pull-off force was measured and divided by the sample width to obtain a line adhesive force.

The electrical resistance was determined with an ohmmeter (RM3544, HIOKI E.E. Corp., Nagano, Japan). Therefore, cathode disks were placed between polished copper cylinders with a diameter of 14 mm and a load of 1 kg.

Imaging of the active material and coated electrodes was performed using a field-emission scanning electron microscope (Supra 55, Carl Zeiss GmbH, Oberkochen, Germany) with an EDS detector (Ultim Extreme, Oxford Instruments, High Wycombe, UK). Cross-sections of the electrodes were prepared by ion-beam milling (EM TIC3X, Leica Microsystems GmbH, Wetzlar, Germany) using argon ions and an accelerating voltage of 6 kV at 2.2 mA gun current. From SEM micrographs, also the primary particle size distribution of the granules was determined by image analysis (ImageJ software 1.53n) based on Feret diameters. The pore size distribution of the electrodes was determined by mercury intrusion porosimetry as described in Section 3.1.

3.3. Cell Preparation and Testing

Swagelok-type cells were built from the cathode layers, a Whatman GF/C separator, a lithium metal anode, and 80 µL of LP30 electrolyte (1:1 *v/v* EC/DMC, 1 M LiPF₆) from Sigma-Aldrich (Taufkirchen, Germany) in a glove box (MBraun GmbH, Garching, Germany) with O₂ and H₂O concentrations < 0.5 ppm. For electrochemical testing, a BT2000 battery cycler from Arbin Instruments was used. Galvanostatic cycling at discharge rates of C/20, C/10, C/5, C/2, 1C, 2C, 3C, 5C, 7C, and 10C with 1C corresponding to 183 mAh/g was performed in the voltage range between 4.3 and 3.0 V, whereas the charging rate was retained at C/2 from 1C on.

For the tortuosity measurements, a symmetrical cell was assembled with two glass fiber separators (GF/C, Whatman plc, Maidstone, UK) and 200 µL of 10 mM tetrabutylammonium perchlorate TBAClO₄ in EC:DMC (1:1 *v/v*) electrolyte (VWR International GmbH, Darmstadt, Germany). EIS measurements were performed in a temperature-controlled chamber (BTZ-175, Espec) at 25 °C using a coin cell holder (Dual CR2032 Coin Cell Holder, Gamry Instruments) with a potentiostat (VSP-300, Biologic SAS, Seyssinet-Pariset, France). The measuring parameters were 10 mV perturbation, a frequency range from 200 kHz to 100 mHz and 20 points per decade. The obtained EIS data were plotted and fitted with an

EIS software (RelaxIS 3.0.21.17, rhd instruments) by using the equivalent circuit model as described in [15].

Pouch cells were assembled with a cathode size of $50 \times 50 \text{ mm}^2$, a ceramic-coated separator foil (Separion, Litarion GmbH, Kamenz, Germany), and graphite anodes with $54 \times 54 \text{ mm}^2$. Electrodes and separator were dried overnight in a vacuum furnace at $130 \text{ }^\circ\text{C}$ and assembled in a dry room at a dew point of below $-50 \text{ }^\circ\text{C}$. An amount of $450 \text{ }\mu\text{L}$ of LP30 (1:1 *v/v* EC/DMC, 1 M LiPF₆) from BASF SE was added as the electrolyte for each cell. After assembly, the cells were rested for 20 h at $40 \text{ }^\circ\text{C}$ to facilitate complete wetting. Cell tests were performed between 3.0 V and a cutoff voltage of 4.2 V, at a constant temperature of $23 \text{ }^\circ\text{C}$. The C-rates were calculated based on 155 mAh/g as the reversible capacity for NCM111. After two initial formation cycles at 0.05C, the rate capability was tested for 0.5C, 1C, 2C, and 3C in constant current (CC) mode by symmetrical charging and discharging and 10 cycles for each C-rate. After 3C, cells were cycled again at 0.5C (10 cycles) and 1C (50 cycles) to see if irreversible capacity losses had appeared. For testing the capacity retention, cycling was continued with selected cells in 2C charge (constant current–constant voltage (CCCV) charge to a 0.05C current limit) and 3C discharge rate. Additional 10 cycles at 1C(CC) separate blocks of 100 cycles of 2C/3C to enable the calculation of incremental capacity (IC) curves regularly.

4. Properties of the Particles

Figure 3 compares the morphology of the original NCM111 particles with the intermediate spray-dried species. The starting material has a particle size of $d_{50} = 9.3 \text{ }\mu\text{m}$. The grain size is less than one micron, and the BET surface area is $0.4 \text{ m}^2/\text{g}$. The milling process produces particles that are much smaller than the original material. Depending on the size of the milling beads, a particle size in the range of 100 nm (BET $49.8 \text{ m}^2/\text{g}$) for 0.1 mm ZrO₂ beads or 200 nm (BET $27.7 \text{ m}^2/\text{g}$) for 0.2 mm beads is obtained after a milling time of 1 h. A particle size below 100 nm should be possible with longer milling times. The smaller particles from the 0.1 mm beads are more uniform in size, while the 0.2 mm beads also produce larger particles. Spray drying produces granules with a spherical shape, while the original particles have a more irregular shape. The size of the granules in Figure 3 is $d_{50} = 7.1 \text{ }\mu\text{m}$ for (c) or $d_{50} = 8.6 \text{ }\mu\text{m}$ for (d).

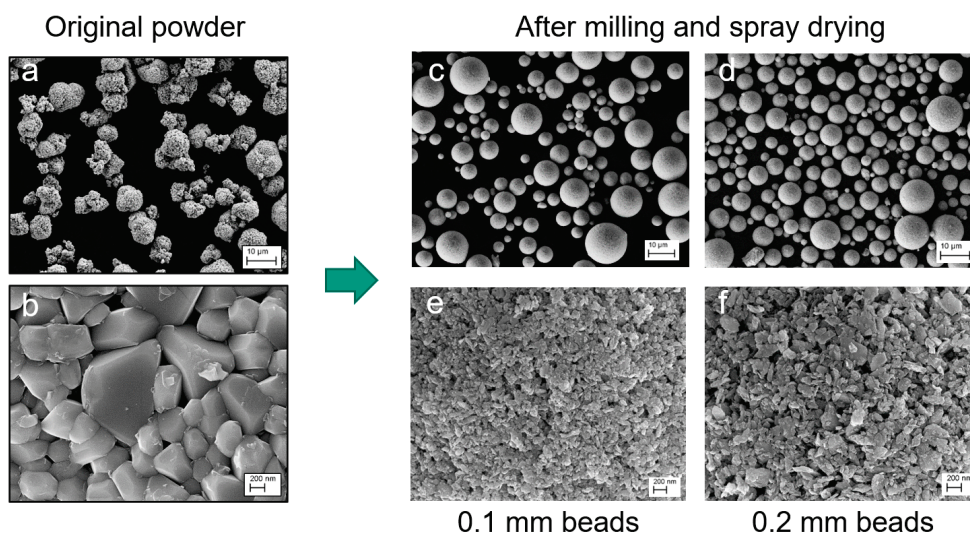


Figure 3. SEM micrographs of the original NCM111 particles at different magnifications (a,b), and after milling for 1 h and spray-drying (c,d). Magnifications of the spray granules show the primary particle size, which is obtained for different ZrO₂ beads (e,f). Scale bars are 200 nm and 10 μm .

The calcination process causes recrystallization and grain growth of the particles (Figure 4). Sinter necks are created, and the primary particles combine to form a secondary

structure with improved mechanical stability. Residual porosity between the primary particles can be seen below a calcination temperature of 1000 °C.

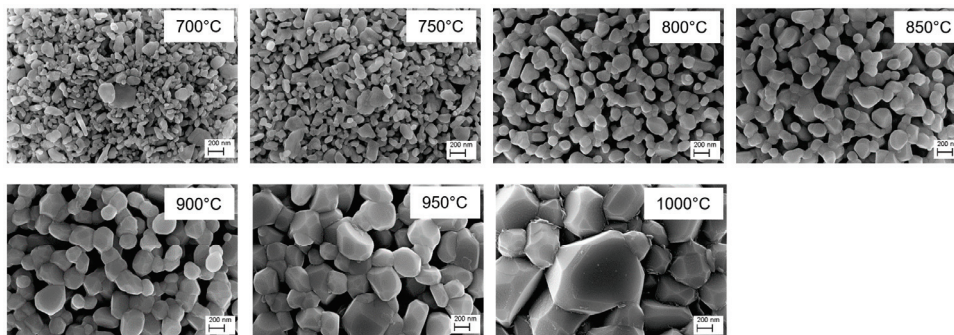


Figure 4. SEM micrographs of the surface of NCM111 granules after calcination at various temperatures and a dwell time of 5 h. Milling was performed with 0.2 mm ZrO₂ beads. Scale bar is 200 nm.

The size of the primary particles was determined from SEM images using ImageJ software. Figure 5 (left) shows that the primary particles of the 0.1 mm beads are smaller only at low calcination temperatures because small particles have a higher sintering activity than larger ones. This results in grain growth that exceeds the primary particle size of the 0.2 mm bead sample at temperatures above 850 °C. The porosity of the granules from the 0.1 mm bead sample is 5% lower in the initial state due to the better packing of the more homogeneous particle shape. During calcination, the porosity of the granules, as determined by a mercury porosimeter, decreases equally for both samples, so that the 0.1 mm bead sample has a lower porosity over the entire temperature range (Figure 5 right). Unlike the primary particles, the size of the granules changes less than 20% during the calcination step.

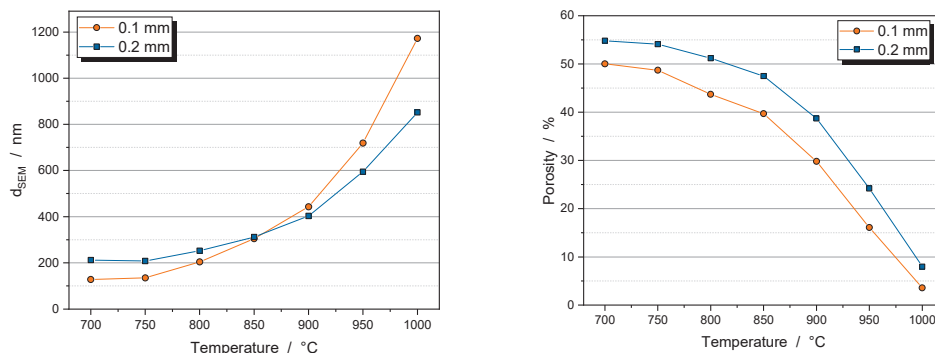


Figure 5. Effect of calcination temperature on primary particle size (left) and internal porosity of the granules (right). Dwell time was 5 h. Primary particles were milled with 0.1 mm beads (orange dots) or 0.2 mm beads (blue squares).

Despite intensive material processing, no chemical or structural changes are usually induced by the synthesis process. X-ray diffraction patterns of the original and synthesized materials show no evidence of structural changes [7]. Chemical analysis by inductively coupled plasma optical emission spectroscopy (ICP-OES) confirms that the composition of the synthesized particles is very close to the original composition [7], even after the intensive contact with water, which usually leaches measurable amounts of Li from cathode materials [16–18]. An explanation is that during spray drying of the milling suspension, the leached ions are retained and re-deposited on the primary particles. The original composition and phase structure are restored by solid-state diffusion processes during the subsequent heat treatment.

The effect of the calcination temperature on the electrochemical properties of the porous NCM111 particles was investigated in coin cells against a lithium anode (Figure 6). The calcination step improves the specific discharge capacity up to a temperature of 750 °C due to the better electrical conductivity between the primary particles caused by the sinter neck formation. However, the advantages of the nanoparticles are lost as the crystallite size increases. This becomes apparent at temperatures above 900 °C, where the capacity drops significantly.

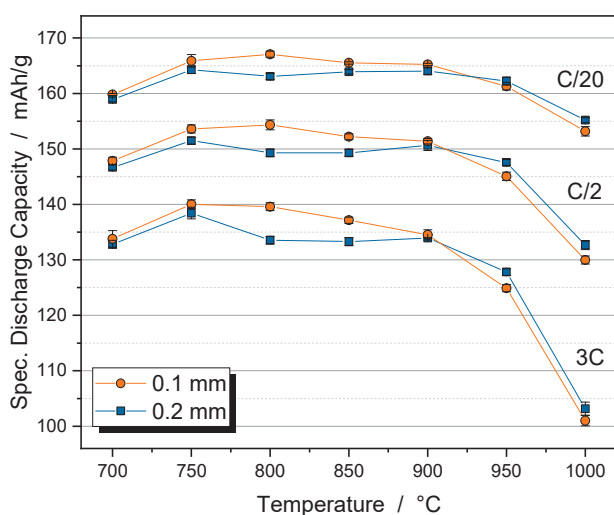


Figure 6. Specific discharge capacity of porous NCM111 particles depending on the calcination temperature. Primary particles were prepared with 0.1 mm beads (orange dots) or 0.2 mm beads (blue squares). Measurement in coin cells with lithium metal as the counter electrode.

5. Processing of Hierarchically Structured Particles

The manufacturing processes for electrodes from hierarchically structured materials are similar to those of dense materials of the same particle size. However, there are some specific features that have a significant impact on the processing and properties of the electrodes. They occur in almost all process steps because the additional porosity within the particles affects the slurry processing, resulting in a modified additive distribution.

The hierarchically structured NMC111 particles used in the following experiments were prepared using 0.2 mm milling beads and a calcination temperature of 850 °C.

5.1. Slurry Mixing

Slurries with porous particles have a higher viscosity than those with dense particles, even though the same equipment and procedures were used for dispersing and solvent mixing (Figure 7). This is because the pores within the particles result in a higher overall porosity of 65–70 vol%. In comparison, uncalendered electrodes made from dense NCM111 particles have a porosity of only 50–55 vol% after drying. Due to the good solvent wetting and the high capillary forces created by the fine internal pores, the porous particles are completely infiltrated by the solvent. This infiltrated solvent acts as a stationary phase, reducing the available volume of the transport fluid, which in turn increases the efficient volume fraction of the particles and the internal friction in the slurry. Fluid loss remains at all shear rates, and although the viscosity curves show comparable shear thinning behavior, they therefore differ significantly up to high shear rates.

A reduction in the transport fluid between the porous particles alone should increase the binder concentration and its interactions. However, frequency-dependent oscillation measurements on the slurries show a general decrease in storage and loss modulus G' and G'' , which is particularly pronounced in the mid-frequency range (Figure 7 right). This suggests that a significant amount of the binder is also penetrating the pores, reducing

the strength of the gel network. Results confirming this conjecture are presented in the following sections.

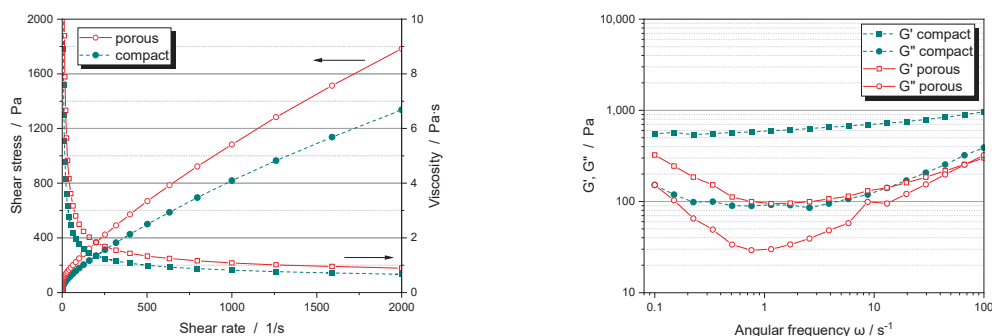


Figure 7. Flow and viscosity curves (left) and frequency dependent oscillation measurement (right) of NCM111 cathode slurries with dense or porous particles at a solid content 50.5 wt%.

5.2. Drying Behavior

The drying behavior of the electrodes is influenced by the additional pore space of hierarchically structured materials, as described in detail by Klemens et al. [19]. At the beginning of the process, drying is similar to that of dense particles. Initially, all pores are filled with solvent (Figure 8). As solvent removal begins, the particles move closer together until they touch and film shrinkage ends. Next, large pores between the particles begin to empty. For dense particles, the drying process ends when all interparticle pores are empty; however, intragranular pores may still contain solvent because drying within the particles is slowed by the higher capillary pressure in smaller pores. An additional drying stage is required, which begins when all interparticle pores surrounding a discrete particle are empty. An evaporation front then gradually moves into the particles. It is hypothesized that this front moves homogeneously due to the narrow pore size distribution within the secondary particles, resulting in slight capillary pressure inhomogeneities. The drying process is completed when the solvent is removed from within the secondary particles.

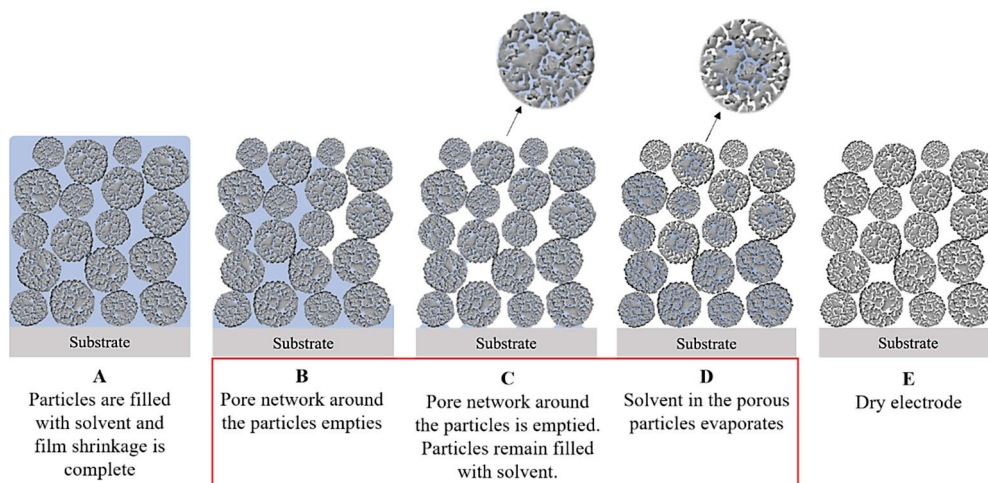


Figure 8. Schematic representation of the drying process of a particulate electrode with porous, nanostructured particles (Reprinted from Ref. [19] under CC BY license).

When electrodes are dried at higher rates, the binder may migrate to the surface of the electrode along with the solvent. This migration reduces the amount of binder at the interphase of the electrode with the current collector and decreases the adhesion [20]. This effect is particularly noticeable for compact particles (Figure 9 left). For porous particles, however, adhesion forces are generally lower and less affected by the drying

rate. Interestingly, as the drying rate increases for porous particles, the adhesion forces can actually increase, bringing them closer to those of compact particles.

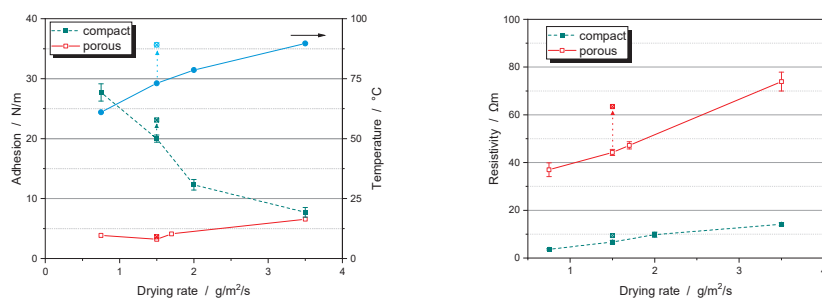


Figure 9. Adhesion force (left) and resistivity (right) of NCM111 cathodes with compact (green filled squares) and porous particles (red open squares) as a function of the drying rate. Also shown is the corresponding film temperature during drying (blue dots, left). Crossed markers indicate the results when a lower heat transfer coefficient is applied, resulting in a higher film temperature.

As the drying rate increases, the electrical resistance of the electrodes increases. This effect occurs for both compact and porous particles (Figure 9 right). However, it is also less pronounced for porous particles. By lowering the heat transfer coefficient, the film temperature can be increased without changing the drying rate. For compact particles, this results in a significant increase in adhesion and electrical resistance. For porous particles, however, there is virtually no change in these properties. In general, porous particles appear to be more tolerant to the drying conditions than compact particles. An explanation for this behavior will be discussed in the upcoming Section 5.3 on binder distribution.

5.3. Additive Distribution

If the size of the additives is smaller than the pore opening between the primary particles, they can enter the pore network of the secondary particles together with the solvent. The oscillation measurements in Section 5.1 have already indicated that this is likely to be the case for a PVDF binder. EDS mapping of the secondary particle cross-sections does indeed show the presence of fluorine, which is used as a marker for the PVDF, both around and within the secondary particles (Figure 10 center). On the other hand, no carbon can be detected inside the secondary particles (Figure 10 right). Therefore, penetration of the conductive additives used, carbon black and graphite, has not occurred.

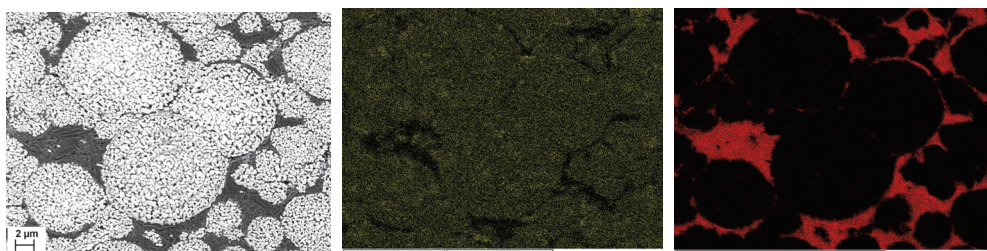


Figure 10. SEM micrograph of an electrode with porous NCM111 particles (left). Corresponding EDS mapping shows fluorine (center) and carbon (right). Images have identical magnification (Scale bar 2 μm).

Polymers form a compliant random coil structure whose dimensions depend on their interaction with the solvent. For example, the z-average radius of gyration of PVDF binder molecules in NMP, is in the range of 100 nm and less [17]. This allows them to enter the pores of the hierarchically structured NMC111 particles studied, which have a mean pore entry size of about 150 nm (see Section 5.4). Carbon black particles typically consist of aggregates of chemically bound primary particles, here with an average diameter of

150 nm for the Super C65 additive used, expressed as the Stokes diameter [8]. This should theoretically allow a minor fraction to penetrate the pores of the secondary particles too. However, carbon black aggregates are always associated with the PVDF to form so-called carbon black-binder domains (CBDs) [18]. The size of these domains depends on the length of the polymer chains and on the efficiency of the dispersion process. In the slurry used, the CBDs are so large that they are prevented from entering the pores of the hierarchically structured particles. As a result, the carbon black and graphite particles, which are also too large, remain in the interparticular pores around the secondary particles and do not penetrate them.

In a typical PVDF slurry formulation, only a fraction of the binder is bound to the surface of the active material or in a CBD. There is also dissolved binder that is not fixed to the surface of a particle. It is this free binder that enters the intragranular pores of the secondary particles, where it remains after drying. In this position it does not contribute to the cohesion between the particles or to the adhesion to the current collector, which explains the reduced adhesion strength of these electrodes (Figure 9 left). Without an additional binder to compensate [21], low adhesion can cause delamination between the additives, the CAM, and the aluminum foil increasing the contact resistance within the electrode [15,22]. The unbound portion of the binder is also responsible for the binder migration as described in Section 5.2, whereas a fixed binder has a limited mobility and is therefore little affected by high drying rates. In fact, binder migration also seems to occur when the porous particles empty in the second phase of the drying process (Figure 8D). With more intense drying, it appears that some of the incorporated binder migrates out, increasing the adhesion strength again. Therefore, at a sufficiently high drying rate, the loss of binder should no longer have a negative effect compared to dense particles, where a larger fraction of the binder is prone to binder migration. In this case, an additional benefit could be derived from pore infiltration as the migrated binder accumulates on the electrode surface, where it blocks ion transport. By fixing the binder in and around the particles, this negative effect can be eliminated and an improved rate capability is observed for porous particles [19].

In waterborne formulations, the situation is more complex because a two-component binder system is typically used. A dissolved polymeric binder such as carboxymethylcellulose (CMC) is augmented by a latex binder dispersion. The size of the latex particles is typically 100–200 nm. This may be small enough to allow pore penetration. However, penetration is hindered because the latex particles easily tend to clog the pore entrances. Since the CMC has the higher affinity for carbon black, virtually all of it is bound in the CBD. Therefore, in aqueous processing, the binder is located in the interparticular pores and hardly any binder is found in the intragranular pores.

5.4. Compaction Behavior

Mercury intrusion studies of uncalendered electrodes with hierarchically structured NMC111 particles reveal the existence of two distinct pore fractions (Figure 11 right). Micron-sized pores belong to the interparticular voids that are also present in electrodes made of dense particles of the same size (Figure 11 left). Calendering reduces the size of these pores only moderately for compact particles, but very effectively for porous particles, and can eliminate them completely at high densification. The pronounced pore fraction of porous particles at about 100 nm is due to the intragranular porosity. Unlike interparticular pores, intragranular pore diameters are not reduced by intensive calendering. A slight decrease in volume indicates that the pore entrance of some of the particles seems to be blocked. The broad pore fraction below 1000 nm belongs to the pores in the CBD. Moderate compression to 40% changes the porosity of the CBD only slightly for compact particles (Figure 11 left). In the case of porous particles, more densification is required to achieve a comparable overall porosity. The CBD are also densified, so that the large pores within the CBD disappear leaving mainly small pores with pore size smaller than the intragranular pores.

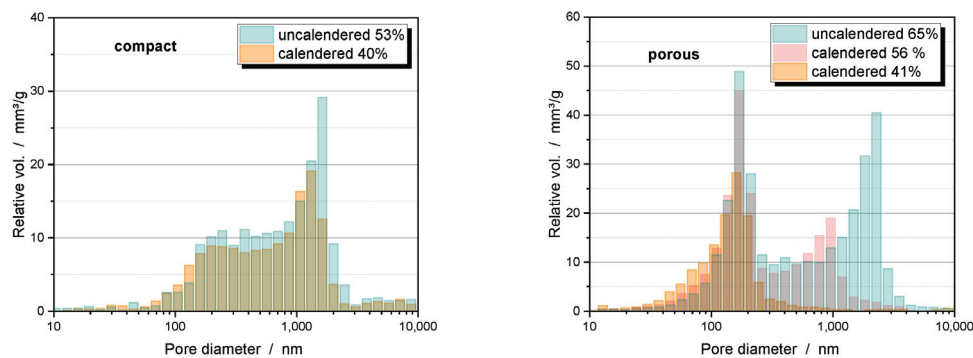


Figure 11. Pore size distribution of uncalendered and calendered electrodes of compact particles (**left**) and hierarchically structured NCM111 particles (**right**) at different porosities. The binder used was PVDF.

The development of pores during calendaring is the result of a unique consolidation behavior of hierarchically structured particles. While compact particles are destroyed by high compaction forces [23], the porous particles can sometimes be deformed without defragmentation (Figure 12, left) [21]. As a result, they can be plastically compacted until the interparticular pores are eliminated and only the plastically deformable CBD remain in the voids between the secondary particles [15]. This behavior is due to PVDF bridges formed by the binder phase within these particles (Figure 12, right). They keep the particles together after the sinter bridges between the primary particles are broken and provide structural integrity. In waterborne formulations, this effect is not observed because the binders have less tendency to penetrate the secondary particles.

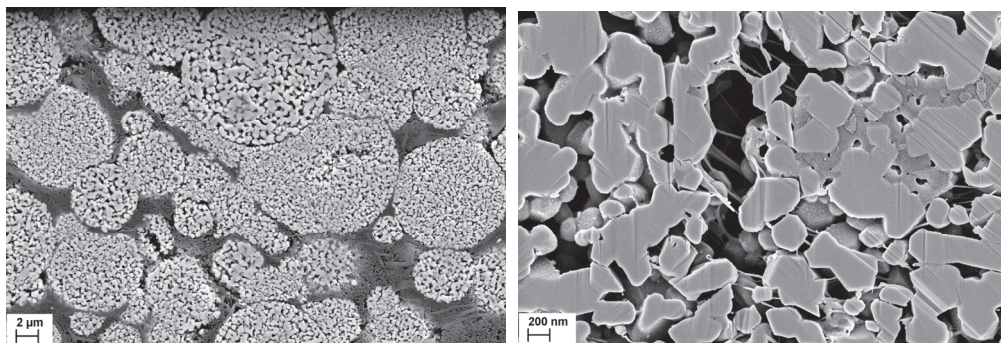


Figure 12. Cross-section of an electrode with deformed, hierarchically structured NMC111 particles after calendaring to ~40% porosity (**left**, scale bar 2 µm). Magnification with PVDF fiber bridges within the secondary particles proofing binder penetration (**right**, scale bar 200 nm).

The tendency for plastic deformation appears to correlate with the primary particle size. Granules that deform more than their neighbors consist of finer primary particles and have weaker sinter bridges. The most likely cause of different primary particle sizes is an inhomogeneous temperature profile within the calcination furnace. As a result, grain growth and sinter neck formation are less pronounced in colder regions, resulting in granules that are less rigid.

The compaction of the electrode reduces the electrical resistance and increases the ionic resistance within the pore structure [15]. While the electrical resistance of compact and porous particles exhibits similar behavior, there are clear differences in ionic resistance. Investigations using electrochemical impedance spectroscopy (EIS) show that the ionic resistance, and from this the tortuosity of the electrode, only increases moderately for compact particles (Figure 13 left), because the continuous system of interparticular pores used for ion transport remains nearly intact even at high densification. With porous particles, these pores can be eliminated due to the deformability of the particles until only

the intragranular porosity and the pores within the CBD remain (Figure 13 right). The intragranular porosity is quite resistant to further densification. The pores in the CBD can be further compacted until they are also closed. However, this prevents the transport of ions through the CBD and the transport paths for the ions are considerably extended. The effect is further enhanced by graphite platelets, which are often added as an additive to improve the electrical conductivity and the compaction behavior of the electrodes. (Figure 13 right). The critical porosity at which this occurs, and at which the tortuosity increases significantly, is well above the minimum porosity that can be achieved with compact particles, although a much higher degree of compaction is required to get the porous particles to this point. Further densification of the pore structure leads to a large increase in tortuosity, and thus to higher ionic resistance, which affects the electrochemical properties of the cell. Therefore, a higher overall electrode porosity must be accepted when using porous particles. Although the intragranular porosity can still be used as a network for lithium-ion transport, the clogging of the CBD prevents an efficient contribution of these pores to the ion transport conditions in the electrode.

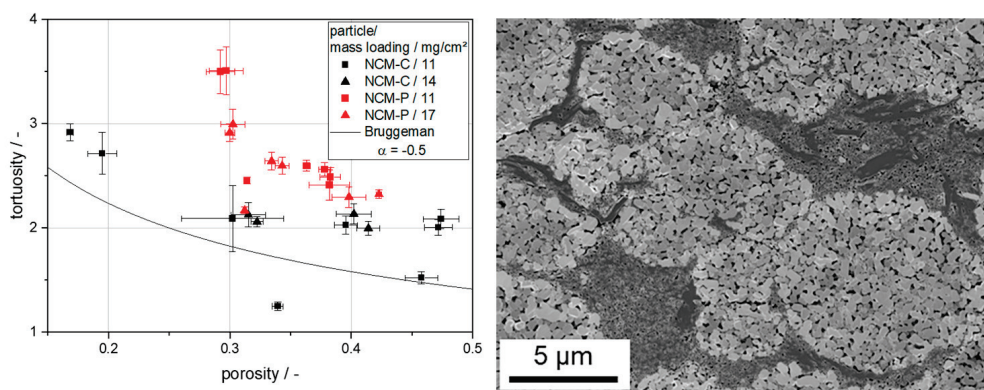


Figure 13. Tortuosity trends during calendaring of electrodes with compact or porous NCM111 (left). Electrode cross-section with porous particles and compacted CBD at a porosity of 30%. The CBD contains carbon black and graphite particles (right) (Reprinted from Ref. [15] under CC-BY-4.0 license).

6. Electrochemical Properties

Hierarchically structured cathodes with porous NCM111 particles show significantly improved rate capability compared to the pristine dense material, when cycled against graphite anodes in pouch cell configuration (Figure 14). This is particularly evident at higher C-rates where the cells can benefit from the shortened solid-state diffusion length. A hierarchically structured half-cell model, which allows the discussion of the local lithium concentration distribution in the solid phase, shows that nanostructured secondary particles benefit not only from the reduced diffusion length but also from a more homogeneous lithium concentration distribution at higher C-rates. In this way, the available active material capacity can be better utilized, which also leads to improved performance [24]. The model also states that the rate-limiting factor for cathodes with dense particles is the diffusion coefficient of the active material, whereas it plays a minor role for hierarchically structured cathodes. Here, the combination of electronic conductivity and connectivity between the primary particles is rate-limiting. Interestingly, an improved capacity can be observed even in the slow formation cycles at C/20. Under these conditions, the electrodes do not benefit from the kinetic advantages of the small primary particles. However, the significantly higher electrochemically active area of the porous material also reduces the charge transfer resistance [5] and decreases the activation overpotential at the particle-electrolyte interphase, leading to a reduced potential rise during charging [25]. In summary, at low C-rates a higher electrochemically active area with reduced phase transfer resistance contributes to the superior capacity, while at high C-rates the shorter diffusion pathways are the main advantage of hierarchically structured electrodes.

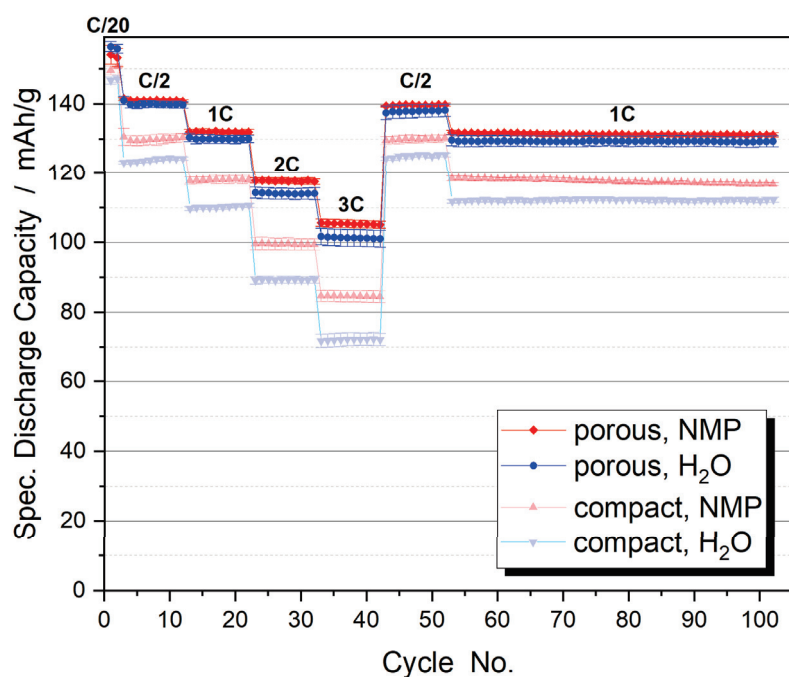


Figure 14. Specific discharge capacities of full cells with varying C-rates for compact NCM111 and hierarchically structured porous NCM111 particles (symmetrical CC charging). Slurry processing was carried out with NMP (red) or H₂O (blue). Electrode porosity is 45%.

The advantages of nanoscale particles are also evident in the aging behavior of the cycled electrodes (Figure 15). The hierarchically structured electrodes show a significantly slower capacity decrease than the electrodes with compact particles. This is probably due to the state of the aged active material particles [21,22]. While the micro-sized compact particles show numerous cracks due to the mechanical stresses generated during cycling, the hierarchically structured particles do not show any large cracks (Figure 16). As expected, the small size of the primary particles leads to lower stress numbers and thus reduces the formation of cracks. The secondary particle structures are not destroyed after more than 1000 cycles. Where cracks occur between the primary particles, the contact is not broken because the two particles can still be held together by binder bridges. In large compact particles, crack formation causes a portion of the particles to lose electrical connectivity resulting in a significant loss of active material over the course of cycling [26].

An interesting result is found for the aqueous processing of the electrodes. One would expect that the increased surface area of the porous particles leads to more interaction with water, resulting in a decrease in capacity and increased degradation. In fact, aqueous processing of hierarchically structured electrodes with porous NCM111 particles results in a rate capability (Figure 14, blue dots) and aging behavior (Figure 15, blue dots) similar to that obtained when NMP is used as the solvent. In contrast, dense NCM111 particles show a significant capacity loss in water, although they do not show extensive aging. Specific advantages of the hierarchically structured electrodes seem to compensate for a stronger interaction with water. For example, a cleaning process could take place during the synthesis of the porous particles or structural defects could heal during calcination. These effects should be the subject of future investigations.

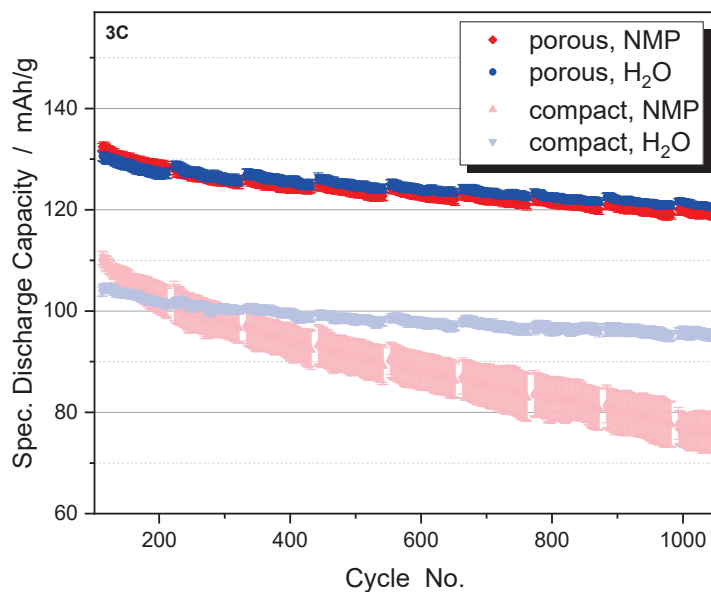


Figure 15. Aging behavior of compact NCM111 and hierarchically structured porous NCM111 particles (CCCV charging at 2C, 3C discharging). Slurry processing was carried out with NMP (red) or H₂O (blue). Electrode porosity is 45%.

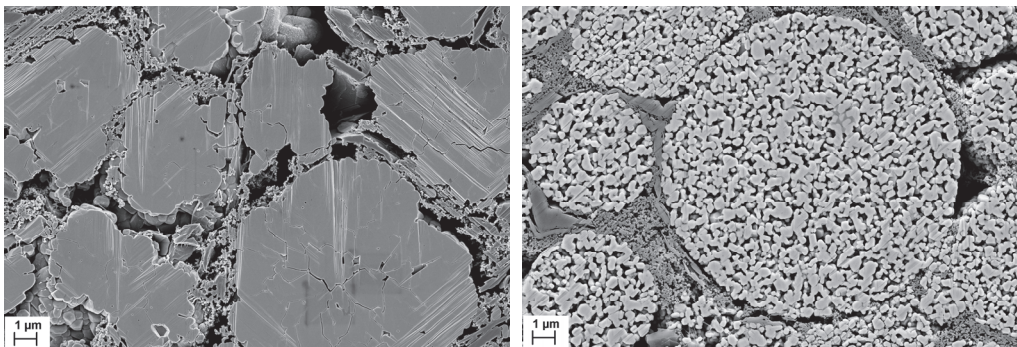


Figure 16. SEM micrographs of electrode cross-sections after 1100 cycles of compact (left) and porous (right) NCM111 particles. Processing was carried out with NMP/PVDF slurry (scale bars are 1 μm).

7. Outlook: Post-Lithium Batteries

Post-lithium batteries using sodium, potassium, magnesium, aluminum, etc., as active elements are of particular interest as low-cost and sustainable alternatives to lithium-ion batteries [27–29]. These systems offer interesting applications for hierarchically structured materials. Due to the larger ions, intercalation/deintercalation leads to larger stresses in the material. Multivalent ions have extremely low diffusion coefficients allowing only a small penetration depth. Therefore, the use of a nanoscale material is necessary to ensure high energy densities and sufficient lifetime, and hierarchically structured particles may be the only chance to establish these materials in commercial applications.

An example of a sodium-ion battery material is Na₃V₂(PO₄)₃ (NVP). It features a highly stable three-dimensional NASICON structure and offers large Na diffusion pathways [30]. However, like all sodium super-ionic conductors it has remarkably low electronic conductivity [31]. To make this material suitable for batteries, it is either necessary to reduce the particle size [32,33] or to combine it with a conductive carbon matrix [34]. The preparation of a hierarchically structured material makes it possible to combine both approaches in a single particle system. SEM micrographs of nanoporous composite particles consisting of an NVP matrix with an embedded carbon phase and an intrinsic porosity of up to 54% are shown in Figure 17. They were synthesized via a bottom-up approach and

show excellent cycling stability when used as either a cathode or anode material [35] or within full cells [36].

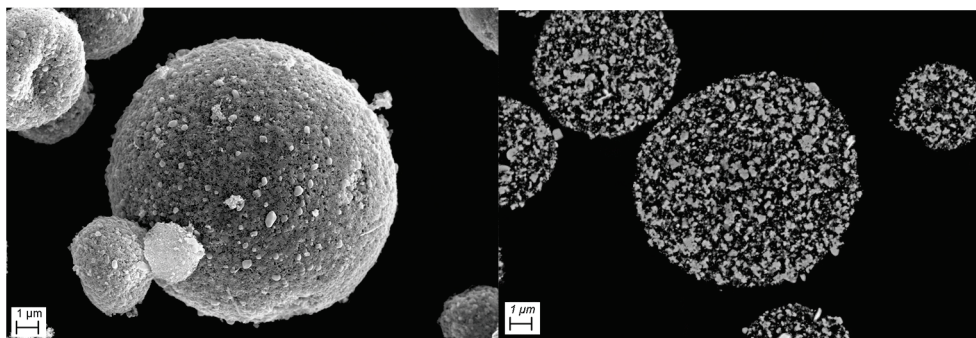


Figure 17. SEM micrograph of NVP/C composite particles (**left**), corresponding cross-sections (**right**). Scale bars are 1 μm .

8. Summary

Hierarchically structured electrode materials combine the advantages of nanomaterials in terms of ion transport and lower susceptibility to mechanically induced defects with the better packing density of micro-sized particles. For this purpose, nanoscale primary particles are granulated to form secondary structures at the microscale. A calcination step is necessary to produce mechanically stable particles with an open pore phase that can be processed similarly to established electrode materials. Electrodes made from this material have a hierarchically structured porosity, i.e., in addition to the usual microscale interparticle pores, there are nanoscale intragranular pores that can be penetrated by the electrolyte. The expected advantages of this setup are confirmed by the improved rate capability and lifetime of the electrodes. Since only short distances need to be bridged by means of solid-state diffusion, high capacities can be achieved even at high C-rates. The increased specific surface area also reduces the phase transfer resistance, which increases the charge capacity even at low C-rates. The small size of the primary particles results in less mechanical stress due to the volume changes during cycling, which increases cell life by reducing particle cracking. Benefits have also been demonstrated for the aqueous processing of cathode materials, as no additional material degeneration is observed despite the increased reaction area with water, and cycling performance is comparable to processing with NMP.

The advantages of nanostructured particles and electrodes are partially offset by the disadvantages of increased additive requirements and reduced energy density. The open pore phase can absorb some of the additives, which then no longer provide the intended effects and must be replaced, for example by additional binder to ensure equivalent adhesion. However, the infiltrated binder has the advantage of holding the primary particles together, even if cracks form in the porous secondary particles during calendaring. As a result, the particles have a quasi-plastic deformation behavior that enables complete elimination of interparticle porosity until only intragranular porosity and the pores in the CBD remain in the electrode. Further densification also occludes the CBD and blocks them to the ions. Although the residual porosity within the secondary particles is still higher than the porosity level achievable by calendaring compact particles, the transport paths lengthen and the ion resistance in the electrode increases significantly so that the advantage of the open particle porosity for ion transport is lost.

The hierarchically structured materials approach is therefore of particular interest for active materials with low electrical or ionic conductivity. Commercial lithium iron phosphate (LFP) materials often have particles with a composite structure and internal porosity. Other examples are fluoride-based cathode materials or many active materials for post-lithium systems, which cannot achieve near-application energy densities without a massively reduced particle size. While improved rate capability and reduced aging are

offset by lower energy density, it is important to consider whether the additional effort in particle synthesis is worthwhile. Nevertheless, it is often only hierarchically structured electrodes that enable the use of such materials in competitive cells.

Author Contributions: Investigation, M.M., L.S., M.H., N.B. and J.K.; writing—original draft preparation, W.B.; writing—review and editing, M.M., L.S., J.R.B. and J.K.; visualization, W.B., M.M., and J.K.; supervision, P.S., W.S. and H.E.; project administration, W.B., J.R.B., P.S., W.S. and H.E.; funding acquisition, W.B., J.R.B., P.S., W.S. and H.E. All authors have read and agreed to the published version of the manuscript.

Funding: This work contributes to the research performed at CELEST (Center for Electrochemical Energy Storage Ulm Karlsruhe) and the Material Research Center for Energy Systems (MZE). It was funded by the Deutsche Forschungsgemeinschaft (DFG, German Research Foundation) under Germany's Excellence Strategy—EXC 2154—Project number 390874152 (POLiS Cluster of Excellence) and by the German Federal Ministry for Economic Affairs and Climate Action (BMWK) under reference number 03ETE039J.

Data Availability Statement: Data that support the findings are available from the corresponding author upon reasonable request.

Conflicts of Interest: The authors declare no conflicts of interest.

References

- Meng, Z.; Ma, X.; Azhari, L.; Hou, J.; Wang, Y. Morphology controlled performance of ternary layered oxide cathodes. *Commun. Mater.* **2023**, *4*, 90. [CrossRef]
- Ren, D.; Padgett, E.; Yang, Y.; Shen, L.; Shen, Y.; Levin, B.D.A.; Yu, Y.; Disalvo, F.J.; Muller, D.A.; Abruña, H.D. Ultrahigh Rate Performance of a Robust Lithium Nickel Manganese Cobalt Oxide Cathode with Preferentially Orientated Li-Diffusing Channels. *ACS Appl. Mater. Interfaces* **2019**, *11*, 41178–41187. [CrossRef] [PubMed]
- Jiang, M.; Zhang, Q.; Wu, X.; Chen, Z.; Danilov, D.L.; Eichel, R.A.; Notten, P.H.L. Synthesis of Ni-Rich Layered-Oxide Nanomaterials with Enhanced Li-Ion Diffusion Pathways as High-Rate Cathodes for Li-Ion Batteries. *ACS Appl. Energy Mater.* **2020**, *3*, 6583–6590. [CrossRef]
- Yang, Z.; Lu, J.; Bian, D.; Zhang, W.; Yang, X.; Xia, J.; Chen, G.; Gu, H.; Ma, G. Stepwise co-precipitation to synthesize $\text{LiNi}_{1/3}\text{Co}_{1/3}\text{Mn}_{1/3}\text{O}_2$ one-dimensional hierarchical structure for lithium ion batteries. *J. Power Sources* **2014**, *272*, 144–151. [CrossRef]
- Lin, B.; Wen, Z.; Gu, Z.; Huang, S. Morphology and electrochemical performance of $\text{Li}[\text{Ni}_{1/3}\text{Co}_{1/3}\text{Mn}_{1/3}]\text{O}_2$ cathode material by a slurry spray drying method. *J. Power Sources* **2008**, *175*, 564–569. [CrossRef]
- Oljaca, M.; Blizanac, B.; Du Pasquier, A.; Sun, Y.; Bontchev, R.; Suszko, A.; Wall, R.; Koehlert, K. Novel $\text{Li}(\text{Ni}_{1/3}\text{Co}_{1/3}\text{Mn}_{1/3})\text{O}_2$ cathode morphologies for high power Li-ion batteries. *J. Power Sources* **2014**, *248*, 729–738. [CrossRef]
- Wagner, A.C.; Bohn, N.; Geßwein, H.; Neumann, M.; Osenberg, M.; Hilger, A.; Manke, I.; Schmidt, V.; Binder, J.R. Hierarchical Structuring of NMC111-Cathode Materials in Lithium-Ion Batteries: An In-Depth Study on the Influence of Primary and Secondary Particle Sizes on Electrochemical Performance. *ACS Appl. Energy Mater.* **2020**, *3*, 12565–12574. [CrossRef]
- Deng, W.N.; Li, Y.H.; Xu, D.F.; Zhou, W.; Xiang, K.X.; Chen, H. Three-dimensional hierarchically porous nitrogen-doped carbon from water hyacinth as selenium host for high-performance lithium–selenium batteries. *Rare Met.* **2022**, *41*, 3432–3445. [CrossRef]
- Naumann, J.; Bohn, N.; Birkholz, O.; Neumann, M.; Müller, M.; Binder, J.R.; Kamlah, M. Morphology-Dependent Influences on the Performance of Battery Cells with a Hierarchically Structured Positive Electrode. *Batter. Supercaps* **2023**, *6*, e202300264. [CrossRef]
- Chen, D.; Kramer, D.; Mönig, R. Chemomechanical fatigue of $\text{LiMn}_{1.95}\text{Al}_{0.05}\text{O}_4$ electrodes for lithium-ion batteries. *Electrochim. Acta* **2018**, *259*, 939–948. [CrossRef]
- Spahr, M.E.; Goers, D.; Leone, A.; Stallone, S.; Grivei, E. Development of carbon conductive additives for advanced lithium ion batteries. *J. Power Sources* **2011**, *196*, 3404–3413. [CrossRef]
- Bockholt, H.; Haselrieder, W.; Kwade, A. Intensive powder mixing for dry dispersing of carbon black and its relevance for lithium-ion battery cathodes. *Powder Technol.* **2016**, *297*, 266–274. [CrossRef]
- McLachlan, D.S.; Blazkiewicz, M.; Newnham, R.E. Electrical Resistivity of Composites. *J. Am. Ceram. Soc.* **1990**, *73*, 2187–2203. [CrossRef]
- Radin, M.D.; Hy, S.; Sina, M.; Fang, C.; Liu, H.; Vinckeviciute, J.; Zhang, M.; Whittingham, M.S.; Meng, Y.S.; Van der Ven, A. Narrowing the Gap between Theoretical and Practical Capacities in Li-Ion Layered Oxide Cathode Materials. *Adv. Energy Mater.* **2017**, *7*, 1–33. [CrossRef]
- Schneider, L.; Klemens, J.; Herbst, E.C.; Müller, M.; Scharfer, P.; Schabel, W.; Bauer, W.; Ehrenberg, H. Transport Properties in Electrodes for Lithium-Ion Batteries: Comparison of Compact versus Porous NCM Particles. *J. Electrochem. Soc.* **2022**, *169*, 100553. [CrossRef]

16. Loeffler, N.; Kim, G.T.; Mueller, F.; Diemant, T.; Kim, J.K.; Behm, R.J.; Passerini, S. In Situ Coating of $\text{Li}[\text{Ni}_{0.33}\text{Mn}_{0.33}\text{Co}_{0.33}]\text{O}_2$ Particles to Enable Aqueous Electrode Processing. *ChemSusChem* **2016**, *9*, 1112–1117. [CrossRef] [PubMed]
17. Lutringer, G.; Weill, G. Solution properties of poly(vinylidene fluoride): 1. Macromolecular characterization of soluble samples. *Polymer* **1991**, *32*, 877–883. [CrossRef]
18. Wood, M.; Li, J.; Ruther, R.E.; Du, Z.; Self, E.C.; Meyer, H.M.; Daniel, C.; Belharouak, I.; Wood, D.L. Chemical stability and long-term cell performance of low-cobalt, Ni-Rich cathodes prepared by aqueous processing for high-energy Li-Ion batteries. *Energy Storage Mater.* **2020**, *24*, 188–197. [CrossRef]
19. Klemens, J.; Schneider, L.; Herbst, E.C.; Bohn, N.; Müller, M.; Bauer, W.; Scharfer, P.; Schabel, W. Drying of NCM Cathode Electrodes with Porous, Nanostructured Particles Versus Compact Solid Particles: Comparative Study of Binder Migration as a Function of Drying Conditions. *Energy Technol.* **2022**, *10*, 2100985. [CrossRef]
20. Zhang, Y.S.; Courtier, N.E.; Zhang, Z.; Liu, K.; Bailey, J.J.; Boyce, A.M.; Richardson, G.; Shearing, P.R.; Kendrick, E.; Brett, D.J.L. A review of lithium-ion battery electrode drying: Mechanisms and metrology. *Advanced Energy Materials* **2022**, *12*, 2102233. [CrossRef]
21. Muller, M.; Schneider, L.; Bohn, N.; Binder, J.R.; Bauer, W. Effect of Nanostructured and Open-Porous Particle Morphology on Electrode Processing and Electrochemical Performance of Li-Ion Batteries. *ACS Appl. Energy Mater.* **2021**, *4*, 1993–2003. [CrossRef]
22. Dreizler, A.M.; Bohn, N.; Geßwein, H.; Müller, M.; Binder, J.R.; Wagner, N.; Friedrich, K.A. Investigation of the Influence of Nanostructured $\text{LiNi}_{0.33}\text{Co}_{0.33}\text{Mn}_{0.33}\text{O}_2$ Lithium-Ion Battery Electrodes on Performance and Aging. *J. Electrochem. Soc.* **2018**, *165*, A273–A282. [CrossRef]
23. Oswald, S.; Pritzl, D.; Wetjen, M.; Gasteiger, H.A. Novel Method for Monitoring the Electrochemical Capacitance by In Situ Impedance Spectroscopy as Indicator for Particle Cracking of Nickel-Rich NCMs: Part I. Theory and Validation. *J. Electrochem. Soc.* **2020**, *167*, 100511. [CrossRef]
24. Birkholz, O.; Kamlah, M. Electrochemical Modeling of Hierarchically Structured Lithium-Ion Battery Electrodes. *Energy Technol.* **2021**, *9*, 2000910. [CrossRef]
25. Lu, X.; Daemi, S.R.; Bertei, A.; Kok, M.D.R.; O'Regan, K.B.; Rasha, L.; Park, J.; Hinds, G.; Kendrick, E.; Brett, D.J.L.; et al. Microstructural Evolution of Battery Electrodes During Calendering. *Joule* **2020**, *4*, 1–23. [CrossRef]
26. Ryu, H.H.; Park, N.Y.; Noh, T.C.; Kang, G.C.; Maglia, F.; Kim, S.J.; Yoon, C.S.; Sun, Y.K. Microstrain Alleviation in High-Energy Ni-Rich NCMA Cathode for Long Battery Life. *ACS Energy Lett.* **2021**, *6*, 216–223. [CrossRef]
27. Kundu, D.; Talaie, E.; Duffort, V.; Nazar, L.F. The emerging chemistry of sodium ion batteries for electrochemical energy storage. *Angew. Chem. Int. Ed.* **2015**, *54*, 3432–3448. [CrossRef]
28. Wang, Y.; Chen, R.; Chen, T.; Lv, H.; Zhu, G.; Ma, L.; Wang, C.; Jin, Z.; Liu, J. Emerging non-lithium ion batteries. *Energy Storage Mater.* **2016**, *4*, 103–129. [CrossRef]
29. Ponrouch, A.; Bitenc, J.; Dominko, R.; Lindahl, N.; Johansson, P.; Palacin, M.R. Multivalent rechargeable batteries. *Energy Storage Mater.* **2019**, *20*, 253–262. [CrossRef]
30. Song, W.; Ji, X.; Wu, Z.; Zhu, Y.; Yang, Y.; Chen, J.; Jing, M.; Li, F.; Banks, C.E. First exploration of Na-ion migration pathways in the NASICON structure $\text{Na}_3\text{V}_2(\text{PO}_4)_3$. *J. Mater. Chem. A* **2014**, *2*, 5358–5362. [CrossRef]
31. Lan, T.; Ma, Q.; Tsai, C.L.; Tietz, F.; Guillon, O. Ionic Conductivity of $\text{Na}_3\text{V}_2\text{P}_3\text{O}_{12}$ as a Function of Electrochemical Potential and its Impact on Battery Performance. *Batter. Supercaps* **2021**, *4*, 479–484. [CrossRef]
32. Jiang, Y.; Yang, Z.; Li, W.; Zeng, L.; Pan, F.; Wang, M.; Wei, X.; Hu, G.; Gu, L.; Yu, Y. Nanoconfined carbon-coated $\text{Na}_3\text{V}_2(\text{PO}_4)_3$ particles in mesoporous carbon enabling ultralong cycle life for sodium-ion batteries. *Adv. Energy Mater.* **2015**, *5*, 1402104. [CrossRef]
33. Zheng, W.; Huang, X.; Ren, Y.; Wang, H.; Zhou, S.; Chen, Y.; Ding, X.; Zhou, T. Porous spherical $\text{Na}_3\text{V}_2(\text{PO}_4)_3/\text{C}$ composites synthesized via a spray drying -assisted process with high-rate performance as cathode materials for sodium-ion batteries. *Solid State Ion.* **2017**, *308*, 161–166. [CrossRef]
34. Jian, Z.; Zhao, L.; Pan, H.; Hu, Y.S.; Li, H.; Chen, W.; Chen, L. Carbon coated $\text{Na}_3\text{V}_2(\text{PO}_4)_3$ as novel electrode material for sodium ion batteries. *Electrochem. Commun.* **2012**, *14*, 86–89. [CrossRef]
35. Akçay, T.; Häringer, M.; Pfeifer, K.; Anhalt, J.; Binder, J.R.; Dsoke, S.; Kramer, D.; Mönig, R. $\text{Na}_3\text{V}_2(\text{PO}_4)_3$ -A Highly Promising Anode and Cathode Material for Sodium-Ion Batteries. *ACS Appl. Energy Mater.* **2021**, *4*, 12688–12695. [CrossRef]
36. Stüble, P.; Müller, C.; Klemens, J.; Scharfer, P.; Schabel, W.; Häringer, M.; Binder, J.R.; Hofmann, A.; Smith, A. Enabling Long-term Cycling Stability of $\text{Na}_3\text{V}_2(\text{PO}_4)_3/\text{C}$ vs. Hard Carbon Full-cells. *Batter. Supercaps* **2023**, *2*, e202300375. [CrossRef]

Disclaimer/Publisher's Note: The statements, opinions and data contained in all publications are solely those of the individual author(s) and contributor(s) and not of MDPI and/or the editor(s). MDPI and/or the editor(s) disclaim responsibility for any injury to people or property resulting from any ideas, methods, instructions or products referred to in the content.



Article

Electrochemical Performance of Thick-Film $\text{Li}(\text{Ni}_{0.6}\text{Mn}_{0.2}\text{Co}_{0.2})\text{O}_2$ Cathode with Hierarchic Structures and Laser Ablation

Zelai Song ^{1,2}, Penghui Zhu ^{1,*}, Wilhelm Pfleging ¹ and Jiyu Sun ²

¹ Institute for Applied Materials—Applied Materials Physics (IAM-AWP), Karlsruhe Institute of Technology, Hermann-von-Helmholtz-Platz 1, 76344 Eggenstein-Leopoldshafen, Germany; songzelai@foxmail.com (Z.S.); wilhelm.pfleging@kit.edu (W.P.)

² Key Laboratory of Bionic Engineering (Ministry of Education, China), Jilin University, Changchun 130022, China; sjy@jlu.edu.cn

* Correspondence: penghui.zhu@kit.edu

Abstract: The electrochemical performance of lithium-ion batteries is directly influenced by type of active material as well as its morphology. In order to evaluate the impact of particle morphology in thick-film electrodes, $\text{Li}(\text{Ni}_{0.6}\text{Mn}_{0.2}\text{Co}_{0.2})\text{O}_2$ (NMC 622) cathodes with bilayer structure consisting of two different particle sizes were manufactured and electrochemically characterized in coin cells design. The hierarchical thick-film electrodes were generated by multiple casting using NMC 622 (TA) with small particle size of 6.7 μm and NMC 622 (BA) with large particle size of 12.8 μm . Besides, reference electrodes with one type of active material as well as with two type of materials established during mixing process (BT) were manufactured. The total film thickness of all hierarchical composite electrodes were kept constant at 150 μm , while the thicknesses of TA and BA were set at 1:2, 1:1, and 2:1. Meanwhile, three kinds of thin-film cathodes with 70 μm were applied to represent the state-of-the-art approach. Subsequently, ultrafast laser ablation was applied to generate groove structures inside the electrodes. The results demonstrate that cells with thin-film or thick-film cathode only containing TA, cells with bilayer electrode containing TBA 1:2, and cells with laser-structured electrodes show higher capacity at C/2 to 5C, respectively.

Keywords: lithium-ion battery; cathodes; NMC 622; multilayer; hierarchical structure; laser structure; cyclic voltammetry; impedance spectroscopy

1. Introduction

Lithium-ion batteries (LIBs) are widely used in daily life for electric vehicles, mobile applications, and electric energy storage devices [1,2]. Although they had been making our lives convenient and clean, their charge and discharge capacity needed to be improved with the development of electronic devices [3]. The cathode and anode can influence the electrochemical performance of LIBs. Lithium-ion migration in electrodes is the necessary electrochemical process to store energy [4]. $\text{LiNi}_{1-x-y}\text{Mn}_x\text{Co}_y\text{O}_2$ (NMC) materials are very promising candidates for energy storage due to their high energy density and excellent charge-discharge capacity compared to LiCoO_2 , LiMn_2O_4 (LMO), and LiNiO_2 [5], and NMC 622 is a cathode material with a higher specific discharge capacity of 170 mAh/g (2.5–4.3 V) than NMC 111, LFP, and LCO [6]. Increasing the electrode thickness can improve LIBs' areal capacity, but the performance at higher C-rates is limited as a result of the degradation of the thick-film electrode [7]. The poor lithium-ion diffusion kinetics in cells with thick-film NMC electrodes lead to poor rate capability, capacity loss at high current rate, and low capacity retention during long-term cycling due to an increased cell polarization [8]. Increasing the thickness or reducing porosity of thick-film electrodes can achieve high specific energy [9]. Therefore, other methods

such as laser processing is of great importance for batteries with thick-film electrodes to achieve high energy density as well as high power at the same time.

The application of ultrafast laser processing in manufacturing of LIBs has attracted more and more attention. Laser electrode cutting can improve the qualities of the cut edges, forming less debris while shortening the processing time [1], and therefore is advantageous for industrial mass production. Recent studies show that electrochemical performances of LIBs containing laser-structured electrodes are enhanced using different laser patterning [10], such as lines [11], grids [12], and holes [13]. Cells with laser-structured NMC and LMO electrodes exhibit increased capacity retention and longer cycle life-time while being cycled at 1C [14]. In comparison to cells with unstructured electrodes, the lithium-ion diffusion kinetics in cells with structured electrodes are higher due to new diffusion pathways along the sidewalls of channel or grid structures. Besides, the cell polarization of cells with structured electrodes is decreased. These advantages lead to simultaneous enhancement of power and energy densities of electrodes [9,15]. Therefore, their charge/discharge rate and specific energy density at cell level can be greatly increased [11,16]. For example, a recent study showed that cells containing thick-film laser-structured NMC 622 electrodes exhibit higher discharge capacities at C/2 to 5C compared with the ones without structures [17].

The cycle stability and the energy density of LIBs can be influenced by the thickness of electrodes [18]. The power of LIBs is reduced dramatically because the total internal resistance is strongly influenced by both ionic resistance in pores and charge-transfer resistance for lithium intercalation [19]. The additives of polyvinylidene difluoride (PVDF) binder and conductive carbon black in electrode can influence LIBs' electrochemical properties [20,21]. The high-energy LIBs can be achieved by the ultra-thick cathodes with thickness of up to 700 μm [22]. Besides, suitable electrolyte compositions, for example, with EC:EMC (3:7) as solvents and suitable additives, are needed to improve the cycling performance and reduce the volume expansion [23]. The optimal porosity of thick-film electrodes after calendaring should be adjusted to 30% to 40%, in order to increase electric contact between active material particles as well as between active materials and carbon black [24]. Another way to improve the electrochemical performance is by using blended active materials. Suitable materials blending leads not only to balancing the constituents' properties but also can surpass the performance of each constituent [25]. Nanomaterials are much more reactive than submicron particles such as $\text{LiMn}_{1/3}\text{Ni}_{1/3}\text{Co}_{1/3}\text{O}_2$ [26]. Two cathode materials, $\text{LiNi}_x\text{Co}_{1-x-y}\text{Al}_y\text{O}_2$ and LiMn_2O_4 , blended by physical mixtures minimize the shortcomings of the parent materials, and can be tailored to get a high power density or higher energy LIBs with the high stability and low cost [27]. The blended cathode displays an average electrochemical performance of the two cathode materials according to the simulation [28]. The material with high rate capability can help the other material to retain 75% capacity relative to the initial value during the long-term test [4]. Intermediate crystallite size NMC acquired by ball milling shows better performance, such as high rate capabilities compared to the base material [29,30]. The simulations reveal that coin cells with bilayer cathodes exhibit promising performance with 39% higher discharge capacity at 2C and an improved lithium-ion diffusion due to the small particle size [31].

In this paper, the electrochemical performance of hierarchical cathodes containing NMC 622 powders with different particle sizes is investigated. The multilayer thick-film electrodes with 150 μm thickness were manufactured by multiple casting using slurries containing NMC 622 powder with different particle size, while the thicknesses of electrode containing polycrystalline NMC 622 (BA) with large particle size of 12.8 μm and NMC 622 (TA) with small particle size of 6.7 μm were set at 1:2, 1:1, and 2:1. After drying and calendaring, different electrodes were structured using femtosecond (fs) fiber laser to generate line structures. Rate capability test, long-term test, cyclic voltammetry, as well as electrochemical impedance spectroscopy (EIS) were used to characterize coin cells assembled with different electrodes.

2. Materials and Methods

2.1. Cathode Materials

In order to manufacture cathodes with hierarchical structures, two commercially available NMC 622 powders were used in this work, which are single crystalline NMC 622 (TA, supplier 1) with small particle size of 6.7 μm , and polycrystalline NMC 622 (BA, supplier 2) with large particle size of 12.8 μm . The particle sizes of TA and BA were characterized using laser scattering particle size distribution analyzer (LA-950, Horiba Ltd., Kyoto, Japan). Polyvinylidene fluoride (PVDF) Solef[®] 5130 (Solvay Specialty Polymers, Paris, France) was used as binder, while carbon black C-ENERGY Super C65 (Imerys G & C Belgium, Willebroek, Belgium) and KS6L Graphite (Imerys G&C Switzerland Ltd., Bodio, Switzerland) were applied as conductive agent and compaction aid, respectively.

PVDF powder was dissolved in N-methyl-2-pyrrolidone solvent (NMP, Merck KGaA, Darmstadt, Germany) with a weight proportion of 1:10 and was homogenized using a planetary mixer (SpeedMixer DAC 150 SP, Hauschild GmbH & Co. KG, Hamm, Germany) with rotation speeds of 1000 to 3000 rpm for 30 min. Afterwards, electrode slurry was prepared with 92 wt.% NMC 622, 3 wt.% carbon black, 2 wt.% KS6L graphite, and 3 wt.% PVDF (dissolved in NMP) using SpeedMixer with rotation speeds of 1000 rpm to 3500 rpm for 1.5 h. During the mixing process, extra 3 g NMP was added into the cathode slurry to adjust the solid content of slurries to 66.7 wt.%.

Afterwards, cathode slurry was casted on a 20 μm aluminum foil on the film coater (MSK-AFA-L800-LD, MTI Corporation, Richmond, CA, USA) with a coating speed of 5 mm/s. A doctor blade (ZUA 2000.100, Proceq, Schwerzenbach, Switzerland) was used to control the wet film thickness of the cathode by adjusting the gap between the blade and current collector. To make the cathodes with hierarchical structure, the basis film was firstly casted and dried for 3 h at 90 °C. Then, the heater was turned off and the film as well as coater were cooled down to room temperature. The second film was subsequently casted on top of the previous film.

Three different types of cathodes were manufactured, which are with single type of NMC 622 powder; mixture of two NMC 622 powders in one film; and hierarchical structures with two layers containing different NMC 622 particle sizes. The total film thickness was kept constant at 150 μm , while the ratios of hierarchical films were set to 1:1 and 1:2 (2:1). In order to distinguish the position of different layers in the hierarchical films, the following abbreviations were used: TA represents the film with small NMC particles, while BA means the film with large NMC particles. According to the position of bottom film and upper film, different notations are used. For example, TBA indicates that TA layer with small particle size is at the bottom (near current collector), while BA layer is on the top. Therefore, BTA suggests that in this electrode, BA is the bottom layer and TA is the top layer. BT means that two NMC 622 powders were added simultaneously into the slurry during mixing process, thus no multilayer exists in final electrode. Besides, thin-film electrodes with 70 μm in thickness with single type of powder were manufactured as references representing the state-of-the-art approach.

The calendering procedure can achieve an overall homogenous cathode film thickness and improve the particle contact inside the cathode. According to other research, the optimal porosity of LIBs should be in the range of 30–40% [24]. Thus, the porosity of different cathodes in the work were adjusted to about 35% after calendering. The cathode film was calendered by an electric precision rolling press (MSK-2150, MTI Corporation, Richmond, CA, USA) at room temperature with a forward rolling speed of 35 mm/s. The porosity of electrodes is defined as follows [9]:

$$\text{Porosity} = \frac{V - W \left\{ \frac{C_{\text{NMC}}}{\rho_{\text{NMC}}} + \frac{C_{\text{Super C}}}{\rho_{\text{Super C}}} + \frac{C_{\text{KS6L Graphite}}}{\rho_{\text{KS6L Graphite}}} + \frac{C_{\text{PVDF}}}{\rho_{\text{PVDF}}} \right\}}{V} \times 100\% \quad (1)$$

where V is the volume of the composite electrode without current collector, C is the mass ratio of each material in the composite electrode, W is the weight per area, and ρ is the density of each material.

2.2. Laser Structuring

An ultrafast femtosecond fiber laser (Tangerine, Amplitude Systèmes, Pessac, France) with a pulse duration of 380 fs and an operational wavelength of 515 nm ($M^2 < 1.2$) was applied to generate laser structures and cut cathodes into 12 mm circles for coin cell assembly. The laser processing was performed in ambient air. Line structures with 200 μm pitch and with depths down to the current collector were generated, with a laser repetition rate of 500 kHz and an average laser power of 2.5 W. The laser scanning speed was kept constant at 500 mm/s, while the number of scan passes varied from 8 to 23 with regard to the active materials, film thickness, as well as hierarchical structures.

Cross-sectional analyses of electrodes using different scan passes were performed in order to find appropriate structuring parameters. Samples with a size of 2×1.3 cm (width \times height) were cut from the cathode film using the same laser. The laser-structured samples were held vertically with two glass sheets and fixed at the bottom using a plastic clip. They were placed in a holder filled with embedding solution consisted of resin, hardener and fluorescent powder. After 16 h drying, the samples were ground by a grinder-polisher (Ecoment 3, Buehler Ltd., Esslingen, Germany) and polished using a metallographic laboratory polisher (Saphir 350, ATM Qness GmbH, Mammelzen, Germany).

A scanning electron microscope (SEM, Phenom XL G2 Desktop, Thermo Fisher Scientific Inc.-FEI Deutschland GmbH, Dreieich, Germany) was used to obtain the images of two NMC 622 powders, the electrodes with hierarchical structures, and laser-structured electrodes. The crystal structure and the surface chemistry of electrode materials were investigated by X-ray diffraction (XRD) measurement. The XRD measurements (Empyrean, Malvern Panalytical Ltd., Malvern, UK) were performed using with $\text{CuK}\alpha$ radiation in 2θ range of $0\text{--}90^\circ$ (200 s/step) at 40 mA and 40 kV.

2.3. Coin Cell Assembly

The laser cut electrodes (diameter 12 mm) were stored in a vacuum oven (VT 6025, Heraeus GmbH, Hanau, Germany) at 130°C for 16 h. The cathodes were then assembled versus lithium foil in coin cells CR2032 in an argon-filled glove box with $\text{H}_2\text{O} < 0.1$ ppm and $\text{O}_2 < 0.1$ ppm (LABmaster sp, M. Braun Inertgas-Systeme GmbH, München, Germany). Each electrode was soaked in electrolyte for 30 min to be homogeneously and completely wetted. The electrolyte consists of ethylene carbonate and ethyl methyl carbonate (EC/EMC 3:7), with 1.3 M lithium hexafluorophosphate (LiPF_6) as conducting salt and 5 wt.% fluoroethylene carbonate (FEC) as additive, respectively. In total, 120 μL electrolyte were added into the coin cell. Polypropylene separator (Celgard, Charlotte, NC, USA) with a thickness of 25 μm and a diameter of 15 mm was used. After stacking, the coin cell was pressed together using an electric crimper machine (MSK-160E, MTI Corporation, Richmond, CA, USA).

2.4. Electrochemical Analysis

2.4.1. Rate Capability Tests

A battery cycler (BT 2000, Arbin Instruments, College Station, TX, USA) was used to test the rate capability of coin cells. During charging, the so-called “constant current-constant voltage” (CCCV) method was applied, while only constant current (CC) was used for discharging. The C-rate was calculated based on the discharge time and applied current from the formation step at $C/20$. Then 1C and a specific capacity of 172 mAh/g were applied for the current calculation under different C-rates. At the beginning, 3 cycles at $C/20$ were carried out as the formation step, which ensures the homogeneous growth of solid electrolyte interface on the electrode. Then, 5 cycles were performed at $C/10$

and C/5. After this, the C-rate increased from C/2 to 1C, 2C, 3C, and 5C, and the coin cells were cycled 10 times at each C-rates. Finally, 5 cycles at C/5 was applied to test the capacity retention after fast charging/discharging. In order to analyze the irreversible capacity loss during long-term tests, coin cells containing thin-films were cycled at 1C for 100 cycles, while C/2 was applied for cells with thick-film electrodes for 40 cycles. The cut-off voltages were set from 3.0 to 4.3 V.

2.4.2. Cyclic Voltammetry

After rate capability test, cyclic voltammetry (CV) test was performed using a battery cyler (BCS-810, BioLogic, Seyssinet-Pariset, France) in order to determine the redox reaction of coin cells during charging and discharging processes. A scan rate of 0.02 mV/s was applied, while the voltage range for CV was set from 3.0 to 4.3 V. For each coin cell, CV was repeated three times.

2.4.3. Electrochemical Impedance Spectroscopy

Electrochemical impedance spectroscopy (EIS) was used to determine the impedance of coin cells with different kinds of electrodes. After formation, the coin cell voltage gradually increased from 3.0 V to a stable voltage at around 3.6 V, where EIS analyses were performed using a battery cyler (VMP3, BioLogic, Seyssinet-Pariset, France) in an oven with a constant temperature of 25 °C. The scanning range was from 1 to 0.01 Hz, while a sinus amplitude of 10 mV was applied.

3. Results

3.1. Characterization of Electrodes

The SEM images of NMC 622 powders with small particles NMC 622 (TA) and big particle size (BA) are shown in Figure 1a,b. TA particles have diameters ranging from 1–6 μm , while BA particles have about 10 to 14 μm diameter and have spherical morphology. Figure S3 provides SEM images of the two NMC 622 particles with 20000 times magnification. The secondary particles and primary particles can be clearly distinguished. Laser scattering was applied to measure the particle size distribution of secondary particles, as shown in Figure 1d. TA NMC 622 particles have a D90 of 6.7 μm , which is about 1/2 compared to BA with D90 of 12.8 μm . Figure 1c presents the XRD patterns for two NMC 622 particles, demonstrating their purity as the single-phase layered materials. TA sample showed similar reflexes and reflex positions as BA.

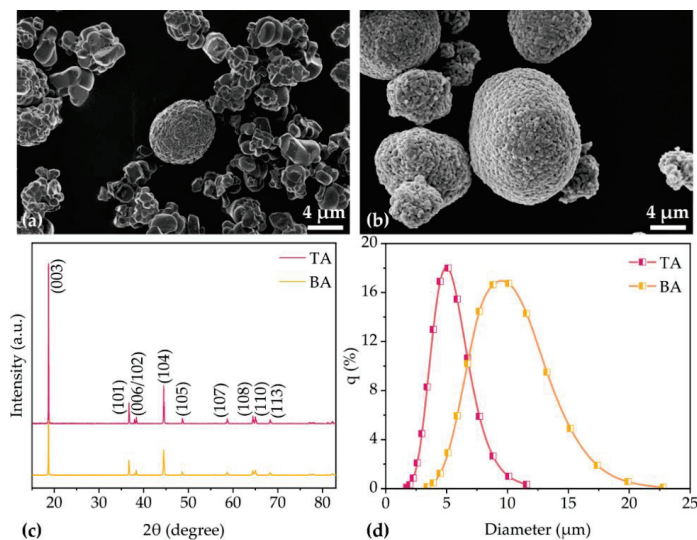


Figure 1. The SEM images of (a) TA NMC 622 particles and (b) BA NMC 622 particles. The (c) XRD patterns and (d) particle size distribution of two NMC 622 samples.

The porosities of different cathodes decreased to 35% after calendaring. The thicknesses of thin-film and thick-film electrodes are about 70 and 150 μm . The thickness ratios of TA and BA film inside hierarchical electrodes were set to 1:2, 1:1, and 2:1. The details of various cathodes are summarized in Table 1. Active mass loading is the mass of NMC 622 per unit area and areal capacity is calculated based on the mass loading.

Table 1. The thickness, porosity, active mass loading, and areal capacity of electrodes consisted of different NMC 622 powder and with different multilayer structures.

Cathode	Thickness without Al Foil (μm)	Porosity (%)	Active Mass Loading (mg/cm^2)	Areal Capacity (mAh/cm^2)
TA thin	73 ± 1	35.1	18.2 ± 0.1	3.13 ± 0.02
BA thin	74 ± 1	35.3	18.4 ± 0.1	3.16 ± 0.02
BT thin	73 ± 1	35.2	18.1 ± 0.1	3.13 ± 0.02
TA thick	157 ± 1	35.3	38.9 ± 0.1	6.71 ± 0.01
BA thick	152 ± 1	35.4	37.6 ± 0.1	6.49 ± 0.02
BT thick	155 ± 2	35.3	38.5 ± 0.3	6.63 ± 0.05
TBA 1:2	152 ± 1	35.3	37.7 ± 0.2	6.50 ± 0.03
TBA 1:1	155 ± 1	35.2	38.5 ± 0.2	6.64 ± 0.03
TBA 2:1	153 ± 1	35.2	37.9 ± 0.1	6.53 ± 0.01
BTA 1:2	153 ± 1	35.2	38.0 ± 0.1	6.55 ± 0.02
BTA 1:1	151 ± 1	35.1	37.6 ± 0.1	6.47 ± 0.01
BTA 2:1	154 ± 1	35.1	38.3 ± 0.2	6.61 ± 0.03

Figure 2 shows the cross-sections of laser-structured samples. For electrodes with different multilayers, the laser scan was adjusted to achieve channel structures reaching from electrode surface down to the current collector.

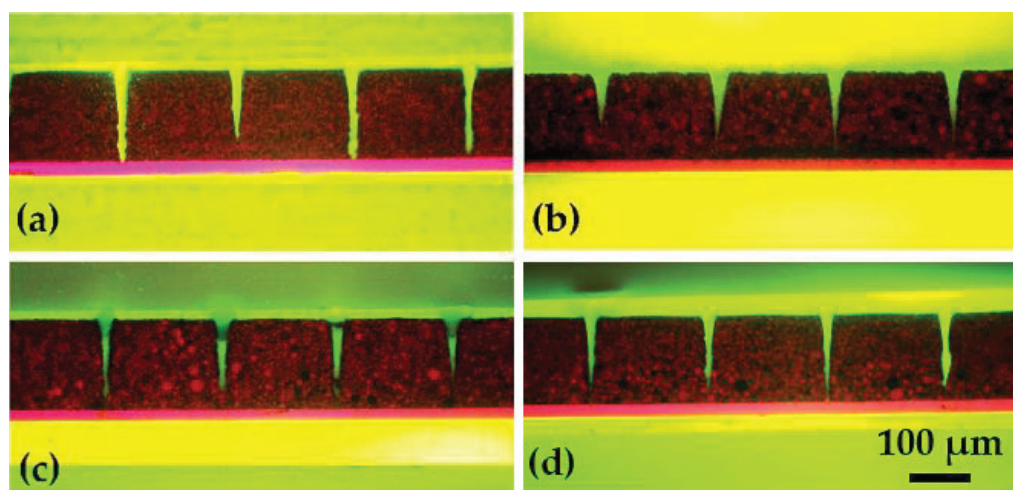


Figure 2. Microscopic images of thick-film electrodes in cross-sectional views. The number of laser scans has been adjusted to enable ablation down to the current collector: (a) TA, 14 scans; (b) BA, 22 scans; (c) BT, 15 scans; (d) BTA 1:1, 15 scans.

The SEM images of laser-structured hierarchical cathodes are shown in Figure 3. In the first image, it is found that the channels are homogenous with a width of about 25 μm near the surface, which is consistent with the result from cross-sections. Figure 3b shows a BT film, in which NMC 622 powders with two different sizes are mixed together. No significant aggregation of the NMC 622 particles is observed and the two powders are mixed homogeneously. Figure 3c shows thick-film hierarchical cathodes with BA NMC 622 at the bottom and TA NMC 622 on the top, a clear boundary is observed at about 75 μm .

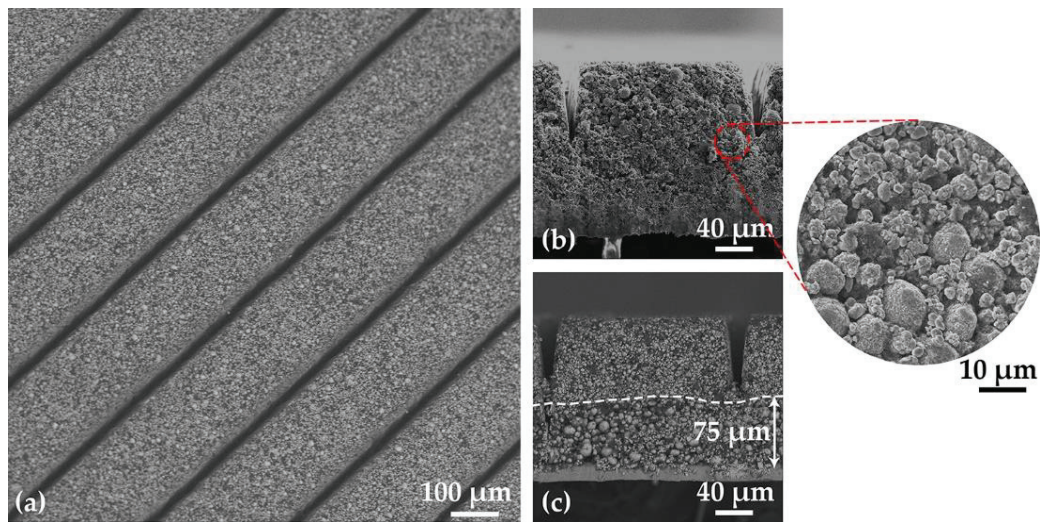


Figure 3. SEM images of (a) thick-film electrodes with BT from top view, and the cross section of thick-film electrode with (b) BT and (c) bilayer BTA 1:1.

The mass loss due to laser ablation includes the removal of active material, conductive additive, and binder. The active mass loading and areal capacity of laser-structured electrodes are summarized in Table 2.

Table 2. Active mass loading, areal capacity, and mass loss of laser-structured thick-film cathodes in comparison to unstructured ones.

Cathode (Laser Structured)	Active Mass Loading (mg/cm ²)	Areal Capacity (mAh/cm ²)	Mass Loss (%)
TA	34.3 ± 0.2	5.91 ± 0.04	11.2
BA	35.3 ± 0.1	6.09 ± 0.01	6.1
BT	35.8 ± 0.1	6.17 ± 0.02	6.6
TBA 1:2	35.6 ± 0.1	6.15 ± 0.02	5.4
TBA 1:1	36.1 ± 0.2	6.22 ± 0.03	6.2
TBA 2:1	35.8 ± 0.2	6.17 ± 0.03	5.5
BTA 1:2	34.1 ± 0.4	5.87 ± 0.02	10.3
BTA 1:1	34.5 ± 0.1	5.95 ± 0.01	8.1
BTA 2:1	36.3 ± 0.2	6.27 ± 0.01	5.1

3.2. Electrochemical Analysis

All NMC 622 electrodes were assembled vs. lithium in coin cells. The results from the rate capability test, cyclic voltammetry, as well as electrochemical impedance spectroscopy are presented in this chapter.

3.2.1. Rate Capability Tests

The specific discharge capacity of the coin cells with various electrodes are shown in Figure 4. Coin cells with thin-film electrodes show higher discharge capacity from C/2 to 3C in comparison to cells with thick-film electrodes. However, at the discharge rates 2C and 3C, the discharge capacity of coin cells with thin-film electrodes decrease from 120 mAh/g to 30 mAh/g. At 5C, coin cells with thin-film electrode maintain about 10 mAh/g capacity.

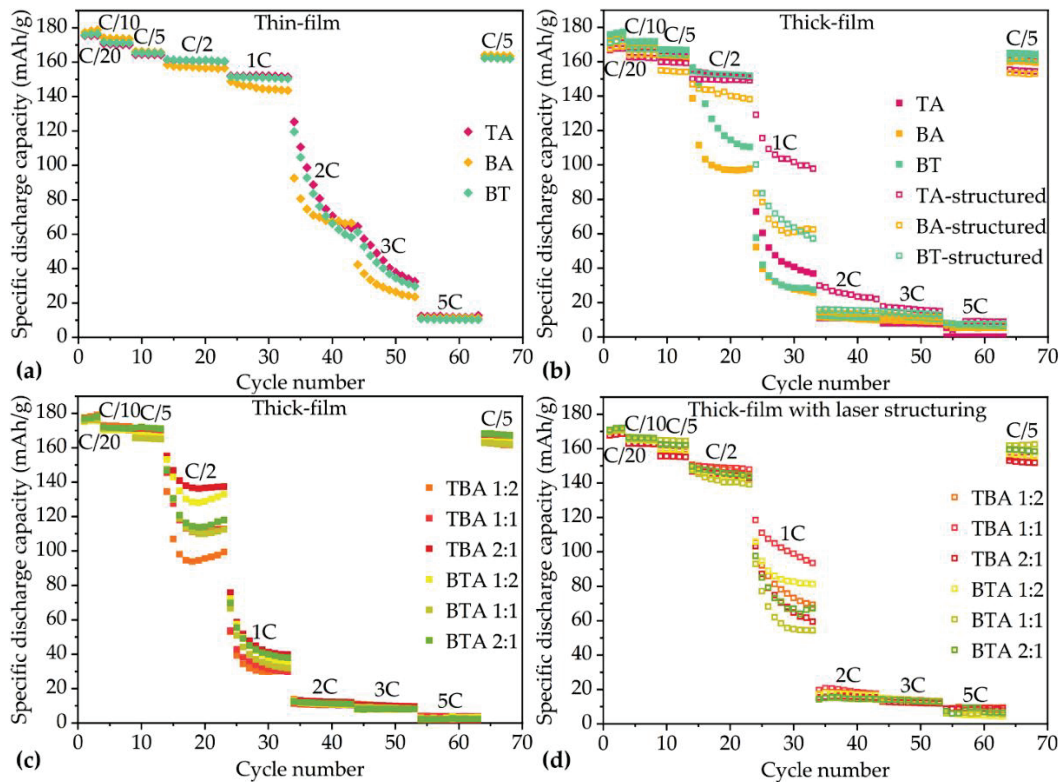


Figure 4. Rate capability tests of cells containing (a) thin-film electrodes with TA, BA, and BT. (b) Cells containing thick-film electrodes with TA, BA, and BT. Coin cells containing (c) unstructured thick-film multilayer electrodes and (d) structured multilayer thick-film electrodes.

During the formation step at C/20, the specific discharge capacities of all coin cells increase slightly. For example, for coin cell with BT electrode, its specific discharge capacity increases from 176 to 177 mAh/g, while coin cell with TA electrode achieves 173 mAh/g after the third C/20 cycle. For the bilayer electrodes, the electrode containing TBA 1:2 achieves 179 mAh/g capacity, while electrode containing BTA 1:2 reaches 176 mAh/g capacity after the last C/20 cycle. At C/10, the cell with BT electrode retains the highest specific discharge capacity of 172 mAh/g, while the cell with BTA 1:1 electrode shows the lowest specific discharge capacity of 165 mAh/g. When the C-rate rises to C/5, coin cell with BTA 2:1 electrode holds the highest capacity of 171 mAh/g, while the lowest specific capacity of 162 mAh/g belongs to the coin cells containing BA electrode. At C/2, coin cell with TA electrode has the highest specific discharge capacity of 152 mAh/g, while the lowest specific capacity of 98 mAh/g is the coin cell containing BA electrode. From 1C to 2C, all coin cells with thick-film electrodes exhibit a capacity decrease of 80% relative to the initial discharge capacity. The coin cell with TBA 2:1 electrode maintains the highest capacity of 38 mAh/h at 1C and 11 mAh/g at 2C, respectively. The coin cell with BT electrode maintains the highest capacity of 11 mAh/g, while coin cell with TA electrode shows the lowest discharge capacity of 8 mAh/g at 3C. For the discharge rates 5C, all coin cells with unstructured thick-film electrodes show almost no capacity.

Rate capability test shows that the specific discharge capacities of coin cells with unstructured thick-film electrodes drop from 160 to 10 mAh/g with increasing current rate from C/2 to 2C. On the contrary, coin cells with laser-structured electrodes maintain about 150 mAh/g, while the capacities of cells with unstructured electrodes continuously decrease from 150 to 110 mAh/g at C/2. At 1C, the discharge capacities of cells with laser-structured electrodes are at least 69% higher than that of cells with unstructured electrodes. This difference between the laser-structured and unstructured electrodes in coin cells increases with increasing current rate. For example, the discharge capacity of the coin cell

with laser-structured electrode at 1C was five times higher than that of the unstructured one. Meanwhile, Figure 4d shows the discharge capacity of coin cells containing laser-structured hierarchical electrodes. In comparison to cell with unstructured electrodes, the cell with laser-structured electrode shows about 2–4% lower capacity at C/10. However, at C/2, the discharge capacities of cells containing laser-structured electrodes are about 4–46% higher than ones with unstructured electrodes. With increasing C-rates to 5C, the cells with laser-structured electrodes show at least two times higher capacity than those of the cells with unstructured electrodes.

3.2.2. Cyclic Voltammetry

CV measurements were performed on coin cells with single-layer and bilayer cathodes to investigate the effect of hierarchical structures on the electrochemical reaction of the active material. Each coin cell was measured three times and the results overlap with each other as shown in Figure 5, which proves good reproducibility of the prepared bilayer electrodes. The recorded current signals formed a closed loop during charging and discharging. For bilayer cathodes, only one current peak appears during charging and discharging process, indicating the presence of an oxidation ($\text{Ni}^{2+} \rightarrow \text{Ni}^{3+} \rightarrow \text{Ni}^{4+}$) during charging and reduction ($\text{Ni}^{4+} \rightarrow \text{Ni}^{3+} \rightarrow \text{Ni}^{2+}$) during discharging. The oxidation peak shifts from 3.85 to 3.89 V, while the reduction peak shifts from 3.64 to 3.62 V.

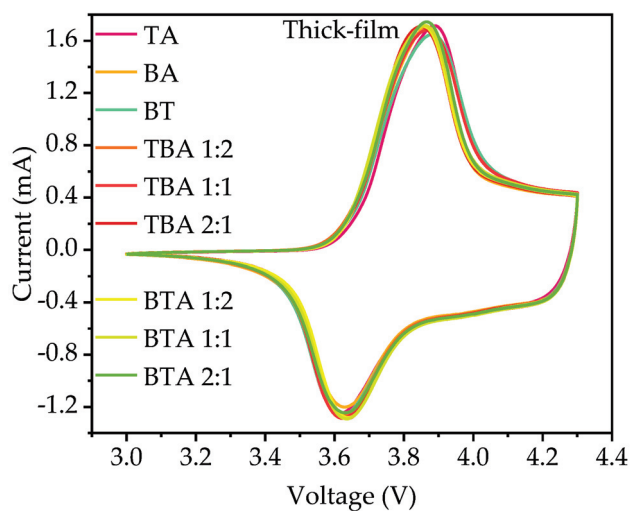


Figure 5. The CV measurements of the coin cells with unstructured single-layer and bilayer electrodes.

3.2.3. Electrochemical Impedance Spectroscopy

EIS is an effective technique to study the electrochemical reaction of the bilayer NMC 622 cathodes at different time scales [32]. Figure 6 shows the Nyquist plot of cells with unstructured single-layer as well as single-layer electrode. The complex Nyquist plot generally reveals a high-frequency semicircle and a low-frequency tail. The high-frequency semicircle is attributed to the interfacial charge-transfer processes, and the low-frequency feature is attributed to diffusion processes of lithium-ions in either the liquid electrolyte and in the bulk phase of the active material [26]. The EIS data were fitted by ZView using an equivalent circuit model as shown in Figure 6. The circuit element R_e represents series resistance of liquid electrolyte, separator, and bilayer electrodes. R_{SEI} and CPE_{SEI} are the resistance and capacity of the solid electrolyte interface (SEI), while R_{ct} represents the charge transfer resistance. A Warburg element (W) in parallel with constant phase elements (CPE) represents the diffusional process of lithium-ions inside the composite electrodes.

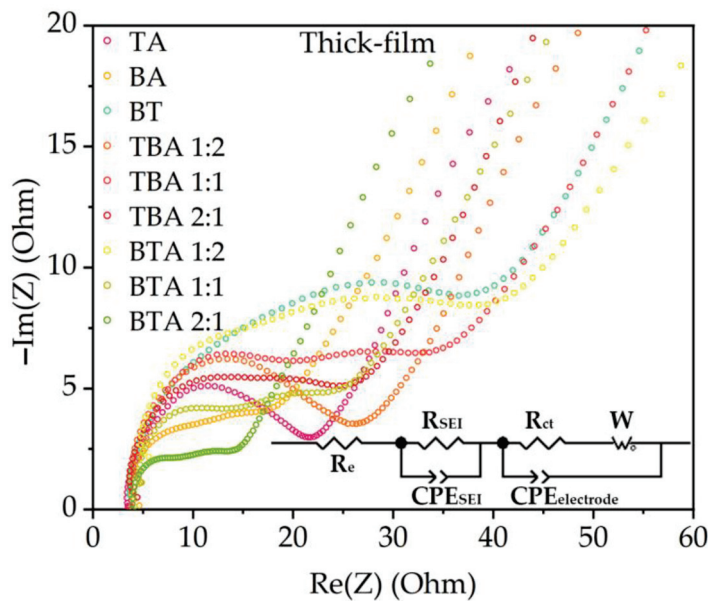


Figure 6. The EIS measurements of the coin cells with various hierarchical structured electrodes and the equivalent circuit model.

4. Discussion

4.1. Electrode Manufacturing and Laser Structuring

XRD measurement shows that TA sample and BA powders have similar reflexes and reflex positions, which indicates that the chemical composition as well as phase of BA and TA are equivalent. All the identified reflexes are in agreement with data of NMC from another study [29].

Multiple casting with different doctor blade height was used to manufacture bilayer electrodes. The separation of bilayer is clearly visible, as shown in SEM images and cross sections (Figures 2d and 3c). However, it is observed that at the interface between two layers, the NMC particles in the top layer can infiltrate into the underlying layer. The binder is used to improve the mechanical strength and the adhesion of the cathode on the aluminum foil [21]. During the second casting, slurry with NMP was cast onto the first layer. Before the electrode is fully dried, part of the PVDF binder near the surface of the bottom layer could dissolve again into the NMP, causing mechanical instability near the interface of both layers and resulting in a relocation of NMC particles. When large NMC 622 particles are at the top, they will infiltrate deeper into the bottom layer due to gravity, as shown in Figure S1d–f. The BT electrodes with a mixture of both types of NMC 622 powders show a homogeneous particle distribution (Figure 3b) without agglomeration of the smaller NMC 622 particles.

The porosities of different cathodes were adjusted to about 35% in this work, since a porosity below 30% is very detrimental for the electrochemical performance of electrode, and porosities above 40% may generate electronic limitations [24]. With increasing electrode thickness from 70 to 150 μm , the active mass loading and areal capacity increases from 18 to 38 mg/cm^2 and 3.1 to 6.6 mAh/cm^2 , respectively.

Figure S2 shows the surface of a BA-electrode close to a laser-ablated channel. The sidewall of the generated channel is smooth, indicating a sublimation of electrode materials from solid to vapor state without any evidence of melting. Different numbers of laser scans were applied during laser structuring of electrodes in order to achieve ablation through the entire composite electrode. BA electrode with large particle size and bilayer electrode with BA on the top need more scans in comparison to TA electrode with small particles, which means that the ablation depth per pulse for BA electrode is smaller than for the TA electrode. Since the laser fluence is constant by applying an average laser power of 2.5 W and a repetition rate of 500 kHz, the difference in ablation rate indicates

that the ablation threshold fluence of BA NMC 622 with large particles is higher compared to TA NMC 622 with small particles. By mixing small particles into the electrodes, the laser processing time is decreased due to an increased ablation rate. Besides, Figure 2 shows that the channels of structured TA electrode are wider and rectangular, while BA electrodes have more Gaussian-like shaped channels with narrow width close to the current collector. For bilayer electrodes, it is found that the mass loss of laser-structured electrode is about 5% higher with TA layer on the top in comparison to bilayer electrodes with BA layer on the top. Thus, it is effective to reduce mass loss by using multilayer with large particle size in the top layer.

4.2. Electrochemical Analysis

4.2.1. Rate Capability Tests

The electrochemical performance of LIBs depends strongly on the electrode composition and processing parameters [24], thus the mixing procedure as well as other components such as conductive agent and binder remain the same in this work. Lithium-ion migration in electrodes is the necessary electrochemical process to store energy for the battery [4]. The charge storage processes involve highly coupled, multiple transport phenomena that effect all electrode performance containing interfacial charge transfer, solid-state ion diffusion, electronic conductivity between and within particles, and diffusion of lithium-ions within the electrode [29].

Figure 4 shows the cells with BT have moderate discharge capacity between cells with TA and BA. The reason is that the blended electrode has the average electrochemical performance of two different positive active materials [28]. This phenomenon is also observed for cells with bilayer electrodes. With increasing thickness of TA as bottom layer, the discharge capacities of cells increase at 2C. The hierarchical structures and the position of TA and BA layer in cathodes play an important role in the electrochemical performance and will be discussed further.

With reducing the thickness of electrodes, the lithium-ion diffusion distance within electrodes is decreased [29]. Cells with thin-film electrodes show high discharge capacity during C/2, 1C, 2C, 3C, and 5C. Increasing the electrode thickness can indeed increase capacity at cell level, for example, cells containing unstructured thick-film electrodes have about 6.5 mAh/cm² areal capacity, while cells with thin-film electrodes provide 3.1 mAh/cm². However, the increasing of electrode thickness can enhance its energy density, but is accompanied by the significant loss of power density that results in the deterioration of rate capability [8]. For example, the discharge capacity of thick-film electrode containing BA decreases from 162 to 10 mAh/g at C/2 to 2C. The degradation of rate capability with increasing electrode thickness results from lithium-ion diffusion within the electrode [8]. The deterioration of energy density with cathode thickness and discharge rate increasing is due to the increase of the internal resistance and the damage of the mechanical integrity of the thick-film cathode materials [11]. Besides, insufficient wetting of electrodes can also result in rapid decrease of the discharge capacity at high current rates [9], therefore, during cell assembly, pre-wetting of electrodes and abundant amount of electrolyte was applied to avoid this issue.

The simulation from Chowdhury et al. [31] suggests that the cells containing bilayer electrodes with small particles next to current collector should have higher capacity at C-rates of 3C and 4C in comparison to cells with single-layer electrodes and bilayer electrodes with big particles close to the current collector. However, experimental studies in this work show that at C/2 to 5C, the position of layer with small or large particles has no influence on the electrochemical performance of the cells. Yet a difference in electrochemical performance is observed after laser structuring: cells containing structured electrodes with small particles next to current collector show higher capacity at C/2 and 1C in comparison to ones with big particles next to current collector. The cells containing NMC with an intermediate crystallite size of 86 nm own higher capacities as suggested by Malcolm et al. [29]. Figure 4b shows that a cell with TA has higher capacity compared

to cells with BA and BT from C/10 to 1C. The beneficial effect of the smaller crystalline NMC 622 might due to the reduced diffusion distance of lithium-ions.

Cells with laser-structured thick-film cathodes have higher rate capability in comparison to cells with unstructured electrodes regardless of the C-rates [9]. This phenomenon is also observed in this work for all investigated cells. Geometric changes of thick-film electrodes by laser processing contributes to the decrease of electronic and ionic resistances, decrease of the tortuosity, and enhancement of lithium-ion diffusion without thermal damage, chemically negative reaction, or failure of the electrode structure [22]. The lithium-ion diffusion kinetics is increased due to channels inside the laser-structured electrodes filled with liquid electrolyte [10]. Channels in electrode can reduce the diffusion distance of lithium-ions in electrode pores filled with electrolyte by connecting pores with the free electrolyte in the cell.

From rate capability tests, it is concluded that cells with thin-film electrodes have a higher discharge capacity than cells with thick electrodes. Thus, the cells with thin-film electrodes were tested at 1C for 100 cycles, while cells containing thick-film electrodes were cycled at C/2 for 40 cycles in order to determine the long-term capacity retention. The results of long-term tests of the cells with different electrodes are shown in Figure 7. With regard to cells with thin-film electrodes, BT and BA own the highest capacity retention, with 86% after 100 cycles, while TA shows 62% capacity after 100 cycles. The discharge capacities of cells with unstructured thick-film electrodes deteriorate during long-term tests. This is because of the high internal resistance and the poor mechanical integrity of thick-film electrodes [8]. All cells with laser-structured thick-film electrodes are more stable than the ones without laser structuring. Thus, laser structuring of the thick-film electrodes is a viable approach for the high-energy battery [22].

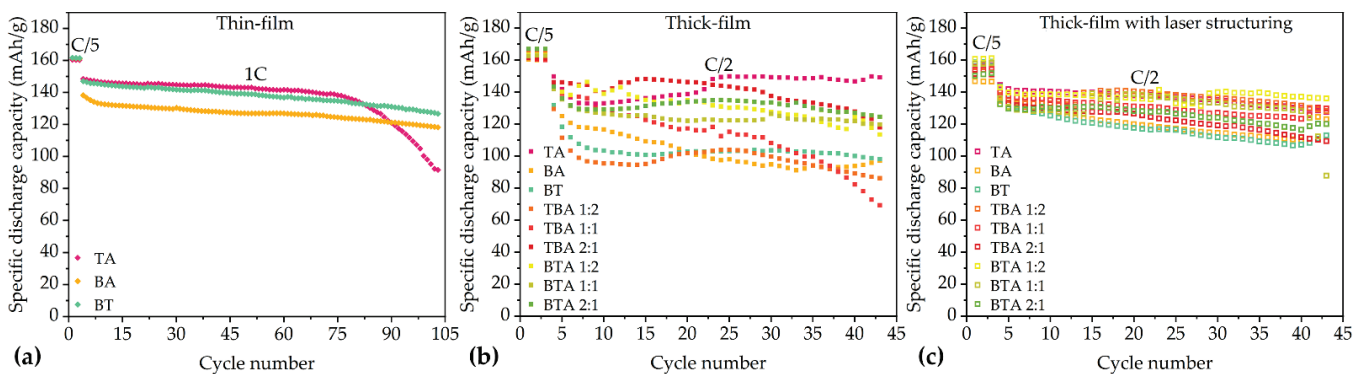


Figure 7. The results of long-term tests of the coin cells with different electrodes containing: (a) thin-film cathodes at 1C with 100 cycles; (b) thick-film cathodes at C/2 with 40 cycles; and (c) laser-structured thick-film cathodes at C/2 with 40 cycles.

4.2.2. Cyclic Voltammetry

The peaks measured in CV correspond to the oxidation/reduction of $\text{Ni}^{2+}/\text{Ni}^{3+}/\text{Ni}^{4+}$ [20]. The position of the redox peaks depends on the component of the sample. Since TA and BA NMC 622 powders have the same chemical composition as determined by XRD, the redox peaks should locate at the same voltage. When there is a high barrier to electron transfer, electron transfer reactions are sluggish so that more positive (negative) potentials are required to observe oxidation (reduction) reactions, giving rise to larger differences in the potential between both peaks [33]. The cell with TBA 2:1 electrode has the minimum difference in the potential between both two peaks of 0.2 V, while the cell with TA electrode has the largest difference in the potential between both two peaks of 0.3 V, which indicates that thick-film TA electrode has a high barrier to electron transfer. The peaks reflect the insertion/deinsertion reactions that form solid solutions. These peaks indicate the $\text{Ni}^{2+}/\text{Ni}^{3+}/\text{Ni}^{4+}$ oxidation/reduction reactions, which accompany the lithium insertion and deinsertion processes into/from the cathode materials [26]. Since Figure 8

shows that the redox peaks of all cells are located at the same position with only 0.2–0.3 V difference, this may indicate similar electrochemical kinetics of thick-film NMC 622 electrodes with different hierarchical structures.

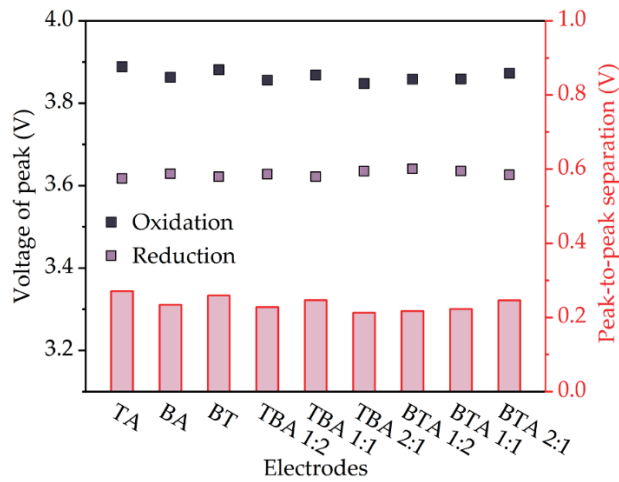


Figure 8. The voltages correspond to redox peaks and the separation of two peaks from CV measurement of cells with different electrodes.

4.2.3. Electrochemical Impedance Spectroscopy

It is possible to obtain important values from each component in a LIBs from the EIS analysis [34]. R_{SEI} is the first semicircle in the Nyquist plot and associates with the SEI layer deposited on the electrode. R_{ct} is the second semicircle and relates to the kinetics of the electrochemical reaction, which is changed by the surface coating, phase transition, band gap structure, or particle size. The precise equivalent circuit model shown in Figure 6 is established to perform an EIS analysis. SEI resistance (R_{SEI}) and charge transfer resistance (R_{ct}) of cells with thick-film electrodes are obtained and shown in Table 3. Similar equivalent circuits are also used to describe the impedance response of the cathodes [29].

Table 3. SEI resistance (R_{SEI}) and charge transfer resistance (R_{ct}) of cells containing thick-film electrodes.

R	TA	BA	BT	TBA 1:2	TBA 1:1	TBA 2:1	BTA 1:2	BTA 1:1	BTA 2:1
R_{SEI} (Ω)	11.5	4.5	6.5	3.0	9.2	8.6	3.3	7.3	3.1
R_{ct} (Ω)	6.7	9.1	42.4	15.3	36.7	23.8	39.2	16.2	8.5

The value of R_{SEI} can be used to analyze the formation of the SEI layer, which is the result of the decomposition of the electrolyte, and the value of R_{ct} represents the faradic charge-transfer resistance and is used to clarify the reaction mechanism or temperature dependent characteristics of LIBs [34]. The cell with TA electrode shows the highest R_{SEI} of 11.5 Ω , which might be due to enlarged SEI film with increasing contact area of cathode with electrolyte and more side reactions [31]. The resistance of LIBs is affected by the cathodic charge transfer resistance [23]. On the contrary, bilayer cells with TBA 1:2, BTA 1:2, and BTA 2:1 have the lowest R_{SEI} at about 3 Ω . The electrode with TA displays the smallest R_{ct} value, while electrode with BT displays the highest R_{ct} value in comparison to electrodes with TA and BA. Bilayer electrode with BTA 2:1 displays the smallest R_{ct} value in comparison to the other bilayer electrodes and BT. Finally it can be concluded, that the bilayer electrode architecture can significantly influence the overall interfacial resistance.

5. Conclusions

Single-layer (TA, BA), blended (BT), and bilayer cathodes containing NMC 622 with two distinguishing particle sizes were manufactured. After drying and calendaring process, ultrafast laser ablation was applied to create channel structures in thick-film electrodes. Ultrafast laser ablation was used to generate groove structures inside electrode, in order to increase capacity retention at high C-rates. Rate capacity measurements, CV, and EIS were performed on all cells. Rate capability investigations show that the cell with TA electrodes owns the highest discharge capacity, while cells with bilayer electrodes exhibit different performances. Cells with BT display the highest capacity retention with 86% after 100 cycles. For cells with multilayer electrodes, the discharge capacity increases by 13% with increasing TA thickness (with small particle size) compared to cells with only BA at C/2. Cells with TA as bottom layer in bilayer electrodes (TBA) show higher capacity than cells containing bilayer electrode with TA on top. Cells with TBA 2:1 display the higher discharge capacity in bilayer electrodes at C/2. Besides, a layer with big particle size (BA) on the top can reduce mass loss resulted from laser structuring. Cells with laser-structured thick-film cathodes have higher discharge capacity than those with unstructured electrodes at C/2 to 5C. Only a slight peak shift in the order of 0.2–0.3 V was observed in redox peaks from CV measurements. The electrodes with hierarchical structures can decrease the interfacial resistance of coin cells. Cells with BA displays lower R_{SEI} than TA, while cells with TA own lower R_{ct} . Cells with bilayer electrodes containing TBA 1:2 display the smallest R_{SEI} . The electrochemical performance of cells containing hierarchical cathodes varies as a function of thickness of TA and BA.

Supplementary Materials: The following are available online at <https://www.mdpi.com/2079-4991/11/11/2962/s1>, Figure S1: SEM images of the cross sections of thick-film electrodes with laser structures: (a) TA; (b) BA; (c) BT; (d) TBA 1:2; (e) TBA 1:1; (f) TBA 2:1; (g) BTA 1:2; (h) BTA 1:1 and (i) BTA 2:1. Figure S2: SEM images of BA-electrode close to a laser-ablated channel with (a) 2000 times and (b) 10,000 times magnification. Figure S3: SEM images of NMC 622 powders with (a) big particle size (BA) and (b) with small particle size (TA), with 20,000 magnification. The secondary particles and primary particles can be clearly distinguished.

Author Contributions: Conceptualization, W.P. and P.Z.; Methodology, Z.S. and P.Z.; Software, Z.S. and P.Z.; Validation, Z.S., P.Z. and W.P.; Formal analysis, Z.S.; Investigation, Z.S. and P.Z.; Resources, Z.S.; Data curation, Z.S.; Writing—original draft preparation, Z.S.; Writing—review and editing, Z.S., P.Z., W.P. and J.S.; Visualization, Z.S.; Supervision, W.P. and P.Z.; Project administration, W.P. and J.S. All authors have read and agreed to the published version of the manuscript.

Funding: This research was funded by the Federal Ministry of Education and Research (BMBF), project NextGen-3DBat, project No. 03XP01798F, National Natural Science Foundation of China (grant numbers 31970454), the Aviation Science Foundation of China (2020Z0740R4001), the China Scholarship Council (CSC). We acknowledge support by the KIT-Publication Fund of the Karlsruhe Institute of Technology.

Acknowledgments: We are grateful to the help of our colleagues A. Meyer, H. Besser, U. Rist, and M. Kapitz for their technical support and scientific discussions. We would also like to thank Y. Zheng and A. Reif for their support in SEM. In addition, we like to acknowledge support from K. Seemann, J. Gebauer, and J. Fels in XRD measurement.

Conflicts of Interest: The authors declare no conflict of interest.

References

1. Pflöging, W. A review of laser electrode processing for development and manufacturing of lithium-ion batteries. *Nanophotonics* **2017**, *7*, 549–573. [CrossRef]
2. Song, Z.; Tong, J.; Pflöging, W.; Sun, J. A review: Learning from the flight of beetles. *Comput. Biol. Med.* **2021**, *133*, 104397. [CrossRef] [PubMed]
3. Lee, B.-S. A Review of Recent Advancements in Electrospun Anode Materials to Improve Rechargeable Lithium Battery Performance. *Polymers* **2020**, *12*, 2035. [CrossRef]

4. Kobayashi, T.; Kobayashi, Y.; Miyashiro, H. Lithium migration between blended cathodes of a lithium-ion battery. *J. Mater. Chem. A* **2017**, *5*, 8653–8661. [CrossRef]
5. Zhu, Y.; Huang, Y.; Du, R.; Tang, M.; Wang, B.; Zhang, J. Effect of Ni²⁺ on Lithium-Ion Diffusion in Layered LiNi_{1-x-y}Mn_xCo_yO₂ Materials. *Crystals* **2021**, *11*, 465. [CrossRef]
6. Kosova, N.V.; Devyatkina, E.T.; Kaichev, V.V. Optimization of Ni²⁺/Ni³⁺ ratio in layered Li(Ni,Mn,Co)O₂ cathodes for better electrochemistry. *J. Power Sources* **2007**, *174*, 965–969. [CrossRef]
7. Gallagher, K.G.; Trask, S.E.; Bauer, C.; Woehrlé, T.; Lux, S.F.; Tsché, M.; Lamp, P.; Polzin, B.J.; Ha, S.; Long, B.; et al. Optimizing Areal Capacities through Understanding the Limitations of Lithium-Ion Electrodes. *J. Electrochem. Soc.* **2016**, *163*, A138–A149. [CrossRef]
8. Zheng, H.; Li, J.; Song, X.; Liu, G.; Battaglia, V.S. A comprehensive understanding of electrode thickness effects on the electrochemical performances of Li-ion battery cathodes. *Electrochim. Acta* **2012**, *71*, 258–265. [CrossRef]
9. Park, J.; Hyeon, S.; Jeong, S.; Kim, H.-J. Performance enhancement of Li-ion battery by laser structuring of thick electrode with low porosity. *J. Ind. Eng. Chem.* **2019**, *70*, 178–185. [CrossRef]
10. Pfléging, W. Recent progress in laser texturing of battery materials: A review of tuning electrochemical performances, related material development, and prospects for large-scale manufacturing. *Int. J. Extrem. Manuf.* **2020**, *3*, 012002. [CrossRef]
11. Zhu, P.; Seifert, H.J.; Pfléging, W. The ultrafast laser ablation of Li(Ni_{0.6}Mn_{0.2}Co_{0.2})O₂ electrodes with high mass loading. *Appl. Sci.* **2019**, *9*, 4067. [CrossRef]
12. Pfléging, W.; Gotcu, P. Femtosecond Laser Processing of Thick Film Cathodes and Its Impact on Lithium-Ion Diffusion Kinetics. *Appl. Sci.* **2019**, *9*, 3588. [CrossRef]
13. Kraft, L.; Habedank, J.B.; Frank, A.; Rheinfeld, A.; Jossen, A. Modeling and Simulation of Pore Morphology Modifications using Laser-Structured Graphite Anodes in Lithium-Ion Batteries. *J. Electrochem. Soc.* **2020**, *167*, 013506. [CrossRef]
14. Pfléging, W.; Pröll, J. A new approach for rapid electrolyte wetting in tape cast electrodes for lithium-ion batteries. *J. Mater. Chem. A* **2014**, *2*, 14918–14926. [CrossRef]
15. Mangang, M.; Seifert, H.J.; Pfléging, W. Influence of laser pulse duration on the electrochemical performance of laser structured LiFePO₄ composite electrodes. *J. Power Sources* **2016**, *304*, 24–32. [CrossRef]
16. Park, D.; Lee, D. Effect of fluence and multi-pass on groove morphology and process efficiency of laser structuring for 3D electrodes of lithium-ion batteries. *Materials* **2021**, *14*, 1283. [CrossRef]
17. Zhu, P.; Han, J.; Pfléging, W. Characterization and Laser Structuring of Aqueous Processed Li(Ni_{0.6}Mn_{0.2}Co_{0.2})O₂ Thick-Film Cathodes for Lithium-Ion Batteries. *Nanomaterials* **2021**, *11*, 1840. [CrossRef]
18. Singh, M.; Kaiser, J.; Hahn, H. A systematic study of thick electrodes for high energy lithium ion batteries. *J. Electroanal. Chem.* **2016**, *782*, 245–249. [CrossRef]
19. Ogihara, N.; Itou, Y.; Sasaki, T.; Takeuchi, Y. Impedance Spectroscopy Characterization of Porous Electrodes under Different Electrode Thickness Using a Symmetric Cell for High-Performance Lithium-Ion Batteries. *J. Phys. Chem. C* **2015**, *119*, 4612–4619. [CrossRef]
20. Shaju, K.; Subba Rao, G.; Chowdari, B.V. Performance of layered Li(Ni_{1/3}Co_{1/3}Mn_{1/3})O₂ as cathode for Li-ion batteries. *Electrochim. Acta* **2002**, *48*, 145–151. [CrossRef]
21. Bauer, W.; Nötzel, D. Rheological properties and stability of NMP based cathode slurries for lithium ion batteries. *Ceram. Int.* **2014**, *40*, 4591–4598. [CrossRef]
22. Park, J.; Jeon, C.; Kim, W.; Bong, S.J.; Jeong, S.; Kim, H.J. Challenges, laser processing and electrochemical characteristics on application of ultra-thick electrode for high-energy lithium-ion battery. *J. Power Sources* **2021**, *482*, 228948. [CrossRef]
23. Genieser, R.; Ferrari, S.; Loveridge, M.; Beattie, S.D.; Beanland, R.; Amari, H.; West, G.; Bhagat, R. Lithium ion batteries (NMC/graphite) cycling at 80 °C: Different electrolytes and related degradation mechanism. *J. Power Sources* **2018**, *373*, 172–183. [CrossRef]
24. Fongy, C.; Gaillot, A.C.; Jouanneau, S.; Guyomard, D.; Lestriez, B. Ionic vs Electronic Power Limitations and Analysis of the Fraction of Wired Grains in LiFePO₄ Composite Electrodes. *J. Electrochem. Soc.* **2010**, *157*, A885. [CrossRef]
25. Heubner, C.; Liebmann, T.; Schneider, M.; Michaelis, A. Recent insights into the electrochemical behavior of blended lithium insertion cathodes: A review. *Electrochim. Acta* **2018**, *269*, 745–760. [CrossRef]
26. Sclar, H.; Kovacheva, D.; Zhecheva, E.; Stoyanova, R.; Lavi, R.; Kimmel, G.; Grinblat, J.; Girshevitz, O.; Amalraj, F.; Haik, O.; et al. On the Performance of LiNi_{1/3}Mn_{1/3}Co_{1/3}O₂ Nanoparticles as a Cathode Material for Lithium-Ion Batteries. *J. Electrochem. Soc.* **2009**, *156*, A938. [CrossRef]
27. Chikkannanavar, S.B.; Bernardi, D.M.; Liu, L. A review of blended cathode materials for use in Li-ion batteries. *J. Power Sources* **2014**, *248*, 91–100. [CrossRef]
28. Appiah, W.A.; Park, J.; Van Khue, L.; Lee, Y.; Choi, J.; Ryou, M.H.; Lee, Y.M. Comparative study on experiments and simulation of blended cathode active materials for lithium ion batteries. *Electrochim. Acta* **2016**, *187*, 422–432. [CrossRef]
29. Stein, M.; Chen, C.F.; Mullings, M.; Jaime, D.; Zaleski, A.; Mukherjee, P.P.; Rhodes, C.P. Probing the Effect of High Energy Ball Milling on the Structure and Properties of LiNi_{1/3}Mn_{1/3}Co_{1/3}O₂ Cathodes for Li-Ion Batteries. *J. Electrochem. Energy Convers. Storage* **2016**, *13*, 1–10. [CrossRef]
30. Kim, S.-B.; Kim, S.J.; Kim, C.H.; Kim, W.S.; Park, K.-W. Nanostructure cathode materials prepared by high-energy ball milling method. *Mater. Lett.* **2011**, *65*, 3313–3316. [CrossRef]

31. Chowdhury, R.; Banerjee, A.; Zhao, Y.; Liu, X.; Brandon, N. Simulation of bi-layer cathode materials with experimentally validated parameters to improve ion diffusion and discharge capacity. *Sustain. Energy Fuels* **2021**, *5*, 1103–1119. [CrossRef]
32. Yuan, L.; Qiu, X.; Chen, L.; Zhu, W. New insight into the discharge process of sulfur cathode by electrochemical impedance spectroscopy. *J. Power Sources* **2009**, *189*, 127–132. [CrossRef]
33. Elgrishi, N.; Rountree, K.J.; McCarthy, B.D.; Rountree, E.S.; Eisenhart, T.T.; Dempsey, J.L. A Practical Beginner's Guide to Cyclic Voltammetry. *J. Chem. Educ.* **2018**, *95*, 197–206. [CrossRef]
34. Choi, W.; Shin, H.-C.; Kim, J.M.; Choi, J.Y.; Yoon, W.S. Modeling and Applications of Electrochemical Impedance Spectroscopy (EIS) for Lithium-ion Batteries. *J. Electrochem. Sci. Technol.* **2020**, *11*, 1–13. [CrossRef]



Article

Characterization and Laser Structuring of Aqueous Processed $\text{Li}(\text{Ni}_{0.6}\text{Mn}_{0.2}\text{Co}_{0.2})\text{O}_2$ Thick-Film Cathodes for Lithium-Ion Batteries

Penghui Zhu *, Jiahao Han and Wilhelm Pfleging *

Institute for Applied Materials-Applied Materials Physics (IAM-AWP), Karlsruhe Institute of Technology (KIT), Hermann-von-Helmholtz-Platz 1, 76344 Eggenstein-Leopoldshafen, Germany; jiahao.han@student.kit.edu

* Correspondence: penghui.zhu@kit.edu (P.Z.); wilhelm.pfleging@kit.edu (W.P.)

Abstract: Lithium-ion batteries have led the revolution in portable electronic devices and electrical vehicles due to their high gravimetric energy density. In particular, layered cathode material $\text{Li}(\text{Ni}_{0.6}\text{Mn}_{0.2}\text{Co}_{0.2})\text{O}_2$ (NMC 622) can deliver high specific capacities of about 180 mAh/g. However, traditional cathode manufacturing involves high processing costs and environmental issues due to the use of organic binder polyvinylidene fluoride (PVDF) and highly toxic solvent *N*-methylpyrrolidone (NMP). In order to overcome these drawbacks, aqueous processing of thick-film NMC 622 cathodes was studied using carboxymethyl cellulose and fluorine acrylic hybrid latex as binders. Acetic acid was added during the mixing process to obtain slurries with pH values varying from 7.4 to 12.1. The electrode films could be produced with high homogeneity using slurries with pH values smaller than 10. Cyclic voltammetry measurements showed that the addition of acetic acid did not affect the redox reaction of active material during charging and discharging. Rate capability tests revealed that the specific capacities with higher slurry pH values were increased at C-rates above C/5. Cells with laser structured thick-film electrodes showed an increase in capacity by 40 mAh/g in comparison to cells with unstructured electrodes.

Keywords: lithium-ion batteries; NMC 622; aqueous processing; thick-film electrode; laser structuring; cyclic voltammetry; rate capability

1. Introduction

Lithium-ion batteries (LIBs) have been widely applied in energy storage applications, especially in personal portable electronic devices, due to their high energy density, long cyclic stability, and good safety [1–5]. Despite the huge success and continuous growing specific energy at 6%/year [6], there are still several technical challenges for the application of LIBs in automotive industries in order to meet or exceed the requirements compared to conventional vehicles with internal combustion engines, such as long cycle life (>500 cycles), a calendar life >10 years, and stability at different temperatures ranging from -30 to 52 °C [7]. The production costs of LIBs, currently about 250 USD/kWh, still limit their widespread use in the automobile industry and should be reduced to below 125 USD/kWh [7,8].

There are two possible approaches for a further significant reduction of the battery costs. The first method is to lower the electrode processing costs, which are associated with the expensive organic solvent and the drying process of the wet electrode. Polyvinylidene fluoride (PVDF) is a state-of-the-art binder in commercial LIBs, especially for cathodes. It must be dissolved by a volatile solvent named *N*-methylpyrrolidone (NMP), which is not only expensive but also highly toxic. Therefore, extra ventilation and filtration devices are necessary for the protection of production lines and workers' safety [9]. In comparison to organic binders, aqueous binders are environmentally benign and have about one order of magnitude lower costs than PVDF [10]. During aqueous processing,

water serves as a solvent for the preparation of electrode slurry, which lowers the material costs and is also favorable for the environment. The removal of water during drying is 4.5 times faster than for NMP and requires nearly 10 times less overall energy for the processing [11].

Water-based binders such as sodium carboxymethyl cellulose (Na-CMC) and styrene butadiene rubber (SBR) have been successfully established for the production of graphite and silicon/graphite anodes [12–14]. Recently, numerous researchers have focused on the development of the aqueous processing of cathode materials. Chen et al. [15] reported the excellent high rate capability and stable cycling performance of $\text{Li}(\text{Ni}_{0.4}\text{Mn}_{0.4}\text{Co}_{0.2})\text{O}_2$ (NMC 442) using Na-CMC as binder compared to electrodes with PVDF binder. Çetinel and Bauer et al. [16,17] studied the rheological properties and electrochemical performance of $\text{Li}(\text{Ni}_{1/3}\text{Mn}_{1/3}\text{Co}_{1/3})\text{O}_2$ (NMC 111) with Na-CMC and fluorine acrylic hybrid latex (TRD 202A) with different amounts of carbon black and binder, while Loeffler et al. [18] characterized pouch cells consisting of aqueous processed NMC 111 cathode and graphite anode with 70% capacity retention after 2000 cycles. Other cathode materials such as LiCoO_2 (LCO), LiFePO_4 (LFP), $\text{LiNi}_{0.80}\text{Co}_{0.15}\text{Al}_{0.05}\text{O}_2$ (NCA), $\text{Li}(\text{Ni}_{0.5}\text{Mn}_{0.3}\text{Co}_{0.2})\text{O}_2$ (NMC 532) have been reported using aqueous binders [19–23]. In addition, guar gum and poly acrylic acid (PAA) binders were applied for cathode manufacturing [17,24]. However, lithium and transition metal leaching from the active material into water and current collector corrosion due to increased slurry pH values are the major challenges for the aqueous processing of cathodes [21].

Another way to lower the production costs of LIBs is to increase the electrode film thickness. The state-of-the-art cathodes are limited to 100 μm thickness with a mass loading of about 20 mg/cm^2 after being deposited onto the current collector [25]. A higher film electrode thickness, i.e., a higher areal capacity, is preferred since this not only increases the electrode specific capacity but also reduces the proportion of inactive materials in batteries. The costs of other manufacturing steps during assembling such as cutting, welding, and stacking, will be reduced [9]. However, the lithium-ion diffusion kinetics inside thick-film electrodes will be the bottleneck to enable high power operation at high charging/discharging rates [26]. In order to solve this problem, structuring of thick-film electrodes (“3-dimensional battery”) using ultrafast laser ablation opens a new path to simultaneously increase energy density and power density [27–30].

Many researchers have studied the effect of different types of acid addition on the cathode materials [31–34]. However, only a few groups have studied the effect of pH value on the electrochemical properties of electrodes. Ibing et al. [35] studied the effect of pH values at 12.5 and 7.6 on the electrochemical performance of NMC 532 electrodes, while Bauer et al. [17] reported the performance of aqueous processed NMC 111 electrodes at pH values of 7–11. So far to the best of our knowledge, no related research was established for NMC 622. Therefore, in the present work, NMC 622 cathodes were manufactured using aqueous binders CMC and TRD 202A. Different amounts of acetic acid were applied during the mixing process in order to investigate the effect of slurry pH value on the electrochemical performance of electrodes assembled in half cells. In addition, ultrafast laser structuring of thick-film electrodes was applied to prove the feasibility of the 3D battery concept for aqueous processed electrodes.

2. Materials and Methods

2.1. Electrode Preparation

Commercially available NMC 622 powder (BASF SE, Ludwigshafen, Germany) with a particle size of 12.8 μm (D90) was used as an active material for cathode, while carbon black C-ENERGY Super C65 (Imerys G & C Belgium, Willebroek, Belgium) was used as a conductive additive. Na-CMC (CRT 2000PA, Doe Wolff Cellulosic, Bomlitz, Germany) with a substitution degree (the average number of substituent groups attached per base unit) of 0.82–0.95 and water-based fluorine acrylic copolymer latex TRD 202A (JSR Micro NV, Leuven, Belgium) were applied as binders for aqueous electrode

preparation. The electrode slurries were mixed in a dissolver equipped with a vacuum pump (CDS, VMA-Getzmann, Reichshof, Germany). NMC 622, carbon black, and deionized water were added into a premixed 5 wt.% CMC solution and were mixed under vacuum using 2000 RPM rotation speed for 20 min. After that, acetic acid was immediately added to the slurry in order to adjust the pH value. The slurry was further stirred for 5 min under vacuum using the same rotation speed as in the previous step, followed by 90 min mixing without vacuum. Finally, TRD 202A was added to the slurry and stirred with 500 rpm under vacuum for 3 min, since TRD 202A is shear sensitive. The solid components were adjusted to a mass ratio of NMC 622:carbon black:Na-CMC:TRD 202A = 100:2:2:3. The pH value of the slurry was measured 10 min after the mixing process was finished via a pH-Meter FE30-Basic FiveEasy (Mettler-Toledo GmbH, Giessen, Germany). The viscosity of the slurries was measured at room temperature with a rheometer (MCR 72, Anton Paar GmbH, Graz, Austria) using the rotational flow measurements with a parallel plate (PP 50, Anton Paar GmbH, Graz, Austria).

The slurry obtained from previous steps was tape cast with a doctor blade (ZUA 2000.100, Proceq, Schwerzenbach, Switzerland) onto a 20 μm aluminum-foil using a tape casting coater (MSK-AFA-L800-LD, MTI Corporation, Richmond, CA, USA) with vacuum pump. The coating speed was set at 5 mm/s and the thickness of the coated cathode film was controlled by varying the gap of the doctor blade. The cast electrodes were dried at room temperature to avoid possible accelerated chemical corrosion which might occur at elevated temperatures. The thicknesses of dried cathodes were kept at 186–240 μm (mass loading: 34–47 mg/cm²) for thick-film and 50–130 μm (mass loading: 10–14 mg/cm²) for thin-film electrodes, respectively. Afterward, the electrodes were calendered using an electric precision rolling press (MSK-2150, MTI Corporation, Richmond, CA, USA) at room temperature with a constant calendering speed of 35 mm/s. The average porosity of the thick-film NMC 622 electrodes was adjusted to 35%, while the thicknesses of thin-film cathodes were reduced by 10–15%. The porosity of the electrodes was calculated based on the weight and density of each component [36].

Afterward, ultrafast femtosecond (fs) fiber laser (Tangerine, Amplitude Systèmes, Pessac, France) with a pulse duration of 380 fs and an operational wavelength of 515 nm ($M^2 < 1.2$) was applied to structure selected thick-film electrodes. Line structures with 200 μm pitch and with depths down to the current collector were generated. A repetition rate of 500 kHz and an average laser power of 4.27 W were applied, while the laser scanning speed was kept constant at 500 mm/s and the number of scan passes was varied from 30 to 50 with regard to the applied cathode film thickness. Cross-sectional analyses of electrodes using different scan passes were performed in order to find appropriate structuring parameters. Samples with a size of 2 cm \times 1.3 cm (width \times height) were cut using an ultrafast laser from the calendered cathode sheets. Then the samples were held vertically with a plastic clip and were placed in a holder and were afterward filled with resin, hardener, as well as fluorescent powder, to acquire metallographic samples. Afterward, the samples were ground and polished. The electrodes were cut in circles with 12 mm in diameter for coin cell design using 200 mm/s scanning speed and 10 scan passes, while the other parameters remained unchanged with regard to laser structuring. The laser processing was performed in ambient air.

2.2. Cell Assembly and Electrochemical Analysis

NMC 622 cathodes were assembled versus 0.25 mm lithium foil (Merck KGaA, Darmstadt, Germany) in coin cells CR2032 in an argon-filled glove box (LAB master pro sp, M. Braun Intergas-Systeme GmbH, Garching, Germany) with H₂O < 0.1 ppm and O₂ < 0.1 ppm. A mixture of ethylene carbonate and ethyl methyl carbonate (EC/EMC 3:7) with 1.3 M lithium hexafluorophosphate (LiPF₆) as conducting salt and 5 wt.% fluoroethylene carbonate (FEC) as additive was used as electrolyte. The separator was polypropylene (PP, Celgard, Charlotte, NC, USA) foil with a thickness of 25 μm and a diameter of

15 mm. A total amount of 120 μL electrolyte was added to the cell. After stacking, all cell components were pressed using a digital pressure controlled electric crimper (MSK-160D, MTI Corporation, Richmond, CA, USA). The assembled batteries were stored at room temperature for 20 h in order to allow the cathode and separator to be fully wetted with liquid electrolyte.

The “constant current–constant voltage” (CCCV) method was carried out for rate capability tests using a battery cycler (BT 2000, Arbin Instruments, College Station, TX, USA). The first 3 cycles were carried out at C/20 as the formation step, followed by increasing C-rates from C/10 to 5C. C/10 and C/5 were carried out for 5 cycles and the others were carried out for 10 cycles. The C-rate was calculated based on the discharge time and applied current during the formation step. In this work, $1\text{C} = 0.99\text{ h}^{-1}$, as well as a specific capacity of 155 mAh/g, were applied for the calculation of currents under different C-rates. The lower and upper cut-off voltages were 3.0 and 4.2 V, respectively. The CV measurements with a scan rate at 0.02 mV/s were carried out to find out the redox reaction that occurred during the charge and discharge processes. The operating window was set to 3.0 to 4.3 V. The electrochemical analyses were performed at room temperature in an ambient atmosphere.

3. Results

3.1. Characterization of Slurries and Electrodes

In order to adjust the pH value, acetic acid was added to the slurry. Since the pH value of slurries with an aqueous binder increased with time [21], the slurry pH values were measured 10 min after slurry completion. As shown in Figure 1, the pH value of the slurry linearly decreases with the amount of added acetic acid. The mass ratio of acetic acid given in Figure 1 is referred to as the mass ratio of acetic acid and NMC 622.

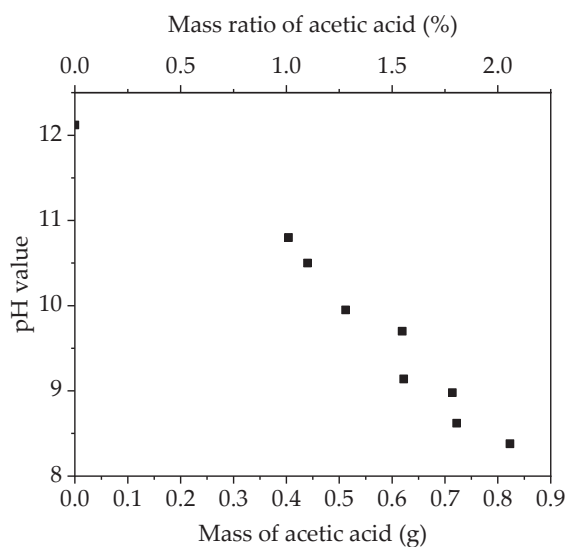


Figure 1. The pH value of slurry as a function of the mass and mass ratio of added acetic acid.

Before tape casting, the viscosity of slurries with different pH values was measured at shear rates from 0 to 100 s^{-1} . As shown in Figure 2a, slurries with different pH values show similar shear thinning behavior which means that the viscosity decreases with increasing shear rate. This indicates the existence of soft agglomerates within the slurries. With decreasing slurry pH value, a distinct increase of viscosity was found, suggesting that higher shear force is needed to break the agglomerates in slurries with lower pH values. Figure 2b shows the viscosity of slurries with different pH values at a reference shear rate of 50 s^{-1} . The functional relationship between viscosity and pH value shows approximately linear correlation. During experiments, it was found that slurries with a viscosity of 3 to $8\text{ Pa}\cdot\text{s}$ at 50 s^{-1} were beneficial to prepare thick-film electrodes. In general,

the manufacturing of thick-film electrodes can be achieved by reducing the solvent (water) content or by increasing the binder content in slurries, which in both cases leads to an increase in viscosity.

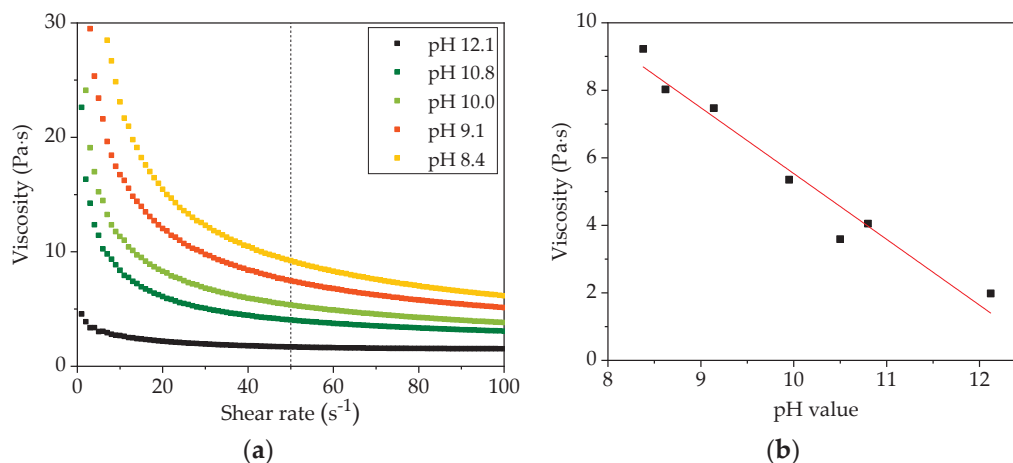


Figure 2. The viscosity of slurries as a function of (a) shear rate and (b) pH value.

Slurries with different pH values were tape cast on 20 μm Al-foil and dried in ambient air. The details of the electrodes are summarized in Table 1. Thick-film electrodes with mass loading from 37 to 46 mg/cm^2 were manufactured, while thin-film electrodes with about 11 mg/cm^2 (1/4 in comparison to thick-film electrodes) were used to represent electrodes with a state-of-the-art film thickness. It was found that without acid addition, the cathodes have a high porosity of about 60%. For example, the cathode with a slurry pH value of 12.1 shows a 50 μm thicker layer in comparison to the cathode with a slurry pH value of 10.8, while the mass loading is reduced by 6 mg/cm^2 .

Table 1. Electrode data after calendaring.

Slurry pH Value	Thickness (μm) ¹	Porosity (%)	Mass Loading (mg/cm^2)
12.1	240 \pm 5	57.5 \pm 0.2	36.9 \pm 0.2
10.8	189 \pm 3	36.6 \pm 0.2	43.3 \pm 0.1
10.0	200 \pm 7	34.6 \pm 0.3	47.4 \pm 0.2
9.0	189 \pm 9	35.1 \pm 0.4	44.2 \pm 0.3
8.6	186 \pm 6	35.5 \pm 0.4	43.7 \pm 0.3
8.4	191 \pm 3	31.7 \pm 0.5	47.1 \pm 0.4
12.0	130 \pm 3	68.1 \pm 0.2	13.7 \pm 0.1
10.7	82 \pm 3	57.7 \pm 0.2	10.3 \pm 0.2
9.2	51 \pm 2	38.8 \pm 0.4	11.3 \pm 0.1
7.4	76 \pm 2	40.7 \pm 0.5	12.7 \pm 0.2

¹ The film thickness is the value without the aluminum current collector of 20 μm .

Cross-sectional analyses were performed with electrodes whose slurries had different pH values, see Figure 3. In the electrode film with a slurry pH value of 12.1, many cavities with diameters ranging from 60 to 284 μm were formed owing to the generation of H_2 , which is produced when aluminum is directly exposed to the alkaline slurry [19]. The cavity structures are distributed across the electrode film, leaving openings with diameters from 25 to 105 μm on the electrode surface. When the slurry pH value decreases to 10.8, the diameters of cavities are reduced to 104 to 198 μm , as shown in Figure 3c. Meanwhile, the amount of cavities is decreased. For example, Figure 3d shows a segment of the cathode with a slurry pH value of 10.8 without obvious cavities. With further decreasing of slurry pH values to 10.0 and 9.1, the electrodes become flat without any cavities, as shown in Figure 3e,f.

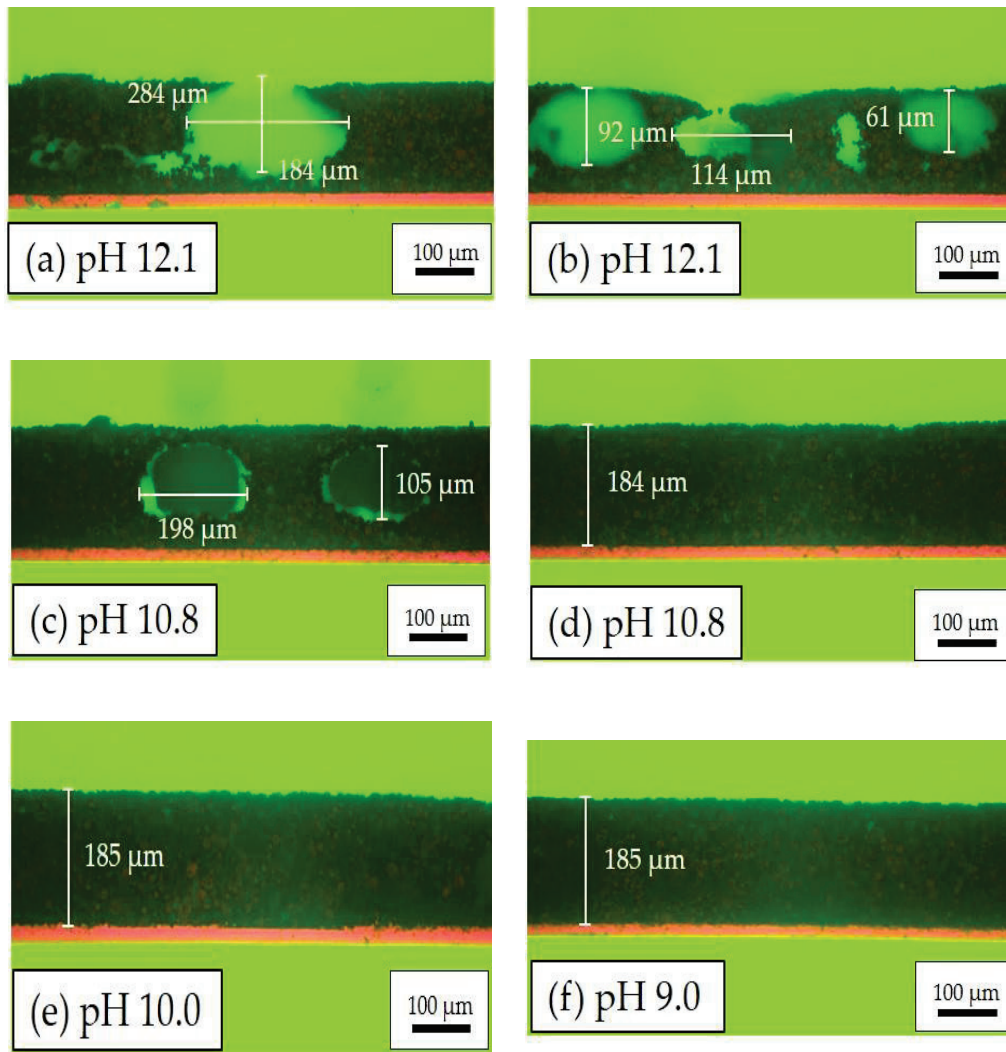


Figure 3. Microscope images of electrodes in cross-sectional view with different slurry pH values: (a,b) pH = 12.1; (c,d) pH = 10.8; (e) pH = 10.0; and (f) pH = 9.0.

In addition to the slurry pH values, the film thickness is another decisive factor that influences electrode homogeneity. Inhomogeneous distribution of cathode materials is observed in thick-film electrodes (Figure 4). The dark regions marked with red circles are craters that were created by the inward collapse of electrode materials during the drying process. For thick-film cathodes (slurry pH value 12), craters with diameters ranging from 150 μm to 700 μm have been formed. By decreasing the slurry pH value to 10.8, the craters on the surface became smaller and shallower with diameters of 190 to 200 μm . As for thin-film electrodes with a slurry pH value of 12.0 and a thickness of 67 μm , the crater diameters were around 80 to 150 μm which is about a quarter in size compared to those in thick-film electrodes. In thin-film electrodes with slurry pH values of 10.7, the active material particles were uniformly distributed. No obvious cavities were found on the film surface. This proves that the corrosion of the current collector in thick-film electrodes has more impact in comparison to thin-film electrodes which is due to the longer drying time of thick-film electrodes.

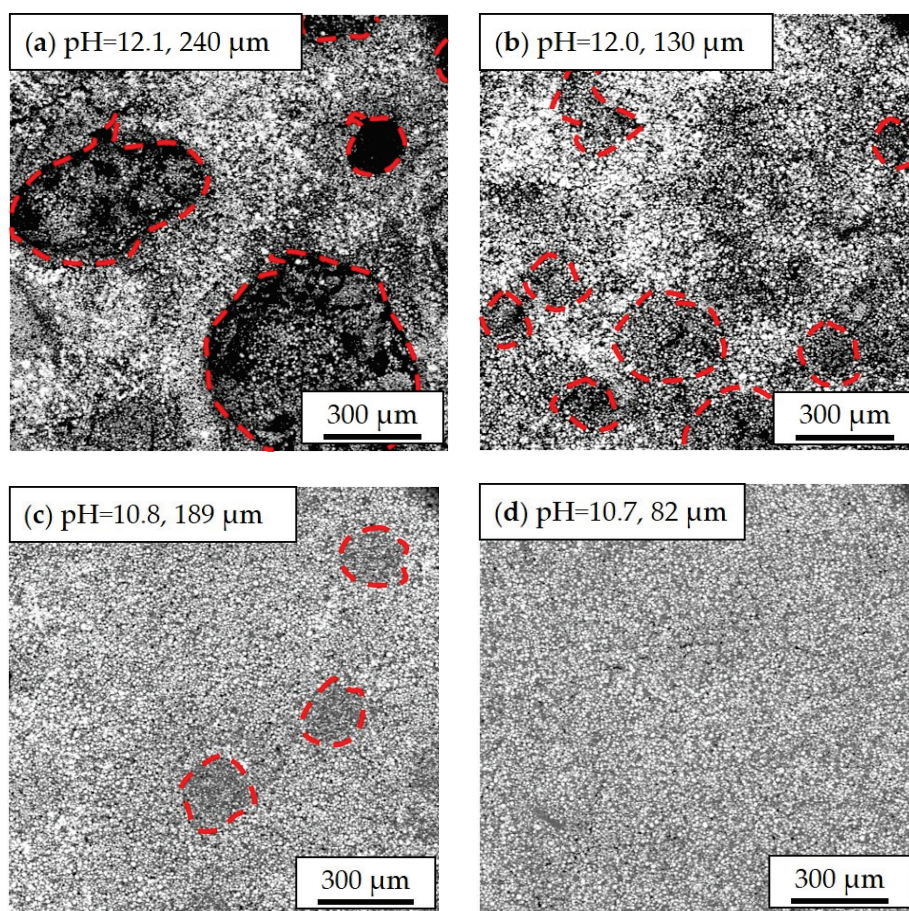


Figure 4. Scanning electron microscope (SEM) images of cathode films with different slurry pH values and different thicknesses: (a) pH = 12.1, 240 μm ; (b) pH = 12.0, 130 μm ; (c) pH = 10.8, 189 μm ; (d) pH = 10.7, 82 μm . The craters on the electrode surface with different diameters are marked with red dot lines.

For the purpose of improving lithium-ion diffusion kinetics, thick-film electrodes with slurry pH values of 12.1, 10.0, and 9.0 were structured via ultrafast laser ablation prior to cell assembling and subsequent galvanostatic measurements. The data of laser structured electrodes are summarized in Table 2. The mass loss due to laser ablation includes the removal of active material, binder, and conductive additive.

Table 2. Active mass loading, areal capacity, and respective mass loss of laser structured electrodes compared to unstructured ones.

Electrode Type	Active Mass Loading (mg/cm^2)	Areal Capacity (mAh/cm^2)	Mass Loss (%)
Unstructured, slurry pH 12.1	36.9 ± 0.2	6.13 ± 0.03	—
Structured, slurry pH 12.1	33.3 ± 0.1	5.53 ± 0.02	9.8 ± 1.4
Unstructured, slurry pH 10.0	47.4 ± 0.2	7.88 ± 0.03	—
Structured, slurry pH 10.0	44.0 ± 0.1	7.31 ± 0.02	7.2 ± 0.8
Unstructured, slurry pH 9.0	44.2 ± 0.3	7.35 ± 0.05	—
Structured, slurry pH 9.0	42.7 ± 0.2	7.10 ± 0.03	3.4 ± 0.5

The SEM images of laser structured electrodes (slurry pH values of 12.1, 10.0, and 9.0) are shown in Figure 5. On the surface of electrodes manufactured with a slurry pH value of 12.1, holes with diameters varying from 10 μm to 100 μm were observed. Furthermore, cracks originated from the holes that were formed. As the slurry pH value decreased to 10.0, no crack formation and holes with diameters larger

than 50 μm were obtained. At a slurry pH value of 9.0, no holes or craters were found in the entire electrode. Figure 5d shows the line structure with 200 μm pitch which was generated using ultrafast laser ablation without damaging the aluminum current collector. A width of $30 \pm 2 \mu\text{m}$ is achieved at the top of the groove, and the half-peak-width is $10 \pm 1 \mu\text{m}$. The sidewalls of the generated grooves show a slight curvature of $7.0^\circ \pm 0.3^\circ$ and the orientation is perpendicular to the cathode surface. The laser fluence calculated from pulse energy and laser focus diameter is 14.7 J/cm^2 , while the pulse overlap is 96.7%. The active mass loss owing to the laser structuring process amounts 3% to 10%. No obvious debris formation is found on the electrode surface and inside the channel structures.

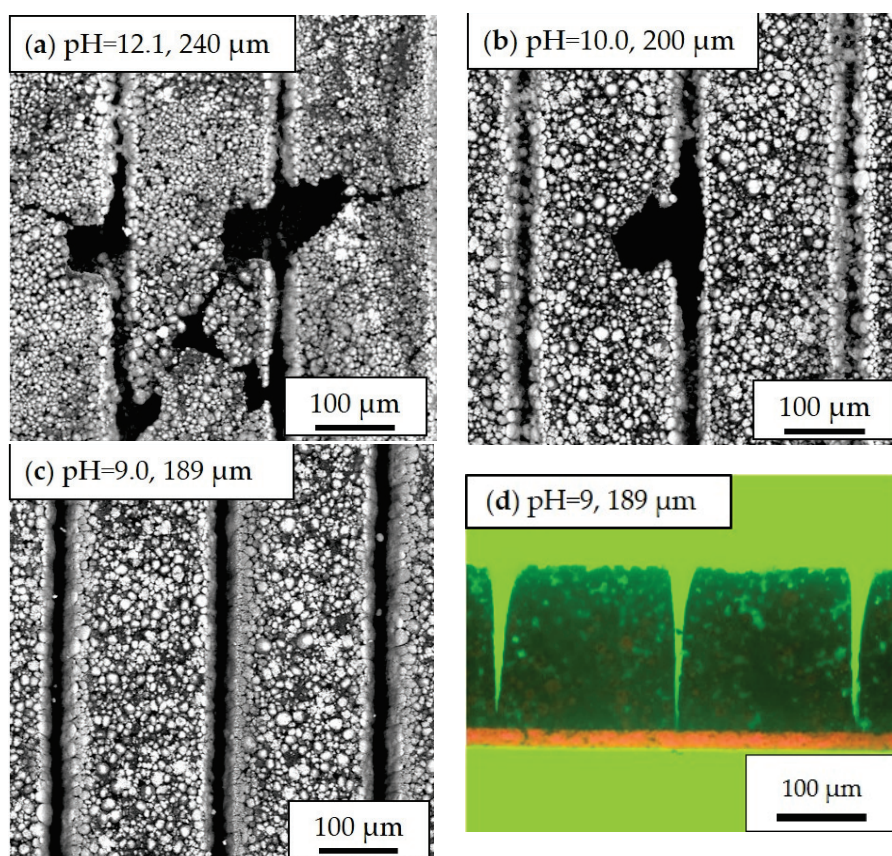


Figure 5. SEM images of structured cathodes with slurry pH values of (a) 12.1; (b) 10.9; and (c) 9.0; (d) Microscope image of cross sectional view of a laser structured cathode deposited with a slurry pH value of 9 and a film thickness of 189 μm .

3.2. Electrochemical Performance of Cells

Thick-film and thin-film NMC 622 electrodes with different slurry pH values were assembled vs. lithium in coin cells. Laser structured thick-film electrodes with pH 12.1, 10, and 9 were assembled in order to study the effect of laser structuring on cell performance. The results from the rate capability test as well as cyclic voltammetry are presented and discussed.

3.2.1. Rate Capability Test

The specific discharge capacity of water-based NMC 622 electrodes is shown in Figure 6. In the formation step at C/20, the specific capacities of all cells with thick-film electrodes are slightly increased. For example, for cells containing electrodes produced with slurry pH values of 10.0, 9.0, and 8.6, the specific capacity increased from 153 mAh/g to 158 mAh/g after formation, while cells containing cathodes produced with slurry pH

values of 12.1 and 10.8 achieve about 150 mAh/g capacity at the third C/20 cycle. At C/10, the cell with the electrode produced with a slurry pH value of 9.0 retains the highest specific capacity of 150 mAh/g, while the cell with the electrode produced with a slurry pH value of 8.4 shows the lowest specific capacity of 136 mAh/g. As the C-rate rises to C/5 and C/2, cells containing electrodes produced with a slurry pH value of 12.1 hold the highest capacity of 130 mAh/g and 91 mAh/g at C/5 and C/2, respectively, while the lowest specific capacities (90 mAh/g at C/5 and 37 mAh/g at C/2) belong to the electrode produced with a slurry pH value of 8.4. At 1C and 2C, all cells with thick-film electrodes show a drop in capacity by more than 80% with regard to the initial capacity, except those cells containing electrodes that were produced without acid addition (slurry pH value 12.1). The cell with the electrode produced without acid addition maintains the highest capacity of 35 mAh/h at 1C and 9 mAh/g at 2C. For discharge rates of 3C and 5C, all cells with thick-film electrodes no longer show any capacity.

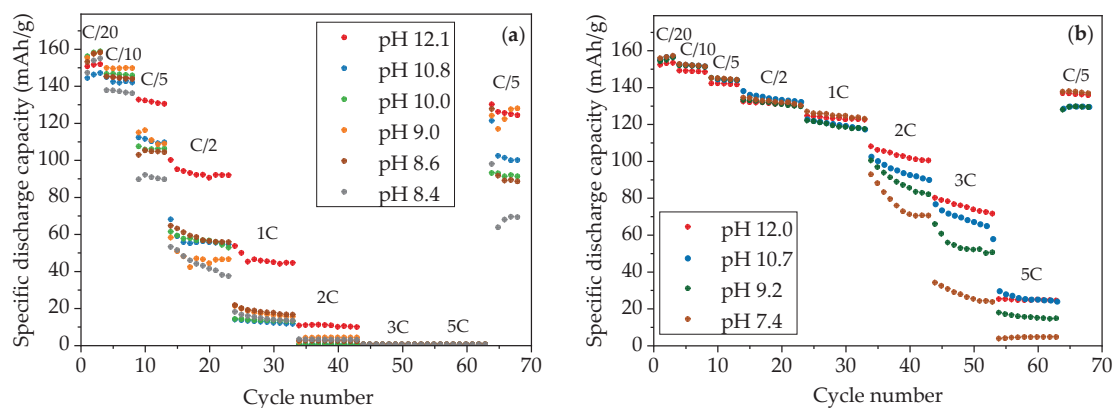


Figure 6. Specific discharge capacity of cells containing (a) thick-film electrodes and (b) thin-film electrodes produced with different slurry pH values.

In order to verify the capacity retention of electrodes after being cycled at high discharge rates up to 3C, the C-rate was reduced to C/5. All cells show less specific capacity compared to the previous C/5 cycles. The cell with the electrode produced with a slurry pH value of 12.1 provides the highest specific capacity of 124 mAh/g with a capacity retention of 95%, while the lowest capacity belongs to the electrode produced with a slurry pH value of 8.4 with a specific capacity of 69 mAh/g and 77% capacity retention.

The specific capacities of cells with thin-film electrodes are higher than cells containing thick-film electrodes produced with the same slurry pH value (Figure 6b), especially at high discharge rates ($\geq C/2$). After the C/20 formation step, all cells achieve similar specific capacities of 153–157 mAh/g, which are similar to those obtained with thick-film electrodes. With increasing C-rate, the specific capacity of all cells shows successive deterioration. For C/10 up to 1C, cells with thin-film electrodes show similar discharge capacities: 149–152 mAh/g at C/10, 143 mAh/g at C/5, 133 mAh/g at C/2, and 120 to 125 mAh/g at 1C. In this C-rate range, electrodes produced with different slurry pH values show no significant difference. However, from 2C to 5C, the capacity of thin-film electrodes decreases with increasing cycle number, especially for electrodes that were produced with a slurry pH value of 7.4. The drop in capacity at high C-rates with decreasing slurry pH values is also observed in cells with thick-film electrodes. For the final C/5 cycles, the electrodes produced with slurry pH values of 12.0 and 7.4 show the highest reversible specific capacity of 137 mAh/g, which had 95% capacity retention compared to the initial C/5 cycles (144 mAh/g), while other cells containing cathodes produced with slurry pH values of 10.7 and 9.2 show lower reversible specific capacity of 130 mAh/g with capacity retention of 90%.

Figure 7 shows the discharge capacities of cells containing structured thick-film electrodes which were produced with slurry pH values of 12.1, 10.0, and 9.0. During the formation step and C/10 cycles, all cells with structured electrodes show discharge capacities reduced by 4 mAh/g in comparison to cells with unstructured electrodes produced with the same slurry pH values and same film thicknesses. In following cycling steps at C/5, a capacity increase of 14 mAh/g and 18 mAh/g is observed for cells containing structured cathodes produced with slurry pH values of 9.0 and 10.0 in comparison to cells with unstructured electrodes, respectively, while cells with laser structured electrodes without acid addition have 7 mAh/g lower capacity than cells with unstructured electrodes. However, when the C-rate is increased above C/2, laser structured electrodes begin to show a great improvement regarding specific discharge capacity retention regardless of the slurry pH values used during electrode preparation. The cell with structured electrode produced with a slurry pH value of 12.1 retains the highest discharge capacity from C/2 to 3C, while the cell containing structured cathode produced with a slurry pH value of 10.0 shows 46% higher capacity at C/2 compared to the cell with an unstructured cathode. After being cycled at elevated C-rates, the cell with the structured cathode (slurry pH value of 12.1) shows a capacity retention of 97% compared to the previous first cycle at C/5, while cells produced with slurry pH values of 10.0 and 9.0 maintain 96% discharge capacity.

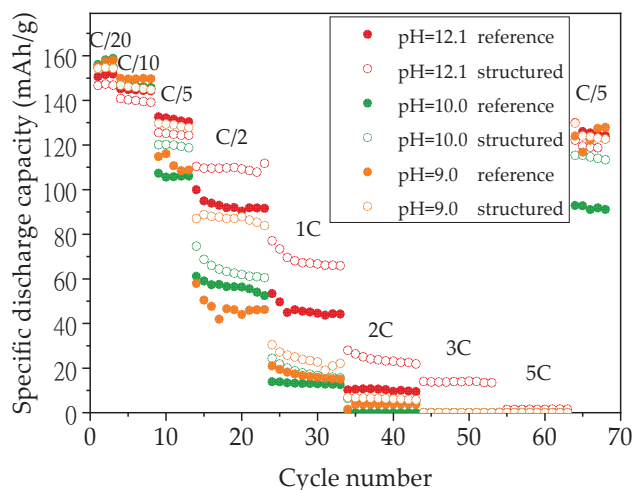


Figure 7. Specific discharge capacity of cells containing unstructured and laser structured thick-film electrodes which were produced with different slurry pH values.

3.2.2. Cyclic Voltammetry

CV measurements of cells with unstructured cathodes were performed in order to investigate the impact of the added amount of acetic acid on the electrochemical reaction of the active material. The current peaks in CV correspond to redox reactions and can be assigned to different phase transitions. The recorded signals were fitted using the Gaussian window function in MATLAB (MathWorks Inc., Version: R2019b, Natick, MA, USA). The recorded current signals in Figure 8 during the charging and discharging process formed a closed loop with hysteresis. For each sample, the measured three cycles for each cell overlap with each other, which proves quite good cycle stability of the prepared electrodes.

During each charging and discharging process, only one current peak is clearly observed, which indicates on the cathode side the presence of an oxidation and reduction reaction, respectively. In the charging process, the peak maximum shifts from 3.80 V to 3.86 V with decreasing slurry pH value from 12.0 to 10.8. However, when the slurry pH value decreases further below 10.8, the corresponding peak voltage remains at 3.87 V. In discharging process, the maximum peak shifts from 3.70 V to 3.66 V voltage with

decreasing slurry pH value to 10.8, while the voltage of the peak maximum remains unchanged at 3.64 V for cells with electrodes produced with slurry pH values from 9.2 to 7.4.

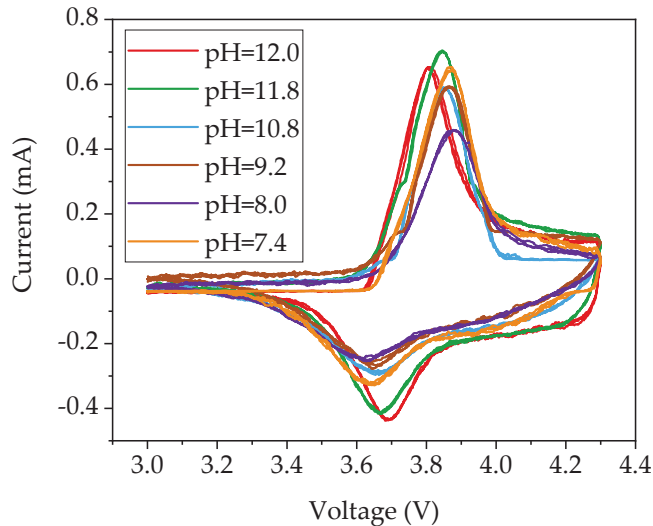


Figure 8. CV plots of cells containing cathodes that were produced with different slurry pH values.

4. Discussion

The effect of slurry pH value on electrode processing as well as on the electrochemical performance of cells with dried electrodes is discussed in detail. Cells with laser structured electrodes show higher specific capacity in comparison to cells with unstructured electrodes. This confirms the conducive effect of the 3D battery concept with the combination of a thick-film electrode and laser structuring.

4.1. Effect of Acid Addition on The Electrode Processing

During aqueous processing, the pH value of NMC 622 slurries without acid addition reached 12.1 after the mixing process, which is similar to already published results [17,37]. The increase of the slurry pH value is due to the Li^+/H^+ exchange mechanism between layered oxide electrode materials and water, which leads to the formation of lithium hydroxide (LiOH) and other products such as LiHCO_3 and Li_2CO_3 [38]. Since the cation exchange only takes place on the edges of the active material, a part of the protons in the surface of NMC 622 can be swapped with Li^+ upon cycling. This may explain the increase of the discharge capacity of all cells with aqueous-based cathodes during the formation step, as shown in Figure 6. When exposed to alkaline slurries, a local breakdown of the natural oxide layer on the aluminum current collector takes place, leading to the corrosion of the aluminum substrate and hydrogen formation [39–41]. The generation of the hydrogen along the interface between the current collector and slurry results in a high porosity with values above 57% and cavities having a diameter larger than 100 μm inside the electrodes after the drying process, as shown in Figure 3a. The size and number of pores inside the electrode are assumed to depend not only on the slurry pH value but also on wet film thickness (doctor blade height) and drying temperature. In this work, all electrodes were dried at room temperature. Therefore, the influence of temperature can be neglected. With increasing wet film thickness, the drying time is increased, which leads to a longer reaction time between alkaline slurry and Al-foil. This can be verified from the SEM images in Figure 4, where the thin-film electrodes show fewer pores and cavities in comparison to the thick-film electrode with the same slurry pH value. Since the surface of the deposited slurry was dried faster due to stronger air convection, while the electrode close to the current collector stayed humid for a longer period of time. The formation of hydrogen along the current collector surface continued until the electrode

is dried. Thus, the hydrogen bubbles were trapped inside the film during the drying process, forming craters on the surface which could be seen from cross section images in Figure 3b as well as SEM images in Figure 4a,b. The high porosity is disadvantageous for achieving high volumetric energy densities and thus counteracts the benefit of increasing the electrode thickness. Therefore, the slurry pH value adjustment is of great importance for aqueous electrode manufacturing.

Figure 2 shows that slurries with different pH values have similar shear thinning behavior, which is typical rheological behavior of CMC since it is often used as a thickening agent in suspension due to its long-chain molecular and network structures [42]. The long-chain molecules tend to orient themselves in flow direction with increasing shear stress, thus the shear resistance to flow as well as viscosity decreases [43]. It is observed that with an increasing amount of acetic acid addition, the slurry pH value decreases from 12 to 8, while the viscosity increases from 2 to 9 Pa·s at a reference shear rate of 50 s^{-1} . The tendency is not the same compared to the viscosity of NMC 111 slurries from Bauer et al. [17], where the viscosity remains constant at around 4 Pa·s in a pH range of 8 to 11. However, the viscosity rise with decreasing pH value from 12 to 8 is consistent with the study on the viscosity of CMC solution under different pH values from Lee et al. [44]. Na-CMC is very sensitive to pH value changes. The variation of pH value affects the protonation of the derivative sites on CMC, which in turn impacts the molecular conformation [45]. In the neutral region (pH value around 7), the dissociation of CMC produces negatively charged polymer chains, the mutual repulsion among carboxylate ions ($-\text{COO}^-$) results in an expansion of the network chains to form a hydrogel [46], thus leads to high viscosity. When the pH value increases to an alkaline region, sodium ions dissolve from Na-CMC in the water. The number of dissolved sodium ions increases with elevated pH value, resulting in the restraint of the extension of the tangled molecular chain in the hydrogel, therefore, the viscosity decreases [46]. The rheological property of the slurry has a significant influence on the manufacturing process of cathodes, such as mixing and coating. With high viscosity, the sedimentation of active material particles, convection of conductive additives, and binder migration can be limited [47]. Therefore, the addition of acetic acid can not only adjust the slurry pH value to avoid corrosion on the current collector but is also beneficial for thick-film manufacturing.

4.2. Electrochemical Performance of Electrodes with Acid Addition

Figure 8 displays the redox couple of cells containing cathodes produced with different slurry pH values. The peaks measured in cyclic voltammetry (CV) correspond to the oxidation/reduction of $\text{Ni}^{2+}/\text{Ni}^{4+}$ [48]. The voltage of each redox peak in CV measurements and the voltage difference of the redox couple (ΔE_p) are summarized in Figure 9. With decreasing slurry pH values, the oxidation and reduction peaks shift to higher and lower potential, leading to an increase in voltage difference ΔE_p of the redox couple. The rise of ΔE_p indicates an increased cell polarization and therefore a sluggish electrochemical reaction [49]. This occurs as a result of the less porous structure in the electrode film. Due to the increased size and number of cavities inside the electrode film with high slurry pH values, the contact surface between electrode and electrolyte is enlarged and the lithium-ions diffusion from the liquid electrolyte to the electrode is enhanced in comparison to electrodes with lower porosity.

The functional dependence of discharge capacity vs. C-rate of cells with both thick-film and thin-film electrodes is summarized in Figure 10. A decrease in capacity of about 10 mAh/g for cells with aqueous processed electrodes is observed compared to cells with NMP-based electrodes [30], which may originate from the loss of lithium-ions and dissolution of transition metal ions [21]. In addition, a strong dependence of the specific discharge capacity on electrode thickness and discharge rate was found. At small C-rates of C/20, all cells show a similar initial capacity of about 150 mAh/g. Cells with thick-film electrodes suffer severe capacity fade with increasing discharge current, losing over 60% of the capacity at C/2 compared to capacities at C/20. This may be due to the limited lithium-

ion charge transfer resistance, local material degradation, and micro-cracks formation on the electrode surface owing to the inhomogeneity of applied current [26]. Although cells with electrodes without acid (slurry pH value of 12.1) show the highest discharge capacity after C/10, the extremely high porosity around 60% hinders the possibility of achieving high volumetric energy densities. Additionally, cathodes with high porosity have reduced adhesion strength to the current collector. The corrosion of the aluminum current collector can lead to a deteriorated cycle stability and a shortened cycle lifetime. Not to mention the shedding of electrode materials during handling, which makes the post-processing of electrodes more difficult, such as calendaring, winding, laser structuring, cutting, and packaging. In addition, the cells containing thick-film electrodes produced with slurry pH values of 8.4 and thin-film electrodes produced with slurry pH values of 7.4 show the lowest discharge capacity above C/10 and C/2, respectively. This indicates that an excessive amount of acid deteriorates the electrochemical performance of cells at high C-rates, leading to increased cell polarization and low capacity retention. However, in the pH range of 4–9, the aluminum current collector is chemically protected due to the existence of a natural alumina passivation layer [39]. Therefore, the pH value of NMC 622 slurry should be adjusted to 9–10 considering the balance between rate capability and current collector corrosion.

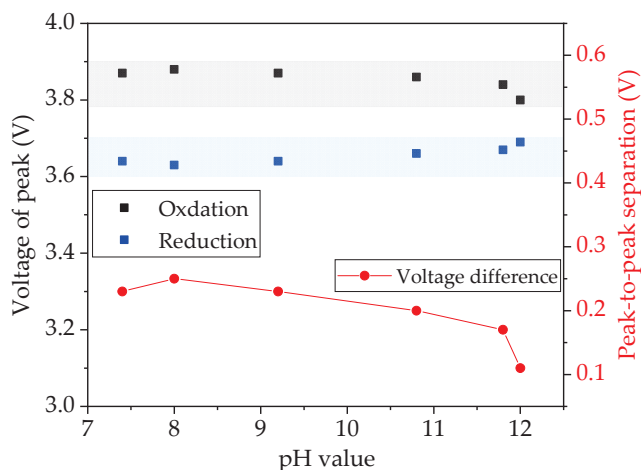


Figure 9. Redox peak voltage extracted from Figure 8 and the redox couple voltage difference of cells with electrodes produced with different slurry pH values.

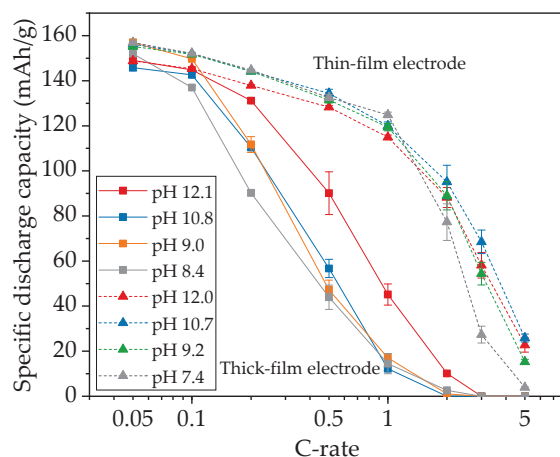


Figure 10. Average discharge capacity as a function of C-rate for cells containing electrodes produced with different slurry pH values.

Figure 11 depicts voltage profiles of cells at selected C-rates of C/5, 1C, 3C, and finally C/5 to discuss in detail the influence of slurry pH values and film thicknesses on the electrochemical performance of the electrodes. At initial C/5, the discharge capacities of thin-film electrodes show no substantial difference, while thick-film electrodes show a 40 mAh/g difference between electrodes with different slurry pH values. With decreasing pH values, the lithium insertion along the voltage plateau is shortened. From 1C to 3C, the discharge capacities of thick-film electrodes drop sharply from less than 50 mAh/g to 0 mAh/g, while the discharge capacities of thin-film electrodes are reduced by 20 mAh/g for each step. The term “IR-drop” refers to the voltage drop resulted from the product of current (I) passing through resistance (R). A sudden voltage drop can be observed at the beginning of the discharge curves in Figure 11. At 1C the IR-drop of cell with thin-film electrode produced with slurry pH value 7.4 is higher (from 4.20 V to 3.87 V) in comparison to cells containing electrodes with slurry pH values 12.0 and 10.7 (from 4.20 V to 3.99 V), which indicates a higher ohmic resistance for the cell containing electrodes produced with lower slurry pH values. After the C-rate is reduced to C/5, thin-film electrodes show $91 \pm 4\%$ capacity retention, while thick-film electrodes have a disperse capacity retention of 75%, 92%, and 95% for slurry pH values of 8, 11, and 12, respectively.

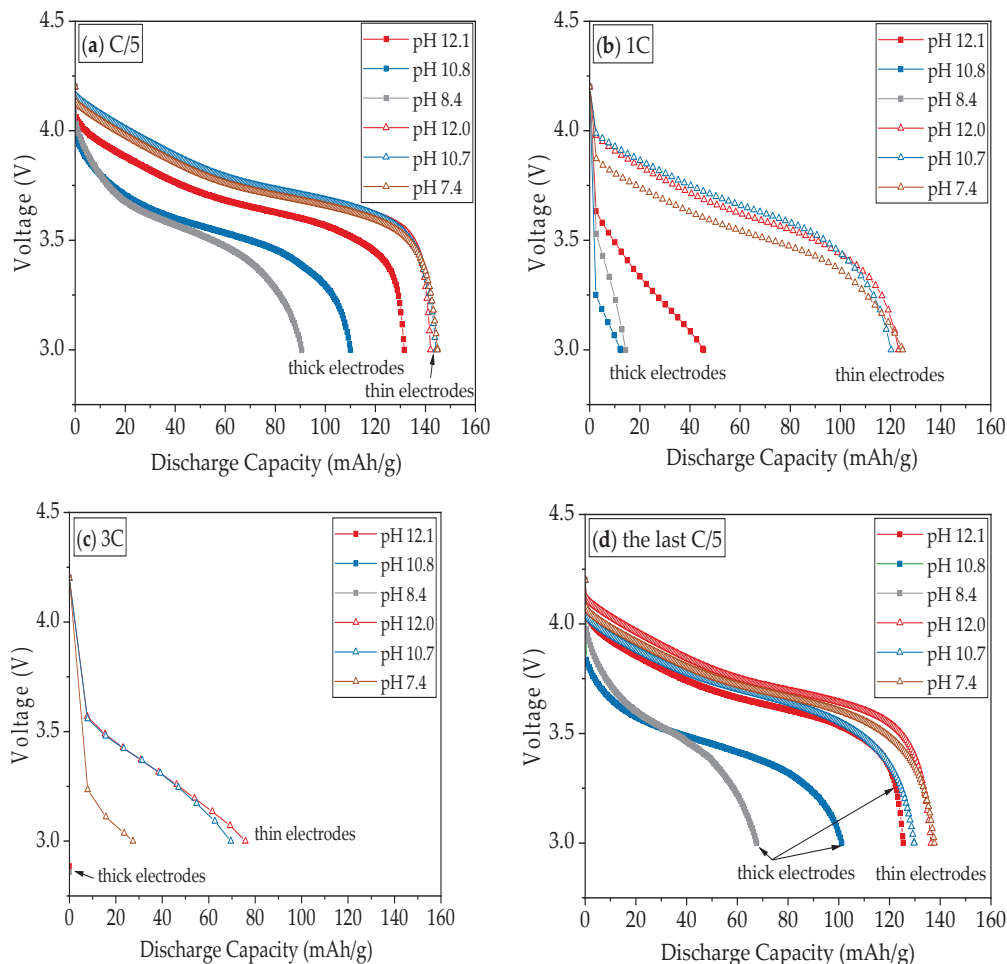


Figure 11. Comparison of the discharge capacity of cells containing thin-film and thick-film cathodes produced with slurry pH values 12, 11, and 8 from Figure 6 at discharge rates of (a) C/5, (b) 1C, (c) 3C, and (d) the last C/5.

The lowering of the discharge curve at a high C-rate is due to cell polarization induced by ohmic resistance, charge transfer resistance, and diffusion overpotential [50]. The electrodes with larger film thicknesses have longer diffusion and migration pathways for lithium-ions to enter and leave the bulk electrode material. The particles in the upper

region of the electrode, which are kinetically favored, are intercalating more lithium-ions than the underlying regions. This overpotential in the electrode contributes to additional mass transport losses. The effect is more pronounced for thick-film electrodes, which require higher electrical current density to overcome the mass transport potential. Therefore, the internal resistance of lithium-ion diffusion increases with increasing C-rate. The electronic resistance of the electrode is proportional to its thickness [51], which is in reverse to its electronic conductivity. Thus the thick-film electrode causes an additional ohmic loss. This can be directly observed by the IR-drop at the initial voltage change in each cycle. For example, the voltages for thick-film electrodes decrease from 4.2 V to 3.2–3.6 V at 1C, while the voltages for thin-film electrodes remain at about 4.0 V.

4.3. Influence of Laser Structuring on Electrochemical Performance

Laser structuring via ultrafast laser ablation is an appealing method to improve capacity retention at high C-rates, especially for thick-film electrodes. During the formation step at C/20 as shown in Figure 7, the specific discharge capacity of cells containing unstructured electrodes is slightly higher compared to cells with structured electrodes. Such phenomena are also observed in the study from Park et al. using structured NMC 532 electrodes with PVDF as binder material [29]. This might be explained by the formation of a solid electrolyte interface (SEI) between electrode and electrolyte [52]. With a higher slurry pH value, there are more cavities inside the electrode. During cycling, the electrolyte could be pressed into the cavities inside the electrode. The increased interface between the electrode and free electrolyte owing to laser structuring leads to the formation of an extended SEI area. This would consume a higher amount of active material and electrolyte. Another assumption is that the SEI formation might be completed in a short period since the electrolyte wetting of laser structured electrodes is faster, while the SEI in unstructured electrodes could form during the cycling over a longer time period. Electrochemical impedance spectroscopy (EIS) might be applied in order to verify these assumptions.

Figure 12 shows the increase in specific capacity and areal capacity of cells with structured electrodes compared to cells with unstructured electrodes. The areal capacities can evaluate the capacity increase including the effect of active material loss due to the laser structuring, the areal capacities are calculated from the data shown in Figure 7. When the C-rate increases to C/2, laser structuring begins to show an advantage in capacity with an increase of 14–17 mAh/g (0.2–1.6 mAh/cm²) in comparison to cells with unstructured electrodes. This is similar to previous results of cells containing structured electrodes with PVDF as a binder [30]. At C/2, cell containing structured electrodes produced with slurry pH value of 9 retains 40 mAh/g more capacity due to laser structuring, while cells with electrodes produced with slurry pH values of 12.1 and 10 show 16.5 and 8 mAh/g higher capacity in comparison to cells containing unstructured electrodes produced with the same slurry pH value, respectively. This proves that for aqueous processed electrodes with porosities larger than 50% (slurry pH value of 12.1, without acid addition), laser structuring is still feasible to further increase the cell capacity at high C-rates relatively to cells with unstructured electrodes. This may be due to the connection of cavities inside the electrode as shown in Figure 3, which might lead to new diffusion pathways of lithium-ions from electrolyte to the bulk electrode. However, due to the high porosity and the uneven distribution of film thickness, the ablation depth is not stable during laser processing. This might cause local damage to the current collector. Therefore, slurry pH values should be adjusted to 9–10 in order to meet a suitable precondition for subsequent laser structuring.

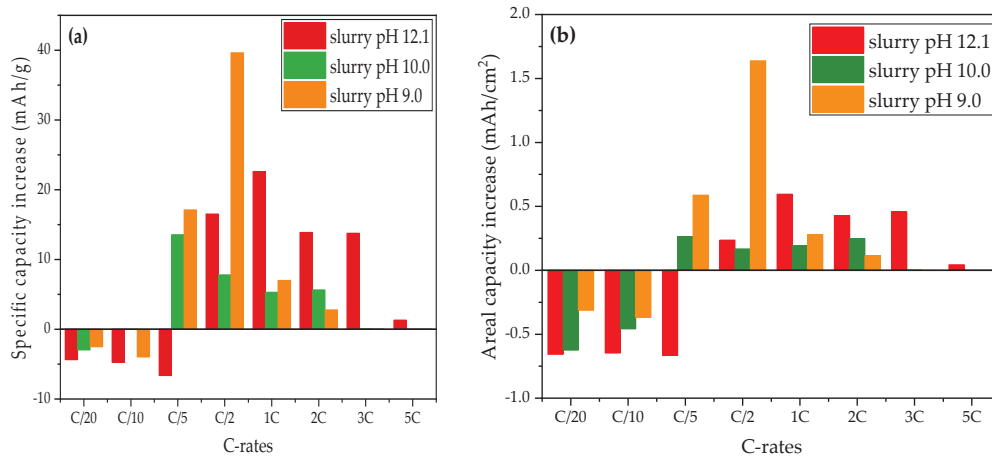


Figure 12. Comparison of (a) specific capacity increase and (b) areal capacity increase of cells with structured electrodes processed with different slurry pH values compared to cells with unstructured electrodes produced with the same slurry pH value.

5. Conclusions

Water-based binders CMC and TRD 202A were applied for the preparation of NMC 622 slurry, while acetic acid was added to balance the slurry pH value. Electrodes with different slurry pH values and thicknesses were tape cast on the aluminum foil and calendered afterward. In the last step, laser structuring using an ultrafast laser was performed to improve the electrochemical performance of cells at high C-rates.

The chemical reaction between the slurry without pH modification (pH 12.1) and the aluminum current collector, accompanied by hydrogen release during tape casting, leads to a large number of cavities in the dried cathode film. When the slurry pH is decreased below 10, no cavities inside the thick-film electrode or craters on the electrode surface were observed. With an increasing amount of acid, the viscosity of cathode slurries raised from 2 to 9 Pa·s at a shear rate of 50 s^{-1} , which is beneficial for thick-film manufacturing. However, the corrosion and hydrogen generation are stronger with increasing electrode thickness due to the fact that the drying time is necessarily increased with increasing film thickness.

Cyclic voltammetry proves that the addition of acetic acid did not affect the electrochemical reaction of the cathode active material. The voltage difference was increased with decreasing slurry pH values. This occurs as a result of an increased cell polarization caused by a decreased electrode film porosity. A strong impact of the slurry pH value and cathode film thickness on the discharge capacity was observed in rate capability tests. At high C-rates above C/5 for thin-film electrodes and above C/10 for thick-film electrodes, the specific capacity of the electrode with a larger slurry pH value was increased. Thick-film electrodes without acid addition showed the highest capacity, while the electrodes with the highest amount of acid (pH 8.4) retain less capacity at C/10 to 1C. The same tendency is observed for cells with thin-film electrodes. This is due to an improved electrolyte lithium-ion diffusion kinetics inside the electrode with high porosity. Laser structuring is feasible to increase the rate capability of aqueous processed thick-film electrodes, especially at discharge rates above C/2, which is due to an enlarged surface between the active material and free electrolyte, and new diffusion pathways for lithium-ions. In addition, unlike cathodes with high porosity, laser structuring has no significant impact on the post-processing as well as the adhesion of the electrode film to the current collector. Therefore, the pH value of NMC 622 slurry should be adjusted to 9–10, taking into account the balance between rate capability and corrosion of the current collector, as well as the precondition for laser structuring.

Author Contributions: Conceptualization, P.Z. and W.P.; methodology, P.Z.; validation, W.P.; investigation, J.H.; resources, P.Z. and W.P.; data curation, J.H. and P.Z.; writing—original draft preparation, P.Z. and J.H.; writing—review and editing, P.Z. and W.P.; supervision, W.P. All authors have read and agreed to the published version of the manuscript.

Funding: This research was funded by the Federal Ministry of Education and Research (BMBF), project NextGen-3DBat, project No. 03XP01798F. We also acknowledge support from the KIT-Publication Fund of the Karlsruhe Institute of Technology.

Institutional Review Board Statement: Not applicable.

Informed Consent Statement: Not applicable.

Data Availability Statement: Data sharing is not applicable to this article.

Acknowledgments: We are grateful for the help of our colleagues, A. Reif, A. Meyer, Y. Zheng, H. Besser, and M. Kapitz for their technical support and assistance in laser processing, material characterization, and battery analyses. In addition, we would like to acknowledge equipment support in the slurry mixing from W. Bauer and U. Kaufmann.

Conflicts of Interest: The authors declare no conflict of interest.

References

1. Goodenough, J.B.; Park, K.-S. The Li-Ion Rechargeable Battery: A Perspective. *J. Am. Chem. Soc.* **2013**, *135*, 1167–1176. [CrossRef]
2. Kwade, A.; Haselrieder, W.; Leithoff, R.; Modlinger, A.; Dietrich, F.; Droeder, K. Current status and challenges for automotive battery production technologies. *Nat. Energy* **2018**, *3*, 290–300. [CrossRef]
3. Choi, J.W.; Aurbach, D. Promise and reality of post-lithium-ion batteries with high energy densities. *Nat. Rev. Mater.* **2016**, *1*, 16013. [CrossRef]
4. Blomgren, G.E. The Development and Future of Lithium Ion Batteries. *J. Electrochem. Soc.* **2016**, *164*, A5019. [CrossRef]
5. Nitta, N.; Wu, F.; Lee, J.T.; Yushin, G. Li-ion battery materials: Present and future. *Mater. Today* **2015**, *18*, 252–264. [CrossRef]
6. Pistoia, G.; Liaw, B. *Behaviour of Lithium-Ion Batteries in Electric Vehicles: Battery Health, Performance, Safety, and Cost*; Springer: Berlin/Heidelberg, Germany, 2018; ISBN 3319699504.
7. Masias, A.; Marcicki, J.; Paxton, W.A. Opportunities and Challenges of Lithium Ion Batteries in Automotive Applications. *ACS Energy Lett.* **2021**, *6*, 621–630. [CrossRef]
8. Liu, P.; Ross, R.; Newman, A. Long-range, low-cost electric vehicles enabled by robust energy storage. *MRS Energy Sustain.* **2015**, *2*, 2. [CrossRef]
9. Wood, D.; Li, J.; Daniel, C. Prospects for reducing the processing cost of lithium ion batteries. *J. Power Sources* **2015**, *275*, 234–242. [CrossRef]
10. Kim, G.; Jeong, S.; Joost, M.; Rocca, E.; Winter, M.; Passerini, S.; Balducci, A. Use of natural binders and ionic liquid electrolytes for greener and safer lithium-ion batteries. *J. Power Sources* **2011**, *196*, 2187–2194. [CrossRef]
11. Susarla, N.; Ahmed, S.; Dees, D.W. Modeling and analysis of solvent removal during Li-ion battery electrode drying. *J. Power Sources* **2018**, *378*, 660–670. [CrossRef]
12. Ling, M.; Qiu, J.; Li, S.; Zhao, H.; Liu, G.; Zhang, S. An environmentally benign LIB fabrication process using a low cost, water soluble and efficient binder. *J. Mater. Chem. A* **2013**, *1*, 11543–11547. [CrossRef]
13. Buqa, H.; Holzapfel, M.; Krumeich, F.; Veit, C.; Novák, P. Study of styrene butadiene rubber and sodium methyl cellulose as binder for negative electrodes in lithium-ion batteries. *J. Power Sources* **2006**, *161*, 617–622. [CrossRef]
14. Zheng, Y.; Seifert, H.; Shi, H.; Zhang, Y.; Kübel, C.; Pflöging, W. 3D silicon/graphite composite electrodes for high-energy lithium-ion batteries. *Electrochim. Acta* **2019**, *317*, 502–508. [CrossRef]
15. Chen, Z.; Kim, G.-T.; Chao, D.; Loeffler, N.; Copley, M.; Lin, J.; Shen, Z.; Passerini, S. Toward greener lithium-ion batteries: Aqueous binder-based $\text{LiNi}_{0.4}\text{Co}_{0.2}\text{Mn}_{0.4}\text{O}_2$ cathode material with superior electrochemical performance. *J. Power Sources* **2017**, *372*, 180–187. [CrossRef]
16. Çetinel, F.A.; Bauer, W. Processing of water-based $\text{LiNi}_{1/3}\text{Mn}_{1/3}\text{Co}_{1/3}\text{O}_2$ pastes for manufacturing lithium ion battery cathodes. *Bull. Mater. Sci.* **2014**, *37*, 1685–1690. [CrossRef]
17. Bauer, W.; Çetinel, F.A.; Müller, M.; Kaufmann, U. Effects of pH control by acid addition at the aqueous processing of cathodes for lithium ion batteries. *Electrochim. Acta* **2019**, *317*, 112–119. [CrossRef]
18. Loeffler, N.; Zamory, J.; Laszczynski, N.; Doberdo, I.; Kim, G.-T.; Passerini, S. Performance of $\text{LiNi}_{1/3}\text{Mn}_{1/3}\text{Co}_{1/3}\text{O}_2$ /graphite batteries based on aqueous binder. *J. Power Sources* **2014**, *248*, 915–922. [CrossRef]
19. Li, C.-C.; Lee, J.-T.; Tung, Y.-L.; Yang, C.-R. Effects of pH on the dispersion and cell performance of LiCoO_2 cathodes based on the aqueous process. *J. Mater. Sci.* **2007**, *42*, 5773–5777. [CrossRef]
20. Li, J.; Armstrong, B.L.; Kiggans, J.; Daniel, C.; Wood, D.L., III. Lithium ion cell performance enhancement using aqueous LiFePO_4 cathode dispersions and polyethyleneimine dispersant. *J. Electrochem. Soc.* **2012**, *160*, A201. [CrossRef]

21. Hawley, W.B.; Parejiya, A.; Bai, Y.; Meyer, H.M., III; Wood, D.L., III; Li, J. Lithium and transition metal dissolution due to aqueous processing in lithium-ion battery cathode active materials. *J. Power Sources* **2020**, *466*, 228315. [CrossRef]
22. Du, Z.; Rollag, K.; Li, J.; An, S.; Wood, M.; Sheng, Y.; Mukherjee, P.; Daniel, C.; Wood, D. Enabling aqueous processing for crack-free thick electrodes. *J. Power Sources* **2017**, *354*, 200–206. [CrossRef]
23. Bichon, M.; Sotta, D.; Dupré, N.; De Vito, E.; Boulineau, A.; Porcher, W.; Lestriez, B. Study of Immersion of $\text{LiNi}_{0.5}\text{Mn}_{0.3}\text{Co}_{0.2}\text{O}_2$ Material in Water for Aqueous Processing of Positive Electrode for Li-Ion Batteries. *ACS Appl. Mater. Interfaces* **2019**, *11*, 18331–18341. [CrossRef]
24. Carvalho, D.V.; Loeffler, N.; Hekmatfar, M.; Moretti, A.; Kim, G.-T.; Passerini, S. Evaluation of guar gum-based biopolymers as binders for lithium-ion batteries electrodes. *Electrochim. Acta* **2018**, *265*, 89–97. [CrossRef]
25. Wu, X.; Xia, S.; Huang, Y.; Hu, X.; Yuan, B.; Chen, S.; Yu, Y.; Liu, W. High-Performance, Low-Cost, and Dense-Structure Electrodes with High Mass Loading for Lithium-Ion Batteries. *Adv. Funct. Mater.* **2019**, *29*, 1903961. [CrossRef]
26. Park, K.-Y.; Park, J.-W.; Seong, W.M.; Yoon, K.; Hwang, T.-H.; Ko, K.-H.; Han, J.-H.; Jaedong, Y.; Kang, K. Understanding capacity fading mechanism of thick electrodes for lithium-ion rechargeable batteries. *J. Power Sources* **2020**, *468*, 228369. [CrossRef]
27. Pflöging, W. A review of laser electrode processing for development and manufacturing of lithium-ion batteries. *Nanophotonics* **2018**, *7*, 549–573. [CrossRef]
28. Pflöging, W. Recent progress in laser texturing of battery materials: A review of tuning electrochemical performances, related material development, and prospects for large-scale manufacturing. *Int. J. Extrem. Manuf.* **2020**, *3*, 012002. [CrossRef]
29. Park, J.; Hyeon, S.; Jeong, S.; Kim, H.-J. Performance enhancement of Li-ion battery by laser structuring of thick electrode with low porosity. *J. Ind. Eng. Chem.* **2019**, *70*, 178–185. [CrossRef]
30. Zhu, P.; Seifert, H.J.; Pflöging, W. The Ultrafast Laser Ablation of $\text{Li}(\text{Ni}_{0.6}\text{Mn}_{0.2}\text{Co}_{0.2})\text{O}_2$ Electrodes with High Mass Loading. *Appl. Sci.* **2019**, *9*, 4067. [CrossRef]
31. Hamam, I.; Zhang, N.; Liu, A.; Johnson, M.; Dahn, J.R. Study of the Reactions between Ni-Rich Positive Electrode Materials and Aqueous Solutions and their Relation to the Failure of Li-Ion Cells. *J. Electrochem. Soc.* **2020**, *167*, 130521. [CrossRef]
32. Kazzazi, A.; Bresser, D.; Birrozzi, A.; Von Zamory, J.; Hekmatfar, M.; Passerini, S. Comparative Analysis of Aqueous Binders for High-Energy Li-Rich NMC as a Lithium-Ion Cathode and the Impact of Adding Phosphoric Acid. *ACS Appl. Mater. Interfaces* **2018**, *10*, 17214–17222. [CrossRef]
33. Kuenzel, M.; Bresser, D.; Diemant, T.; Carvalho, D.V.; Kim, G.; Behm, R.J.; Passerini, S. Complementary Strategies Toward the Aqueous Processing of High-Voltage $\text{LiNi}_{0.5}\text{Mn}_{1.5}\text{O}_4$ Lithium-Ion Cathodes. *ChemSusChem* **2018**, *11*, 562–573. [CrossRef] [PubMed]
34. Kuenzel, M.; Choi, H.; Wu, F.; Kazzazi, A.; Axmann, P.; Wohlfahrt-Mehrens, M.; Bresser, D.; Passerini, S. Co-Crosslinked Water-Soluble Biopolymers as a Binder for High-Voltage $\text{LiNi}_{0.5}\text{Mn}_{1.5}\text{O}_4$ | Graphite Lithium-Ion Full Cells. *ChemSusChem* **2020**, *13*, 2650–2660. [CrossRef] [PubMed]
35. Ibing, L.; Gallasch, T.; Friesen, A.; Niehoff, P.; Hintennach, A.; Winter, M.; Börner, M. The role of the pH value in water-based pastes on the processing and performance of Ni-rich $\text{LiNi}_{0.5}\text{Mn}_{0.3}\text{Co}_{0.2}\text{O}_2$ based positive electrodes. *J. Power Sources* **2020**, *475*, 228608. [CrossRef]
36. Rakebrandt, J.H.; Smyrek, P.; Zheng, Y.; Seifert, H.J.; Pflöging, W. (Eds.) Laser Processing of Thick $\text{Li}(\text{NiMnCo})\text{O}_2$ Electrodes for Lithium-Ion Batteries. In *Laser-Based Micro- and Nanoprocessing XI*; International Society for Optics and Photonics: Bellingham, WA, USA, 2017.
37. Wood, M.; Li, J.; Ruther, R.E.; Du, Z.; Self, E.C.; Meyer, H.M.; Daniel, C.; Belharouak, I.; Wood, D.L. Chemical stability and long-term cell performance of low-cobalt, Ni-Rich cathodes prepared by aqueous processing for high-energy Li-Ion batteries. *Energy Storage Mater.* **2020**, *24*, 188–197. [CrossRef]
38. Shkrob, I.A.; Gilbert, J.A.; Phillips, P.J.; Klie, R.; Haasch, R.; Bareño, J.; Abraham, D.P. Chemical Weathering of Layered Ni-Rich Oxide Electrode Materials: Evidence for Cation Exchange. *J. Electrochem. Soc.* **2017**, *164*, A1489. [CrossRef]
39. Sukiman, N.L.; Zhou, X.; Birbilis, N.; Hughes, A.E.; Mol, J.M.; Garcia, S.J.; Thompson, G.E. Durability and corrosion of aluminium and its alloys: Overview, property space, techniques and developments. In *Aluminium Alloys-New Trends in Fabrication and Applications*; IntechOpen: London, UK, 2012; pp. 47–97.
40. Church, B.C.; Kaminski, D.T.; Jiang, J. Corrosion of aluminum electrodes in aqueous slurries for lithium-ion batteries. *J. Mater. Sci.* **2014**, *49*, 3234–3241. [CrossRef]
41. Li, S.Y.; Church, B.C. Effect of aqueous-based cathode slurry pH and immersion time on corrosion of aluminum current collector in lithium-ion batteries. *Mater. Corros.* **2016**, *67*, 978–987. [CrossRef]
42. Lee, J.-H.; Kim, J.-S.; Kim, Y.C.; Zang, D.S.; Paik, U. Dispersion properties of aqueous-based LiFePO_4 pastes and their electrochemical performance for lithium batteries. *Ultramicroscopy* **2008**, *108*, 1256–1259. [CrossRef] [PubMed]
43. Yang, X.H.; Zhu, W.L. Viscosity properties of sodium carboxymethylcellulose solutions. *Cellulose* **2007**, *14*, 409–417. [CrossRef]
44. Lee, J.-H.; Choi, Y.-M.; Paik, U.; Park, J.-G. The effect of carboxymethyl cellulose swelling on the stability of natural graphite particulates in an aqueous medium for lithium ion battery anodes. *J. Electroceram.* **2006**, *17*, 657–660. [CrossRef]
45. Michailova, V.; Titeva, S.; Kotsilkova, R.; Krusteva, E.; Minkov, E. Influence of aqueous medium on viscoelastic properties of carboxymethylcellulose sodium, hydroxypropylmethyl cellulose, and thermally pre-gelatinized starch gels. *Colloids Surf. A Physicochem. Eng. Asp.* **1999**, *149*, 515–520. [CrossRef]

46. Liu, P.; Zhai, M.; Li, J.; Peng, J.; Wu, J. Radiation preparation and swelling behavior of sodium carboxymethyl cellulose hydrogels. *Radiat. Phys. Chem.* **2002**, *63*, 525–528. [CrossRef]
47. Hawley, W.; Li, J. Electrode manufacturing for lithium-ion batteries—Analysis of current and next generation processing. *J. Energy Storage* **2019**, *25*, 100862. [CrossRef]
48. Shaju, K.M.; Rao, G.S.; Chowdari, B.V. Performance of layered $\text{Li}(\text{Ni}_{1/3}\text{Co}_{1/3}\text{Mn}_{1/3})\text{O}_2$ as cathode for Li-ion batteries. *Electrochim. Acta* **2002**, *48*, 145–151. [CrossRef]
49. Elgrishi, N.; Rountree, K.J.; McCarthy, B.D.; Rountree, E.S.; Eisenhart, T.T.; Dempsey, J.L. A practical beginner's guide to cyclic voltammetry. *J. Chem. Educ.* **2018**, *95*, 197–206. [CrossRef]
50. Zheng, H.; Li, J.; Song, X.; Liu, G.; Battaglia, V.S. A comprehensive understanding of electrode thickness effects on the electrochemical performances of Li-ion battery cathodes. *Electrochim. Acta* **2012**, *71*, 258–265. [CrossRef]
51. Ogihara, N.; Itou, Y.; Sasaki, T.; Takeuchi, Y. Impedance Spectroscopy Characterization of Porous Electrodes under Different Electrode Thickness Using a Symmetric Cell for High-Performance Lithium-Ion Batteries. *J. Phys. Chem. C* **2015**, *119*, 4612–4619. [CrossRef]
52. Peled, E. The electrochemical behavior of alkali and alkaline earth metals in nonaqueous battery systems—The solid electrolyte interphase model. *J. Electrochem. Soc.* **1979**, *126*, 2047. [CrossRef]



Article

Ultrafast-Laser Micro-Structuring of $\text{LiNi}_{0.8}\text{Mn}_{0.1}\text{Co}_{0.1}\text{O}_2$ Cathode for High-Rate Capability of Three-Dimensional Li-ion Batteries

Minh Xuan Tran ^{1,2}, Peter Smyrek ^{3,4}, Jihun Park ⁵, Wilhelm Pfleging ^{3,4,*} and Joong Kee Lee ^{1,2,*}

¹ Division of Energy and Environmental Technology, KIST School, Korea University of Science and Technology (UST), Deajeon 34113, Korea

² Center for Energy Storage Research, Green City Research Institute, Korea Institute of Science and Technology (KIST), Seoul 02792, Korea

³ Karlsruhe Institute of Technology, Institute for Applied Materials, P.O. Box 3640, 76021 Karlsruhe, Germany

⁴ Karlsruhe Nano Micro Facility, Hermann-von-Helmholtz-Platz 1, 76344 Eggenstein-Leopoldshafen, Germany

⁵ APC Technology, 108 68 Gangbyeonyeok-ro-4-gil, Gwangjin-gu, Seoul 05116, Korea

* Correspondence: wilhelm.pfleging@kit.edu (W.P.); leejk@kist.re.kr (J.K.L.)

Abstract: Femtosecond ultrafast-laser micro-patterning was employed to prepare a three-dimensional (3D) structure for the tape-casting Ni-rich $\text{LiNi}_{0.8}\text{Mn}_{0.1}\text{Co}_{0.1}\text{O}_2$ (NMC811) cathode. The influences of laser structuring on the electrochemical performance of NMC811 were investigated. The 3D-NMC811 cathode retained capacities of 77.8% at 2 C of initial capacity at 0.1 C, which was thrice that of 2D-NMC811 with an initial capacity of 27.8%. Cyclic voltammetry (CV) and impedance spectroscopy demonstrated that the 3D electrode improved the Li^+ ion transportation at the electrode–electrolyte interface, resulting in a higher rate capability. The diffusivity coefficient D_{Li^+} , calculated by both CV and electrochemical impedance spectroscopy, revealed that 3D-NMC811 delivered faster Li^+ ion transportation with higher D_{Li^+} than that of 2D-NMC811. The laser ablation of the active material also led to a lower charge–transfer resistance, which represented lower polarization and improved Li^+ ion diffusivity.

Keywords: three-dimensional batteries; $\text{LiNi}_{0.8}\text{Mn}_{0.1}\text{Co}_{0.1}\text{O}_2$ cathode; femtosecond ultrafast laser; electrode micro-structuring

1. Introduction

The conventional Li-ion batteries (LIBs) have several limitations, such as low energy density, high cost of the active material, and poor thermal stability [1–3]; hence, their use is limited. However, $\text{LiNi}_x\text{Mn}_y\text{Co}_z\text{O}_2$ (NMC) has been attracting increasing attention as a promising cathode material with a higher specific capacity and energy density than that of the conventional LiCoO_2 (LCO) [4,5]. The Ni-rich NMC cathode, particularly $\text{LiNi}_{0.8}\text{Mn}_{0.1}\text{Co}_{0.8}\text{O}_2$ (NMC811), is more cost efficient and has a higher practical specific capacity (200 mAh g^{-1}) than that of the lower-Ni-contained NMC cathode (160 mAh g^{-1}) at an average discharge potential of 3.8 V (vs. Li^+/Li) [6,7]. However, batteries for electric vehicles and applications in smart grid systems require high power to sufficiently charge in a very short time. The output power of LIBs is determined by the transport rate of the Li^+ ion in an electrolyte and active material. Although the NMC cathode materials exhibit superior features in comparison with those of LCO, the NMC cathode is unable to demonstrate the high rate capabilities of conventional electrodes caused by structure disruption and cation-mixing between Li^+ and Ni^{2+} [8–10]. Moreover, the final cell weight and specific cell capacity are functions of the cathode film thickness [11]. Thus, when the thickness of the cathode film increases from 50 μm to 200 μm , the specific cell capacity increases by 29% [12]. Electrodes with thicknesses of 100–200 μm exhibit high energy density, whereas thin electrodes with thicknesses of 10–50 μm exhibit high power density [13,14].

However, the Li^+ diffusion kinetics and mechanical integrity of the film decrease with the electrode film thickness because the active material expands and contracts during continuous charge/discharge processes [15]. Three-dimensional (3D) electrode configuration in LIBs is one of the approaches to overcome the limitations of thick electrode films, such as power losses and mechanical degradation during charge and discharge operations because of high volume expansion [16,17]. Three-dimensional structuring of electrodes improves the electron and ion diffusion kinetics in the electrodes. Moreover, 3D-electrode architectures lead to an increased active surface area, reduced mechanical tensions during electrochemical cycling, and an overall reduced cell impedance [18]. Common methods for 3D configuration in electrodes are the structuring of the substrate or current collector via template deposition of nano-rods or anisotropic etching of silicon. These approaches are only available for thin-film micro batteries and are not feasible for thick-film electrodes [19]. Nonetheless, ultrafast laser structuring is a novel approach to realize the 3D battery concept, and has been applied for thin-film electrodes, including LiCoO_2 , $\text{Li}_2\text{Mn}_2\text{O}_4$ and SnO_2 [17,20,21]. Moreover, composite electrodes that were patterned with ultrafast lasers have exhibited improved capacities at high charge and discharge currents. The enhancement in the electrochemical performance can also be attributed to the improvement in the wetting of the electrode surface, which results in a decrease in the time and cost required for the vacuum and storage processes during the assembly of LIB cells [12].

In this work, commercial NMC811 was employed as the active material to obtain high energy density. Femtosecond ultrafast laser structuring technology was applied to tape-casted composite electrodes to improve the rate capability of LIBs. In order to investigate the balance of active material loss by ablation from laser structuring and increase in interfacial surface area, ultrafast laser patterning was carried out on NMC811 cathodes with two different thicknesses of 40 and 100 μm . Without structuring, the thin film electrode could deliver better rate capability. When 3D structuring was performed, the rate capability of the thick film electrode was improved to 133 mAh g^{-1} at 5 C. Meanwhile, the structured thin film electrode could not deliver capacity as high as that of post-structuring due to more severe loss of active material. Therefore, the balancing of loss material and increment of interfacial area was a factor that affected improvement in rate capability. The diffusivity of Li^+ ions was studied using cyclic voltammetry (CV) and electrochemical impedance spectroscopy. When laser structuring of the electrode was performed, the transportation of the Li^+ ions improved significantly, with a higher value of D_{Li^+} , which could be attributed to the high aspect ratio of 3.7 and increase in surface area of 78%.

2. Materials and Methods

2.1. Material Characterization

The commercial NMC811 powders, with particle size of 10 μm (ECOPro BM, Chungcheongbuk-do, Korea), were used as obtained as the electrode active material. X-ray diffraction (XRD, Rigaku, Tokyo, Japan) analysis was performed using $\text{Cu K}\alpha$ radiation ($\lambda = 0.15406 \text{ \AA}$) in the 2θ range of $20\text{--}80^\circ$ at a continuous scan mode with a step size of 0.02° and a scan rate of 2° min^{-1} . The morphology and structure of the NMC811 particles were observed using field-emission scanning electron microscopy (FE-SEM, Inspect F50, ThermoFisher, Hillsboro, OR, USA) with an accelerating voltage of 10 kV.

2.2. Ultrafast-Laser Structuring of NMC811 Electrode

The cathode slurry, comprised of NMC811: acetylene black (DB100, Denka, Tokyo, Japan): polyvinylidene fluoride (PVDF, Aldrich, MO, USA), in a weight ratio of 85:10:5, was well mixed in *N*-methylpyrrolidone (NMP, Aldrich, MO, USA) solvent. Then, the slurry was tape-casted on an 18 μm thick aluminum foil as the current collector. After being dried in an oven at 60°C overnight, a calendaring roll pressure was applied to reduce 10% of the original thickness of the as-prepared cathode to decrease the porosity of the electrodes. The average thickness of the cathodes was 100 μm (exclusive of the Al foil thickness).

Ultrafast-laser-assisted structuring was performed on the calendared electrodes using a fiber laser (Tangerine, Amplitude Systèmes, Pessac, France) operating at a wavelength of $\lambda = 1030$ nm with a pulse duration of 380 fs and a laser pulse repetition of 500 kHz. The laser beam was scanned over the sample surface using deflection mirrors with scanning velocities in the range of 100–1500 mm s⁻¹. All experiments were conducted under ambient air and the ablated material was removed by an exhaust.

2.3. Electrochemical Tests

The 2032 coin cell was prepared after the electrodes were dried in a vacuum oven at 80 °C for 12 h. The cathodes were laser cut into discs of 12 mm diameter. A Li metal foil (Wellcos Co., Gyeonggi-do, Korea) disk of Ø18 mm was used as the anode. The cathode and anode in the coin cells were separated by microporous polypropylene (PP) membranes (Celgard 2400, North Carolina, USA) in an electrolyte of 1 M LiPF₆ in ethylene carbonate (EC): ethyl methylene carbonate (EMC): diethylene carbonate (DMC) (1:1:1 volume ratio). The cell assembly was performed in a dry room with a dew point temperature of less than -100.2 °C. The electrochemical testing experiments were conducted using a Maccor automated battery tester (MACCOR series-4000, Tulsa, OK, United States) at room temperature of 25 °C. The Li-ion cells were galvanostatically charged/discharged at various currents in the working voltage range of 3.0–4.3 V, after being allowed to rest for 12 h. CV was conducted at scan rates of 0.3–1 mV s⁻¹ in the potential range of 3.0–4.3 V. The coin cell was measured by electrochemical impedance spectroscopy (EIS) by applying a frequency range of 1 mHz to 100 kHz to a potentiostat (Bio-Logic Science Instruments, Seyssinet-Pariset, France) with a voltage amplitude of 5 mV.

2.4. Diffusivity Coefficient Calculation

2.4.1. Diffusivity Coefficient by Cyclic Voltammetry

The diffusion coefficient of lithium ion can be determined by the Randles–Sevcik equation:

$$i_p = 0.4463 \text{ mAF} \left(\frac{F}{RT} \right)^{1/2} C_{\text{Li}} D_{\text{Li}}^{1/2} \omega \nu^{1/2}, \quad (1)$$

where i_p is peak current (A), m is the mass of active materials-NMC811 (g), A is the effective area of the electrode (cm²), F is the Faraday constant (96,485 s A mol⁻¹), R is the gas constant (8.314 J K⁻¹ mol⁻¹), T is the absolute temperature (K), C is the initial concentration of lithium ion (1.0 mol cm⁻³), D_{Li^+} is the chemical diffusion coefficient of Li⁺ (cm² s⁻¹), and ν is the scan rate in mV s⁻¹ [22].

2.4.2. Diffusivity Coefficient by EIS

The diffusivity coefficient is calculated using the following equation:

$$D_{\text{Li}^+} = \frac{R^2 T^2}{2A^2 n^4 F^4 C^2 \sigma^2}, \quad (2)$$

where A (cm²) is the effective surface area of the electrode, n is the number of exchanged electrons ($n = 1$), F is Faraday constant, R is gas constant, T is temperature (285 K), C is the initial concentration of Li⁺ in electrolyte, and σ is the Warburg factor [23].

The Warburg factor can be determined with the real resistance according to the equation below:

$$Z_{re} = R_s + R_{ct} + \sigma \omega^{1/2}, \quad (3)$$

where R_s (Ω) denotes solution resistance, and ω (Hz) is frequency. The value of σ is extracted from the slope of linear correlation between Z_{re} and $\omega^{-1/2}$.

The effective surface area of electrode (A) used in both Equations (1) and (2) was estimated as the surface area of the electrode. For the 2D-NMC811 electrode, the value of A was calculated as the surface area of the electrode with a diameter of Ø1.2 cm. Effec-

tive surface area of 3D-NMC811 was calculated based on the increasing surface area, as summarized in Table S1.

3. Results and Discussion

The as-received NMC811 particles had a uniform spherical shape with average diameters, D50, of approximately 10 μm , as depicted by the FE-SEM images in Figure S1. The NMC811 spheres were primarily comprised of polyhedral grains of sub-micron size that aggregated to form secondary NMC811 particles, which were consistent with other reports [24,25]. As shown in Figure S1d, the result from the EDX of the selected area suggested that the surface of the NMC811 particles was represented by a composition of a Ni:Mn:Co atomic ratio of 8:1:1, approximately. The crystalline structure of NMC was confirmed by conducting XRD measurements. As illustrated in Figure S2a, the XRD patterns indicated that NMC811 had a layer structure, based on hexagonal $\alpha\text{-NaFeO}_2$ with space group R3 m. There were no impurity or secondary phases detected. NMC811 powder had a highly well-defined layer structure, indicated by the appearance of peak splitting of 006/102 and 108/110 (Figure S2b,c) [26,27]. Moreover, the intensity ratio of 003 and 104 peaks, $I_{(003)}/I_{(104)}$, was 1.1, approximately, which indicated a low degree of cation mixing and a good layered structure [7].

The morphologies of the electrodes before and after the structuring by the ultrafast laser are illustrated in Figure 1. After calendaring of the electrodes using a rolling press, the thicknesses of the electrodes were determined as 40 μm and 100 μm , approximately, indicated by the microscopy images in Figure 1. Both electrodes denoted as 2D-NMC811 were used for the laser structuring experiments. The femtosecond laser could remove the composite active materials down to the Al current collector. As depicted in Figure 1a,b, the electrodes were patterned to linear structure with a pitch distance of 200 μm . Figure 1c,d illustrates cross-sectional images of the structured electrodes, denoted as 3D-NMC811. The laser ablated active materials deep to the Al current collector to form a V-shaped channel. The 40 μm -thick NMC811 channel dimensions were determined to be ~ 25 μm wide and ~ 38 μm deep, while the 100 μm -thick cathode channels were found to be ~ 25 μm wide and ~ 90 μm deep. The edges of the cathode channels were observed to be smooth and uniform.

In order to compare with ablation studies on electrodes with different thicknesses, the aspect ratio AR (channel depth divided by channel width of half height), amounts of material loss and interfacial area increments were estimated and listed in Table S1. When the thickness of the electrodes increased from 40 μm to 100 μm , the AR value and interfacial area increment increased 4 times, from 0.96 to 3.72, and 20% to 78%, respectively. Along with the AR value, loss of active material by ablation from laser structuring decreased from 10% to 6.4% for the 40 μm - and the 100 μm -thick electrodes, respectively. The changes in the above parameters suggested that the laser structuring of electrodes would have more significant effect to improve electrochemical performance of the thick film, 3D-NMC811.

Figure 2a,b exhibits the rate capabilities of 2D- and 3D-NMC811 at various C-rates with thicknesses of 40 and 100 μm , respectively. The 40- μm -thick 2D-NMC811 cathode showed high capacities of 165, 102 and 66 mAh g^{-1} at C-rates of 0.1 C, 1 C and 2 C, respectively. When the thickness of the cathode increased to 100 μm , the capacities at 2 C and 5 C decreased drastically to 48 and 6 mA h g^{-1} , respectively, which was 2 times lower than that of the 40- μm cathode. The deterioration of capacity at high current density in the thick electrode was caused by two aspects: (1) the longer diffusion and migration path of Li^+ ions and (2) the higher local ion-current densities at the electrode/separator interface [28,29]. However, when the ultrafast-laser-structuring was performed, the tendency of rate capability changed remarkably. The 40- μm -thick cathode showed worsened performance with capacity at a high C-rate of 2 C and 5 C decreasing twice to 76 and 31 mAh g^{-1} , respectively, compared to that of 2D-NMC811. On the other hand, the thick 3D-NMC811 electrode (100 μm) showed capacities at 2 C increasing thrice from 48 to 133 mAh g^{-1} , which was higher than that of thin 3D-NMC811 at the same C-rate, as shown in Figure S3. As mentioned above, 3D laser-structuring can drastically improve the electrolyte wetting, and

the active material ablation from laser patterning could provide artificial porosity and an electrolyte reservoir. Thus, laser-induced micro-structuring of the electrode could enhance the electrochemical activation of NMC811 active particles in deeper layers, which resulted in an improvement in the rate capability of thick-film electrodes. Moreover, although interfacial surface area and porosity could increase by means of laser-induced ablation, the negative effect observed for the thin film electrode could be attributed to loss of up to 10% of active material and low AR value.

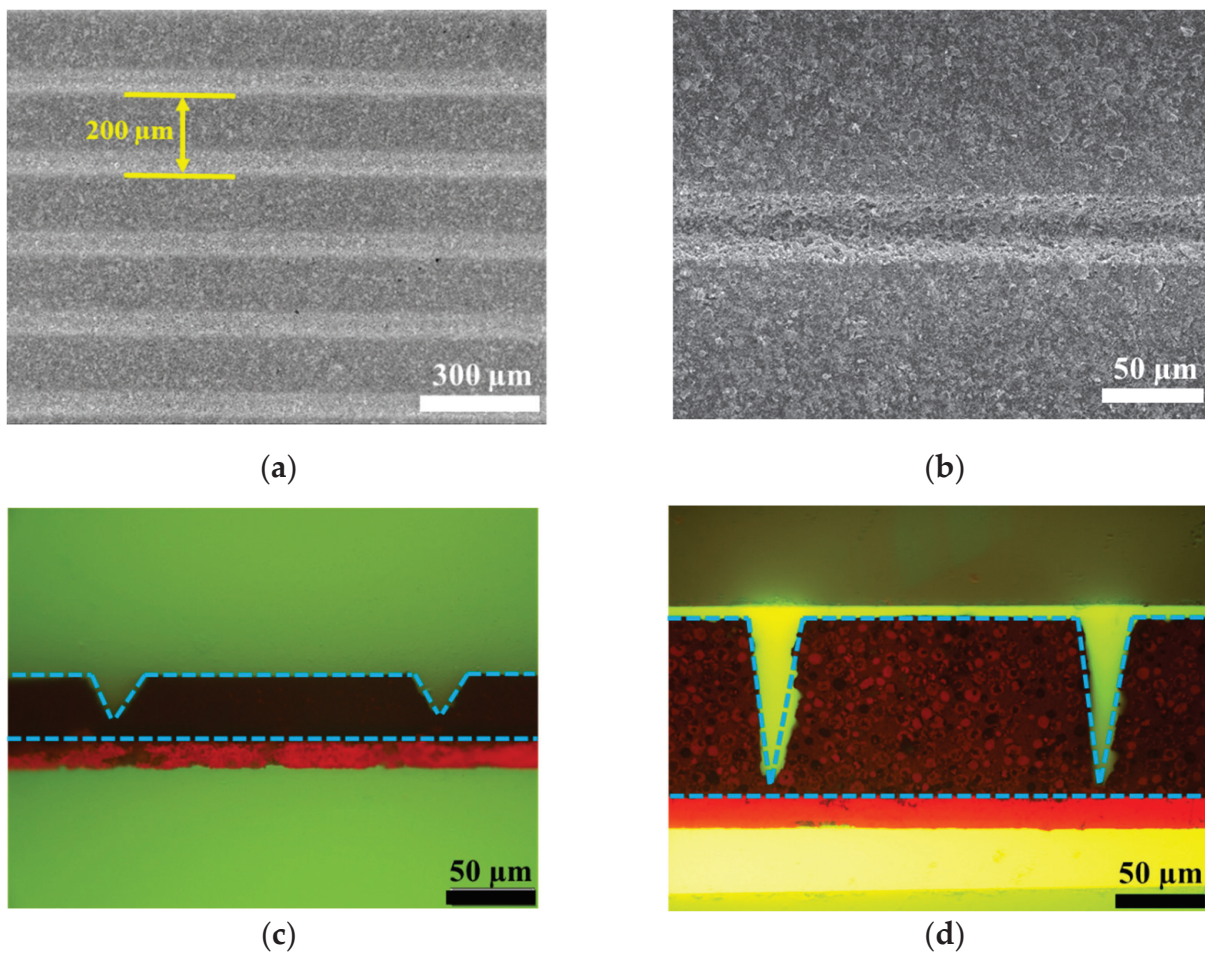


Figure 1. SEM and microscopic images of NMC electrodes (a,b) top-view of structured electrodes (SEM) at different magnifications, cross section of electrode at (c) 40 μm and (d) 100 μm (microscope).

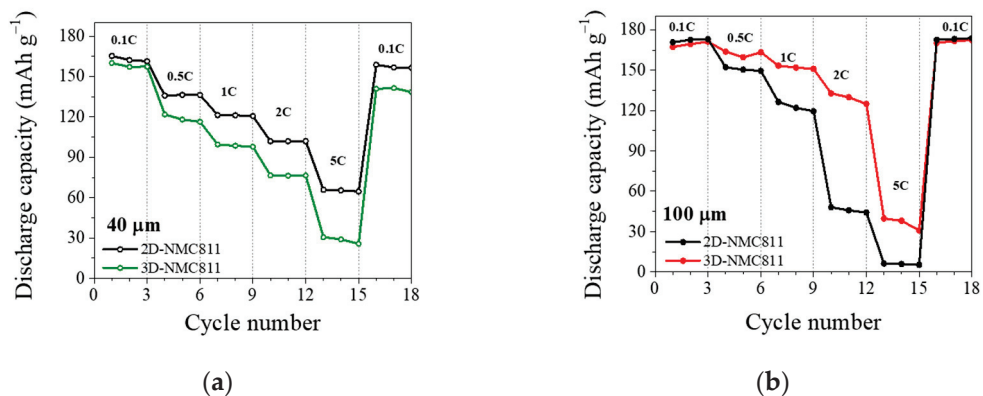


Figure 2. Rate capability performance for unstructured and structured NMC electrodes with thicknesses of (a) 40 μm and (b) 100 μm .

To study the promotion of Li^+ transportation in the case of a 100- μm -thick structured electrode, CV was performed. The CV curves of NMC811 at a scan rate of 0.3 mV s^{-1} (Figure 3a,b) indicated three distinct anodic/cathodic peaks, which could be assigned to distinct features of the Ni-rich NMC cathode materials. In the positive sweep, the first anodic peaks in the region of 3.4–3.8 V were assigned to the phase transition from a hexagonal to a monoclinic ($\text{H}_1 \rightarrow \text{M}$) lattice. In the region of potential higher than 3.8 V, there were two anodic peaks at approximately 4.0 and 4.2 V, which were caused by the phase transition from $\text{M} \rightarrow \text{H}_2$ and $\text{H}_2 \rightarrow \text{H}_3$, respectively [30,31]. In the first anodic scan, the potential downshifting could be attributed to the initial activation and stabilization of the active material. The current in the first anodic peak did not decrease drastically for the subsequent sweep scan in 3D-NMC811. In contrast, there was a significant change in the intensity of current from the first scan to the following scans in 2D-NMC811. This result indicated a decrease in the interfacial polarization and better reversibility of the 3D-electrode.

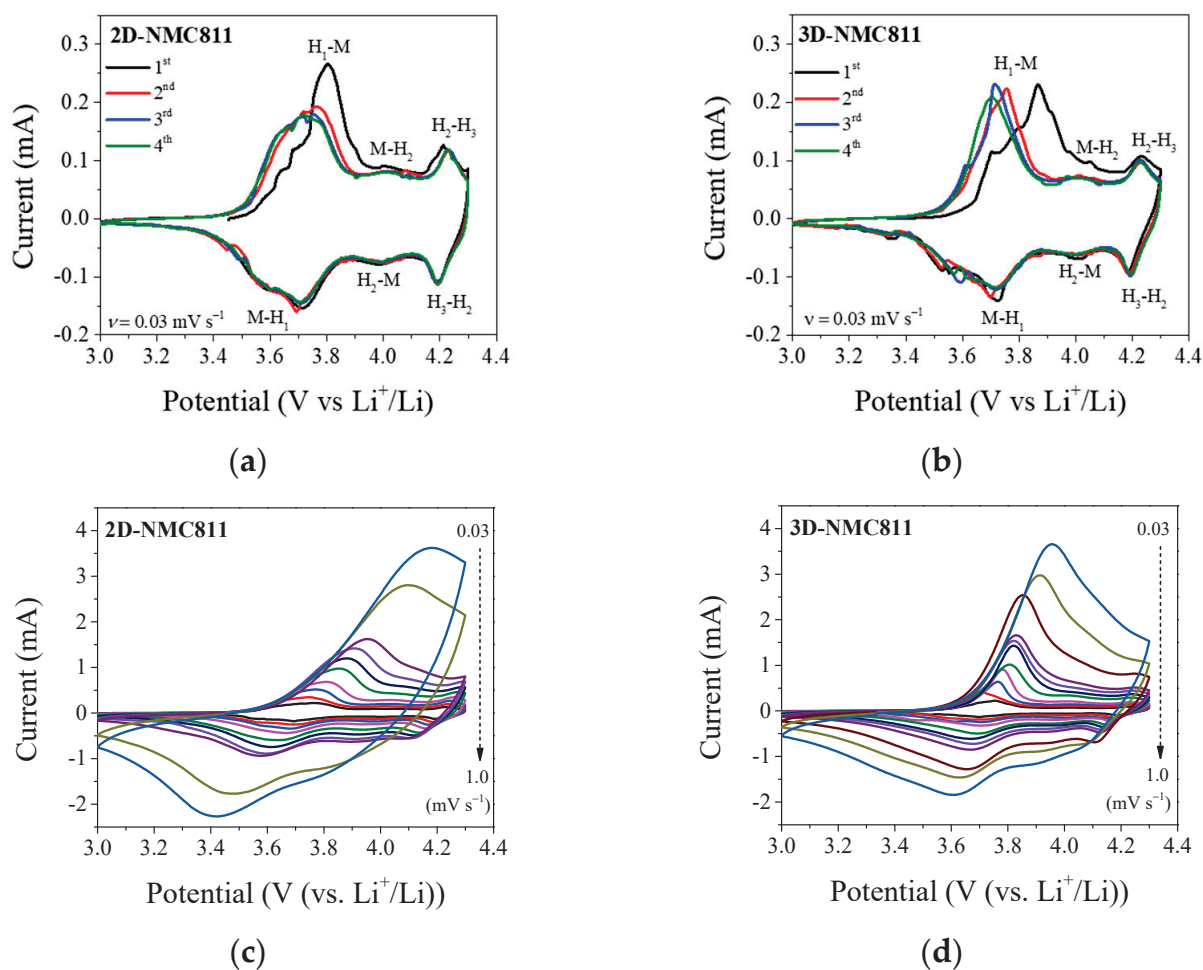


Figure 3. Cyclic voltammetry (CV) data of 2D- and 3D-NMC811 electrodes at (a,b) 0.3 mV s^{-1} and (c,d) various scan rates from 0.03 to 1.0 mV s^{-1} .

The potential of the cells with 2D- and 3D-NMC811 were swept at scan rates of $0.03\text{--}1.0 \text{ mV s}^{-1}$ to calculate the diffusion coefficient (D_{Li^+}). As illustrated in Figure 3c,d, the value of the peak currents increased proportionally with the increase in the scan rates, because of the increase in the flux of the charge carrier species at the electrode surface [32]. Since the polarization increased with scan rates, the redox peak positions also shifted to higher and lower voltages for the oxidation (anodic) and the reduction (cathodic) processes, respectively. The redox peak potentials of the structured electrode were significantly higher

than those of the unstructured electrode at the same scan rate. The differences related to the polarization influence were more obvious at a sweep rate higher than 0.5 mV s^{-1} . The mass transfer at the electrode–electrolyte interface was a major factor that caused the polarization in Li-ion cells [33]. The redox peak positions in the CVs upshift and downshift in the charge and discharge processes, respectively, indicated that the enhancement in the mass transfer led to the hindering of the polarization. The 3D-structuring of the electrode by an ultrafast laser could improve the rate performance of NMC811 by enhancement of mass transfer upon electrode. In addition, the diffusion coefficient of the Li^+ ions could be determined by Equation (1) [34]. As depicted in Figure S4, a linear correlation of the peak current density (j) and the square root of scan rate ($\nu^{1/2}$) was obtained. Accordingly, the diffusivity coefficients of 2D-NMC cathode were 16.6×10^{-11} and $2.0 \times 10^{-11} \text{ cm}^2 \text{ s}^{-1}$ for the oxidation and reduction processes, respectively, as shown in Table S2. When laser patterning was employed, there was an increase in D_{Li^+} for the anodic peak to $18.9 \times 10^{-11} \text{ cm}^2 \text{ s}^{-1}$. This result implied that laser structuring of the electrode could improve the Li^+ ion diffusivity in the 3D-NMC811 electrode, due to the increase in the interfacial surface area and improvement in the electrolyte wetting, thereby facilitating fast Li^+ ion transportation.

Moreover, to understand more about the effect of laser structuring on the electrochemical characteristics, impedance analysis was conducted, as illustrated in Figure 4a. The impedance spectroscopy results were consistent with results from CV and diffusivity coefficient. A semicircle in the high frequency range, representing charge transfer resistance (R_{ct}), and a sloping line in the low frequency range, representing Warburg resistance, were observed in both the 2D- and 3D-electrodes. In the Nyquist plots, the semicircle of the 3D-electrode was smaller than that of the 2D electrode. In general, the semicircle in the Nyquist plot represented the impedance values related to the charge–transfer resistance (R_{ct}) obtained by fitting the Nyquist plots, using ZView software, with the corresponding equivalent circuit (Table S2). Moreover, the diffusivity coefficient could also be calculated using σ from Equation (2), which was the Warburg factor extracted from the slope of linear correlation between Z_{re} and $\omega^{-1/2}$, as depicted in Figure S5 [23]. As shown in Figure 4b and Table S2, fresh cells with 3D-NMC811 possessed a lower R_{ct} of 107.7Ω and a higher D_{Li^+} of $3.5 \times 10^{-11} \text{ cm}^2 \text{ s}^{-1}$ than those of the 2D-NMC811 electrode (136.6Ω and $1.6 \times 10^{-11} \text{ cm}^2 \text{ s}^{-1}$). The above results indicated that the 3D-patterning of electrodes could improve Li^+ transportation and decrease electrode polarization [23,35]. The differences in R_{ct} and D_{Li^+} values between 2D- and 3D-NMC811 were well-correlated with the data obtained from the CV studies. This result demonstrated that the 3D-structuring of the composite cathode could improve the transportation of Li ions, resulting in enhancement of the rate capability.

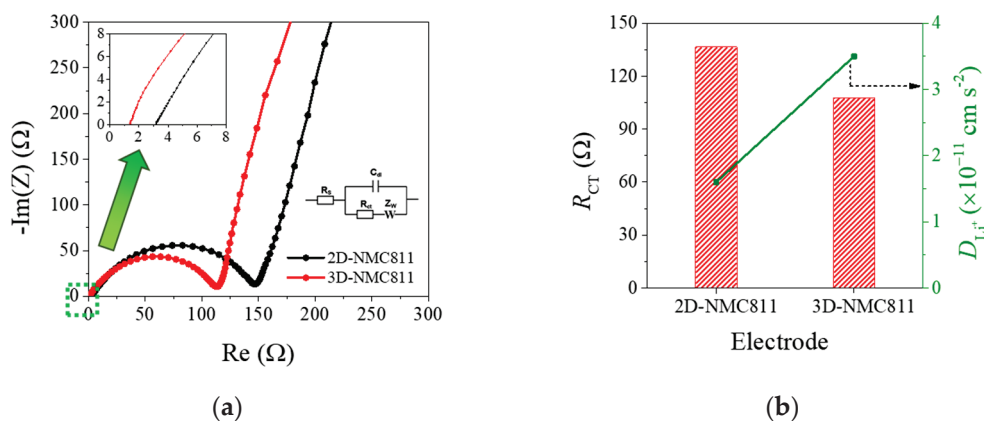


Figure 4. (a) Nyquist plots of 2D- and 3D-NMC811 electrodes before galvanostatic measurements; (b) Fitting results for impedance spectra and calculated D_{Li^+} from EIS.

4. Conclusions

Commercially available Ni-rich $\text{LiNi}_{0.8}\text{Mn}_{0.1}\text{Co}_{0.1}\text{O}_2$ (NMC811), with a high capacity and energy density, was used as the cathode material for a Li ion battery. The tape-casted composite electrodes were micro-structurally modified by a femtosecond ultrafast laser to generate 3D-electrode configuration. The 3D-patterning of electrodes with different thicknesses resulted in different aspect ratio values and material losses. Higher aspect ratio and increment of interfacial surface area, and lower active material loss were observed in the thick-film 3D-NMC811. The laser structuring improved the capacity of the thick film cathode at a high rate but failed to have a positive effect on that of the thin film electrode. The 3D-modification of the cathode improved the mass transfer of Li^+ ions into the deep layers of the electrode, as well as the wetting capability of the electrolyte. The diffusivity coefficient of the Li^+ ions, determined by CV and EIS, demonstrated that the 3D-NMC811 possessed a lower value of D_{Li^+} than that of 2D-NMC811. The charge transfer resistance was lower, which indicated a lower polarization and improved Li^+ ion diffusivity. Faster ion transportation in 3D-NMC811 resulted in a higher rate capability of 133 mAh g^{-1} at a C-rate of 2 C, which was 77.8% of the initial capacity at 0.1 C and thrice that of 2D-NMC811. Laser structuring to realize the 3D-battery concept could be an approach to commercialize high-energy NMC811 cathode materials with high power output.

Supplementary Materials: The following supporting information can be downloaded at: <https://www.mdpi.com/article/10.3390/nano12213897/s1>, Figure S1: Morphology of NMC811 particles; Figure S2: XRD patterns of NMC particles; Figure S3: Galvanostatic charge/discharge profiles; Figure S4: Diffusivity coefficient calculation; Figure S5: Linear fit lines demonstrating correlation between Z_{re} and $\omega^{-1/2}$; Table S1: Summary of effect of laser structuring on electrodes at various thicknesses; Table S2: Fitting results for impedance spectra and calculated D_{Li^+} from CVs and electrochemical impedance spectroscopy.

Author Contributions: Conceptualization, M.X.T. and J.K.L.; methodology, P.S.; software, P.S.; validation, M.X.T. and P.S.; formal analysis, M.X.T.; investigation, P.S.; resources, J.K.L. and W.P.; data curation, M.X.T.; writing—original draft preparation, M.X.T.; writing—review and editing, J.K.L. and W.P.; visualization, M.X.T.; supervision, J.K.L.; project administration, J.K.L., J.P. and W.P.; funding acquisition, J.K.L. and W.P. All authors have read and agreed to the published version of the manuscript.

Funding: This project received funding from the German Research Foundation (DFG, project No. 392322200).

Data Availability Statement: Not applicable.

Acknowledgments: This study was supported by the KIST Institutional Program (2E31863, 2V09284). We are grateful to Jan Rakebrandt for technical assistance in laser processing. In addition, the support for laser materials processing by the Karlsruhe Nano Micro Facility (KNMF, <http://www.knmf.kit.edu/>), a Helmholtz research infrastructure at KIT, is gratefully acknowledged.

Conflicts of Interest: The authors declare no conflict of interest.

References

1. Yang, Y.; Okonkwo, E.G.; Huang, G.; Xu, S.; Sun, W.; He, Y. On the sustainability of lithium ion battery industry—A review and perspective. *Energy Storage Mater.* **2021**, *36*, 186–212. [CrossRef]
2. Liu, J.; Long, J.; Du, S.; Sun, B.; Zhu, S.; Li, J. Three-Dimensionally Porous Li-Ion and Li-S Battery Cathodes: A Mini Review for Preparation Methods and Energy-Storage Performance. *Nanomaterials* **2019**, *9*, 441. [CrossRef]
3. Hu, X.; Xu, L.; Lin, X.; Pecht, M. Battery Lifetime Prognostics. *Joule* **2020**, *4*, 310–346. [CrossRef]
4. Pimlott, J.L.; Street, R.J.; Down, M.P.; Banks, C.E. Electrochemical Overview: A Summary of $\text{ACo}_x\text{Mn}_y\text{Ni}_z\text{O}_2$ and Metal Oxides as Versatile Cathode Materials for Metal-Ion Batteries. *Adv. Func. Mater.* **2021**, *31*, 2107761. [CrossRef]
5. Xu, C.; Reeves, P.J.; Jacquet, Q.; Grey, C.P. Phase Behavior during Electrochemical Cycling of Ni-Rich Cathode Materials for Li-Ion Batteries. *Adv. Energy Mater.* **2021**, *11*, 2003404. [CrossRef]
6. You, B.; Wang, Z.; Shen, F.; Chang, Y.; Peng, W.; Li, X.; Guo, H.; Hu, Q.; Deng, C.; Yang, S.; et al. Research Progress of Single-Crystal Nickel-Rich Cathode Materials for Lithium Ion Batteries. *Small Methods* **2021**, *5*, 2100234. [CrossRef] [PubMed]

7. Li, L.; Wang, D.; Xu, G.; Zhou, Q.; Ma, J.; Zhang, J.; Du, A.; Cui, Z.; Zhou, X.; Cui, G. Recent progress on electrolyte functional additives for protection of nickel-rich layered oxide cathode materials. *J. Energy Chem.* **2022**, *65*, 280–292. [CrossRef]
8. Zhang, H.; He, X.; Chen, Z.; Yang, Y.; Xu, H.; Wang, L.; He, X. Single-Crystalline Ni-Rich $\text{LiNi}_x\text{Mn}_y\text{Co}_{1-x-y}\text{O}_2$ Cathode Materials: A Perspective. *Adv. Energy Mater.* **2022**, 2202022. [CrossRef]
9. Li, X.; Gao, A.; Tang, Z.; Meng, F.; Shang, T.; Guo, S.; Ding, J.; Luo, Y.; Xiao, D.; Wang, X.; et al. Robust Surface Reconstruction Induced by Subsurface Ni/Li Antisites in Ni-Rich Cathodes. *Adv. Funct. Mater.* **2021**, *31*, 2010291. [CrossRef]
10. Xia, Y.; Zheng, J.; Wang, C.; Gu, M. Designing principle for Ni-rich cathode materials with high energy density for practical applications. *Nano Energy* **2018**, *49*, 434–452. [CrossRef]
11. Wood, D.L.; Li, J.; Daniel, C. Prospects for reducing the processing cost of lithium ion batteries. *J. Power Sources* **2015**, *275*, 234–242. [CrossRef]
12. Pflöging, W. A review of laser electrode processing for development and manufacturing of lithium-ion batteries. *Nanophotonics* **2018**, *7*, 549–573. [CrossRef]
13. Johnson, B.A.; White, R.E. Characterization of commercially available lithium-ion batteries. *J. Power Sources* **1998**, *70*, 48–54. [CrossRef]
14. Kim, U.S.; Shin, C.B.; Kim, C.-S. Modeling for the scale-up of a lithium-ion polymer battery. *J. Power Sources* **2009**, *189*, 841–846. [CrossRef]
15. Du, Z.; Wood, D.L.; Daniel, C.; Kalnaus, S.; Li, J. Understanding limiting factors in thick electrode performance as applied to high energy density Li-ion batteries. *J. Appl. Electrochem.* **2017**, *47*, 405–415. [CrossRef]
16. Pflöging, W.; Pröll, J. A new approach for rapid electrolyte wetting in tape cast electrodes for lithium-ion batteries. *J. Mater. Chem. A* **2014**, *2*, 14918–14926. [CrossRef]
17. Hudaya, C.; Halim, M.; Pröll, J.; Besser, H.; Choi, W.; Pflöging, W.; Seifert, H.J.; Lee, J.K. A polymerized C_{60} coating enhancing interfacial stability at three-dimensional LiCoO_2 in high-potential regime. *J. Power Sources* **2015**, *298*, 1–7. [CrossRef]
18. Baggetto, L.; Niessen, R.A.H.; Roozeboom, F.; Notten, P.H.L. High Energy Density All-Solid-State Batteries: A Challenging Concept Towards 3D Integration. *Adv. Funct. Mater.* **2008**, *18*, 1057–1066. [CrossRef]
19. Lim, D.G.; Chung, D.-W.; Kohler, R.; Proell, J.; Scherr, C.; Pflöging, W.; García, R.E. Designing 3D Conical-Shaped Lithium-Ion Microelectrodes. *J. Electrochem. Soc.* **2014**, *161*, A302–A307. [CrossRef]
20. Pröll, J.; Kohler, R.; Torge, M.; Bruns, M.; Przybylski, M.; Ulrich, S.; Seifert, H.J.; Pflöging, W. Laser-adjusted three-dimensional Li-Mn-O cathode architectures for secondary lithium-ion cells. In Proceedings of the SPIE LASE, San Francisco, CA, USA, 17 February 2012; pp. 1–10.
21. Park, J.H.; Kohler, R.; Pflöging, W.; Choi, W.; Seifert, H.J.; Lee, J.K. Electrochemical behavior of a laser microstructured fluorine doped tin oxide anode layer with a plasma pretreatment for 3D battery systems. *RSC Adv.* **2014**, *4*, 4247–4252. [CrossRef]
22. Xuan Tran, M.; Woo, J.-Y.; Nguyen, T.-A.; Lee, S.-W.; Kee Lee, J. Thermolytically grafted silicon particles with ultrathin carbonaceous coating rich of phenyl moieties as lithium-storage anode material. *Chem. Engin. J.* **2020**, *395*, 125169. [CrossRef]
23. Huang, Y.; Jin, F.-M.; Chen, F.-J.; Chen, L. Improved cycle stability and high-rate capability of Li_3VO_4 -coated $\text{Li}[\text{Ni}_{0.5}\text{Co}_{0.2}\text{Mn}_{0.3}]\text{O}_2$ cathode material under different voltages. *J. Power Sources* **2014**, *256*, 1–7. [CrossRef]
24. Li, J.; Downie, L.E.; Ma, L.; Qiu, W.; Dahn, J.R. Study of the Failure Mechanisms of $\text{LiNi}_{0.8}\text{Mn}_{0.1}\text{Co}_{0.1}\text{O}_2$ Cathode Material for Lithium Ion Batteries. *J. Electrochem. Soc.* **2015**, *162*, A1401–A1408. [CrossRef]
25. Kim, H.; Kim, M.G.; Jeong, H.Y.; Nam, H.; Cho, J. A new coating method for alleviating surface degradation of $\text{LiNi}_{0.6}\text{Co}_{0.2}\text{Mn}_{0.2}\text{O}_2$ cathode material: Nanoscale surface treatment of primary particles. *Nano Lett.* **2015**, *15*, 2111–2119. [CrossRef] [PubMed]
26. Yang, K.; Fan, L.-Z.; Guo, J.; Qu, X. Significant improvement of electrochemical properties of AlF_3 -coated $\text{LiNi}_{0.5}\text{Co}_{0.2}\text{Mn}_{0.3}\text{O}_2$ cathode materials. *Electrochim. Acta* **2012**, *63*, 363–368. [CrossRef]
27. Bie, X.; Du, F.; Wang, Y.; Zhu, K.; Ehrenberg, H.; Nikolowski, K.; Wang, C.; Chen, G.; Wei, Y. Relationships between the crystal/interfacial properties and electrochemical performance of $\text{LiNi}_{0.33}\text{Co}_{0.33}\text{Mn}_{0.33}\text{O}_2$ in the voltage window of 2.5–4.6V. *Electrochim. Acta* **2013**, *97*, 357–363. [CrossRef]
28. Singh, M.; Kaiser, J.; Hahn, H. Thick Electrodes for High Energy Lithium Ion Batteries. *J. Electrochem. Soc.* **2015**, *162*, A1196–A1201. [CrossRef]
29. Wang, J.S.; Liu, P.; Sherman, E.; Verbrugge, M.; Tataria, H. Formulation and characterization of ultra-thick electrodes for high energy lithium-ion batteries employing tailored metal foams. *J. Power Sources* **2011**, *196*, 8714–8718. [CrossRef]
30. Jung, R.; Metzger, M.; Maglia, F.; Stinner, C.; Gasteiger, H.A. Oxygen Release and Its Effect on the Cycling Stability of $\text{LiNi}_x\text{Mn}_y\text{Co}_z\text{O}_2$ (NMC) Cathode Materials for Li-Ion Batteries. *J. Electrochem. Soc.* **2017**, *164*, A1361–A1377. [CrossRef]
31. Yang, J.; Xia, Y. Suppressing the Phase Transition of the Layered Ni-Rich Oxide Cathode during High-Voltage Cycling by Introducing Low-Content Li_2MnO_3 . *ACS Appl. Mater. Interfaces* **2016**, *8*, 1297–1308. [CrossRef]
32. Laskar, M.R.; Jackson, D.H.; Xu, S.; Hamers, R.J.; Morgan, D.; Kuech, T.F. Atomic Layer Deposited MgO: A Lower Overpotential Coating for $\text{Li}[\text{Ni}_{0.5}\text{Mn}_{0.3}\text{Co}_{0.2}]\text{O}_2$ Cathode. *ACS Appl. Mater. Interfaces* **2017**, *9*, 11231–11239. [CrossRef] [PubMed]
33. Liu, X.; Li, H.; Li, D.; Ishida, M.; Zhou, H. PEDOT modified $\text{LiNi}_{1/3}\text{Co}_{1/3}\text{Mn}_{1/3}\text{O}_2$ with enhanced electrochemical performance for lithium ion batteries. *J. Power Sources* **2013**, *243*, 374–380. [CrossRef]

34. Bard, A.J.; Faulkner, L.R. *Electrochemical Methods: Fundamentals and Applications*; Wiley: New York, NY, USA, 2000.
35. Bai, Y.; Wang, X.; Yang, S.; Zhang, X.; Yang, X.; Shu, H.; Wu, Q. The effects of FePO₄-coating on high-voltage cycling stability and rate capability of Li[Ni_{0.5}Co_{0.2}Mn_{0.3}]O₂. *J. Alloys Compd.* **2012**, *541*, 125–131. [CrossRef]



Article

Aqueous Manufacturing of Defect-Free Thick Multi-Layer NMC811 Electrodes

Lukas Neidhart^{1,2,*}, Katja Fröhlich¹, Nicolas Eshraghi¹, Damian Cupid¹, Franz Winter² and Marcus Jahn^{1,*}

¹ Electric Vehicle Technologies, Center for Low Emission Transport, Austrian Institute of Technology GmbH (AIT), Giefinggasse 2, 1210 Vienna, Austria; katja.froehlich@ait.ac.at (K.F.); nicolas.eshraghi@ait.ac.at (N.E.); damian.cupid@ait.ac.at (D.C.)

² Institute of Chemical, Environmental and Bioscience Engineering, TU Wien, Getreidemarkt 9, 1060 Vienna, Austria; franz.winter@tuwien.ac.at

* Correspondence: lukas.neidhart@ait.ac.at (L.N.); marcus.jahn@ait.ac.at (M.J.)

Abstract: Manufacturing thick electrodes for Li-ion batteries is a challenging task to fulfill, but leads to higher energy densities inside the cell. Water-based processing even adds an extra level of complexity to the procedure. The focus of this work is to implement a multi-layered coating in an industrially relevant process, to overcome issues in electrode integrity and to enable high electrochemical performance. $\text{LiNi}_{0.8}\text{Mn}_{0.1}\text{Co}_{0.1}\text{O}_2$ (NMC811) was used as the active material to fabricate single- and multi-layered cathodes with areal capacities of 8.6 mA h cm^{-2} . A detailed description of the manufacturing process is given to establish thick defect-free aqueous electrodes. Good inter-layer cohesion and adhesion to the current collector foil are achieved by multi-layering, as confirmed by optical analysis and peel testing. Furthermore, full cells were assembled and rate capability tests were performed. These tests show that by multi-layering, an increase in specific discharge capacity (e.g., 20.7% increase for C/10) can be established for all tested C-rates.

Keywords: multi-layer coating; aqueous electrode processing; NMC811; thick electrode

1. Introduction

The demand for Lithium-ion batteries (LIBs) used in xEVs has grown steadily over the past years alongside the interest to increase driving range and lower prices. A decrease in manufacturing cost combined with more environmentally friendly cell production methods are key aspects in battery research, helping e-mobility to establish itself as a day-to-day form of transportation.

One way of tackling the issue of high production costs is to exchange the organic solvent, used in state-of-the-art electrode slurry formulations, with water [1–3]. Commercially available cathodes are produced with polyvinylidene fluoride (PVDF) as the binder material. Unfortunately, due to its low solubility, PVDF is commonly dissolved in the high-priced N-methylpyrrolidone (NMP) organic solvent. Furthermore, expensive measures must be implemented to properly trap and filter the highly toxic NMP, which evaporates during the drying process of the electrodes. Binder materials, which are essential components in slurries, must fulfill several requirements. First, they are essential to guarantee good adhesion between the particle components as well as to the current collector foil. Uniform coatings rely on well dispersed slurries, which in turn depend on properly chosen binders. Moreover, the harsh environment inside the battery cell also requires chemically inert materials. Aqueous slurry preparation is advantageous, as it eliminates the utilization of both PVDF and NMP, leading to an overall reduction of material and production costs. Additionally, evaporation of water is not only more efficient but also needs up to 90% less energy during the drying process [4].

Although there are several advantages associated with replacing NMP by water, there are also some disadvantages due to the reactions of the cathode active materials with

water. For example, cathode active materials are prone to react with water, causing extra complexity to the whole procedure. Li^+ ions are leached from the lattice of the cathode active material, which is accompanied by the oxidation of the transition metal cations and loss of charge capacity. Furthermore, the leached Li^+ ions induce a raise in the pH of the slurry, due to the formation of LiOH . However, oxide layers on aluminum current collectors are only stable up to a pH lower than 8.6 [5] before the Al foil corrodes. The corrosion is not only associated with an increase in interface resistance, but also with the evolution of hydrogen gas, which can result in large cavities inside the electrode layer. To prevent the development of defects during and after the coating process, several strategies exist to regulate pH values during slurry mixing. The usage of different acids, such as phosphoric acid [6–8], hydrochloric acid [9,10], poly acrylic acid [11] or acetic acid [12] is the most common method for maintaining the pH of the slurry within an adequate range between 4 and 8.6. The utilization of certain acids has another positive effect on the Li^+ leaching mechanism. For example, adding phosphoric acid to the slurry can lead to the formation of an insoluble layer of phosphate compounds deposited on the surface of the active material particles, which suppress the ongoing leaching of transition metal cations from $\text{LiNi}_x\text{Mn}_y\text{Co}_z\text{O}_2$ (NMC) [13,14]. Zhu et al. showed that the viscosity of the slurry is also affected by the amount of acid added [12], as increasing the quantity of acetic acid leads to an increase in viscosity. Especially when targeting thick coatings, the viscosity has a significant influence on the film quality, which is influenced by the solid content of the slurry and binder characteristics. The solid loading of the slurry impacts the sedimentation rate of the coating and needs to be balanced carefully with solvent evaporation [15]. Binder concentration and molecular weight also affect the rheological behavior [15,16] and, consequently, the morphology of the electrode. In addition, a certain viscosity is necessary to maintain the desired thickness and shape of the electrode after the coating and drying process.

Increased energy densities can be realized by maximizing the ratio of active to inactive material [17–19]. Reducing separator and current collector materials leads not only to an increase in energy density, but also reduces the time required for cell assembly [19–21]. Energy density can further be increased by manufacturing thicker electrodes. However, thick electrodes tend to exhibit lower rate capabilities due to higher charge transfer resistance and blocked pore structures. The use of slurry additives and adjustment of coating parameters are widespread strategies to create crack free thick films. Controlling capillary pressures during the drying procedure by adding isopropyl alcohol to the slurry to regulate surface tensions [18] is one approach to reduce crack formation. Vapor grown graphite tubes as a replacement for carbon black can also help to minimize the amount of pinholes as recommended by Sahore et al. [22]. Beside maintaining mechanical integrity of the coating, a homogeneous distribution of the electrode material components are desirable, as accumulations of binder material can lead to unwanted side effects and diminished electrochemical performance. Binder migration is a large challenge during drying, thereby necessitating well optimized coating parameters. For example, the higher concentration of binder particles near the electrode-separator interface is a phenomenon that can be observed during the drying of thick coatings [23–27]. Light binder particles float on top of the layer due to a lack of liquid linkage between the surface and current collector. As a result, ion pathways are blocked and Li^+ transport is impeded. The absence of binder at lower regions is also problematic for adhesion between coating and current collector [28].

This manuscript presents an alternative strategy to circumvent these difficulties in thick layer manufacturing by multi-layer coating. Applying multiple layers of coating on top of each other can help control film properties in a desired manner. Graded porosity was already investigated and presented as an interesting opportunity in the past [29–33]. Reduction in resistance, a more uniform overpotential distribution, and an increase in diffusivity of Li-ions are affected by establishing low porosity regions near the substrate and areas with high porosity in the vicinity of the separator [29–32]. However, implementing such a gradient is complicated as several subsequent calendaring steps are necessary, which

reduces the expected positive effects [33]. Multi-layering also opens the doors to realize different material combinations inside the electrode. Blends of active materials can lead to higher ionic current densities [34], improvements against overcharging [35] and higher discharge rates [36]. For example, NMC442 cathodes [37] and graphite anodes that were fabricated [38] via dual layered slot-die coating show better electrochemical performance when the binder content of the top layer is reduced.

The purpose of this manuscript is to highlight the benefits of using multi-layering as a method to achieve high energy densities in cathode production. An industry oriented roll-to-roll (R2R) process was used to demonstrate the procedure using NMC811 as the cathode active material, which was coated in aqueous slurries. The resulting improvements in mechanical integrity and electrochemical performance are displayed. Due to its simplicity for industrial implementation, this technique is a stepping stone for the fabrication of unique electrode architectures. To the best of our knowledge, no defect free water-based NMC811 cathodes were established before with presented high areal capacity using the multi-layer approach.

2. Materials and Methods

Two different cathode coatings were performed—one thick single-layer (SL) of Ni-rich lithium nickel manganese cobalt oxide (NMC811) and one multi-layer (ML) coating with similar total electrode thickness. Each of the electrodes were analyzed with respect to their physical properties. In addition, coin cells were assembled to investigate their electrochemical performance.

2.1. Electrode Preparation

The cathode coatings consist of 92 wt% NMC811 powder (BASF SE, Ludwigshafen am Rhein, Germany; $d_{\text{avg}} = 7.8 \mu\text{m}$) as active material, 3 wt% carbon black (C-ENERGY™ SUPER C65, TIMCAL Ltd., Bodio, Switzerland; $d_{\text{avg}} = 37 \text{ nm}$) and 2 wt% artificial graphite (C-ENERGY™ KS6L, TIMCAL Ltd.; $d_{50} = 3.5 \mu\text{m}$) as conducting agents, 2 wt% of CMC (WALOCCEL™ CRT 2000 PA, DuPont de Nemours Inc., Wilmington, DE, USA) and 1 wt% of poly(meth)acrylate (PMA) (JSR SX8684(A)-64, JSR Micro NV, Leuven, Belgium) as binder. A total of 0.16 g of 1M phosphoric acid (H_3PO_4) per g of NMC811 was added prior to addition of NMC to control the pH-value throughout the mixing process. All solid components used in this study were dried over night at 105 °C.

Slurry mixing was done in a 250 mL container using a dissolver (DISPERMAT CV3-PLUS, VMA GETZMANN GMBH, Reichsdorf, Germany). Under constant stirring at 200 rpm, carbon black (CB) and artificial graphite (KS6L) were added to a 2 wt% CMC solution, following 10 min of stirring at 2000 rpm. H_3PO_4 was added, followed by another 2 min of stirring. NMC811 was added at 3000 rpm for 8 min. Finally, PMA was added at maximum 500 rpm stirring for 2 min to keep material integrity, terminating in a solid content of 60%. The pH was measured (SevenCompact S210, Mettler Toledo, Columbus, OH, USA) to monitor that values are below 8.6 before coating.

Electrode casting was performed continuously on a R2R coating machine (SC 30, COATEMA Coating Machinery GmbH, Dormagen, Germany) on 22 μm aluminum foil (Norsk Hydro ASA, Oslo, Norway). Three consecutively arranged drying chambers were set to temperatures of 45, 55 and 50 °C. The flow rates at the air inlet and outlet valves were set to 70 $\text{m}^3 \text{ h}^{-1}$ and 98 $\text{m}^3 \text{ h}^{-1}$, respectively. The coating speed was fixed at 0.3 m min^{-1} . The gap size of the coating knife was set to 550 μm for the thick single-layer, whereas for the multi-layer coatings, the wet thickness of the bottom layer was set to 250 μm and of the top layer was set to 330 μm . The bottom layer was fully dried before adding the second coating. To remove residual water, all samples were dried at 80 °C under vacuum for 12 h. Afterwards, the porosity ϵ of the electrodes was calculated by using Equations (1)–(3),

where ρ_c , m_c and V_c are the density, mass, and volume of the coating, respectively and ρ_{ph} is the sum of all bulk densities ρ_i with respect to their share p_i of the coating:

$$\rho_c = \frac{m_c}{V_c}, \quad (1)$$

$$\rho_{ph} = \sum_i p_i \rho_i, \quad (2)$$

$$\epsilon = 1 - \frac{\rho_c}{\rho_{ph}}. \quad (3)$$

Dried electrode sheets were calendared at 55 °C roll temperature (GK 300L, SAUER-ESSIG Group, Vreden, Germany) to a target porosity of 40% and a final thickness of approximately 205 μm including the current collector foil.

In the full cell investigations, anodes fabricated at the pilot line facilities were used as standard counter electrodes. All anodes used in this study were made of 90 wt% high energy density graphite (HED graphite 918-A2, Targray Technology International Inc, Kirkland, QC, Canada.; $d_{50} = 14.93 \mu\text{m}$), 4 wt% carbon black (C-ENERGY™ SUPER C65, TIMCAL Ltd.) and 6 wt% PVDF (Solef® PVDF, Solvay SA, Brussels, Belgium). The slurry was prepared in a planetary mixer (HIVIS DISPER MIX Model 3D-2, PRIMIX Corporation, Awaji-shi, Japan). First the active material and the carbon black were mixed together. PVDF, which was dissolved in an 8 wt% solution of NMP, was added and the slurry was mixed with increasing rotational speed. Additional NMP was added to dilute to a final solid content of 50%. The anode was coated on 11 μm copper foil (Carl Schlenk AG, Roth, Germany) with a wet thickness of 560 μm and afterwards dried and calendared to a porosity of 38%. A practical specific capacity for the graphite active material was assumed to be 350 mA h g^{-1} . An areal capacity of 9.5 mA h cm^{-2} for graphite anodes leads to a N/P ratio of 1.1.

Coating parameters and electrode materials are changed as little as necessary compared to a standardized manufacturing process to demonstrate the feasibility of the water based multi-layering technique to an existing production procedure.

2.2. Cell Assembly and Electrochemical Analysis

For coin cell tests, cathodes and anodes were cut into discs of 1.5 cm and 1.6 cm diameter, respectively. The anodes were dried at 120 °C and the cathodes at 80 °C under vacuum for 12 h before being transferred in vacuum into an Ar-filled glove box ($\text{O}_2 < 0.1 \text{ ppm}$, $\text{H}_2\text{O} < 0.1 \text{ ppm}$) (LabMaster Glove Box MB200-G, MBRAUN, Garching, Germany). Then, 2032 coin cells (CR2032) were assembled with 1.1 mm springs, 1.5 mm spacers and a Celgard 2500 separator. In total 150 μL of the electrolyte were added before crimping (MSK-110 Hydraulic Crimping Machine, MTI Corporation, Richmond, CA, USA) at 60 bar pressure.

After a resting time of 4 h, cycling tests were performed on an Arbin BT-21084, assuming 200 mA h g^{-1} capacity for the cathode active material. Two cycles with a C-rate of C/20 were carried out for formation, followed by five preconditioning cycles at C/10. The discharge capacity for further tests was adjusted to be in-line with the capacity of the third C/10 cycle. Thus, further tests were carried out with a specific capacity of 146 mA h g^{-1} and 177 mA h g^{-1} for SL and ML electrodes, respectively. Constant current constant voltage (CCCV) rate capability tests with symmetric charge/discharge rates of C/5, C/2, 1C and C/10 were also conducted in a voltage window of 3 to 4.2 V. To determine the long term cycling behavior, 50 cycles at a C-rate of C/5 were performed for both cell types.

Electrochemical impedance spectroscopy (EIS) was used to investigate the influence of multi-layering on the kinetics during cycling within the cell. Measurements were performed at 4.2 V/100% state of charge (SOC) during the two formation cycles at a C-rate of C/20. Potentiostatic electrochemical impedance was measured between 20 kHz and 100 mHz with a voltage amplitude of 10 mV on a Biologic MPG-2 instrument. Cyclic voltammetry (CV) measurements were performed to compare reduction and oxidation processes for

SL and ML electrodes in half cell configurations. The applied range of potential was set between 2.8 V and 4.5 V with a scan rate of 0.05 mV s^{-1} on an Arbin BT-21084.

2.3. Slurry and Electrode Properties

Surface topologies and cross-sectional imaging of the electrode samples were carried out via a digital microscope (VHX7000, Keyence Corporation, Osaka, Japan), to evaluate coating homogeneity and investigate inter-layer transitions of the multi-layered electrodes. The electrode samples were also investigated via scanning electron microscopy (SEM) at an electron acceleration voltage of 5 kV (SUPRA 40, Carl Zeiss AG, Oberkochen, Germany). Furthermore, the adhesive strength of the coating to the current collector foil was characterized using a 180° peel test (EKM-5KN, Jinan Marxtest Technology Co., Ltd., Jinan, China).

Viscosity measurements were performed under ambient conditions (DV-II+Pro Viscometer, AMETEK Brookfield, Middleboro, MA, USA), and dynamic viscosity was recorded with respect to increasing shear rates between 0 and 14 s^{-1} .

3. Results and Discussion

3.1. Characterization of Slurries and Electrodes

Since the pH of the slurry has a huge impact on the process, the pH evolution was carefully monitored to stay below the recommended coating limit of 8.6 [5] to suppress possible corrosion of the Al substrate. This is also important with regard to the emergence of agglomerations within the slurry reported to occur when the pH of 10 is exceeded in the slurry mixing process as described above in Section 2.1. Viscosity measurements showed a shear thinning behavior of 18 Pa s at zero shear rate and 4 Pa s at the shear rate applied during the coating process. Porosity and areal capacity were calculated based on the measured thicknesses and mass loadings in SL and ML electrodes. The values of the measured parameters are given in Table 1. Coating thicknesses are slightly higher than $200 \mu\text{m}$ for both types of electrodes. The as-coated porosity values of the SL and ML samples are calculated to be almost identical with each other, attaining values of 52.7 and 52.6% for the SL and ML electrodes, respectively. Both coatings show the same areal capacity of 8.6 mA h cm^{-2} , which was calculated assuming a 200 mA h g^{-1} specific capacity for the NMC811 active material. The lower layer constitutes a 43% share of the overall bi-layer electrode thickness. On average, a porosity of 59.3% was calculated for the base layer with an areal capacity of 3.1 mA h cm^{-2} .

Table 1. Coating parameters after coating and drying.

Electrode Type	Total Thickness [μm]	Porosity [%]	Areal Capacity [mA h/cm^2]
Single-layer	202 ± 2	52.7 ± 0.3	8.6 ± 0.1
Multi-layer	208 ± 4	52.6 ± 0.2	8.6 ± 0.2
Bottom layer	89 ± 5	59.3 ± 0.9	3.1 ± 0.0

Investigating the surface of each coating, it is evident that a continuous film without defects of any kind was fabricated (Figure 1a,c). Even before calendaring, a smooth homogeneous surface was present in both samples. This is a huge improvement considering the high thickness and aqueous processing of the electrode [18,22].

Analysis of cross sectional images taken via digital microscope are shown in Figure 1b,d for single- and multi-layer electrodes, respectively. Both samples are determined to have a thickness of $190 \mu\text{m}$ after calendaring to 40% porosity, verifying the measurements via a thickness gauge. Slightly inhomogeneous distribution of lighter gray particles is noticeable for SL samples, but overall no severe irregularities, such as entrapped air, cracks, or delamination from the substrate are recognizable. No distinct transition line between top and bottom layer is visible for the multi-layer sample, which is evidence of a good mechanical connection of both layers. SEM images of the multi-layer sample are displayed

in Figure 2. Merging of the layers is visible in agreement with the analysis via digital microscope. Images of higher magnification reflect an intertwining behavior of the secondary NMC811 particles of the top and bottom layers, which is necessary for strong cohesion. The indistinguishability of the two layers can also be accredited to the slight “dissolution” of the surface of the bottom layer into the freshly applied electrode slurry of the upper layer during coating. Furthermore, the surface film of the prime coating absorbs the slurry of the second coating forming a diffuse transition layer. This is a key aspect in guaranteeing good mechanical linkage of both layers.

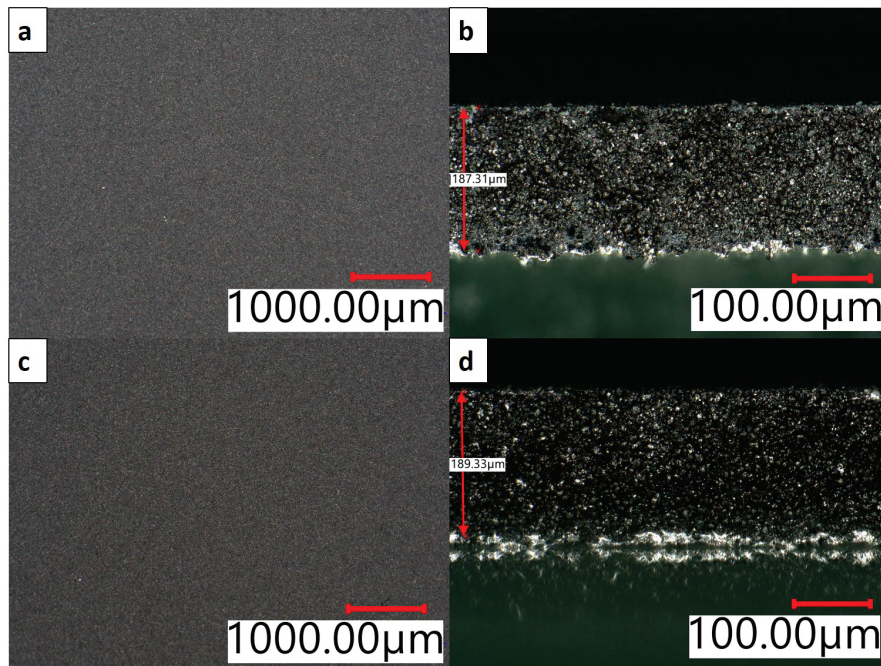


Figure 1. Digital microscope images of (a) SL top-view, (b) SL cross-section, (c) ML top-view, (d) ML cross-section after drying in air.

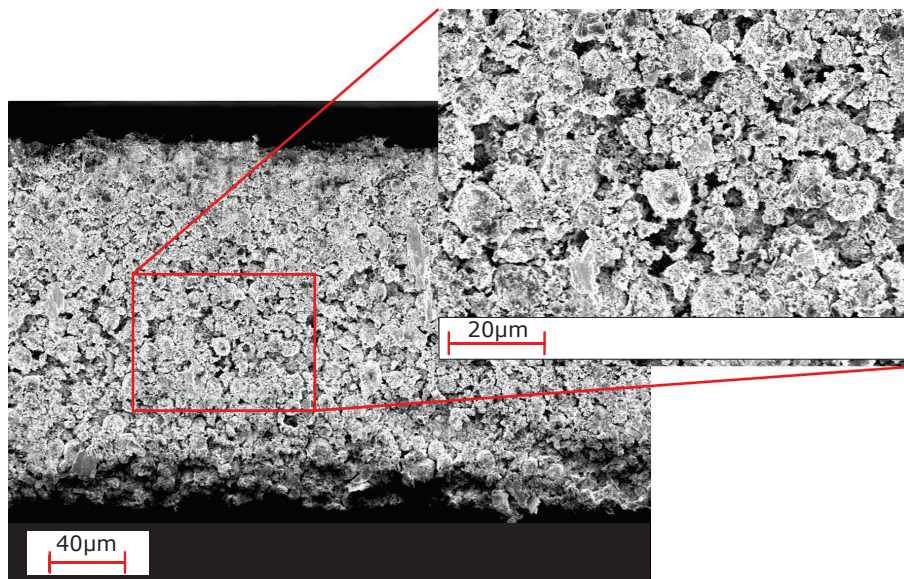


Figure 2. SEM image of the transition area from top to bottom layer of a multi-layer coated sample.

The significantly higher porosity of the lower layer also implies either a change in porosity of the layer itself due to the coating of the upper layer, or a porosity gradient with remarkably higher porosity in the vicinity of the current collector. Assuming no porosity

transition of the base after the second coating, the porosity of the top layer should be 47.5%. According to both Qi et al. [30] and Fang et al. [31] this lower porosity of the top layer would lead to a decreased cell performance as they suggest an electrode design with an opposite porosity gradient (higher porosity at the top of the electrode with decreasing porosity in the direction of the current collector) to reduce electrode resistance and enhance performance at high C-rates by increasing Li-ion diffusivity. However, the higher observed porosity of the upper layer, as well as the observed bubbles which develop after the second coating is applied, imply that cavities inside the base layer are filled with applied slurry. Figure 3 illustrates this mechanism. First, the slurry of the second coating comes in contact with the low porosity base layer (Figure 3a). As the water evaporates, porosity decreases in the top layer (Figure 3b) and the particles from the top layer migrate, and occupy the cavities in the bottom layer. This causes a mixing of both coatings (Figure 3c) and results in an increase in porosity of the initial layer (Figure 3d). This influences the porosity gradient to generate lower porosity values near the substrate foil and higher porosity values closer to the coating surface.

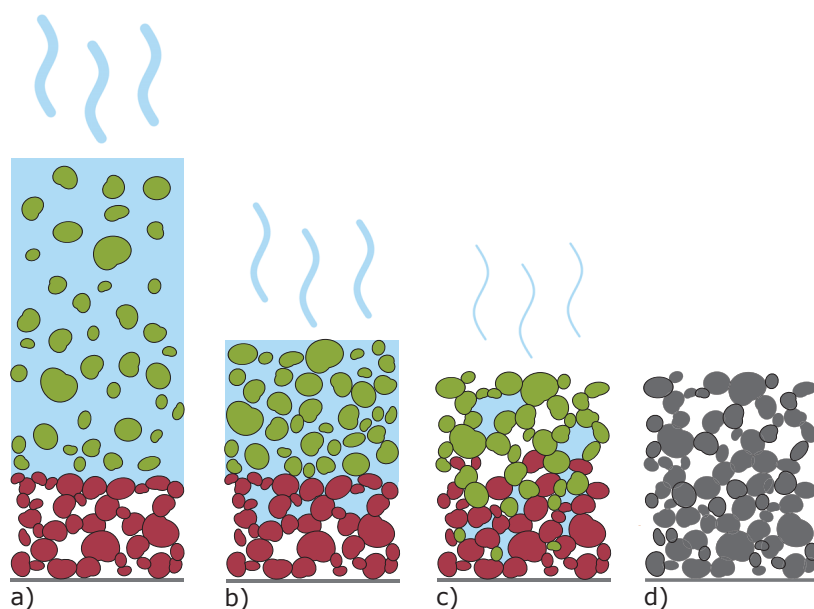


Figure 3. Visualization of the trickling behaviour after the second coating is applied. Particles in red and green, of the first and second layer, respectively. (a) situation right after coating the second layer, (b) sedimentation of particles during water evaporation, (c) mixing of second and first layer particles creating a diffuse interface, (d) coating after full solvent evaporation with higher porosity close to the current collector.

The results of the peel testing measurements confirm significant improvement following the multi-layer approach. In comparison to SL samples with $\sim 45 \text{ Nm}^{-1}$, ML coatings show values of $\sim 66 \text{ Nm}^{-1}$ (Figure 4). Therefore, on account of the second coating, an increase of approximately 45% in adhesion can be achieved. The reason for this vast enhancement is due to more homogeneously distributed binder particles, which is enhanced by the multi-layer processing.

3.2. Electrochemical Performance of Cells

Rate capability tests were performed to assess the electrochemical performance of both cell configurations. Results of statistically significant cells are displayed for clear visualization (Figure 5a). Formation cycles are not presented in the graph. It is worth mentioning, that after preconditioning at C/10 for 5 cycles, the C-rate was adjusted according to the measured cell discharge capacity of cycle number 3 (these preconditioning cycles are labels as C/10* in Figure 5a). Therefore, all cathodes are exposed to the same C-rate independent

of the actual specific capacity of the cathode after the preconditioning cycles. In accordance, the ML cells show higher specific discharge capacities throughout all the tests, even though the same C-rates are applied. Especially for low current densities, cells with ML cathodes outperform the SL samples by over 20%, which is a remarkable enhancement considering that both electrodes are fabricated using the same materials. Therefore, changing the coating procedure has a positive impact on material distribution inside the coating. The beneficial effect of multi-layering is even more pronounced for lower C-rates. For thick electrodes, limiting effects on Li^+ diffusion are evident at high current densities, and resulting losses in discharge capacity can not be compensated fully by multi-layering. Therefore the difference in capacity is slightly less distinct for 1C. Approximate improvements of the discharge capacities are listed in Table 2. When returning back to C/10, both cell configurations show initial high capacities, implying that cycling at high rates is not detrimental to their stability. Long term cycling tests show no significant decrease in specific discharge capacity after 50 cycles at C/5 for SL and ML electrodes (Figure 5b). Moreover, the coulombic efficiency for both SL and ML electrodes is determined to be close to 100%.

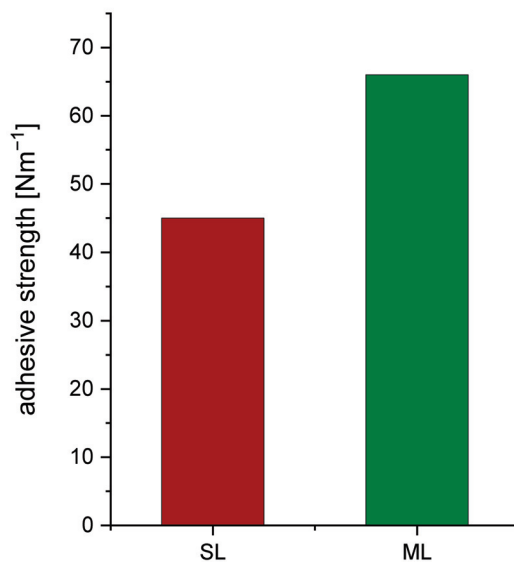


Figure 4. Comparison of the adhesive strength for SL and ML electrodes.

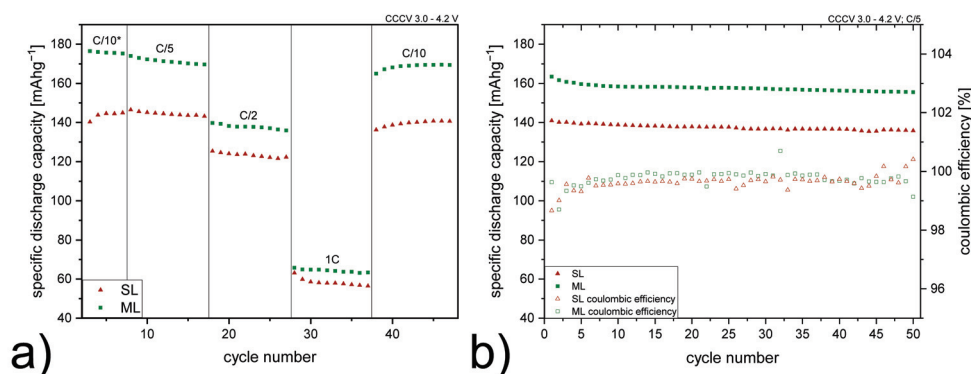


Figure 5. (a) Rate capability tests for single-layer (SL, red) and multi-layer (ML, green) electrodes with C-rates of C/10, C/5, C/2 and 1C. Cycles for preconditioning are labeled with C/10*. (b) Long term cycling at C/5 and coulombic efficiency of both electrode types.

Table 2. Increase of discharge capacities by multi-layering, compared to single-layer cathodes.

	C/10*	C/5	C/2	1C	C/10
Improvement [%]	23.3	18.6	11.7	10.3	20.7

Specific capacities of representative charge and discharge cycles are selected for comparison at each C-rate and are plotted in Figure 6 against applied voltages. The specific discharge capacity data as a function of C-rate are also given in Table 3. SL cells show values of 146 mA h g^{-1} , 128 mA h g^{-1} and 59 mA h g^{-1} for C/5, C/2, and 1C, respectively. ML cells have the overall highest specific discharge capacity of 171 mA h g^{-1} at C/5, whereas at C/2 and 1C, capacities of 136 mA h g^{-1} and 65 mA h g^{-1} are measured. Substantial differences in discharge capacity between the two types of electrodes are present for low current densities. For single layers only the region close to the electrode/separator interface is electrochemically active, since Li ion diffusion lengths are not sufficient enough to reach underlying areas [39]. However, in ML electrodes, areas located closer to the current collector foil also contribute to specific discharge capacity. Figure 6 shows the voltage-capacity curves of the SL and ML electrodes at C-rates of C/5 (a), C/2 (b) and 1C (c). All of them show a sloping profile, which is characteristic for NMC cathode active materials. In all cases, the charge and discharge capacities of the cells with the ML electrodes are larger than those for the SL electrodes, despite the fact that all electrodes have the same mass of active material. At high current densities, the benefits of multi-layering on Li-ion diffusion compensate for the drawbacks accompanied by electrode thickness itself [40]. Li-ion mobility definitely poses the most difficulties for thick electrodes to compete at high C-rates.

The potentiostatic contribution to the specific charge capacity is represented by the plateau at 4.2 V in Figure 6. Its length is directly proportional to the resistance inside the electrode during charge at constant voltage. The presence of multiple layers causes additional interfacial resistances within ML coated electrodes. Especially at C/5 (Figure 6a), a distinct difference in potentiostatic specific charge capacity is noticeable. At low C-rate in particular, a great part of the capacity is reached due to a elongated constant voltage step during charge. Nevertheless, it is worth mentioning that at C/5 higher specific charge capacities are already reached before the constant voltage step takes place.

The cyclic voltammograms shown in Figure 7 were recorded to compare the reduction and oxidation reactions of SL and ML electrodes during cycling. Both electrode types show no peak at 3 V, indicating the absence of Mn^{3+} [41]. Two pairs of oxidation/reduction peaks were observed for each sample. The small reduction peaks for SL and ML at around 3.9 V are not visible in the CV during oxidation due to overlapping with the lower voltage reduction peaks. Table 4 displays the potentials of oxidation/reduction peaks and corresponding polarizations for each electrode type. SL cells show oxidation peaks at $V_{\text{ox1}} = 3.90 \text{ V}$ and $V_{\text{ox2}} = 4.27 \text{ V}$ and reduction peaks at $V_{\text{red1}} = 3.63 \text{ V}$ and $V_{\text{red2}} = 4.09 \text{ V}$, with a polarization of $\Delta V_1 = 0.27 \text{ V}$ and $\Delta V_1 = 0.18 \text{ V}$ respectively. The polarizations for ML cells are $\Delta V_1 = 0.24 \text{ V}$ for peaks at $V_{\text{ox1}} = 3.86 \text{ V}$ and $V_{\text{red1}} = 3.62 \text{ V}$ and $\Delta V_1 = 0.16 \text{ V}$ for $V_{\text{ox2}} = 4.25 \text{ V}$ and $V_{\text{red2}} = 4.09 \text{ V}$. Comparing both electrode types, no significant differences in peak position and polarization are noticeable. However, ML samples show a larger area underneath the curve, which is in direct proportion to the capacity of the cell and is in accordance with the capacity difference shown in the rate capability test mentioned above. Besides the higher capacities, no obvious difference of the reaction kinetics were observed via CV measurements.

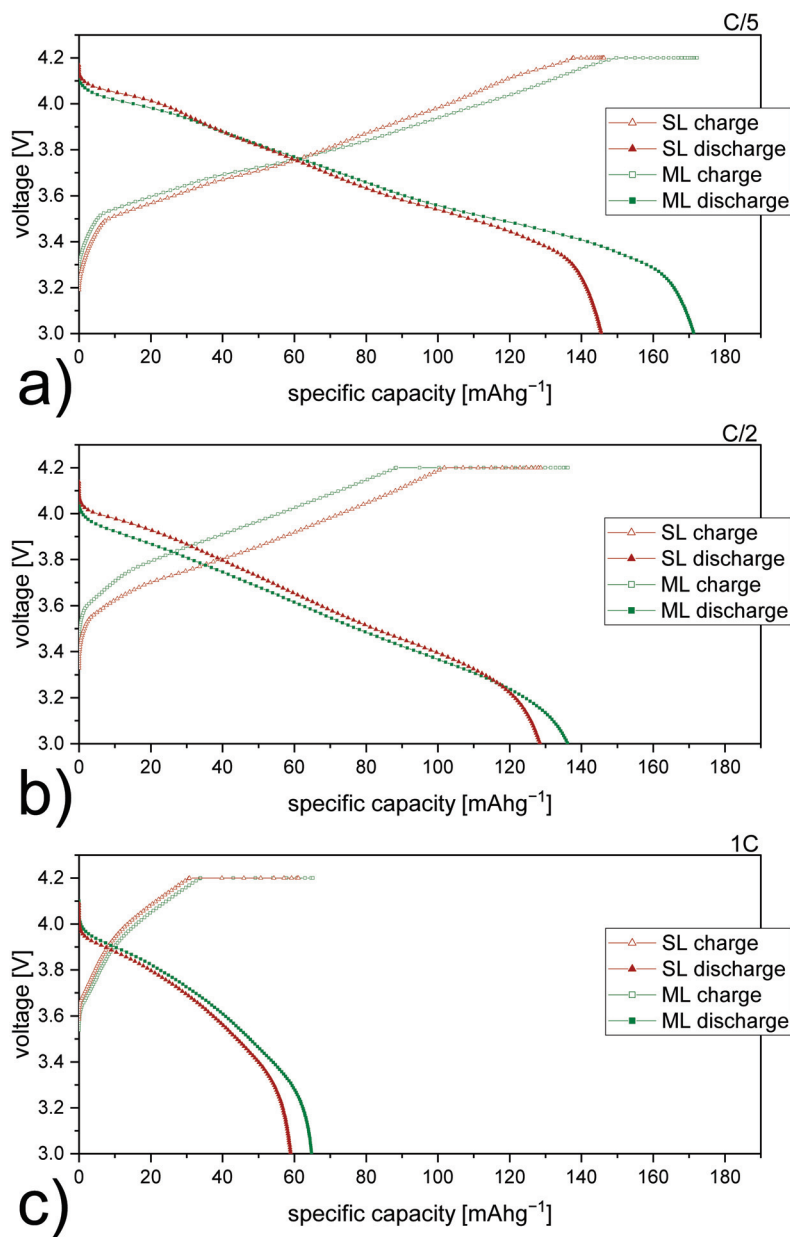


Figure 6. Voltage profiles of single-layer (SL, red) and multi-layer (ML, green) electrodes at (a) C/5, (b) C/2, and (c) 1C.

Table 3. Comparison of specific discharge capacities for different C-rates for SL and ML cells.

C-Rate	Electrode Type	Specific Discharge Capacity [mA h g ⁻¹]
C/5	SL	146
	ML	171
C/2	SL	128
	ML	136
1C	SL	59
	ML	65

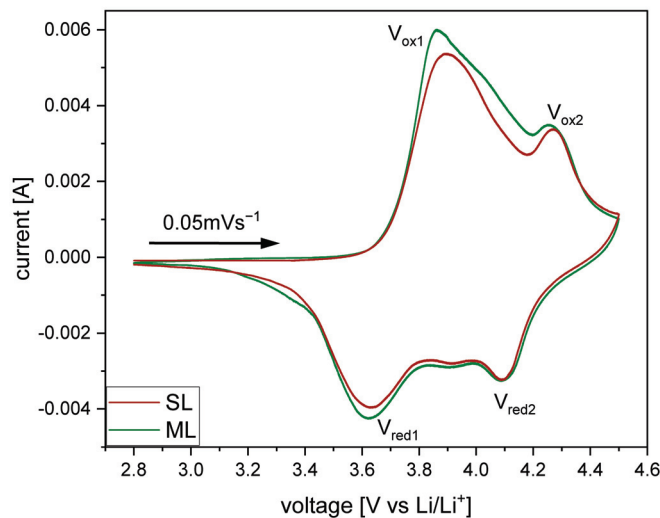


Figure 7. Cyclic voltammograms of single-layer (SL, red) and multi-layer (ML, green) electrodes between 2.8 and 4.5 V, with a scan rate of 0.05 mV s^{-1} .

Table 4. Comparison of anodic and cathodic peak positions and corresponding polarization from CV measurements for SL and ML half cells.

Electrode Type	V_{ox1} [v]	V_{red1} [v]	ΔV_1 [v]	V_{ox2} [v]	V_{red2} [v]	ΔV_2 [v]
SL	3.90	3.63	0.27	4.27	4.09	0.18
ML	3.86	3.62	0.24	4.25	4.09	0.16

EIS measurements were performed to help describe the transfer phenomena inside the cells during the formation cycles. The equivalent circuit used for the fitting is displayed in Figure 8. R_e corresponds to the bulk resistance resulting from the cell components (current collector, separator) and the electrolyte. The resistance contribution from the solid electrolyte interphase (SEI) formed on the graphite anode is fitted using R_{SEI} and a constant phase element Q_{SEI} , expressing its behavior as the non ideal capacitor. The charge transfer resistance R_{ct} and the double-layer capacitance represented by Q_{dl} show the contribution of charge transfer behaviour between the electrolyte and the electrode. The diffusion at low frequencies is represented by the Warburg element (W).

Figure 8 shows Nyquist plots of SL and ML cells during the first and second cycle at 4.2 V. The intercept of $\text{Re}(Z)$ at the high frequency region shows similar values in R_e for both samples, as shown in Table 5 and Figure 9a. This is expected, since all components apart from the cathodes are identical for each cell. The high to medium frequency semicircle shows the contribution of SEI formed during the first cycle on the anode side. At different stages of charge and discharge for the SL and ML electrodes the fitted data is comparable, highlighting the fact that the developed cathode in this work has no negative impact on the development of the SEI and its stability.

The mid to low frequency semicircle illustrates the charge transfer process, where a significant difference was observed between the charge transfer resistance of SL and ML electrodes. The higher specific discharge capacity, as shown in Figure 6, for the multi-layer cells, is attributed to the lower R_{ct} value. Heubner et al. [42] investigated the influence of electrode porosity and thickness on cell performance, with respect to limiting processes. They conclude that among other effects, decreased porosity leads to an increase in charge transfer resistance. Available areas for charge transfer reactions are reduced due to an increase in contacts between particles and particles with current collector foil and a reduction in the total contact area with the particles and the electrolyte [42]. The pore

size distribution in the ML electrode facilitates access of Li-ions from the electrolyte in the whole multi-layer electrode and thus lowering the R_{ct} . Figure 9 displays the acquired data for both electrode types and shows that a lower R_{ct} is achieved and a stable performance is established throughout cycling. The short inclined line at low frequencies represents the Li diffusion into the active material. Similar values for SL and ML samples lead to the conclusion that multi-layering does not negatively influence the diffusion of the Li-ions in the electrode and the mass transport controlled region of the cathode.

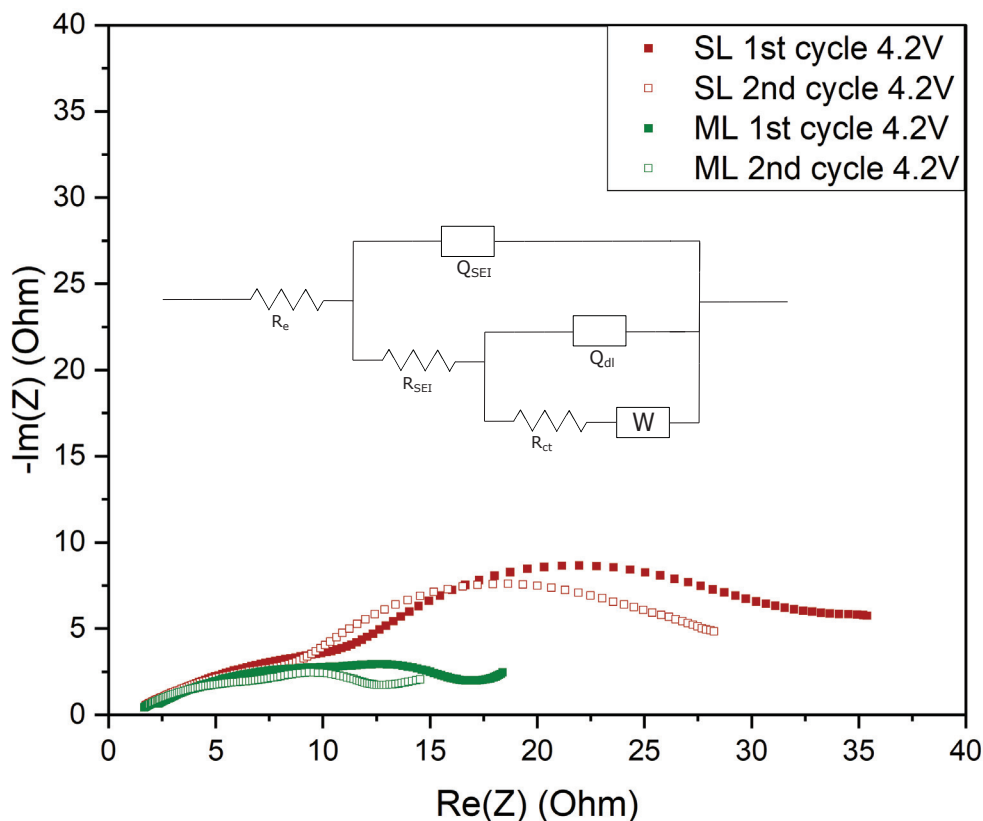


Figure 8. Equivalent circuit used to fit the measured impedance spectra and Nyquist plots of 1st and 2nd cycle at 4.2 V for single and multi-layer cathodes.

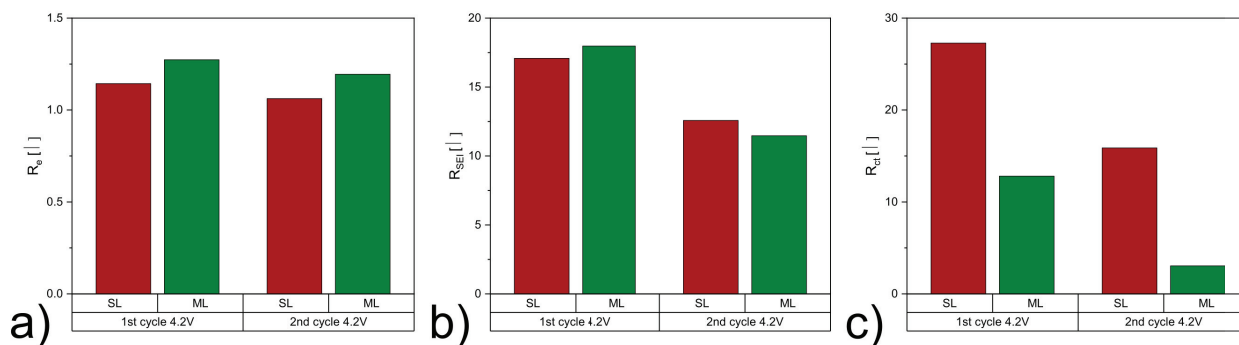


Figure 9. Comparison of resistance contributions (a) R_e , (b) R_{SEI} , and (c) R_{ct} for SL and ML cells during the 1st and 2nd cycle at 4.2 V.

The advantage of better adhesion in ML samples is not expected to be fully realized in coin cell configurations, since the high pressure inside the cells suppresses the delamination. Therefore, we anticipate a more pronounced benefit in pouch-cell configurations. Considering all electrochemical results, more homogeneous binder distribution and the resulting increase in charge transfer leads to higher discharge capacities in ML cells. In

addition, better electrochemical performance roots from a porosity gradient generated inside the cathode – as suggested in literature [30,31].

Table 5. Impedance parameters derived from the fitting of equivalent circuit models for SL and ML electrodes.

	Electrode Type	R_e [Ω]	R_{SEI} [Ω]	R_{ct} [Ω]	Q_{SEI} [mF]	α_{SEI}	Q_{dl} [mF]	α_{dl}	χ^2
1st cycle 4.2 V	SL	1.14	17.08	27.29	4.90	0.45	2.85	1	0.006
	ML	1.27	17.97	12.81	5.91	0.45	7.36	0.99	0.009
2nd cycle 4.2 V	SL	1.06	12.58	15.88	6.50	0.45	4.23	0.98	0.004
	ML	1.19	11.48	3.05	6.48	0.45	7.90	1	0.005

4. Conclusions

Aqueous fabrication of thick NMC811 electrodes was performed using an industrially relevant coating procedure. pH regulation with phosphoric acid and optimized coating parameters lead to smooth thick cathode films with superior areal capacities of 8.6 mA h cm^{-2} . It was demonstrated that multi-layer electrodes of equal active material loading can be fabricated in a subsequent tape casting procedure. The absence of morphological defects was confirmed for the presented manufacturing technique. Both electrodes exhibit sufficient mechanical integrity to be processed on a standard roll-to-roll system. Multi-layer casted cathodes show improved adhesion to the Al current collector, exemplified by a 45% higher adhesion strength for the ML electrodes compared to SL. In addition, optical inspection revealed a diffuse boundary between the separately coated layers, confirming good intra-layer adherence. ML electrodes show an improved electrochemical performance during rate capability tests compared to SL electrodes, expressed by higher specific discharge capacity for all investigated C-rates. It is worth mentioning that, especially for low current densities, improvements of over 20% are measured. This occurs due to more evenly distributed material inside the cathode coating and a possible gradient in coating porosity. All findings emphasize the potential of using multi-layering as a technique to gain energy density through increased electrode thickness. This technique can be easily adapted to R2R processing and a variety of electrode fabrication applications on an industrial scale. This study shows that by multi-layering, great improvements in electrochemical performance and mechanical stability can be achieved within aqueous fabrication of high energy density cathodes. It also opens up new possibilities for multiple design options by implementing various material components and properties into the electrode. The 3D architectures can be easily integrated within coatings in a consecutive large scale casting method. Future work will investigate cell performance for different material gradients, such as binder, conducting agents, and particle size in a two or more layer electrode design. Opportunities to decrease tortuosity and thereby shorten Li-ion pathways can be realized by varying film composition through multi-layer coating. This will be the subject of future investigations.

Author Contributions: Conceptualization, L.N.; methodology, L.N. and N.E.; validation, L.N.; formal analysis, L.N. and N.E.; investigation, L.N.; resources, K.F. and M.J.; writing—original draft preparation, L.N.; writing—review and editing, L.N., K.F., D.C., M.J. and F.W.; visualization, L.N.; supervision, K.F. and F.W.; project administration, K.F. and M.J.; funding acquisition, M.J. All authors have read and agreed to the published version of the manuscript.

Funding: This research was funded by the Austrian Federal Ministry for Climate Action, Environment, Energy, Mobility, Innovation, and Technology (BMK).

Institutional Review Board Statement: Not applicable.

Informed Consent Statement: Not applicable.

Data Availability Statement: The data presented in this study are available on request from the corresponding author.

Acknowledgments: The authors would like to thank Christiane Groher for performing the SEM measurements reported herein. In addition we would like to acknowledge the technical support from Andreas Gigl during electrode preparation.

Conflicts of Interest: The authors declare no conflict of interest.

Abbreviations

The following abbreviations are used in this manuscript:

CB	carbon black
CCCV	constant current constant voltage
CMC	carboxymethyl cellulose
CV	cyclic voltammetry
EIS	electrochemical impedance spectroscopy
ML	multi-layer
NMC	lithium nickel manganese cobalt oxide
NMP	N-Methyl-2-pyrrolidone
N/P ratio	negative/positive capacity ratio
PMA	poly(methyl)acrylate
PVDF	polyvinylidene fluoride
R2R	roll-to-roll
SEI	solid electrolyte interphase
SEM	scanning electron microscopy
SL	single-layer
SOC	state of charge

References

- Wood, D.L., III; Li, J.; Daniel, C. Prospects for reducing the processing cost of lithium ion batteries. *J. Power Sources* **2015**, *275*, 234–242. [CrossRef]
- Bryntesen, S.N.; Strømman, A.H.; Tolstorebrov, I.; Shearing, P.R.; Lamb, J.J.; Stokke Burheim, O. Opportunities for the State-of-the-Art Production of LIB Electrodes—A Review. *Energies* **2021**, *14*, 1406. [CrossRef]
- Li, J.; Du, Z.; Ruther, R.E.; An, S.J.; David, L.A.; Hays, K.; Wood, M.; Phillip, N.D.; Sheng, Y.; Mao, C.; et al. Toward low-cost, high-energy density, and high-power density lithium-ion batteries. *JOM* **2017**, *69*, 1484–1496. [CrossRef]
- Susarla, N.; Ahmed, S.; Dees, D.W. Modeling and analysis of solvent removal during Li-ion battery electrode drying. *J. Power Sources* **2018**, *378*, 660–670. [CrossRef]
- Chatalov, A.Y. Effet du pH sur le comportement électrochimique des métaux et leur résistance à la corrosion. *Dokl. Akad. Naouk SSSR* **1952**, *86*, 775.
- Kazzazi, A.; Bresser, D.; Birrozzi, A.; von Zamory, J.; Hekmatfar, M.; Passerini, S. Comparative analysis of aqueous binders for high-energy li-rich NMC as a Lithium-Ion cathode and the impact of adding phosphoric acid. *ACS Appl. Mater. Interfaces* **2018**, *10*, 17214–17222. [CrossRef] [PubMed]
- Kukay, A.; Sahore, R.; Parejiya, A.; Hawley, W.B.; Li, J.; Wood, D.L., III. Aqueous Ni-rich-cathode dispersions processed with phosphoric acid for lithium-ion batteries with ultra-thick electrodes. *J. Colloid Interface Sci.* **2021**, *581*, 635–643. [CrossRef] [PubMed]
- Carvalho, D.V.; Loeffler, N.; Kim, G.T.; Marinaro, M.; Wohlfahrt-Mehrens, M.; Passerini, S. Study of water-based lithium titanate electrode processing: The role of pH and binder molecular structure. *Polymers* **2016**, *8*, 276. [CrossRef]
- Hamam, I.; Zhang, N.; Liu, A.; Johnson, M.; Dahn, J. Study of the reactions between Ni-rich positive electrode materials and aqueous solutions and their relation to the failure of Li-ion cells. *J. Electrochem. Soc.* **2020**, *167*, 130521. [CrossRef]
- Li, C.C.; Lee, J.T.; Tung, Y.L.; Yang, C.R. Effects of pH on the dispersion and cell performance of LiCoO₂ cathodes based on the aqueous process. *J. Mater. Sci.* **2007**, *42*, 5773–5777. [CrossRef]
- Bauer, W.; Çetinel, F.A.; Müller, M.; Kaufmann, U. Effects of pH control by acid addition at the aqueous processing of cathodes for lithium ion batteries. *Electrochim. Acta* **2019**, *317*, 112–119. [CrossRef]
- Zhu, P.; Han, J.; Pfleging, W. Characterization and Laser Structuring of Aqueous Processed Li (Ni_{0.6}Mn_{0.2}Co_{0.2}) O₂ Thick-Film Cathodes for Lithium-Ion Batteries. *Nanomaterials* **2021**, *11*, 1840. [CrossRef] [PubMed]
- Loeffler, N.; Kim, G.T.; Mueller, F.; Diemant, T.; Kim, J.K.; Behm, R.J.; Passerini, S. In situ coating of Li [Ni_{0.33}Mn_{0.33}Co_{0.33}] O₂ particles to enable aqueous electrode processing. *ChemSusChem* **2016**, *9*, 1112–1117. [CrossRef]
- Kuenzel, M.; Bresser, D.; Diemant, T.; Carvalho, D.V.; Kim, G.T.; Behm, R.J.; Passerini, S. Complementary strategies toward the aqueous processing of high-voltage LiNi_{0.5}Mn_{1.5}O₄ lithium-ion cathodes. *ChemSusChem* **2018**, *11*, 562–573. [CrossRef]
- Ligneel, E.; Lestriez, B.; Hudhomme, A.; Guyomard, D. Effects of the solvent concentration (solid loading) on the processing and properties of the composite electrode. *J. Electrochem. Soc.* **2007**, *154*, A235. [CrossRef]

16. Lee, J.H.; Paik, U.; Hackley, V.A.; Choi, Y.M. Effect of carboxymethyl cellulose on aqueous processing of natural graphite negative electrodes and their electrochemical performance for lithium batteries. *J. Electrochem. Soc.* **2005**, *152*, A1763. [CrossRef]
17. Kuang, Y.; Chen, C.; Kirsch, D.; Hu, L. Thick electrode batteries: Principles, opportunities, and challenges. *Adv. Energy Mater.* **2019**, *9*, 1901457. [CrossRef]
18. Du, Z.; Rollag, K.; Li, J.; An, S.J.; Wood, M.; Sheng, Y.; Mukherjee, P.; Daniel, C.; Wood III, D. Enabling aqueous processing for crack-free thick electrodes. *J. Power Sources* **2017**, *354*, 200–206. [CrossRef]
19. Singh, M.; Kaiser, J.; Hahn, H. Thick Electrodes for High Energy Lithium Ion Batteries. *J. Electrochem. Soc.* **2015**, *162*, A1196–A1201. [CrossRef]
20. Golmon, S.; Maute, K.; Dunn, M.L. A design optimization methodology for Li⁺ batteries. *J. Power Sources* **2014**, *253*, 239–250. [CrossRef]
21. Lu, W.; Jansen, A.; Dees, D.; Nelson, P.; Veselka, N.R.; Henriksen, G. High-energy electrode investigation for plug-in hybrid electric vehicles. *J. Power Sources* **2011**, *196*, 1537–1540. [CrossRef]
22. Sahore, R.; Wood, D.L., III; Kukay, A.; Grady, K.M.; Li, J.; Belharouak, I. Towards understanding of cracking during drying of thick aqueous-processed LiNi_{0.8}Mn_{0.1}Co_{0.1}O₂ cathodes. *ACS Sustain. Chem. Eng.* **2020**, *8*, 3162–3169. [CrossRef]
23. Font, F.; Protas, B.; Richardson, G.; Foster, J.M. Binder migration during drying of lithium-ion battery electrodes: Modelling and comparison to experiment. *J. Power Sources* **2018**, *393*, 177–185. [CrossRef]
24. Müller, M.; Pfaffmann, L.; Jaiser, S.; Baunach, M.; Trouillet, V.; Scheiba, F.; Scharfer, P.; Schabel, W.; Bauer, W. Investigation of binder distribution in graphite anodes for lithium-ion batteries. *J. Power Sources* **2017**, *340*, 1–5. [CrossRef]
25. Kremer, L.S.; Hoffmann, A.; Danner, T.; Hein, S.; Prifling, B.; Westhoff, D.; Dreer, C.; Latz, A.; Schmidt, V.; Wohlfahrt-Mehrens, M. Manufacturing Process for Improved Ultra-Thick Cathodes in High-Energy Lithium-Ion Batteries. *Energy Technol.* **2020**, *8*, 1900167. [CrossRef]
26. Jaiser, S.; Müller, M.; Baunach, M.; Bauer, W.; Scharfer, P.; Schabel, W. Investigation of film solidification and binder migration during drying of Li-Ion battery anodes. *J. Power Sources* **2016**, *318*, 210–219. [CrossRef]
27. Westphal, B.G.; Kwade, A. Critical electrode properties and drying conditions causing component segregation in graphitic anodes for lithium-ion batteries. *J. Energy Storage* **2018**, *18*, 509–517. [CrossRef]
28. Baunach, M.; Jaiser, S.; Schmelzle, S.; Nirschl, H.; Scharfer, P.; Schabel, W. Delamination behavior of lithium-ion battery anodes: Influence of drying temperature during electrode processing. *Dry. Technol.* **2016**, *34*, 462–473. [CrossRef]
29. Liu, L.; Guan, P.; Liu, C. Experimental and simulation investigations of porosity graded cathodes in mitigating battery degradation of high voltage lithium-ion batteries. *J. Electrochem. Soc.* **2017**, *164*, A3163. [CrossRef]
30. Qi, Y.; Jang, T.; Ramadesigan, V.; Schwartz, D.T.; Subramanian, V.R. Is there a benefit in employing graded electrodes for lithium-ion batteries? *J. Electrochem. Soc.* **2017**, *164*, A3196. [CrossRef]
31. Fang, R.; Ge, H.; Wang, Z.; Li, Z.; Zhang, J. A two-dimensional heterogeneous model of lithium-ion battery and application on designing electrode with non-uniform porosity. *J. Electrochem. Soc.* **2020**, *167*, 130513. [CrossRef]
32. Müller, D.; Landa-Medrano, I.; Eguia-Barrio, A.; Boyano, I.; Urdampilleta, I.; de Meatza, I.; Fill, A.; Birke, P. Electrochemical characterization of bi-layered graphite anodes combining high and low porosity in lithium-ion cells to improve cell performance. *Electrochim. Acta* **2021**, *391*, 138966. [CrossRef]
33. Dai, Y.; Srinivasan, V. On graded electrode porosity as a design tool for improving the energy density of batteries. *J. Electrochem. Soc.* **2015**, *163*, A406. [CrossRef]
34. Kespe, M.; Cernak, S.; Gleiß, M.; Hammerich, S.; Nirschl, H. Three-dimensional simulation of transport processes within blended electrodes on the particle scale. *Int. J. Energy Res.* **2019**, *43*, 6762–6778. [CrossRef]
35. Imachi, N.; Takano, Y.; Fujimoto, H.; Kida, Y.; Fujitani, S. Layered cathode for improving safety of Li-ion batteries. *J. Electrochem. Soc.* **2007**, *154*, A412. [CrossRef]
36. Whitacre, J.; Zaghbi, K.; West, W.; Ratnakumar, B. Dual active material composite cathode structures for Li-ion batteries. *J. Power Sources* **2008**, *177*, 528–536. [CrossRef]
37. Liu, D.; Chen, L.C.; Liu, T.J.; Chu, W.B.; Tiu, C. Improvement of lithium-ion battery performance by two-layered slot-die coating operation. *Energy Technol.* **2017**, *5*, 1235–1241. [CrossRef]
38. Diehm, R.; Kumberg, J.; Dörrer, C.; Müller, M.; Bauer, W.; Scharfer, P.; Schabel, W. In Situ Investigations of Simultaneous Two-Layer Slot Die Coating of Component-Graded Anodes for Improved High-Energy Li-Ion Batteries. *Energy Technol.* **2020**, *8*, 1901251. [CrossRef]
39. Zheng, H.; Li, J.; Song, X.; Liu, G.; Battaglia, V.S. A comprehensive understanding of electrode thickness effects on the electrochemical performances of Li-ion battery cathodes. *Electrochim. Acta* **2012**, *71*, 258–265. [CrossRef]
40. Gao, H.; Wu, Q.; Hu, Y.; Zheng, J.P.; Amine, K.; Chen, Z. Revealing the rate-limiting Li-ion diffusion pathway in ultrathick electrodes for Li-ion batteries. *J. Phys. Chem. Lett.* **2018**, *9*, 5100–5104. [CrossRef]
41. Fröhlich, K.; Abrahams, I.; Jahn, M. Determining phase transitions of layered oxides via electrochemical and crystallographic analysis. *Sci. Technol. Adv. Mater.* **2020**, *21*, 653–660. [CrossRef] [PubMed]
42. Heubner, C.; Nickol, A.; Seeba, J.; Reuber, S.; Junker, N.; Wolter, M.; Schneider, M.; Michaelis, A. Understanding thickness and porosity effects on the electrochemical performance of LiNi_{0.6}Co_{0.2}Mn_{0.2}O₂-based cathodes for high energy Li-ion batteries. *J. Power Sources* **2019**, *419*, 119–126. [CrossRef]



Article

Modelling and Optimisation of Laser-Structured Battery Electrodes

Lukas Schweighofer ¹, Bernd Eschelmüller ², Katja Fröhlich ², Wilhelm Pfleging ³ and Franz Pichler ^{1,*}

¹ Virtual Vehicle Research GmbH, Inffeldgasse 21a, 8010 Graz, Austria; lukas.schweighofer@v2c2.at

² Center for Low-Emission Transport, AIT Austrian Institute of Technology GmbH, Giefinggasse 4, 1210 Vienna, Austria; bernd.eschelmuller@ait.ac.at (B.E.); katja.froehlich@ait.ac.at (K.F.)

³ Institute for Applied Materials-Applied Materials Physics (IAM-AWP), Karlsruhe Institute of Technology (KIT), Hermann-von-Helmholtz-Platz 1, 76344 Eggenstein-Leopoldshafen, Germany; wilhelm.pfleging@kit.edu

* Correspondence: franz.pichler@v2c2.at

Abstract: An electrochemical multi-scale model framework for the simulation of arbitrarily three-dimensional structured electrodes for lithium-ion batteries is presented. For the parameterisation, the electrodes are structured via laser ablation, and the model is fit to four different, experimentally electrochemically tested cells. The parameterised model is used to optimise the parameters of three different pattern designs, namely linear, gridwise, and pinhole geometries. The simulations are performed via a finite element implementation in two and three dimensions. The presented model is well suited to depict the experimental cells, and the virtual optimisation delivers optimal geometrical parameters for different C-rates based on the respective discharge capacities. These virtually optimised cells will help in the reduction of prototyping cost and speed up production process parameterisation.

Keywords: battery modelling; laser-structured electrodes; 3D battery concept; lithium-ion battery; multi-physics multi-domain modelling; virtual optimisation

1. Introduction

Batteries are still the centrepiece components of electrical vehicles (EVs), which calls for their ongoing optimisation in terms of power density, energy density, cycle and calendrical lifetime, and safety. The present state-of-the-art is still formed by the lithium-ion technology. Here, a trend towards nickel-rich materials that allow a decrease of the utilisation of cobalt content dominates the cathode material development, and the transformation from pure graphite to graphite–silicon composites or pure silicon alloys determines the anode material development [1–4]. Furthermore, electrode structure optimisation is a promising pathway for improved cell performance characteristics, especially for increased high current capability.

Electrode structuring is either performed additively, similar to 3D printing (e.g., LIFT [5]) or erosively, which includes mechanical structuring (e.g., embossing [6]), chemical structuring (e.g., etching [7,8]), or laser-based methods [9–11].

Furthermore, methods that structure the electrodes in the synthesis process are available, e.g., the creation of interdigitated electrodes or, on an even finer level, the production of gyroid structures, which are usually applicable in special applications due to their complex structures [12–15].

Structuring of electrodes brings many advantages for batteries. In production, it can reduce the formation time of electrodes due to an enhanced wetting of electrodes with liquid electrolyte, which saves storage time and production costs [9]. Cell performance is increased due to the shortened Li-ion transport pathways through the porous electrodes, which impact the power and energy density, especially for thicker electrodes and higher

C-rates [16,17]. In terms of the safety and lifespan of batteries, the improved transport characteristics in the cell lead to smaller local concentration and potential peaks, which helps avoid harmful side reactions, which can lead to accelerated ageing and thermal runaway [11].

In order to utilise the benefits of this structuring method to their full extent, a thorough understanding of their effects in the complex interaction of all involved components of a Li-ion cell sandwich is needed. This understanding can be improved and supported by computer-aided engineering (CAE) techniques. Several such CAE methods are applied by different groups to support the optimisation of electrode structuring techniques.

A simple, yet effective approach was chosen by Kraft et al. [18], where the electrode structures were condensed into improved effective conductivities in a pseudo-2D approach as developed by Newman et al. [19]. This approach keeps the simple structure of the Newman model and quantifies the overall impact of structuring, but cannot deliver insights into its role in the development of local concentration and potential gradients, minima, and maxima. Kraft et al. also published a more sophisticated approach [20], similar to the one by Chen et al. [16], where blind-hole-structured anodes were simulated with finite elements that actually resolved the shape of the hole structuring in a homogenised manner. An unhomogenised approach was presented by Latz et al. [21], where they also investigated cathode hole structuring with the holes on both electrodes set up directly opposite each other. The use of unhomogenised and separated electrolyte and active material domains supports better mapping of inhomogeneities in the electrodes at a higher computational cost. All these publications dealt with blind hole structures only. Salvadori et al. published a theoretical analysis [22] of linearly structured electrodes without a comparison to measured experimental data.

In the presented work, an electrochemical multi-scale simulation framework is developed that is capable of simulating arbitrarily structured electrodes. Both electrodes can be structured as long as a representative periodic cell can be found for the cell sandwich. The electrode 3D patterns are homogenised similar to the ones used by Chen et al. and Kraft et al. [16,18]. The model is parameterised using experimental data of line-structured electrodes.

The framework is extended by an automated meshing toolchain that allows sweeping the geometrical parameters of the structured electrodes. The impact of each parameter and their respective cross-effects on the discharge capacity at different C-rates are studied with these simulations. Specifically, the laser pitch, laser channel widths, and electrode thicknesses are varied in the frame of this publication. The results of these simulations allow for a better understanding of the influences of the varied parameters and can be used to reduce prototyping costs in production.

2. Materials and Methods

2.1. Cell Manufacturing

The pouch cells used in the discussed experiments consisted of NMC811 cathodes and graphite anodes. The cathode slurry consisted of 92% NMC811 (Targray, Kirkland, QC, Canada), 4% SUPER C65 (Imerys, Paris, France), and 4% PVDF-binder (Sigma Aldrich, St. Louis, MO, USA). The anode slurry was prepared in an aqueous formulation. It consisted of 95% artificial graphite (Hitachi, Chiyoda, Japan), 1% SUPER C45 (Imerys) and 1.5% CMC (Walocel CRT 2000 PA), and 2.5% of SBR latex (Zeon BM-451B). The electrodes were dried and compacted and used in single-layer pouch cells with a bi-cell design (1 double-sided cathode, 2 double-sided anodes) with a PP/PE/PP composite separator of 20 μm (Celgard, Charlotte, NC, USA). The cells were filled with a Solvionic electrolyte (EC:EMC 3:7, 2% VC, 1 M Li concentration). The areal capacity of the electrodes was 3.95 mAh/cm² and 4.7 mAh/cm² on the cathode and anode, respectively. This gives a high balancing factor of 1.19. Due to the laser-induced active material removal on the anode side, the balancing factor of the cells with structured anodes was effectively decreased,

which explains the need for slightly higher balancing factors in the cells with unstructured electrodes.

The 3D structuring of electrodes was established in ambient air applying a laser micromachining system (PS450-TO, Optec s.a., Frameries, Belgium), which was equipped with an ultrafast laser radiation source (Tangerine, Amplitude Systèmes, Pessac, France). After second harmonic generation, the femtosecond laser operates at a wavelength of 515 nm with a pulse length of 350–400 fs ($M^2 < 1.2$). For the laser ablation of the electrodes, a laser pulse repetition rate of 1 MHz was applied while adjusting the laser scanning speed of 1000 mm/s. Laser ablation generally removes electrode material locally down to the current collector in order to achieve homogeneous and accelerated wetting of the composite electrode with the liquid electrolyte [6]. In the presented studies for laser processing of the anode and cathode materials, an average laser power of 5 W was used, while according to the material-dependent ablation rates, the number of laser scans was adjusted to 15 and 7, respectively.

Altogether, four different cell configurations were built for the parameterisation of the presented model. The main difference in their configuration was established by the use of either structured or unstructured anodes and cathodes. The four cell configurations were:

- (a) Unstructured cell;
- (b) Anode structured (80 μm channels with a 300 μm pitch);
- (c) Cathode structured (60 μm channels with a 300 μm pitch);
- (d) Both electrodes structured (80 μm at the anode and 60 μm at the cathode, both with a 300 μm pitch).

These are referred to as Configurations (a), (b), (c), and (d), as in the given list. Schematic depictions of these configurations are given by an exemplary finite element discretisation in Figure 1.

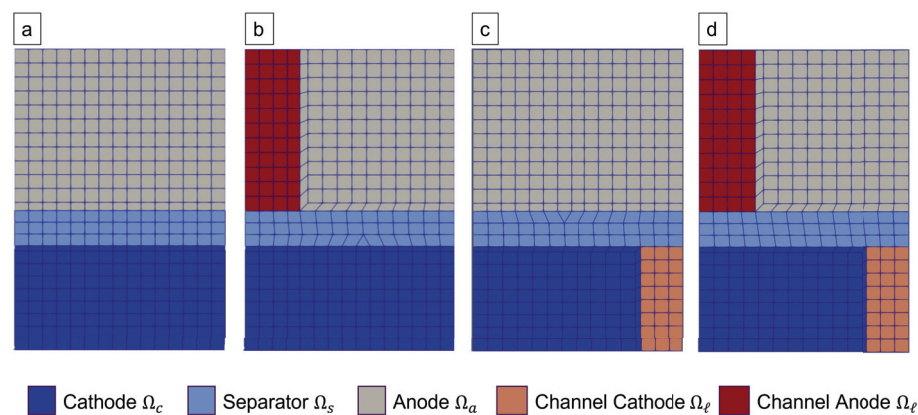


Figure 1. Periodic 2D finite element discretisation of the four different cell configurations used for fitting. We remark that Configuration (a) represents unstructured electrodes, which are equivalently simulated by a 1D cut as in the known Newman configuration. (b–d) represent the used meshes corresponding to the cell configurations as described in Section 2.1.

2.2. Electrochemical Measurements

In the cycling measurements utilised for the model parameterisation, the four cell types were discharged with a constant current until the lower cut-off voltage of 3 V was reached. The discharges were followed by short pauses (300 s for C/10 and 14 s for the other C-rates) and eventually were charged with a constant current until the upper cut-off voltage of 4.2 V, followed by a constant voltage step until a tenth of the constant current and a pause. These resulting voltage profiles were used to parameterise the model equations. Altogether, three different discharge and charge cycles at C/10, 1 C, and 2 C were used for all four cell types.

2.3. Mathematical Model

The mathematical model used in this work is based on the derivation by Pichler [23] and summarised in Table 1.

These governing equations describe the concentration of lithium-ions in the electrolyte c_ℓ , the concentration of lithium-ions in the active material particles c_s , the electrolyte potential ϕ_ℓ , the cathode potential ϕ_c , and the anode potential ϕ_a . Note that ϕ_c and ϕ_a are assumed to be spatially constant over their respective electrode and only change in time. This simplification is feasible when the electrical conductivity of the solid particles (~ 100 S/m) is magnitudes higher than the one in the electrolyte (~ 1 S/m), which is assumed here. Under this assumption, the classical partial differential equation usually solved to govern the distribution of ϕ_c and ϕ_a is replaced by the constraints (11), in the case of a prescribed cell current I_{cell} , or (12), in the case of a prescribed cell voltage U_{cell} .

Equations (5)–(8) describe the transport of lithium-ions in the electrolyte domain and are applicable in one-, two-, or three-dimensional domains. For structured electrodes, we have to distinguish four different electrolyte sub-domains, namely the cathode domain Ω_c , the anode domain Ω_a , the separator domain Ω_s , and the blank parts of the electrodes Ω_ℓ that were removed by the ablation process. The cathode, anode, and separator domains are all treated as porous, but homogenised structures, expressed by their respective effective electrolyte conductivity $\kappa_{eff} = \kappa \frac{\varepsilon}{\tau}$. Here, the porosity ε and the tortuosity τ express the impact of the micro-geometry on the effective conductivity. Note that the anode, with graphite basal planes oriented parallel to the current collector, is treated as an anisotropic material due to the flat-shaped particles of graphite. This means that the conductivity in the anode electrolyte domain is actually expressed by a diagonal tensor, where each entry defines the conductivity in the respective coordinate direction. The structured domain Ω_ℓ is treated as an ideal electrolyte space with no porosity or tortuosity hindering the lithium transport (i.e., $\varepsilon = \tau = 1$).

In the electrode domains Ω_c and Ω_a , the macroscopic lithium-ion transport, described by Equations (5) and (6), is coupled with the microscopic particle Equation (9), which describe the solid diffusion of lithium into the active material particles. The coupling condition is given by the Butler–Volmer Equation (13), which describes the intercalation and deintercalation of lithium. The particles are assumed to be spherically symmetric, such that a one-dimensional cut in the radial direction can be used to describe the solid diffusion process (i.e., $\Omega_{sc} = [0, R_c]$, $\Omega_{sa} = [0, R_{p,a}]$, $\Gamma_{sc} = \{R_{c,p}\}$ and $\Gamma_{sa} = \{R_a\}$).

Note that if the electrolyte domain is chosen to be a one-dimensional cut through the electrode sandwich, then the model would resemble the structure of the famous Newman model [19]. In the presented work, the electrolyte domains $\Omega_c, \Omega_s, \Omega_\ell$ and Ω_a are one-, two-, or three-dimensional, which allows for the description of structured electrodes as they are presented in the next subsection.

2.4. Structuring Designs

In this work, the laser-generated electrode structures were divided into three major groups: line, grid, and pinhole patterns; see Figure 2. Line and grid structures consist of parallel, continuous micro-channels. The latter includes perpendicular channels in both the x and y direction. The pinhole structures are formed by cone-shaped blind holes in the electrodes on a regular grid. For these designs, the pitch is defined by the distance of either the channel centre lines or the hole centre points. The degree of active material removal is controlled by either the channel width or the pinhole diameter.

For unstructured electrodes, the properties of particles within the electrodes are more or less independent of the in-plane position (with the exception of the boundaries of the electrodes, which should have little impact on the cell's behaviour, thus neglected here). This is a basis for the assumption of the Newman model, which allows the usage of a representative macroscopic 1D cross-section of the cell.

However, this last assumption is not feasible for structured electrodes. In the most general cases, a three-dimensional representation of the homogenised electrodes is used

to describe the electrode. Symmetries in the structures are utilised to reduce the electrode to a representative periodic unit cell, as depicted in red in Figure 2 for the discussed geometries. In the case of the linear structure, this leads to a reduction to a two-dimensional representation, in the grid case, a cuboid representation, and in the pinhole case, a prismatic representation, with a triangle base shape. These periodic cells are the geometric simulation domains of the presented model, discretised by the finite element method.

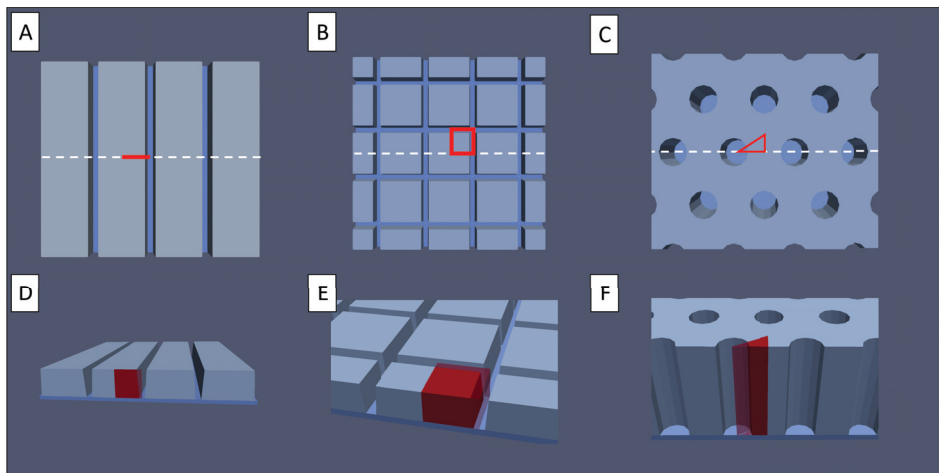


Figure 2. (A–C) Top view of (A) line structured, (B) grid structured, and (C) pinhole structured electrodes. The red marked area depicts a possible representative cross-section of the electrode. (D–F) Bird's eye view of the same structures.

2.5. Parameterisation

The model parameters used in this work were partially extracted from the manufacturing process, partially taken from the literature, and partially fit to the cycling data. They are summarised in Table 2, where the respective source is indicated. Measurements of the four different manufactured cell configurations (see Sections 2.1 and 2.2) were used to fit unknown model parameters. These cells have the same electrode and electrolyte composition, but differ in their structuring. A depiction of the two-dimensional finite element mesh used to simulate them is shown in Figure 1.

These different configurations yield different anode to cathode balancing for each cell, which is advantageous in parameter fitting. Often, only measurements based on one balancing factor are available for parameterisation. In such measurements, the impact of the anode and the cathode cannot be distinguished without enough prior knowledge. For example, the *OCV* curve of the cell is a superposition of the two open circuit potentials of the cathode and the anode. Furthermore, any ohmic drops are superpositions of all the overpotentials occurring in the anode, cathode, and electrolyte. The four different cell configurations give more independent information on each electrode, due to the respective shift of their lithiation windows and local current densities in comparison to the other scenarios. Therefore, it is reasonable to fit electrode-specific parameters from the available full-cell measurements.

The presented model was fit to multiple measurements simultaneously, including all four cell types and their respective $C/10$, $1C$, and $2C$ discharge voltage curves. Each simulation respected the individual parameter adjustments due to the respective laser structures, but other than that, there was one set of parameters used for all simulations.

The cost function in the fitting process is defined by

$$f(p) = \sum_{i=1}^{12} \frac{1}{T_i} \int_{t=0}^{T_i} (u_{sim,i}(t;p) - u_{meas,i}(t))^2 dt, \quad (1)$$

where the index i indicates the specific measurement index, T_i the respective terminal time, and p the set of fitting parameters that is evaluated.

The fitted parameters are the diffusion coefficients D_s , the Butler–Volmer reaction rate constants k_{BV} , and the electrode tortuosities τ . Furthermore, the coefficients \hat{U}_0 and \hat{A}_k , $k \in (0, \dots, 10)$ of the Redlich–Kister expansion (17) used to model the cathodes open circuit potential were fit.

The individual simulations were performed via an in-house-developed finite element code (based on [24]), which is highly optimised for single-thread transient simulations of several thousand degrees of freedom. This yielded an average simulation time of around 6 s per conducted simulation. The fitting algorithm used a mix of steepest descent, random evaluations, and single parameter sweeps to minimise the cost function (1). The random evaluations and single parameter sweeps around the best parameter candidates help leaving local minima, which is a well-known problem for the steepest gradient and Newton-like optimisation methods. Due to their single-thread nature, the individual simulation could easily be performed in parallel by the python multiprocessing library `pathos`.

2.6. Initialisation

The consistent initialisation of the discussed models for the individual structured electrodes is non-trivial and will therefore be explained here in detail.

For every experiment, the initial voltage U_0 and the degree of ablation of active material x_c and x_a influenced the specific initialisation. The assumptions here were that initially (before formation), all the cyclable lithium a_{Li} is contained in the cathode. Therefore a_{Li} in *mol* is given by $a_{Li} = c_{max,c}m_c/\rho_c$, where $c_{max,c}$ is the maximum concentration of lithium, m_c is the mass, and ρ_c is the density of the cathode. A part a_{SEI} of the lithium was lost in the initialisation due to the SEI formation on the anode. This part was assumed to be proportional to the size of the anode and therefore given by $a_{SEI} = x_{SEI}c_{max,a}m_a/\rho_a$, where x_{SEI} is the respective proportionality factor, and $c_{max,a}$, m_a , and ρ_a are the maximum concentration of lithium, the mass, and the density of the anode, respectively. Under these assumptions, any feasible tuple of fully relaxed lithium concentrations $(c_{0,c}, c_{0,a})$ has to fulfil the equations

$$c_{0,c}m_c/\rho_c + c_{0,a}m_a/\rho_a = a_{Li} - a_{SEI} \quad (2)$$

and

$$U_{ocv,c}(c_{0,c}) - U_{ocv,a}(c_{0,a}) = U_0. \quad (3)$$

Expressing $c_{0,c}$ from (2) and putting it into (3) yield

$$U_{ocv,c}\left(\frac{\rho_c}{m_c}(a_{Li} - a_{SEI} - c_{0,a}m_a/\rho_a)\right) - U_{ocv,a}(c_{0,a}) = U_0, \quad (4)$$

which was solved for $(c_{0,c}, c_{0,a})$ at the beginning of each simulation via a bi-section method. We remark that the proportionality factor x_{SEI} was fit to 9.89%, which agrees with the literature values [25,26].

2.7. Parameter Studies

The model, which was parameterised based on the measurements acquired from the four cell types, as described in Section 2.5, was used for the simulation of all possible cell structures and their virtual optimisation. All the discussed models share the same set of electrochemical parameters and differ only in their macroscopic geometry, which describes the structured electrodes and the electrolyte space embedding them.

All three structuring methods were varied and analysed with respect to the applied laser pitch and the degree of ablation of the active material due to structuring and the electrode thicknesses (i.e., loading). This allowed for a comparison of the different structuring methods and an estimation of their respective performance gain, which was quantified by the discharge capacity of a cell configuration at different C-rates. This was chosen due to its

simplicity, alongside its capability to quantify the performance at different C-rates. For most of the configurations, the discharge capacities were compared to a C/10 discharge capacity.

All the discussed studies were performed using an automated toolchain that was developed for this purpose. It consisted of a python script collection that automates the distribution of multiple simulations to a CPU cluster and the automated evaluation of their results. Each simulation then used a scripted meshing algorithm (utilizing SALOME [27]) and an in-house-developed FEM toolbox [24] that performs the simulation of the discussed cycling protocols. Altogether, about 8400 such simulations were performed to deliver the presented results. Each of these simulations included several charge and discharge cycles at different C-rates. The computational time for these simulations varied from around 6 s to around 1 h. This range stems from the range of the necessary degrees of freedom, which grew with the size of the periodic computational domain. This domain grew with the applied laser pitch distance, electrode thickness, and the dimension of the computational domain.

3. Results

3.1. Parameterisation

The parameterisation process described in Section 2.5 delivered a set of parameters that is presented as a part of the parameter summary in Table 2. A direct comparison of the measurement and fitted simulation discharge capacities is shown in Figure 3. It can be seen that the simulations of all four cell configurations over all C-rates delivered results that were very close to the measured discharge capacities.

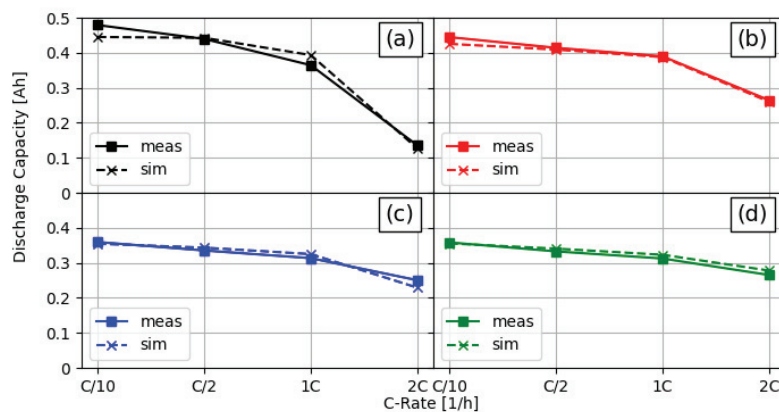


Figure 3. Comparison of measured and simulated discharge capacities for different C-rates and linear structured cell setups. (a) Unstructured reference cell, (b) structured anode (80 μm channels and 300 μm pitch), (c) structured cathode (60 μm channels and 300 μm pitch), and (d) both electrodes structured (80 μm anode and 60 μm cathode channels, both with 300 μm pitch).

The parameterised model was used to simulate NMC811/graphite full cells for multiple laser structure settings. There were multiple parameters/settings that could be varied and possibly influence the effects of the laser structure on the capacity.

The results of the evaluated simulations are presented and are described in the following subsections.

We remark that when the figures show C-rates for different values for the degree of ablation, then the C-rates always represent the C-rates with respect to the reference cell with unstructured electrodes. For example, consider a 2 Ah cell, then 2 C are equivalent to a current of 4 A. If a simulation shows the capacity at 2 C for a cell with an ablation of 10%, then these 2 C are equivalent to 4 A, albeit the 10% reduction of the active material.

3.2. Variation of the Degree of Ablation

First, a simple study of the impact of laser-structured electrodes is presented. For this purpose, simulations were conducted where either one or both electrodes were laser

structured in a line pattern design. The laser pitch was fixed to 200 μm , which is a value commonly used in the literature [9,28]. The material loading and electrode thicknesses were the same as in the measured cells. The degree of ablation was varied from 0% to 50%. The results of the simulations where only one electrode was structured are shown in Figure 4. The figure shows the discharge capacity of full cells, where either the cathode or the anode were structured. In a second step, both electrodes were structured with an individual degree of ablation. The results are shown in Figure 5.

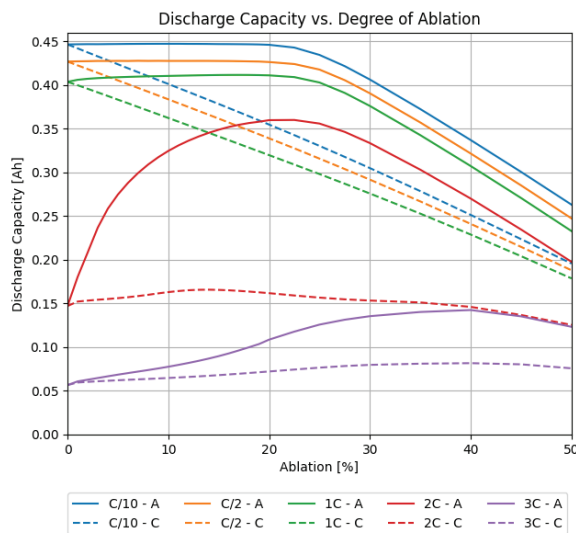


Figure 4. Simulated discharge capacities for full cells for different C-rates, versus the degree of ablation, where (solid) only the anode or (dashed) only the cathode was structured.

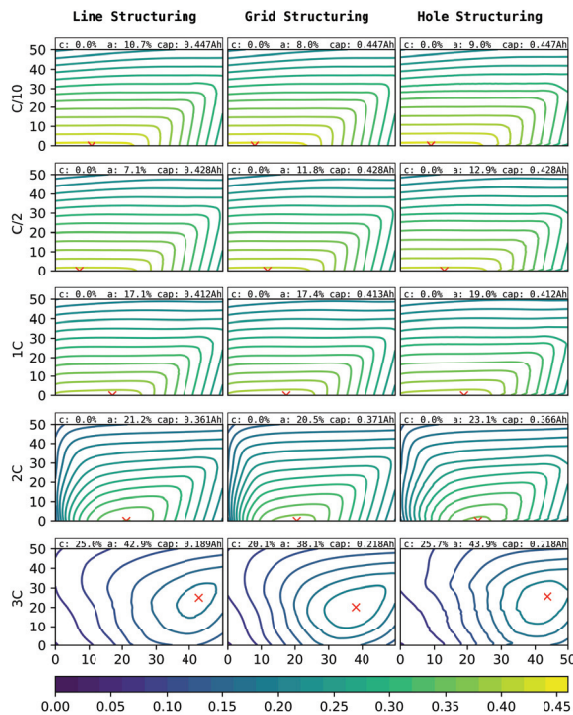


Figure 5. Discharge capacities [Ah] for full cells with line (left, pitch = 200 μm), grid (centre, pitch = 200 μm), and hole (right, pitch = 70 μm) structures, for C-rates C/10–3C. The x-axis shows the degree of ablation as a percentage of the anode, the y-axis for the cathode. At the top of each plot, the optimal degree of ablation for the cathode and anode and the corresponding discharge capacity are shown.

For these simulations, the virtual cell was charged with a constant current at $C/2$ until the upper cut-off voltage of 4.2 V was reached, followed by a constant voltage step until the current was below $C/20$. The discharge steps were a constant current ($C/10$ – $3C$) until the lower cut-off voltage of 3 V was reached. Between each charge and discharge, the simulated cells rested for 14 s.

To show the influence of optimal structuring on the electrode utilisation, several snapshots of the lithium concentration in the electrolyte and the electrodes are shown in Figure 6. Here, the optimal structuring for a linear structuring method, at 3 C discharge, is depicted at the moment where the 3 C discharge cycle reaches its cut-off voltage of 3 V. To be able to compare this to non-optimal structuring, also 1/2 and 1/10 of the respective degree of ablation were simulated, and each version is depicted at the moment where it reached the lower cut-off voltage. The snapshots show how the optimal structuring allowed for a deeper lithiation and de-lithiation of the anode and cathode, respectively. The broader channels at the respective optimal structuring allowed for better replenishment of lithium ions from the anode to the cathode, which only stopped when the reaction front enveloped a very small, unutilised area. The local current density caused very high local concentration gradients and an over-potential high enough to reach the cut-off voltage. In addition to the improved discharge properties, the previous charging led to higher initial lithiation and de-lithiation of the respective optimally structured electrodes. This can be seen, e.g., from the higher anode lithiation in the unutilised area. For completeness, similar snapshots are shown for the optimal grid and pinhole structures in Figures 7 and 8.

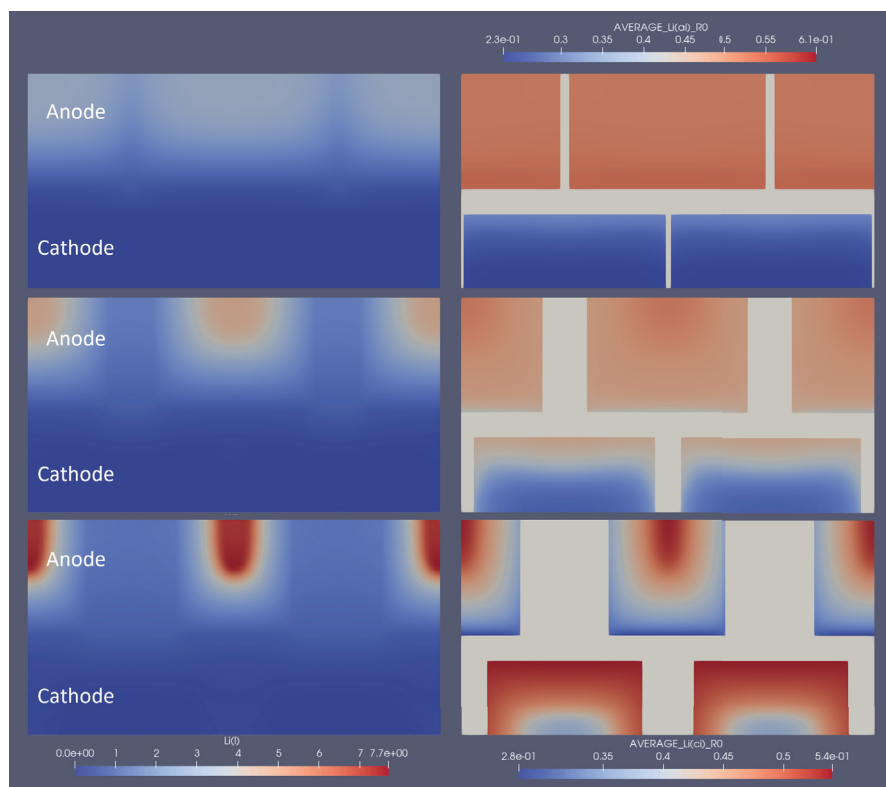


Figure 6. Snapshot of the lithium concentrations in electrolytes and solids for line structuring at the end of the 3 C discharge cycle. The left part shows the concentration in the electrolyte, and the right part shows the average particle concentration in the respective electrodes. The bottom shows the optimal parameters, whereas the middle row shows 50% of that structuring amount, and the top part shows 10% for comparison. $2.3e-01$ represents 2.3×10^{-1} , the same rule applies to other E notations.

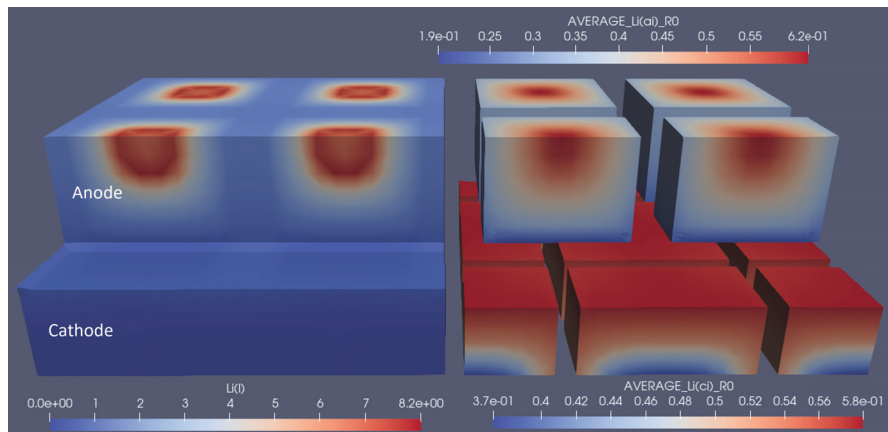


Figure 7. Snapshot of the lithium-ion concentrations in electrolytes and solids for the optimal grid structuring at the end of the 3C discharge cycle. The left part shows the concentration in the electrolyte, and the right part shows the average particle concentration in the respective electrodes. $1.9e-01$ represents 1.9×10^{-1} , the same rule applies to other E notations

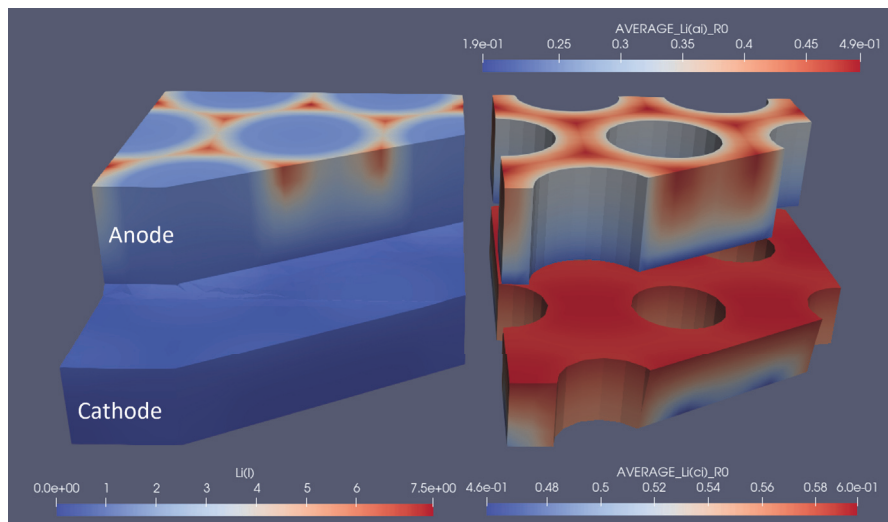


Figure 8. Snapshot of the lithium concentrations in electrolytes and solids for the optimal pinhole structuring at the end of the 3C discharge cycle. The left part shows the concentration in the electrolyte, and the right part shows the average particle concentration in the respective electrodes. $1.9e-01$ represents 1.9×10^{-1} , the same rule applies to other E notations.

3.3. Variation of Pitch

In the next step, also the pitch of the laser generated channels and pinholes was varied. The presented model does not describe the mechanical stability of the structured electrodes. This means that even the thinnest walls, which were created by a small laser pitch, performed ideally in a mechanical sense, and the following results have to be interpreted under the consideration of these simplifications. A consequence of this simplification is that a smaller laser pitch, in combination with thin laser channels or holes, always resulted in the best performance due to its increase of the macroscopic electrode area. As a consequence, a smaller laser pitch would always be preferable, but is only realistically advantageous as long as the mechanical stability of the electrodes can handle cycling. Still, it is of interest to study the variation, in the presented way, to quantify its impact. The model limitation, which is given by the neglected mechanical stability of the electrode structures, has to be kept in mind when interpreting these results.

The simulated discharge capacities for structure pitches between $20 \mu\text{m}$ and $300 \mu\text{m}$ and the ablation of 0–50% for line (left), grid (centre), and hole (right) structures for C-rates

of C/10–3C can be seen in Figure 9. Due to the higher impact of the structuring on the anode, as can be seen in Figure 4, only anode structuring was considered for this study.

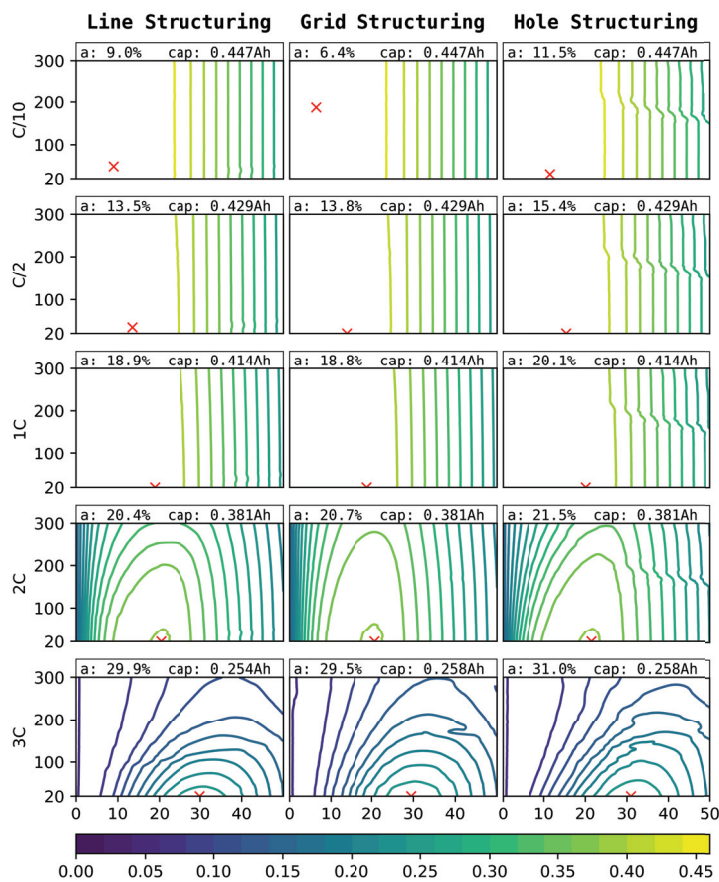


Figure 9. Simulated discharge capacities (Ah) for different C-rates (outer y-axis), laser pitches (μm), inner y-axis), structure types (outer x-axis), and degrees of ablation of the anode ($\%$), inner x-axis).

3.4. Variation of Electrode Loading

In the third and final virtual variation, not only the degree of ablation and the laser pitch were varied, but also the electrode loading, which is represented by the electrode thickness under the assumption of constant porosity. The results are shown in Figure 10. Here, the volumetric capacity is given instead of the absolute capacity. The specific capacity was calculated under the assumption of a $12\ \mu\text{m}$ anodic and a $20\ \mu\text{m}$ cathodic current collector foil per cell stack.

As a representative quantification of the theoretically possible performance gain, the optimal degree of ablation for the anode and its respective volumetric discharge capacity are indicated in Figure 10. Some of these results are only theoretically reachable due to the mechanical instability of the electrodes at the small optimal pitch of $20\ \mu\text{m}$. From experience, values of $50\ \mu\text{m}$ are realisable.

The thicknesses of both electrodes were varied from 0.5- to 3-times the initial thicknesses of the reference cell electrodes of $75\ \mu\text{m}$ and $115\ \mu\text{m}$, for the cathode and anode, respectively. For this study, similar load profiles as for the previous ones were used, where the C-rates were adjusted according to the new loading of the electrodes.

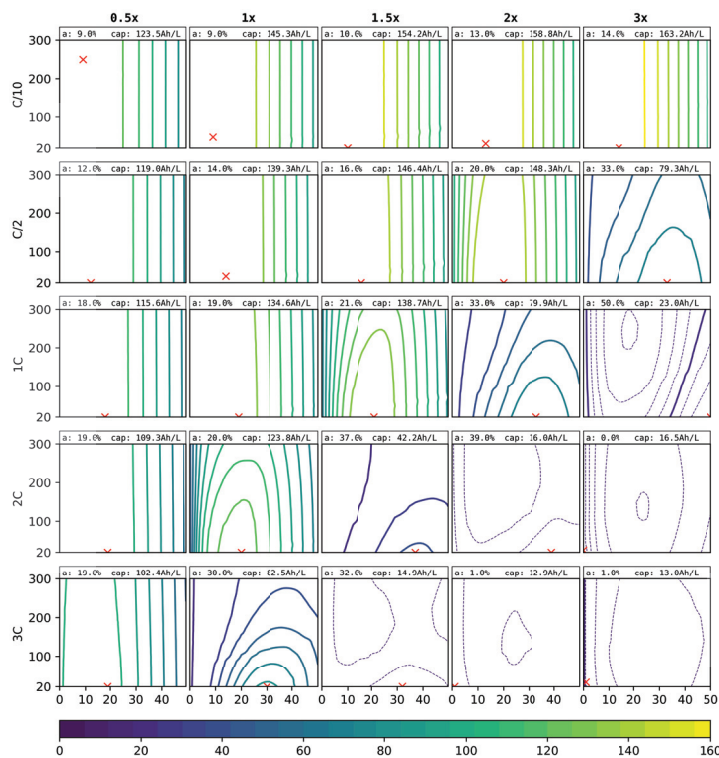


Figure 10. Simulated discharge capacity (Ah) for different C-rates (outer y-axis), laser pitches (μm), inner y-axis), thicknesses (outer x-axis), and degrees of ablation ($\%$), inner x-axis). The red crosses show the optimal degrees of ablation and pitch for each C-rate and structuring method. The optimal parameters and the respective discharge capacity are indicated at the top of each graph. Solid lines differ by 10 Ah/L and dashed lines by 1 Ah/L.

4. Discussion

The model resulting from the fitting process presented in Section 3.1 shows good agreement with the measured cell capacities. Therefore, it is shown that the parameterised model is capable of reproducing and predicting the structuring experiments to a satisfying degree. This allows for the virtual analysis and optimisation of electrode structuring as presented in this work.

The impact of laser-structuring either one or both electrodes, as presented in Section 3.2, shows that the initial electrode load balancing is a major factor in the difference of the individual electrode impacts. For low C-rates, structuring the cathode showed a decrease of capacity directly proportional to the degree of ablation of the active material. This is explained by its limiting role in the initial electrode balancing. For the anode, this decrease in discharge capacity was only observed when the loss of material outweighed its oversize due to the balancing. Here, the neglect of fresh SEI growth in the presented model possibly forms a model limitation that has to be considered when interpreting these results. Nevertheless, for higher C-rates, a trend emerged that favoured the anode for structuring. This can be explained by the distinction in the electrochemical differences of the electrodes, the anisotropic properties of the anode due to its flake-like-shaped particles, and the higher electrode thickness in comparison to the cathode [29].

In general, the structuring benefits increased for higher C-rates. For these, higher lithium-ion concentration gradients built up, leading to worse transport properties due to the decreased conductivity of very low and very high concentrations. The additional pathways for lithium-ion transportation due to the laser ablation reduced the resulting gradients within the electrolyte.

The definition of an optimal structuring is non-trivial and must be aligned with the final cell application and correlated performance indicators.

The simulations showed similar potential performance improvement for all three structuring methods, as can be seen in Figure 5, which would indicate that the choice of the method can be driven by other parameters, i.e., production cost and ease of application. However, the line patterns have the additional benefit of providing capillary structures, which boost the electrolyte wetting performance.

The two-dimensional parameter variation, where both electrodes are structured, emphasises the higher impact of structuring the anode as compared to the cathode.

In Figure 5, it can be seen that the cathode should be structured for high current applications, e.g., high power tools. At the top of each plot, the optimal material loss for the cathode and anode and the corresponding discharge capacity are shown. Besides, from the experimental data, we can conclude that the structuring of cathodes is also beneficial to reduce cell polarisation when high mass loading is applied [10,30].

The variation of the loading and its volumetric discharge performance for the structured anodes are presented in Figure 10. First of all, for C-rates up to 1 C, it can be beneficial to increase the cell loading of around 4 mAh/cm². For the low C/10 discharge, the best performance is shown by the cell loading of a factor of 3. For 1 C, a load increase of a factor of 1.5 would still be beneficial. For higher C-rates, the increased local current densities neutralise these beneficial effects, where the 3 C discharge capacity would be highest for the lower cell loading of a factor of 0.5.

For high C-rates and thick film electrodes, an interesting effect occurred. The best values, as can be seen in the lower right plots of Figure 10, were achieved with no structuring here. This indicates that the beneficial effects of the structuring are additionally counteracted by other effects, namely the loss of the macroscopic interface of the cathode to the separator. This surface forms the initial reaction front for the intercalation and deintercalation of lithium. Due to the high local current densities for those high loaded cells, the reaction front cannot really go much deeper without reaching the cutoff voltage, and so, any loss in the electrode to separator interfaces directly decreases the possible discharge capacity. Therefore, the unstructured cell, where the surface is still intact, performed better than the structured versions. We remark here that the discharge capacities were very low anyway due to these effects. Overall, the implemented active materials, their natural limitations, and general characteristics should be taken into account and considered.

5. Conclusions

An electrochemical multi-scale model, capable of simulating electrode structuring effects, was presented. It was fit to four different cell configurations that were acquired by four different structuring scenarios, all based on the same initial cell setup. The resulting parameterised model was then used to virtually optimise the cell structuring parameters degree of ablation of the active material, the structural pitch distance, and the electrode thickness based on the discharge capacities for different C-rates as a performance measure.

The quality of the parameterised model showed that the approach is fully capable of mapping electrode structuring to its impact on cell performance.

The virtual optimisation of the cells showed that all three discussed methods have roughly the same capability, but might differ in cost or production considerations, which were not discussed here and which would go beyond the scope of this work. For more details, refer to [31].

The presented model could be further extended in terms of mechanical aspects to also predict the instabilities that arise at small laser pitches. Furthermore, a full simulation of the SEI formation would allow the prediction of the long-term effects of the structuring.

6. Tables with Captions

The summarised model equations are presented in Table 1 and the respective parameters are presented in Table 2. The source of each parameter or the formula used to calculate the parameter from other parameters is indicated in the table.

Table 1. Summary of model equations.

Electrolyte transport in homogenised electrodes:

$$\varepsilon \frac{\partial c_\ell}{\partial t} - \nabla \cdot \left(\frac{RTt_+}{F^2} \frac{\kappa\varepsilon}{\tau c_\ell} \nabla c_\ell + \frac{t_+\kappa\varepsilon}{F\tau} \nabla \phi_\ell \right) = A_i j_{BV}, \quad \text{in } \Omega_c \cup \Omega_a \quad (5)$$

$$-\nabla \cdot \left(\frac{RTt_+}{F} (2t_+ - 1) \frac{\kappa\varepsilon}{\tau c_\ell} \nabla c_\ell + \frac{\kappa\varepsilon}{\tau} \nabla \phi_\ell \right) = FA_i j_{BV}, \quad \text{in } \Omega_c \cup \Omega_a \quad (6)$$

Electrolyte transport in separator and structured areas:

$$\varepsilon \frac{\partial c_\ell}{\partial t} - \nabla \cdot \left(\frac{RTt_+}{F^2} \frac{\kappa\varepsilon}{\tau c_\ell} \nabla c_\ell + \frac{t_+\kappa\varepsilon}{F\tau} \nabla \phi_\ell \right) = 0, \quad \text{in } \Omega_s \cup \Omega_\ell, \quad (7)$$

$$-\nabla \cdot \left(\frac{RTt_+}{F} (2t_+ - 1) \frac{\kappa\varepsilon}{\tau c_\ell} \nabla c_\ell + \frac{\kappa\varepsilon}{\tau} \nabla \phi_\ell \right) = 0, \quad \text{in } \Omega_s \cup \Omega_\ell, \quad (8)$$

Active material lithium diffusion:

$$\frac{\partial c_s}{\partial t} - \frac{1}{r^2} \nabla \cdot (r^2 D_s) \nabla c_s = 0 \quad \text{in } \Omega_{sx} \text{ for } x \in \{c, a\}, \quad (9)$$

Lithium intercalation boundary condition:

$$-D_s \nabla c_s \cdot \vec{n} = j_{BV}, \quad \text{on } \Gamma_{sx} \text{ for } x \in \{c, a\}, \quad (10)$$

Charge conservation conditions when the current I_{cell} is prescribed:

$$\int_{\Omega_c} FA_i j_{BV} = I_{cell}, \quad \int_{\Omega_a} FA_i j_{BV} = -I_{cell} \quad (11)$$

Charge conservation conditions when the voltage U_{cell} is prescribed:

$$\phi_c - \phi_a = U_{cell}, \quad \int_{\Omega_c} FA_i j_{BV} = - \int_{\Omega_a} FA_i j_{BV} \quad (12)$$

Butler–Volmer reaction kinetics at the particle interface:

$$j_{BV} = i_0 \left(\frac{c_\ell}{c_{\ell 0}} \exp\left(\frac{\alpha F}{RT} \eta\right) - \exp\left(\frac{-(1-\alpha)F}{RT} \eta\right) \right) \quad (13)$$

$$i_0 = k_{BV} \exp\left(\frac{F}{RT} \left((\xi - \alpha) U_{OCP} - \int_0^\xi U_{OCP}(x) dx \right)\right). \quad (14)$$

$$\eta = \phi_s - \phi_\ell - U_{OCP}, \quad (15)$$

$$\xi = c_x / c_{x,max} \quad (16)$$

Open circuit potential expressed by the Redlich–Kister expansion:

$$U_{OCP}(\xi) = F\hat{U}_0 + \frac{RT}{F} \ln\left(\frac{1-\xi}{\xi}\right) + \frac{RT}{F} \sum_{k=0}^1 0\hat{A}_k \cdot \left((2\xi - 1)^{k+1} - \frac{2\xi^k(1-\xi)}{(2\xi - 1)^{1-k}} \right) \quad (17)$$

Table 2. Summary of the model parameter values or formulas and an indication of their respective source.

Parameter	Value			Unit	
	Anode	Separator	Cathode		
A_i	inner surface area	$3 \cdot \varepsilon / R_p$	$3 \cdot \varepsilon / R_p$	m^2/m^3	
c_{max}	maximal concentration	50.055×10^3	31.36×10^3	mol/m^3	
D_s	solid diffusivity	3.28×10^{-12}	1.16×10^{-13}	m^2/s	
k_{BV}	reaction rate constant	1.475×10^{-5}	2.634×10^{-4}	$\text{mol}/(\text{m}^2\text{s})$	
l	thickness	115 ⁽²⁾	25 [32]	μm	
l_{cc}	current collector thickness ⁽⁴⁾	12	20	μm	
R_p	particle radius	19 [33]	10 ⁽⁴⁾	μm	
α	transfer coefficient [23]	0.5	0.5	-	
ε	electrode porosity	0.336595 ⁽³⁾	0.39 [32]	0.413318 ⁽³⁾	-
τ	tortuosity (through-plane)	4.008	1.268	1.289	-
	tortuosity (in-plane)	3.682	1.268	1.289	-
Redlich–Kister parameters ⁽¹⁾					
\hat{U}_0		-1.7203	3.9874995	V	
\hat{A}_0		-0.35799×10^6	-6.113×10^4	-	
\hat{A}_1		-0.35008×10^6	5.540×10^3	-	
\hat{A}_2		-0.35247×10^6	4.526×10^3	-	
\hat{A}_3		-0.35692×10^6	1.325×10^3	-	
\hat{A}_4		-0.38633×10^6	-2.740×10^4	-	
\hat{A}_5		-0.35908×10^6	1.894×10^4	-	
\hat{A}_6		-0.28794×10^6	-7.237×10^4	-	
\hat{A}_7		-0.14979×10^6	-3.182×10^4	-	
\hat{A}_8		-0.39912×10^6	8.918×10^4	-	
\hat{A}_9		-0.96172×10^6	8.527×10^3	-	
\hat{A}_{10}		-0.63262×10^6	8.527×10^3	-	
Domain independent:					
κ	electrolyte conductivity [23]	$\frac{c_\ell}{4.93 \times 10^8 + 1.27 \times 10^9 e^{(9.85 \times 10^{-4} c_\ell)}} \frac{F^2}{RT}$		S/m	
$c_{\ell 0}$	initial salt concentration ⁽²⁾	1000		mol/m^3	
F	Faraday constant	96,485.33		As/mol	
R	universal gas constant	8.314		J/(kg mol)	
T	absolute temperature	298.15		K	
t_+	transference number [23]	0.33		-	

⁽¹⁾ All Redlich–Kister parameters for the anode come from [34]. All other values are fit. ⁽²⁾ Measured values. ⁽³⁾ Calculated values. ⁽⁴⁾ Estimated values.

Author Contributions: Conceptualization, F.P.; Investigation, L.S.; Methodology, L.S. and F.P.; Project administration, K.F.; Resources, B.E., K.F. and W.P.; Software, F.P.; Visualization, L.S.; Writing—original draft, L.S. and F.P.; Writing—review and editing, B.E., K.F. and W.P. All authors have read and agreed to the published version of the manuscript.

Funding: This project received funding from the Mobility of the Future programme. Mobility of the Future is a research, technology, and innovation funding programme of the Republic of Austria, Federal Ministry for Climate Action, Environment, Energy, Mobility, Innovation and Technology (BMK). The Austrian Research Promotion Agency (FFG) has been authorised for the programme management. The publication was written at Virtual Vehicle Research GmbH in Graz and partially funded within the COMET K2 Competence Centers for Excellent Technologies from the Austrian Federal Ministry for Climate Action (BMK), the Austrian Federal Ministry for Digital and Economic Affairs

(BMDW), the Province of Styria (Dept. 12), and the Styrian Business Promotion Agency (SFG). The Austrian Research Promotion Agency (FFG) has been authorised for the programme management.

Data Availability Statement: Data available on request due to restrictions.

Conflicts of Interest: The authors declare no conflict of interest.

References

- Ryu, H.-H.; Sun, H.H.; Myung, S.-T.; Yoon, C.S.; Sun, Y.-K. Reducing cobalt from lithium-ion batteries for the electric vehicle era. *Energy Environ. Sci.* **2021**, *14*, 844. [CrossRef]
- Kim, J.; Cha, H.M.H.; Lee, H.; Sung, J.; Seo, M.; Park, P.O.M.; Cho, J. A highly stabilized nickel-rich cathode material by nanoscale epitaxy control for high-energy lithium-ion batteries. *Energy Environ. Sci.* **2018**, *11*, 1449. [CrossRef]
- He, S.; Huang, S.; Wang, S.; Mizota, I.; Liu, X.; Hou, X. Considering Critical Factors of Silicon/Graphite Anode Materials for Practical High-Energy Lithium-Ion Battery Applications. *Energy Fuels* **2021**, *35*, 944–964. [CrossRef]
- Eshetu, G.G.; Zhang, H.; Judez, X.; Adenusi, H.; Armand, M.; Passerini, S.; Figgemeier, E. Production of high-energy Li-ion batteries comprising silicon-containing anodes and insertion-type cathodes. *Nat. Commun.* **2021**, *12*, 5459. [CrossRef]
- Kim, H.; Auyeung, R.C.Y.; Piqué, A. Laser-printed thick-film electrodes for solid-state rechargeable Li-ion microbatteries. *J. Power Sources* **2006**, *165*, 413–419. [CrossRef]
- Pfleging, W. A review of laser electrode processing for development and manufacturing of lithium-ion batteries. *Nanophotonics* **2018**, *7*, 549–573. [CrossRef]
- Peng, K.; Jie, J.; Zhang, W.; Lee, S.-T. Silicon nanowires for rechargeable lithiumion battery anodes. *Appl. Phys. Lett.* **2008**, *93*, 033105. [CrossRef]
- Li, X.; Yan, P.; Xiao, X.; Woo, J.H.; Wang, C.; Liua, J.; Zhang, J.-G. Design of porous Si/C–graphite electrodes with long cycle stability and controlled swelling. *Energy Environ. Sci.* **2017**, *10*, 1427–1434.
- Pfleging, W.; Pröll, J. A new approach for rapid electrolyte wetting in tape cast electrodes for lithium-ion batteries. *J. Mater. Chem. A* **2014**, *2*, 14918–14926. [CrossRef]
- Zhu, P.; Seifert, H.J.; Pfleging, W. The Ultrafast Laser Ablation of $\text{Li}(\text{Ni}_{0.6}\text{Mn}_{0.2}\text{Co}_{0.2})\text{O}_2$ Electrodes with High Mass Loading. *Appl. Sci.* **2019**, *9*, 4067. [CrossRef]
- Kriegler, J.; Hille, L.; Stock, S.; Kraft, L.; Hagemester, J.; Habedank, J.B.; Jossen, A.; Zaeh, M.F. Enhanced performance and lifetime of lithium-ion batteries by laser structuring of graphite anodes. *Appl. Energy* **2021**, *303*, 117693. [CrossRef]
- Werner, J.G.; Rodriguez-Calero, G.G.; Abruña, H.D.; Wiesner, U. Block copolymer derived 3-D interpenetrating multifunctional gyroidal nanohybrids for electrical energy storage. *Energy Environ. Sci.* **2018**, *11*, 1261. [CrossRef]
- Trembacki, B.; Duoss, E.; Oxberry, G.; Stadermann, M.; Murthy, J. Mesoscale Electrochemical Performance Simulation of 3D Interpenetrating Lithium-Ion Battery Electrodes. *J. Electrochem. Soc.* **2019**, *166*, A923–A934. [CrossRef]
- Horowitz, Y.; Strauss, E.; Peled, E.; Golodnitsky, D. How to Pack a Punch—Why 3D Batteries are Essential. *Isr. J. Chem.* **2021**, *61*, 38–50. [CrossRef]
- Long, J.W.; Dunn, B.; Rolison, D.R.; White, H.S. Three-Dimensional Battery Architectures. *Chem. Rev.* **2004**, *104*, 10. [CrossRef]
- Chen, K.-H.; Namkoong, M.J.; Goel, V.; Yang, C.; Kazemiabnavi, S.; Mortuza, S.M.; Kazayak, E.; Mazumder, J.; Thornton, K.; Sakamoto, J.; et al. Efficient fast-charging of lithium-ion batteries enabled by laser-patterned three-dimensional graphite anode architectures. *J. Power Sources* **2020**, *471*, 228475. [CrossRef]
- Park, J.; Jeon, C.; Kim, W.; Bong, S.-J.; Jeong, S.; Kim, H.-J. Challenges, laser processing and electrochemical characteristics on application of ultra-thick electrode for high-energy lithium-ion battery. *J. Power Sources* **2020**, *482*, 228948. [CrossRef]
- Kraft, L.; Habedank, J.B.; Frank, A.; Rheinfeld, A.; Jossen, A. Modeling and Simulation of Pore Morphology Modifications using Laser-Structured Graphite Anodes in Lithium-Ion Batteries. *J. Electrochem. Soc.* **2020**, *167*, 013506. [CrossRef]
- Doyle, M.; Fuller, T.F.; Newman, J. Modeling of Galvanostatic Charge and Discharge of the Lithium/Polymer/Insertion Cell. *Electrochem. Soc.* **1993**, *6*, 1526–1533. [CrossRef]
- Habedank, J.B.; Kraft, L.; Rheinfeld, A.; Krezdorn, C.; Jossen, A.; Zaeh, M.F. Increasing the Discharge Rate Capability of Lithium-Ion Cells with Laser-Structured Graphite Anodes: Modeling and Simulation. *J. Electrochem. Soc.* **2018**, *165*, A1563–A1573. [CrossRef]
- DeLauri, V.; Krumbein, L.; Hein, S.; Prifling, B.; Schmidt, V.; Danner, T.; Latz, A. Beneficial Effects of Three-Dimensional Structured Electrodes for the Fast Charging of Lithium-Ion Batteries. *ACS Appl. Energy Mater.* **2021**, *4*, 13847–13859. [CrossRef]
- Magri, M.; Boz, B.; Cabras, L.; Salvadori, A. Quantitative investigation of the influence of electrode morphology in the electrochemo-mechanical response of Li-ion batteries. *Electrochim. Acta* **2022**, *405*, 139778. [CrossRef]
- Pichler, F. Derivation of a Multi-Scale Battery Model and Its High-Performance Computing Implementation. Ph.D. Thesis, University of Graz, Graz, Austria, 2018.
- Pichler, F.; Haase, G. Finite-element method completely implemented for graphic processor units using parallel algorithm libraries. *Int. J. High Perform. Comput. Appl.* **2019**, *33*, 53–66. [CrossRef]
- An, S.J.; Li, J.; Daniel, C.; Mohanty, D.; Nagpure, S.; Wood, D.L., III. The state of understanding of the lithium-ion-battery graphite solid electrolyte interphase (SEI) and its relationship to formation cycling. *Carbon* **2016**, *105*, 52–76. [CrossRef]

26. Ng, S.H.; Vix-Guterl, C.; Bernardo, P.; Tran, N.; Ufheil, J.; Buqa, H.; Dentzer, J.; Gadiou, R.; Spahr, M.E.; Goers, D.; et al. Correlations between surface properties of graphite and the first cycle specific charge loss in lithium-ion batteries. *Carbon* **2009**, *47*, 705–712. [CrossRef]
27. SALOME. Available online: <https://www.salome-platform.org/> (accessed on 20 April 2022).
28. Park, J.; Hyeon, S.; Jeong, S.; Kim, H.-J. Performance enhancement of Li-ion battery by laser structuring of thick electrode with low porosity. *J. Ind. Eng. Chem.* **2019**, *70*, 178–185. [CrossRef]
29. Ebner, M.; Chung, D.-W.; Garca, R.E.; Wood, V. Tortuosity Anisotropy in Lithium-Ion Battery Electrodes Studied by Synchrotron X-ray Tomography. *Adv. Energy Mater.* **2013**, *425*, 1–6. [CrossRef]
30. Song, Z.; Zhu, P.; Pfleging, W.; Sun, J. Electrochemical Performance of Thick-film Li(Ni_{0.6}Mn_{0.2}Co_{0.2})O₂ Cathode with Hierarchic Structures and Laser Ablation. *Nanomaterials* **2021**, *11*, 2962. [CrossRef]
31. Pfleging, W. Recent progress in laser texturing of battery materials: A review of tuning electrochemical performances, related material development, and prospects for large-scale manufacturing. *Int. J. Extrem. Manuf.* **2021**, *3*, 012002. [CrossRef]
32. Finegana, D.P.; Cooper, S.J.; Tjaden, B.; Taiwo, O.O.; Gelb, J.; Hinds, G.; Bretta, D.J.L.; Shearing, P.R. Characterising the structural properties of polymer separators for lithium-ion batteries in 3D using phase contrast X-ray microscopy. *J. Power Sources* **2016**, *333*, 184–192. [CrossRef]
33. Linsemann, F.; Trunk, M.; Rapp, P.; Werner, L.; Gernhäuser, R.; Gilles, R.; Märkisch, B.; Révay, Z.; Gasteiger, H.A. A Liquid Electrolyte-Based Lithium-Ion Battery Cell Design for Operando Neutron Depth Profiling. *J. Electrochem. Soc.* **2020**, *167*, 100554. [CrossRef]
34. Karthikeyan, D.K.; Sikha, G.; White, R.E. Thermodynamic model development for lithium intercalation electrodes. *J. Power Sources* **2008**, *185*, 1398–1407. [CrossRef]



Article

The Effect of Silicon Grade and Electrode Architecture on the Performance of Advanced Anodes for Next Generation Lithium-Ion Cells

Alexandra Meyer *, Fabian Ball and Wilhelm Pfleging

Institute for Applied Materials-Applied Materials Physics (IAM-AWP), Karlsruhe Institute of Technology (KIT), Hermann-von-Helmholtz-Platz 1, 76344 Eggenstein-Leopoldshafen, Germany; Fabian.ball2@kit.edu (F.B.); Wilhelm.pfleging@kit.edu (W.P.)

* Correspondence: Alexandra.meyer@kit.edu

Abstract: To increase the specific capacity of anodes for lithium-ion cells, advanced active materials, such as silicon, can be utilized. Silicon has an order of magnitude higher specific capacity compared to the state-of-the-art anode material graphite; therefore, it is a promising candidate to achieve this target. In this study, different types of silicon nanopowders were introduced as active material for the manufacturing of composite silicon/graphite electrodes. The materials were selected from different suppliers providing different grades of purity and different grain sizes. The slurry preparation, including binder, additives, and active material, was established using a ball milling device and coating was performed via tape casting on a thin copper current collector foil. Composite electrodes with an areal capacity of approximately 1.70 mAh/cm² were deposited. Reference electrodes without silicon were prepared in the same manner, and they showed slightly lower areal capacities. High repetition rate, ultrafast laser ablation was applied to these high-power electrodes in order to introduce line structures with a periodicity of 200 μm. The electrochemical performance of the anodes was evaluated as rate capability and operational lifetime measurements including pouch cells with NMC 622 as counter electrodes. For the silicon/graphite composite electrodes with the best performance, up to 200 full cycles at a C-rate of 1C were achieved until end of life was reached at 80% relative capacity. Additionally, electrochemical impedance spectroscopies were conducted as a function of state of health to correlate the used silicon grade with solid electrolyte interface (SEI) formation and charge transfer resistance values.

Keywords: lithium-ion battery; electrode development; silicon anode; laser patterning; electrochemical impedance spectroscopy; galvanostatic characterization

1. Introduction

Due to the advancing electrification in mobility (xEV), for example in hybrid or electric cars (plug-in hybrid electric vehicle (PHEV), battery electric vehicle (BEV)) as well as e-bikes and e-scooters, it is necessary to reduce production costs and increase the production capacity of cells with high power and energy density. The goals of the European Union define a gravimetric energy density of 350 to 400 Wh/kg or a volumetric energy density of 750 Wh/L, which is to be achieved in cell generation 3b by approximately 2025 [1]. In particular, the increase in the driving range of BEVs and the fast-charging capability are current limiting factors for the successful integration of these vehicles into the automotive market. The cost per kilowatt-hour is also a decisive factor for the further establishment of BEVs.

To increase the power and energy density of Li-ion cells, advanced active materials can be utilized. On the cathode side, a decrease in cobalt content leads to the implementation of nickel-rich materials, such as NMC 622 or NMC 811, where the specific capacity is increased compared to the standard cathode material NMC 111 [2]. The use of novel

anode materials with increased specific capacity, compared to the currently established material graphite with a theoretical specific capacity of 372 mAh/g (equivalent to LiC_6), is of particular interest. In frame of the cell generation 3b concept, silicon (Si) is expected to be added to graphite composite anodes. As an anode material, silicon has a high theoretical capacity of 3579 mAh/g at room temperature (under formation of $\text{Li}_{15}\text{Si}_4$) and a potential against Li/Li^+ of 0.4 V [3]. As silicon undergoes a large volume change of about 280% while cycling, the cycle stability and capacity retention are low [4]. To reduce the strain on the electrode material and therefore suppress the mechanical decomposition to a certain extent, a mixture of graphite and silicon can be utilized, which was already shown to be an effective way to implement silicon in anode materials [5]. When silicon nanoparticles (SiNP) with a diameter of <150 nm are applied, the crack formation, propagation, and eventual crumbling of the Si particles during Li insertion can be suppressed, as shown by Liu et al. [6]. Therefore, the ongoing formation of solid electrolyte interface (SEI) on the freshly exposed surface can be reduced and the consumption of electrolyte can be minimized. Several researchers have also utilized other approaches to incorporate silicon in electrodes by using specialized structures, for example with a yolk-shell structure [7,8], nanowires [9–11], hollow nanoparticles [12,13], or other more sophisticated setups [14] as well as by using different coatings [15]; however, the utilization of these materials and compositions in an industrial scale would be cost-intensive, which is why the use of “simple” nanoparticles is preferred.

Laser generated structures in the Si/graphite material are suitable to implement localized porosities, which reduces the residual stresses of the silicon-containing electrodes due to the volume change during electrochemical cycling and thus suppress the delamination of the electrode from the current collector and the resulting crumbling thereof, as well as ensures good electrolyte wettability [16]. This approach was already utilized by Zheng et al. [5,17,18] for silicon-graphite anodes. Habedank et al. [19,20] structured graphite electrodes with blind holes, which also increased the specific discharge capacity. Smyrek et al. [21,22], Zhu et al. [23], and Song et al. [24] implemented line and grid structures for cathodes with various energy densities.

The present publication aims to emphasize the particular importance of selecting the appropriate starting materials, as well as to shed more light on the degradation mechanisms of silicon particles, to re-emphasize the advantages of laser patterning, and to highlight the next development steps that need to be taken for the successful implementation of silicon/graphite anodes in the commercial field. A comparative study of different types of silicon nanopowders was conducted. For this purpose, a silicon nanopowder content for the composite that is close to the current standard (about 3 wt.%) was chosen, i.e., 5 wt.%. The influence of the silicon on the mechanical integrity of the electrode was expected to remain low at this composition. For the same reason, thin electrodes were manufactured, which are also considered state-of-the-art.

2. Materials and Methods

2.1. Electrode Preparation

Silicon/graphite anodes were prepared via ball milling. Three different grades of commercially available SiNPs were used from three different material suppliers, namely manufacturer 1 (TSi), Nanografi Nanotechnology (NGP, Ankara, Turkey), and SkySpring Nanomaterials (SSN, Houston, TX, USA). The grades of silicon varied in purity and grain size, which will be shown later.

The chemical composition of the Si nanoparticles was measured with inductively coupled plasma optical emission spectroscopy (ICP-OES, iCAP 7600 DUO, Thermo-Fisher Scientific, Waltham, MA, USA), carrier gas hot extraction (CGHE, G8 Galilei, Bruker AXS, Karlsruhe, Germany), and a carbon and sulfur analyzer (CS analyzer, TC600, LECO Instrumente, Mönchengladbach, Germany). The crystallinity was measured with X-ray diffraction (XRD, Empyrean, Malvern Panalytical, Malvern, UK) under an argon atmosphere in a non-ambient chamber (TTK 600, Malvern Panalytical, Malvern, UK) for

diffraction angles 2Θ between 20° and 100° . Scanning electron microscope (SEM, Phenom Pro, Thermo Fischer Scientific, Waltham, MA, USA) images were prepared to characterize the shape and size of the SiNPs and their agglomerates.

The particle size of the coke-based graphite (SPGPT808, Targray, Kirkland, QC, Canada) was measured with laser scattering (LA-950, Horiba Europe, Oberursel, Germany), and the Brunauer–Emmet–Teller (BET) surface area was determined using nitrogen adsorption (Gemini VII 2390, Micromeritics, Norcross, GA, USA). The graphite particles were also examined using a SEM (Phenom Pro, Thermo Fischer Scientific, Waltham, MA, USA) to characterize their shape and size.

The spatial distribution of the graphite, silicon, and conductive carbon black at the surface of the electrode was examined with a scanning electron microscope (SEM, Zeiss Merlin, Carl Zeiss SMT AG, Oberkochen, Germany) and the distribution of the elements was measured with energy dispersive X-ray spectroscopy (EDX).

The compositions of the cathode and anode slurries are summarized in Table 1. For the anodes, a water based 2.5 wt.% sodium carboxymethyl cellulose (CMC, MTI Corporation, Richmond, CA, USA) solution was prepared with a vacuum mixer (MSK-SFM-7, MTI Corporation, Richmond, CA, USA) and subsequently stirred for 24 h with a magnetic stirrer. The graphite, conductive carbon black (CB, C-nergy Super C65, Imerys G&C, Paris, France), silicon nanopowder, and CMC solution were then premixed with a centrifugal mixer (Speedmixer DAC 150 SP, Hauschild, Hamm, Germany). The slurry was mixed with a ball mill (PULVERISETTE 7 premium line, Fritsch, Idar-Oberstein, Germany) to achieve a homogeneous distribution of the silicon nanoparticles. Styrene butadiene rubber solution (SBR, 50% solid content, MTI Corporation, Richmond, CA, USA) was added and slowly stirred into the mixture with a centrifugal mixer. The solid content of the anode slurry was 33.33%. The slurry was tape casted on a copper current collector (9 μm thickness) and dried at room temperature. The doctor blade distance was 150 μm . The anodes were subsequently calendered to reach a porosity (P) of 40%, calculated with the following equation:

$$P = \frac{l - w \left(\sum_n \frac{x_n}{d_n} \right)}{l}$$

Table 1. Composition of the electrode slurries.

Anode Material	Mass Fraction /wt.%	Cathode Material	Mass Fraction /wt.%
Graphite	80	NMC 622	92
Si-NP	5	graphite KS6L	2
C65	5	C65	3
CMC	5	PVDF	3
SBR	5		

With l being the thickness of the electrode, w the weight of the electrode per area, x_n the mass fractions of the materials, and d_n their corresponding densities (2.20 g/cm³ graphite; 2.33 g/cm³ silicon; 1.60 g/cm³ CMC; 1.05 g/cm³ SBR; 1.94 g/cm³ CB; 2.24 g/cm³ KS6L; 1.77 g/cm³ PVDF; and 4.63 g/cm³ NMC 622).

Single crystal NMC 622 (Targray, Kirkland, QC, Canada) cathodes were also prepared. PVDF (Solef 5130, Solvay GmbH, Hannover, Germany) and N-methyl-2-pyrrolidone solvent (NMP, BASF, Ludwigshafen, Germany) were premixed, then the NMC 622, conductive carbon black and conductive graphite were added. Additional NMP was used to adjust the viscosity. The solid content of the slurry was 66.67%. The cathode slurry was mixed in a centrifugal mixer and then tape casted on an aluminum current collector (20 μm thickness) with a doctor blade distance of 85 to 100 μm , depending on the required areal capacity to match the anodes with a cell balancing factor of 1.1 to 1.3. For the calculation of the cell balancing factor, a practical specific capacity of 172 mAh/g was

used for the NMC 622, and 330 mAh/g was denoted for the graphite. In the applied voltage window between 3.0 and 4.2 V, a practical capacity of 2000 mAh/g was used for the silicon [4,25]. The NMC 622 electrodes were dried at 60 °C and subsequently calendered to reach a calculated porosity of 35%.

The dynamic viscosity of the anode slurry and the CMC solution was measured with a parallel plates viscometer (MCR72, Anton Paar, Graz, Austria) at 25 °C and a plate distance of 0.5 mm for shear rates from 1 to 100 s⁻¹.

Laser patterning of the calendered anodes was performed with an ultrafast femtosecond (fs) fiber laser source (Tangerine, Amplitude Systèmes, Pessac, France) with a wavelength of 515 nm in ambient air. A repetition rate of 500 kHz and an average power of 1.5 W was applied to structure the electrodes. The scanning speed was kept constant at 500 mm/s. The process of laser ablation via scanning of the laser beam across the electrode surface was repeated several times until ablation up to the current collector was achieved. To assess the laser parameters and find the applicable number of scans, metallographic samples of the material were prepared and examined with a light microscope (Reicher-Jung MeF3, Leica Microsystems, Wetzlar, Germany). The reference electrodes remained unstructured. The laser structure consisted of a line pattern with a pitch of 200 µm. Electrodes for coin cells (CR2032) and pouch cells were laser cut. For the coin cells, circles with a diameter of 12 mm were cut. The pouch cells had a footprint area of 2492.3 mm².

2.2. Cell Assembly and Electrochemical Analysis

The electrodes for the coin cells were heated to 100 °C under vacuum for 24 h to remove excess moisture. The coin cells were assembled as half cells versus metallic lithium (Merck, Darmstadt, Germany) in an argon-filled glove box (argon 6.0, H₂O < 0.1 ppm; O₂ < 0.1 ppm). A polypropylene (PP) separator sheet (Celgard, Charlotte, NC, USA) with a thickness of 25 µm and a diameter of 19 mm was applied. As electrolyte, 120 µL of LP57 (EC:EMC 3:7, 1.3 M LiPF₆) with 5 wt.% FEC (Gotion, Fremont, CA, USA) was utilized. It was previously shown by [26,27] that the addition of up to 5 wt.% FEC improves the performance of silicon/graphite electrodes. After stacking, the cells were sealed with an electric crimper (MSK-160D, MTI, Richmond, CA, USA) and stored at room temperature for 20 h to allow for a homogeneous wetting of the components with liquid electrolyte. The cells were then galvanostatically characterized using a battery cycler (Arbin Instruments, College Station, TX, USA). The voltage window was adjusted depending on the electrode composition: 0.01 to 1.5 V (anodes without silicon) or 0.06 to 1.2 V (anodes with silicon). The formation followed a constant current-constant voltage protocol. The cells that contained silicon were cycled with a C-rate of C/50 for one cycle, where the cut-off current in the constant voltage phase was set to C/100. After that, three more cycles with C/20 and a cut-off current at CV of C/50 followed. The formation of the other electrodes omitted the first formation cycle. After the formation step, the impedance of the cells was measured by electrochemical impedance spectroscopy (EIS) using a battery cycler (BCS810, Biologic, Seyssinet-Pariset, France) at 0% state of charge (SoC) between 30 Hz and 10 MHz with a voltage amplitude of 10 mV. Ten measurements per decade with logarithmic spacing and three measurements per frequency were carried out. Subsequently, the rate capability of the cells was measured with a constant current-constant voltage (CCCV) measurement protocol, the parameters of which are shown in Table 2. The currents were calculated based on the theoretical capacities of the active materials and the mass of the electrodes. Since the coin cells were cycled in a voltage window of 0.01 to 1.5 V/0.06 to 1.2 V, a practical specific capacity of 330 mAh/g was used for the graphite, and 3560 mAh/g for the silicon [4]. After the rate capability test, the cells were again cycled at C/5 for five cycles to characterize the capacity retention.

Table 2. Parameters of constant current-constant voltage (CCCV) measurements.

C-rate	C/10	C/5	C/2	1C	2C	3C	5C
Limit (CV)	C/20	C/10	C/10	C/10	C/10	C/10	C/10
Repetitions	5	5	10	10	10	10	10

The electrodes that were to be assembled in pouch cells were dried inside the heated airlock of the glove box (M. Braun, Germany, argon 6.0, H₂O < 0.1 ppm; O₂ < 0.1 ppm) at 60 °C under vacuum for 24 h to remove the excess moisture. A polypropylene separator (25 µm thickness, Celgard, USA) with dimensions of 60 × 60 mm² was used. After dry stacking, 3 mL LP57 with 5 wt.% FEC (as above) was added. The electrodes were soaked for 30 min, then the excess electrolyte was removed. After the cells were sealed, they were stored at room temperature for 20 h, until homogeneous wetting with the liquid electrolyte was achieved. They were cycled in a voltage window between 3 and 4.2 V at C/50 (CCCV, CV limit C/100) for one cycle, then degassed. For cells without silicon/graphite composite anodes, C/20 was chosen for the first formation cycle (CV limit C/50). The formation continued with three cycles of C/20 (CCCV, CV limit C/50). After a relaxation time of 24 h at 100% SoC, EIS measurements were performed between 10 Hz and 10 MHz with a voltage amplitude of 10 mV. Ten measurements per decade with logarithmic spacing and three measurements per frequency were carried out, followed by the symmetric rate capability test. The parameters of the rate capability test were identical to the parameters for the half cells, and are shown in Table 2. The cells were cycled in a voltage window between 3 and 4.2 V. After the rate capability test, the cells were again cycled at C/5 for five cycles to characterize the capacity retention. Another EIS measurement was performed at 100% SoC after the rate capability test; then, the long-term test with CCCV measuring protocol at a C-rate of 1C was performed. The C-rate was adjusted depending on the specific discharge capacity (SDC) of the cell at the fifth cycle of the rate capability test at 1C. After a minimum of 100 cycles, the EIS measurement was repeated.

3. Results and Discussion

In the following section, the results will be presented and discussed. First, the characterization of the raw materials and the manufactured electrodes will be shown. The galvanostatic characterization and the measurement of the electrochemical impedance spectra conclude the investigations.

3.1. Graphite Active Material

The size and shape of graphite particles were examined using laser scattering and SEM. The results of the measurements are shown in Figure 1. The graphite particles had a flake-like morphology (Figure 1a). The median particle size (D₅₀) of the graphite was 4.9 µm (D₉₀ = 6.5 µm, D₁₀ = 3.5 µm) and the particle size distribution had a Gaussian shape (Figure 1b). The measured BET surface area was 2.02 m²/g.

3.2. Silicon Nanopowders

The results of the XRD measurements can be found in the Appendix A, see Figure A1. Reflections of the silicon were determined, as well as reflections from the tungsten substrate. The SSN silicon was measured with a different setup, where the tungsten crucible was omitted so that tungsten reflections could not be detected.

The Scherrer equation [28] was applied to determine the crystallite size of the silicon particles as follows:

$$L = \frac{K \cdot \lambda}{\Delta(2\theta) \cdot \cos(\theta_0)}$$

where L is the crystallite size, K is a form factor depending on the Miller indices of the analyzed reflections [29], and λ is the wavelength of the applied XRD source (Cu K α

with 1.5406 Å). The full width half maximum $\Delta(2\theta)$ and Bragg angle θ_0 were extracted from the XRD reflections (111), (022), (131), (040), (133), and (242). Applying the Scherrer equation, crystallite sizes of 17.7 ± 2.1 nm, 18.2 ± 0.9 nm, and 15.0 ± 2.9 nm were derived for TSi, SSN, and NGP silicon powder, respectively.

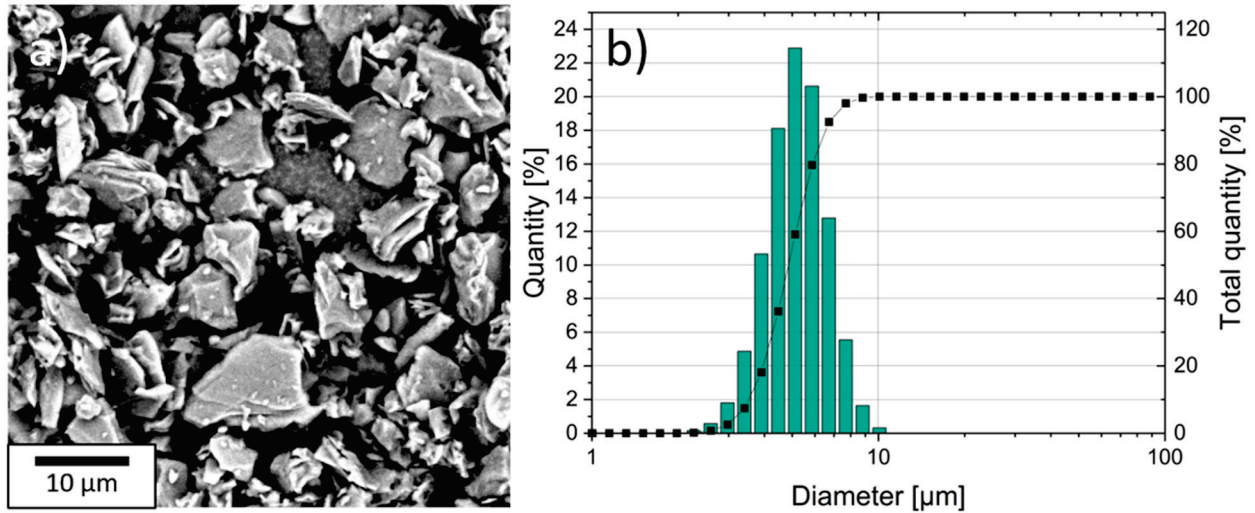


Figure 1. Scanning electrode microscope (SEM) image of the flake-like graphite (a) and particle size distribution (b).

Scanning electron microscopy images of the silicon particles and their agglomerates are shown in Figure A2a–c and Figure 2a–c. The agglomerates of the NGP silicon nanoparticles had a round appearance, while TSi agglomerates were more irregularly shaped and showed cracks. In comparison, SSN agglomerates were smaller and irregularly shaped, with a maximum diameter of approximately 50 μm, while the TSi and NGP silicon both showed agglomerates with a maximum diameter of approximately 200 μm. The SEM images showed large particles of NGP silicon, which can be seen in Figure 2a. The TSi and SSN SiNPs seemed to be in a similar size range, as can be seen in Figure 2b,c. Qualitatively, it was concluded that the particle size illustrated in the SEM images is larger than the crystallinity size evaluated from the XRD measurements. However, the evaluation of particle size with the Scherrer equation has been shown [30] to underestimate the actual size of particles when the particle size is larger than 50 nm, since particles might have more than one crystal boundary and might also show lattice strains, both of which broaden the XRD peaks.

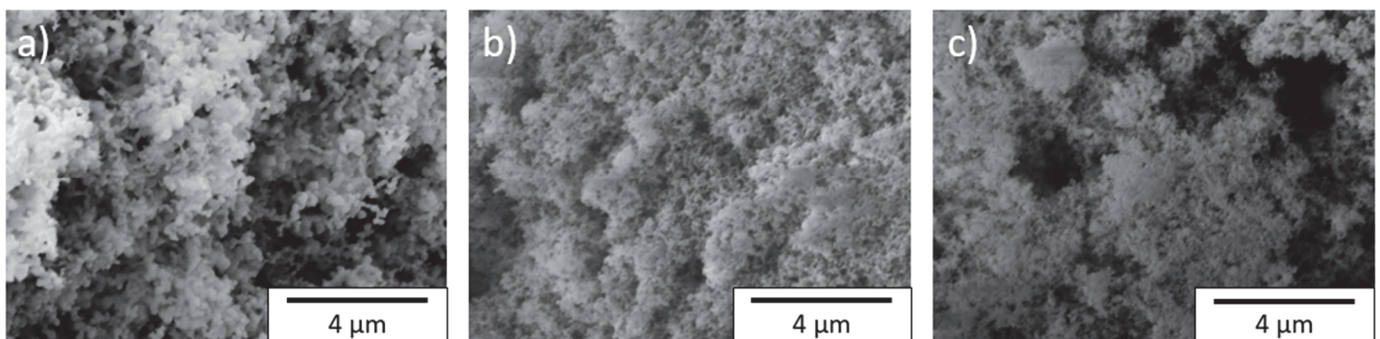


Figure 2. Scanning electrode microscope images of silicon particles at 10,000× magnification: (a) NGP, (b) TSi, and (c) SSN.

The results of the chemical analyses of the silicon nanopowders are shown in Table 3. The SSN silicon powder showed the highest amount of impurities as well as the highest amount of oxygen. Traces of nitrogen, calcium, iron, and copper were also found. The

other silicon nanopowders showed only traces of oxygen and carbon. Some types of impurities could not be assigned, leading to a sum of the mass percentages below 100%.

Table 3. Results of chemical analyses for the silicon nanomaterials used, measured by inductively coupled plasma optical emission spectroscopy (ICP-OES), carrier gas hot extraction (CGHE), and carbon and sulfur (CS) analyzer (LoQ: limit of quantification).

	Unit	NGP		TSi		SSN	
		\bar{x}	\pm	\bar{x}	\pm	\bar{x}	\pm
Si	wt.%	98.2	4.9	98.2	4.9	86.7	4.3
O	wt.%	0.445	0.035	0.866	0.068	11.5	0.9
C	wt.%	0.0037	0.0009	0.0059	0.0030	0.0373	0.0037
N	wt.%	<LoQ	-	<LoQ	-	0.715	0.123
Ca	wt.%	<LoQ	-	<LoQ	-	0.0007	0.0002
Fe	wt.%	<LoQ	-	<LoQ	-	0.0010	0.0002
Cu	wt.%	<LoQ	-	<LoQ	-	0.0029	0.0002
Sum	wt.%	98.65		99.07		98.96	

Measurement uncertainty was calculated based on DIN ISO 11352 with coverage factor $k = 2$.

With the results of the XRD characterization, the SEM imaging, and the chemical characterization, three different grades of silicon nanopowders can be defined. TSi has a high purity and a smaller grain size, SSN has a lower purity and a smaller grain size, and NGP has a higher purity and a larger grain size.

3.3. Characterization of the Manufactured Electrodes

The viscosity of the anode slurries and the CMC solution were measured with a parallel plates viscometer. The results of the measurements are shown in Figure A3 for an application-oriented shear rate range. Since the electrodes were deposited with a velocity of 5 mm/s and a doctor blade gap of 150 μm , the material was sheared with a shear rate of 33.3 s^{-1} , which is marked with a red line in Figure A3. The CMC solution, which is the main ingredient of the slurry and therefore has the highest impact on the viscosity, showed the lowest viscosity of 5.3 Pa s at 34 s^{-1} . The anode slurry without silicon nanopowder showed the highest viscosity of 9.6 Pa s. The slurries with silicon addition showed a viscosity of 6.3 Pa s, 5.7 Pa s, and 5.3 Pa s for TSi, NGP, and SSN, respectively.

After the drying and calendaring of the deposited electrodes, scanning electron microscopy images of the electrodes were prepared (Figure 3). The graphite can be clearly identified and is marked in the figure. Due to the flake-like morphology of the particles, most have aligned horizontally (in parallel to the current collector), which impedes the lithium-ion insertion [31]. The silicon and conductive carbon black are distributed between the graphite and form electronic conductive paths. A small difference in size between the conductive carbon black and the TSi and SSN silicon can be identified by SEM (marked in Figure 3b detail view).

For the NGP silicon electrodes, the distinction between the silicon and the conductive carbon black is much clearer. The silicon is larger than the conductive carbon black and it appears lighter in the SEM image (Figure 3c). The SSN electrodes exhibited particles that appeared as white in the SEM images and therefore were not conductively connected to the rest of the material. They are marked in Figure 3d) and are of unclear origin. The electrodes were chemically characterized to confirm their composition. These analysis results are listed in Table 4. A high total percentage of all present elements was detected. The highest amount of Si was detected in the electrodes with NGP silicon with 5.3 wt.%, and the lowest in electrodes with SSN silicon with 4.5 wt.%.

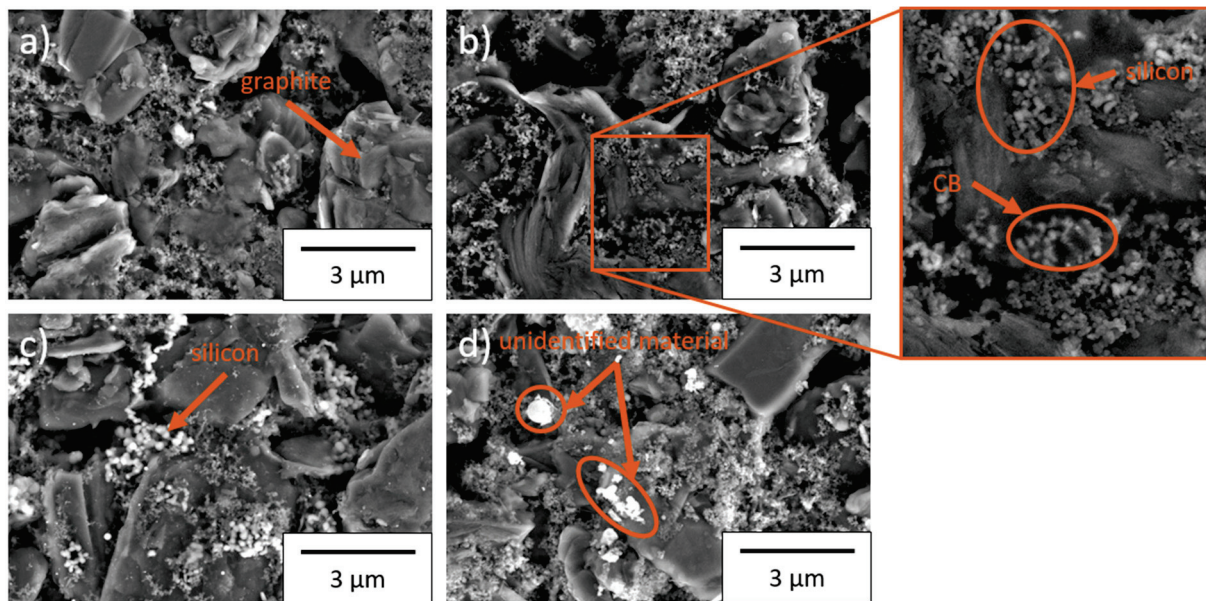


Figure 3. Scanning electron microscope images of the electrode surface at 10,000× magnification: (a) without silicon, (b) TSi, (c) NGP, and (d) SSN.

Table 4. Chemical composition of the manufactured electrodes measured by ICP-OES and CGHE.

	Unit	NGP		SSN		TSi	
		\bar{x}	\pm	\bar{x}	\pm	\bar{x}	\pm
C	wt. %	87.02	7.40	88.38	7.51	87.30	7.42
Si	wt. %	5.29	0.26	4.46	0.22	4.74	0.24
O	wt. %	4.04	0.32	3.55	0.28	5.71	0.45
Na	wt. %	0.46	0.01	0.46	0.01	0.44	0.01
S	wt. %	0.03	0.01	0.03	0.01	0.02	0.01
Sum	wt. %	96.83		96.88		98.21	

Measurement uncertainty was calculated based on DIN ISO 11352 with coverage factor $k = 2$.

The highest oxygen amount of 5.7 wt.% was measured in the electrodes with TSi silicon. The amount of carbon and sodium were very similar in all three types of Si/graphite electrodes, which means that the amount of binder, conductive carbon black, and graphite were almost constant. This leads to the conclusion that the highest amount of silicon oxides is present in the electrodes with TSi silicon. In this case, the ratio of oxygen to silicon was 2.11, while it was 1.34 for NGP electrodes and 1.39 for SSN electrodes. The preceding chemical analysis of the silicon nanopowders showed the highest amount of oxygen for the SSN nanoparticles (see Table 3). A rather constant amount of sulfur could be detected in all three samples. This may result from the synthetic graphite raw material, which is produced from petroleum coke that contains varying amounts of sulfur [32].

EDX measurements of the surface of the electrodes were performed in order to characterize the spatial distribution of the components. The results for the electrodes with TSi silicon are shown in Figure 4, and the others can be found in the Appendix A (Figures A4–A6).

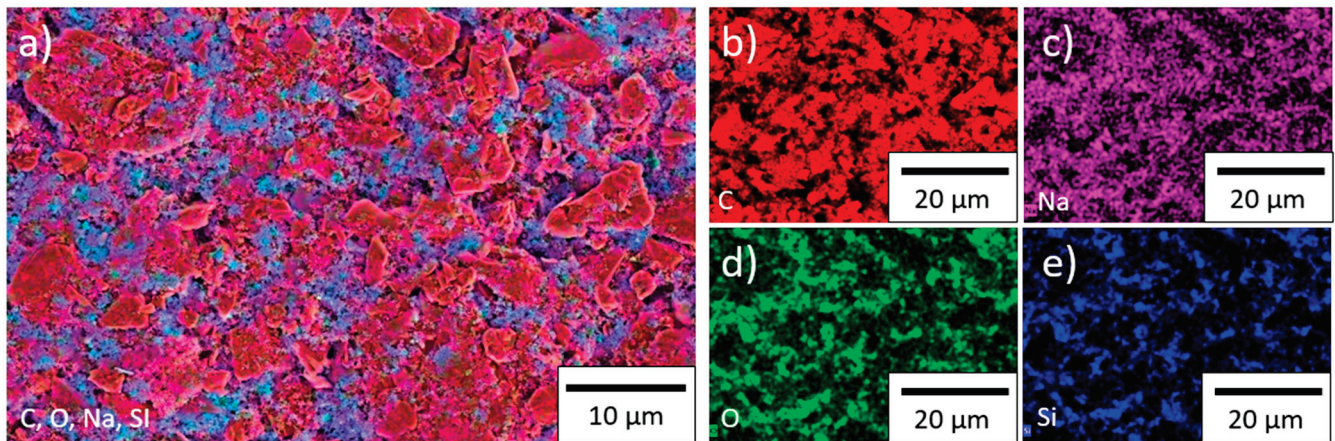


Figure 4. EDX measurements on the surface of a TSi electrode: (a) all detected elements, (b) carbon, (c) sodium, (d) oxygen, and (e) silicon.

The silicon was mostly found in the space between the graphite particles. The binder contains sodium, which was mainly distributed between the graphite particles but could also be found as a layer on top of the graphite. Oxygen was detected between the graphite particles. The distribution of the oxygen and silicon overlapped in most cases, which supports the assumption that silicon and oxygen react during the slurry preparation, as suggested by [32], to form a thin oxide layer of SiO_x ($x \leq 2$) on the silicon nanoparticles; however, it is also in accordance with the previously measured presence of a natural oxide layer that is formed on the silicon raw material before processing (see Table 3). The EDX measurements for the electrode with SSN silicon showed an agglomeration of silicon (Figure A6), which represents a serious film defect that might be responsible for a fast electrochemical degradation during cycling. The other investigated electrodes showed a mostly homogeneous distribution of the elements.

Cross sections of the structured electrodes are shown in Figure 5. The laser patterning process removed the material without damaging the current collector while implementing V-shaped lines. No debris formation on the electrode surface was detected. A line energy of 12 J/m (graphite, TSi, NGP) or 9 J/m (SSN) was applied for ablation. The dimensions of the structures are summarized in Table A1. A maximum aspect ratio of 2 could be achieved. At the top of the electrode, the lines had a mean width of 26.1 μm , while near the current collector they had a width of 11.8 μm .

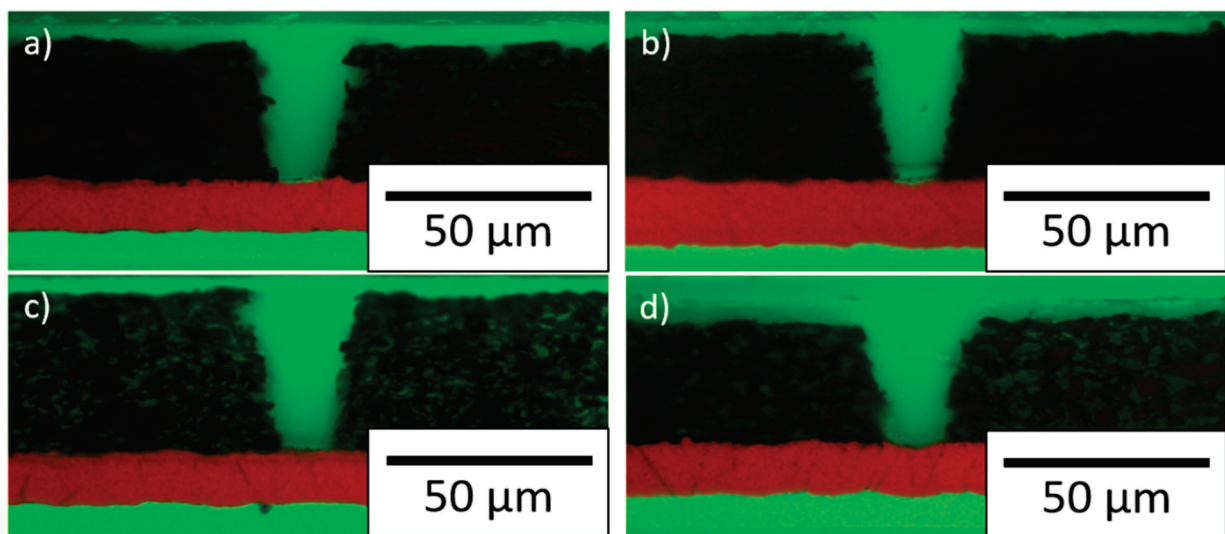


Figure 5. Cross sections of the structured electrodes: (a) graphite without silicon, (b) graphite with TSi, (c) graphite with NGP, and (d) graphite with SSN.

After the drying, calendaring, and patterning of the deposited electrodes, the mean areal capacity was calculated (Table 5). A mass loss was observed due to the laser ablation of the material, which ranged from 6.4 to 14.9 wt.%, depending on the thickness of the electrodes and the shape of the manufactured grooves.

Table 5. Areal capacity and mass loss of the electrodes after manufacturing and subsequent laser structuring.

Electrode	Areal Capacity, Unstructured mAh/cm ²	Areal Capacity, Structured mAh/cm ²	Mass Loss wt. %
Graphite without Si	1.33 ± 0.03	1.15 ± 0.01	13.5
TSi	1.61 ± 0.02	1.37 ± 0.02	14.9
SSN	1.56 ± 0.15	1.46 ± 0.15	6.4
NGP	1.64 ± 0.04	1.40 ± 0.02	14.6

3.4. Galvanostatic Characterization

3.4.1. Rate Capability Tests

The mean specific discharge capacities (SDC) of the half cells for structured and unstructured silicon/graphite and graphite electrodes at C-rates between C/20 and 5C are shown in Figure 6. The mean SDC of all cells with silicon/graphite electrodes was lower than that for the reference cells with graphite electrode at C-rates larger than C/20. The values for the SDCs at C/20 are summarized in Table 6. Cells with unstructured electrodes with SSN silicon showed the highest SDC, while cells with unstructured electrodes with TSi silicon showed the lowest SDC at C/20. Cells with SSN showed the highest SDC during formation compared to the cells with the other types of silicon. For SSN and NGP, the SDC during formation was lower for cells with the structured electrodes, while cells with graphite and TSi showed a higher SDC. The cells with unstructured electrodes with SSN silicon showed a slightly higher mean SDC for C-rates of C/20, C/10, C/2, 1C, and 2C. At 3C and 5C, the SDC of cells with the structured SSN electrodes was 40 to 60 mAh/g higher than that of the unstructured electrode. For cells with the TSi silicon electrodes, the benefit of the laser generated pattern was observed for each C-rate, and at 5C the SDC was increased by 30 mAh/g. Structured electrodes with NGP silicon provided an increased SDC for all C-rates except C/20, compared to the unstructured electrodes. At 5C, the SDC was increased by 80 mAh/g for the structured electrode. It has already been shown in several publications, for example [5,17,19–21,23], that the laser structuring of electrodes increases the SDC. In particular, the increased surface area provides new lithium-ion diffusion pathways, which improves the SDC at elevated C-rates. The reduction of mechanical stresses, particularly for the electrodes containing silicon, is another contributor for increasing SDCs, as was already established by Zheng et al. [18].

Table 6. Specific discharge capacity of the coin cells at formation and capacity retention at C/5 calculated with the first five cycles at C/5 and the last five cycles at C/5.

Electrode	Formation Unstructured /mAh g ⁻¹	Formation Structured /mAh g ⁻¹	Capacity Retention Unstructured /%	Capacity Retention Structured /%
Graphite	368 ± 18	373 ± 20	100	107
SSN	429 ± 27	419 ± 13	116	114
TSi	276 ± 8	306 ± 15	121	112
NGP	381 ± 8	361 ± 51	104	107

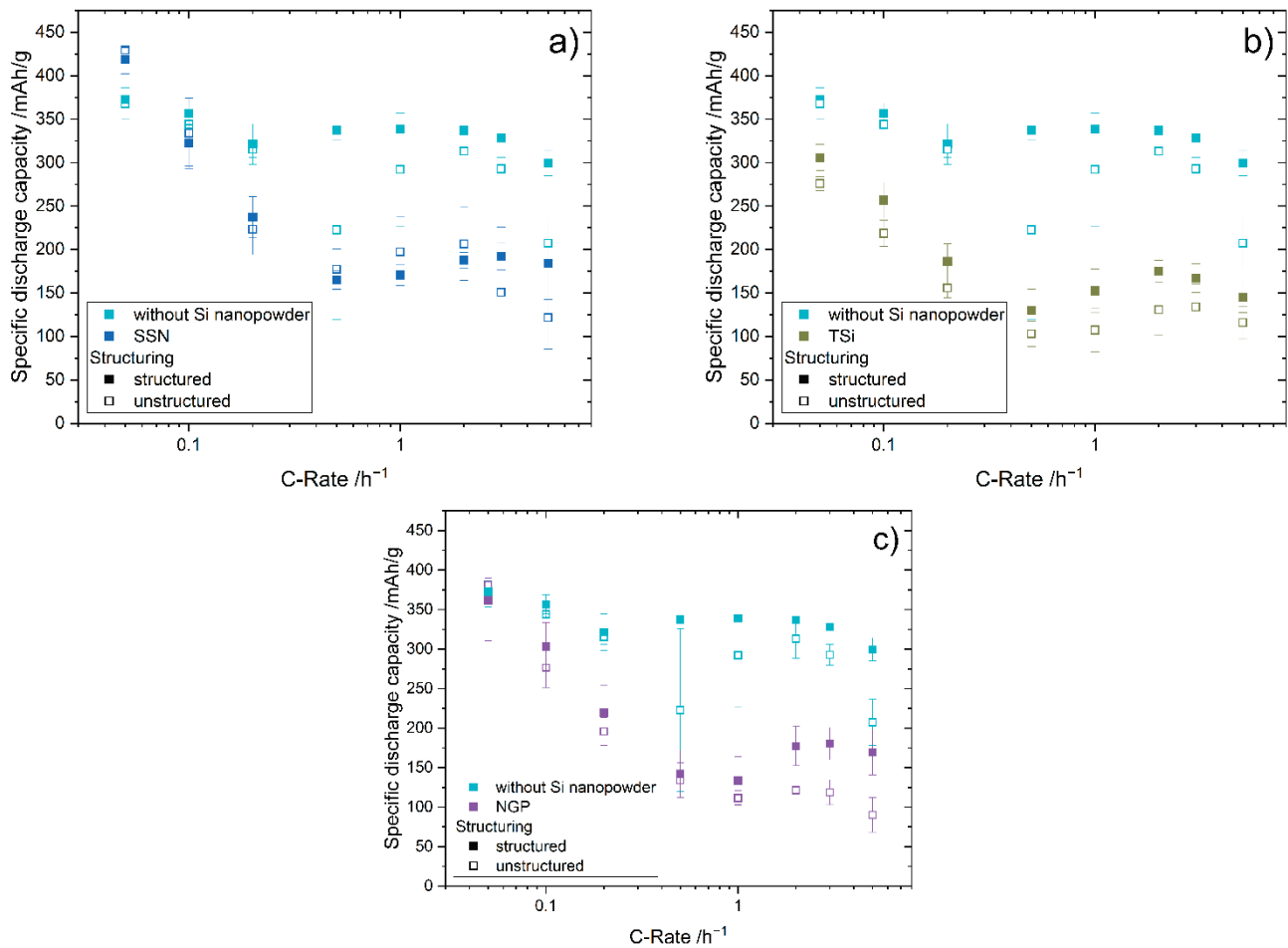


Figure 6. Mean specific discharge capacity of the half-cells depending on the C-rate of the structured and unstructured graphite electrodes without silicon and (a) electrodes with SSN SiNP, (b) electrodes with TSi SiNP, and (c) electrodes with NGP SiNP.

For most electrodes, SDC decreased with increasing C-rates until a minimum was reached at a C-rate of $C/2$ or $1C$, after which the capacity increased again (Figure 6). The second maximum in capacity was reached at $2C$ or $3C$, and at $3C$ or $5C$ the capacity decreased again. This behavior was observed for the unstructured SSN and NGP electrodes and both TSi electrodes, as well as the unstructured graphite electrodes. It was not as apparent for the structured SSN and NGP electrodes, where the capacity drop at $5C$ was not as pronounced as for the other electrodes. The cells with the structured graphite electrodes showed a very stable behavior, and the capacity did not show a strong increase or decrease depending on the C-rate, since they showed a different degradation behavior compared to the silicon/graphite electrodes. Additionally, the laser patterning enabled a high-power operation of these cells. The increase in capacity at higher C-rates might be explainable with an accelerating SEI formation, which binds high amounts of lithium. Hence, the measured capacity is increased, while the actual capacity decreases. At even higher C-rates (e.g., $5C$), the negative impact of electrode degradation intensifies, and the measured capacity decreases again.

Since the standard deviations of the structured electrodes decreased compared to the unstructured electrodes in most cases, a more stable behavior during the rate capability tests was confirmed.

To measure the capacity retention, five additional cycles at a C-rate of $C/5$ were performed after the rate capability test. The results are listed in Table 6, as well as the capacity during the formation steps at $C/20$. The capacity retention increased for the

structured electrodes for graphite and NGP, whereas it decreased slightly for SSN and TSi.

The pouch cells were assembled and the cell balancing factor for each cell is summarized in Table A2. The aspired cell balancing factor of 1.2 was not achieved for all cells, particularly for the pouch cells with structured electrodes without silicon, which had an undersized anode with a cell balancing factor of 1.05. The charge capacities and specific charge capacities of selected pouch cells are shown in Figure 7, and the voltage profiles for the formation step at C/20 are shown in Figure A7.

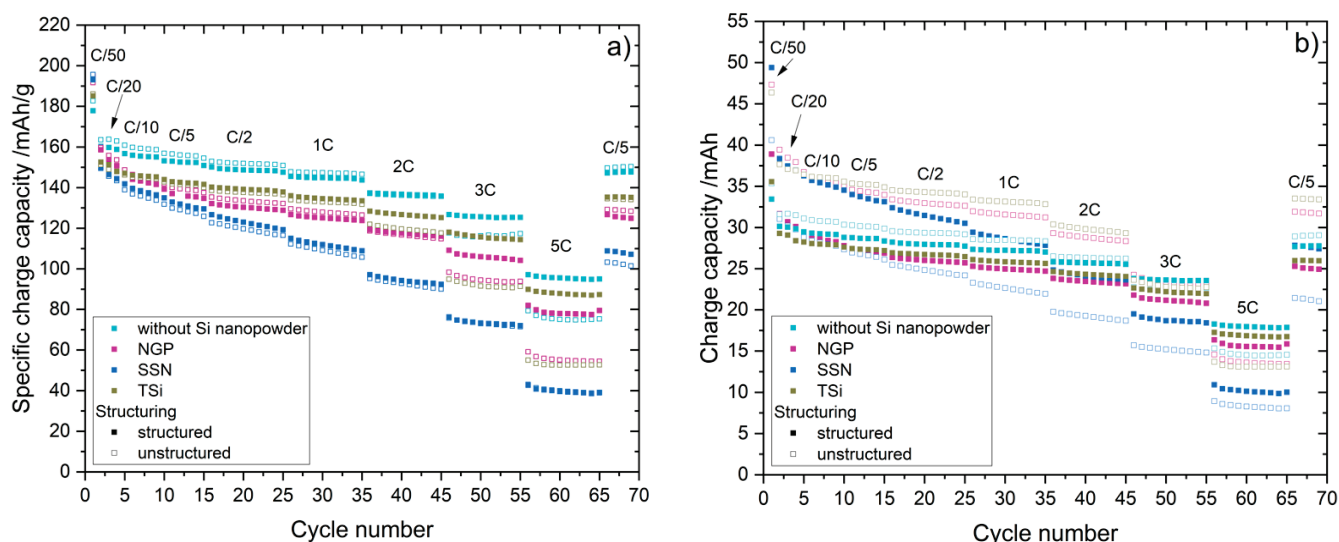


Figure 7. Rate capability tests of the pouch cells with unstructured and structured anodes. (a) Specific charge capacity (charge capacity normalized to the weight of the active material). (b) Charge capacity.

The highest specific capacities during the first formation cycle (C/50) were observed for the SSN electrodes at up to 196 mAh/g. The electrodes without silicon nanoparticles reached the lowest specific capacity of 178 mAh/g at the first formation cycle (C/20). After the first formation cycle, the capacity of all the cells decreased. At the lower C-rates (C/10 to 1C), the cells with unstructured and structured electrodes provided almost the same specific capacity, while at higher C-rates (2C to 5C), the impact of the laser patterning process could be observed, where the cells with structured electrodes had a higher specific capacity compared to those with unstructured ones. The cells with SSN silicon showed the highest drop in capacity with increasing C-rate, and at 5C the specific capacity of the SSN cells only reached approximately 40 mAh/g. The cells with unstructured NGP electrodes had a capacity at 5C ranging from 54 to 60 mAh/g, and the cells with the structured NGP electrodes still reached approximately 80 mAh/g. The cells with unstructured TSi electrodes reached 52 to 55 mAh/g, and the cells with structured TSi electrodes reached 87 to 89 mAh/g. At 5C, the highest specific capacity of 95 to 97 mAh/g was observed for cells with structured graphite electrodes, while the cells with unstructured graphite electrodes reached 75 to 79 mAh/g. The charge capacities of the pouch cells are shown in Figure 7b. The charge capacities of all cells with unstructured electrodes were higher than those with structured electrodes for C-rates up to 2C. At 3C and 5C, the capacity of the cells with structured electrodes was higher. The highest capacity of 49.4 mAh was reached at a C-rate of C/50 for a cell with SSN silicon; however, this cell also showed the highest drop in capacity. At 5C, the cell only had a remaining capacity of 10 mAh. For the pouch cells in general, the higher the capacity at low C-rates (i.e., C/50 and C/20), the lower the capacity at high C-rates (i.e., 3C and 5C). The Coulombic efficiency (CE) of the pouch cells is shown in Figure A8. When the C-rate changed, the CE dropped below 100% for the first cycle at a new C-rate and reached 100% again at the second or third cycle. The

structuring reduced this CE drop. For example, at the first cycle of 5C, the unstructured TSi pouch cell had a CE of 60%, while the structured TSi pouch cell had a CE of 76%.

The capacity retention of the pouch cells is summarized in Table 7. As for the coin cells, the capacity retention increased when the electrode was laser structured. The increase was particularly high for electrodes with NGP silicon nanoparticles with 11.5%.

Table 7. Capacity retention (CR) of the pouch cells with unstructured and structured anodes at C/5, calculated with the first five cycles at C/5 and the last five cycles at C/5.

Material	CR Unstructured/%	CR Structured/%	CR Increase/%
Without Si	86.2	88.8	3.0
NGP	79.9	89.1	11.5
SSN	67.3	72.0	7.0
TSi	84.3	87.6	3.9

3.4.2. Lifetime Tests

The relative capacity of the pouch cells with the best performance with structured and unstructured anodes during the lifetime tests at 1C (charge/discharge) is shown in Figure 8.

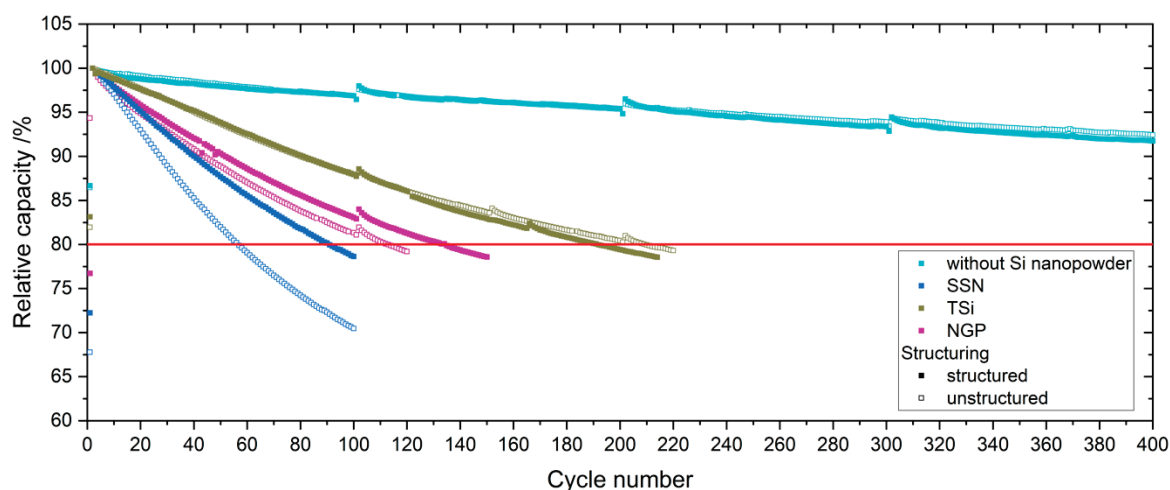


Figure 8. Relative capacity of the pouch cells during lifetime analysis at 1C/1C.

Only the first 400 cycles are shown for the electrodes without silicon. No major differences were observed between the relative capacities of the pouch cells with the structured and unstructured electrodes when only graphite was used as the anode material. When TSi silicon nanopowder was applied, the unstructured cells showed a slightly better performance with a longer lifetime and reached end of life (EoL) at 80% relative capacity after 202 ± 10 cycles, whereas the cells with structured electrodes only reached 182 ± 7 cycles. For NGP and SSN, the structuring of the anodes led to a higher relative capacity of the cells. The cells with unstructured anodes reached EoL after 51 ± 7 cycles and 105 ± 11 cycles for SSN and NGP, respectively. For the cells with structured anodes, the relative capacity dropped under 80% after 77 ± 10 cycles and 131 ± 3 cycles for SSN and NGP, respectively. This meant an increase of lifetime of 50.6% for SSN and 25.1% for NGP, whereas the electrodes with TSi showed a decrease in lifetime of 9.8%. The pouch cells with unstructured and structured reference electrodes did not reach end of life at this point. After 600 full cycles at 1C/1C, the pouch cells with unstructured and structured electrodes showed a relative capacity of 90% and 89%, respectively.

3.5. Electrochemical Impedance Spectroscopy

The impedance of the coin cells was analyzed with electrochemical impedance spectroscopy (EIS) after discharging to 0% SoC (0.06 V for half cells with silicon and 0.01 V for cells with pure graphite) and a relaxation time of 24 h. The pouch cells were analyzed with EIS at 100% SoC, and they were charged to 4.2 V and relaxed for 24 h. All spectra were verified with the Kramers–Kronig relation. The impedance was measured after the formation step, and EIS measurement followed the rate capability test and after EoL was reached for the pouch cells.

3.5.1. EIS on Half Cells

The equivalent circuit used for the interpretation of the EIS data for the coin cells is shown in Figure 9. R_1 accounts for the high frequency resistance of the electric contacts and the ionic pore resistance of the separator. The diffusion is represented by a finite length Warburg element W_1 . Since the measurements did not cover the inductive tail of the spectrum, an inductance was omitted. For the charge transfer processes and the polarization of the SEI, two resistances, R_2 and R_3 , in parallel to constant phase elements (CPE) were chosen. Due to the very porous electrodes that were used in the cells, constant phase elements were chosen instead of capacitors [33].

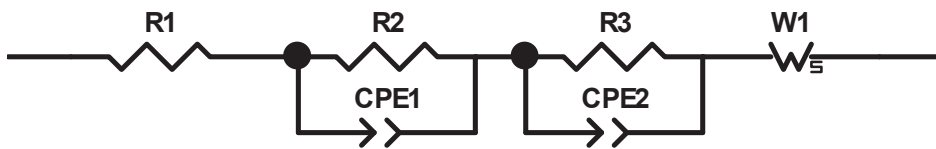


Figure 9. Equivalent circuit for the coin cells with ohmic resistances (R_1 , R_2 , R_3), constant phase elements (CPE1, CPE2), and finite length Warburg element (W_1).

The results of the measurements as well as the corresponding fits can be found in Figure 10a–d, and the resistances are summarized in Table 8. The abscissa (R_1) of the Nyquist plot is reached at an approximate frequency of 400 kHz for all coin cells. Since the same separator and coin cell case as well as the same measuring setup was used to characterize the cells, the ohmic resistance was almost constant for most cells and ranged from 2 Ω to 3 Ω , while the cell with an unstructured SSN electrode is the exception with a resistance R_1 of 5 Ω . The first semicircles of the complex impedance at higher frequencies of the structured and unstructured electrodes showed the same size and curvature. Compared to the coin cells with pure graphite electrodes, all cells with silicon showed a larger semicircle at higher frequencies. This could be assigned to the different SEI composition and thickness. It was shown by Kalaga et al. [34] that the SEI on silicon particles is almost twice as thick as that on graphite particles. This increases the potential drop at the interfaces of electrode–SEI and SEI–electrolyte; therefore, a larger semicircle is observed.

Table 8. Resistances of the coin cells, extracted from Figure 10.

Material	R_1/Ω	R_2/Ω	R_3/Ω
Graphite unstructured	2.500	7.708	113.100
Graphite structured	2.419	9.632	46.980
SSN unstructured	5.000	5.548	20.460
SSN structured	2.124	13.200	21.280
TSi unstructured	3.388	9.985	48.740
TSi structured	3.331	7.046	41.870
NGP unstructured	2.575	20.430	19.880
NGP structured	3.035	12.920	22.700

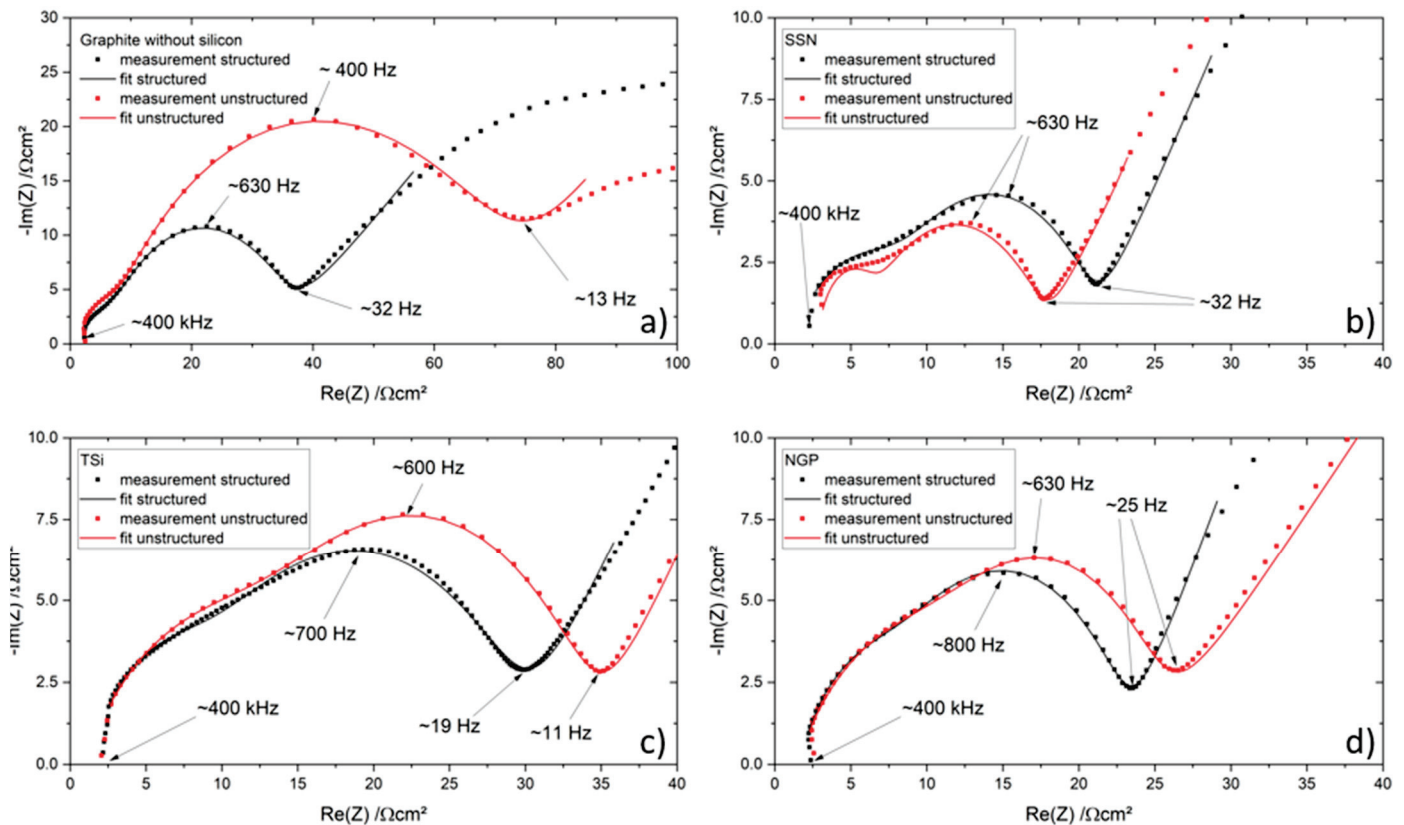


Figure 10. Electrochemical impedance spectra (Nyquist plots) of the coin cells with structured (black) and unstructured (red) electrodes and their corresponding fitting function: (a) pure graphite, (b) SSN, (c) TSi, and (d) NGP.

The second semicircle at lower frequencies (approximately 400 Hz to 800 Hz) of the unstructured electrodes was larger compared to the semicircle of the structured electrode, with the exception of the SSN electrodes (Figure 10b). The frequency at which the maximum imaginary part of the impedance ($\text{Im}(Z)$) of the second semicircle was reached increased when the electrode is structured. Zheng et al. [5] also investigated the impedance of coin cells with structured and unstructured Si/C electrodes and found similar Nyquist plots. There, the smaller second semicircle of the laser structured electrode was assigned to a decreasing charge transfer resistance, due to improved lithium-ion diffusion kinetics and reduced compressive stresses. Habte et al. [35] investigated the effect of graphite electrode tortuosity on the impedance and observed a proportionality between them. Since laser structuring decreases the tortuosity by implementing additional lithium-ion diffusion pathways, the impedance is also reduced. However, the observed behavior of the SSN electrodes cannot be interpreted in the same way as suggested by the mentioned literature. The total capacity of the electrodes may be of importance for the direct comparison of different coin cells and their respective electrochemical impedance spectra. The measured SSN cell with an unstructured electrode had a total capacity of 2.06 mAh, while the SSN cell with a structured electrode had a capacity of 2.31 mAh. For all other setups, the total capacity of the cell with a structured electrode was smaller compared to the capacity of the cell with an unstructured electrode.

3.5.2. EIS on Full Cells

The impedances were measured after the formation step, after the rate capability test, and after EoL was reached, or after 100 cycles at a C-rate of 1C. All spectra satisfied the Kramers–Kronig relation.

An equivalent circuit with three parallel R-CPE elements in series was used to account for the charge transfer processes of the anode and cathode, and the polarization

of the interface between the electrode and the electrolyte due to the SEI [36], which is the most appropriate model for this application [37]. The high frequency resistance of the electric contacts and the ionic pore resistance of the separator was modeled by a resistance, R_1 . Since the maximal applied frequencies were not sufficient to cover the inductive tail of the spectrum, an inductance was omitted. The diffusion of the lithium ions in the bulk material is represented by a finite length Warburg element W_1 , which is incorporated in the third R-CPE element. The equivalent circuit is shown in Figure 11.

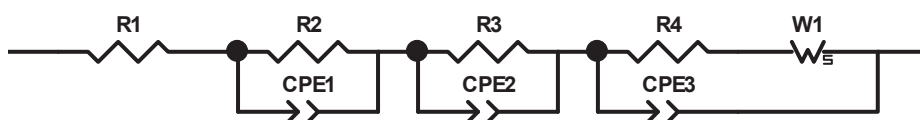


Figure 11. Equivalent circuit for the pouch cells with ohmic resistances (R_1 , R_2 , R_3 , R_4), constant phase elements (CPE1, CPE2, CPE3), and finite length Warburg element (W_1).

The Nyquist plots of the measurements taken after the formation step, as well as the results of the modelling, are shown in Figure 12. The values of the resistances of all measurements are summarized in Table A3. The calculated values for the ohmic resistance R_1 were very similar for all cells, in a range of 0.12Ω to 0.23Ω . When the cell aged, no prominent increase or decrease was observed for R_1 , since the electric contacts of the measurement setup stayed constant. The first semicircle of the pouch cells with the graphite electrodes (unstructured and structured, Figure 12a) did not show a clear separation until the second or third semicircle, which led to a plateau-shaped graph. For the cell with a structured electrode, the first and second semicircles were smaller compared to the cell with an unstructured electrode.

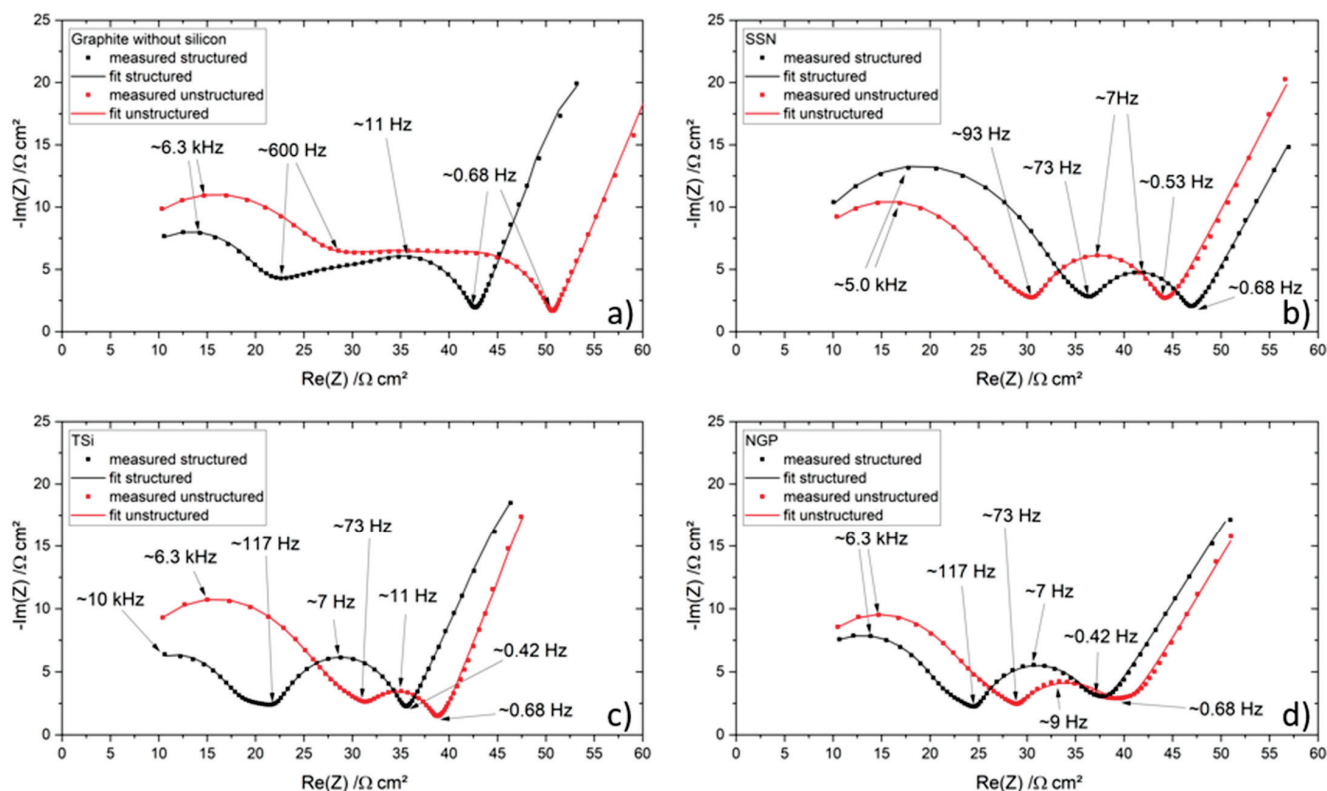


Figure 12. Electrochemical impedance spectra of the pouch cells after the formation step and their respective fit: (a) graphite, (b) SSN, (c) TSi, and (d) NGP anode.

The Nyquist plots of the impedances for the pouch cells with silicon/graphite electrodes showed a more pronounced separation of the first and second semicircle from the third one. Most of the cells with silicon-containing anodes could also be fitted with very good agreement to only two R-CPE elements, which would complicate the interpretation and comparison of the data. In the Nyquist plot, the first semicircle is therefore interpreted as two merged semicircles, when applicable. The pouch cells with TSi and NGP SiNPs behaved in a similar manner regarding the size and relation of the Nyquist plots, while the pouch cells containing SSN behaved inversely (see Figure 12b–d). The transition between the first/second semicircle and the third semicircle occurred for all cells with silicon/graphite anodes in a frequency range of 73 Hz to 117 Hz.

The transition between the mid-frequency range and the low frequency range was identified between 0.42 Hz and 0.68 Hz for all pouch cells. The total resistance of the cells with unstructured graphite, TSi, and NGP silicon was larger compared to the resistance of their structured counterpart, while the SSN pouch cells showed a larger total resistance for the structured pouch cell.

It seems to be evident that the laser structuring of the electrodes led to a diminishment of the two semicircles at higher frequencies (except for the SSN pouch cells), which is mostly associated with the interface between surface films (e.g., SEI) and the liquid electrolyte [38,39]. For the cells containing silicon, with the exception of the SSN pouch cells, the laser patterning process led to a widening of the third semicircle, which is mostly associated with the charge transfer and the double layer capacitance [38–40], while the semicircle at lower frequencies did not change its appearance for the graphite pouch cells regardless of the laser patterning.

After the rate capability test, the pouch cells were again characterized with EIS, and the results are shown in Figure 13. A shift to higher resistances and a widening of the semicircles compared to the results of the EIS measurements after formation due to ongoing degradation processes and hence increasing internal resistance and capacitance of the cell were demonstrated, which was also previously shown in [41,42]. The pouch cells with graphite still showed three separate semicircles, while the first and second semicircle of the unstructured pouch cell were larger, and the third semicircle was just as big as the semicircles of the structured cells (Figure 13a). In total, the resistance of the unstructured pouch cell was larger, as it was also shown after the formation.

For the pouch cells containing silicon (Figure 13b–d), no separation between the first and second or second and third semicircle was observed. For the SSN pouch cell, the total resistance of the unstructured cell was larger compared to the structured cell. For the TSi pouch cells, the resistance of the cell with the structured electrode was bigger. The NGP pouch cells showed a similar behavior to the TSi pouch cells; however, the total resistance of the structured and unstructured cells was comparable.

Figure 14 shows the Nyquist plots of the pouch cells containing silicon after EoL was reached. The pouch cells with a pure graphite anode did not reach EoL in the frame of this study and were therefore excluded. Compared to the Nyquist plots of the measurements taken after the formation step EIS data after the formation and the rate capability test, a shift to larger resistances and an ongoing widening of the semicircles was again observed, as was also reported by [41,42]. The pouch cells with SSN silicon showed a slightly larger first and significantly smaller second semicircle for the structured cell (Figure 14a) while the NGP and TSi pouch cells showed the opposite behavior (Figure 14b,c) as was also observed after the formation (Figure 12c,d) as well as after the rate capability test (Figure 13c,d). The total resistance of the structured TSi pouch cell was increased by about 150% compared to the total resistance of the unstructured cell, while the structured NGP pouch cell showed an increased resistance of 125% compared to the unstructured cell. For the SSN pouch cells, the unstructured cell still showed a higher total resistance than the structured cell. When the impedances of the cells with ongoing ageing are compared, a shift to lower frequencies for the maximum of the two semicircles can be observed, as was

also reported in [41], where it was associated with a decelerating charge transfer process and an increasing cell polarization by the SEI.

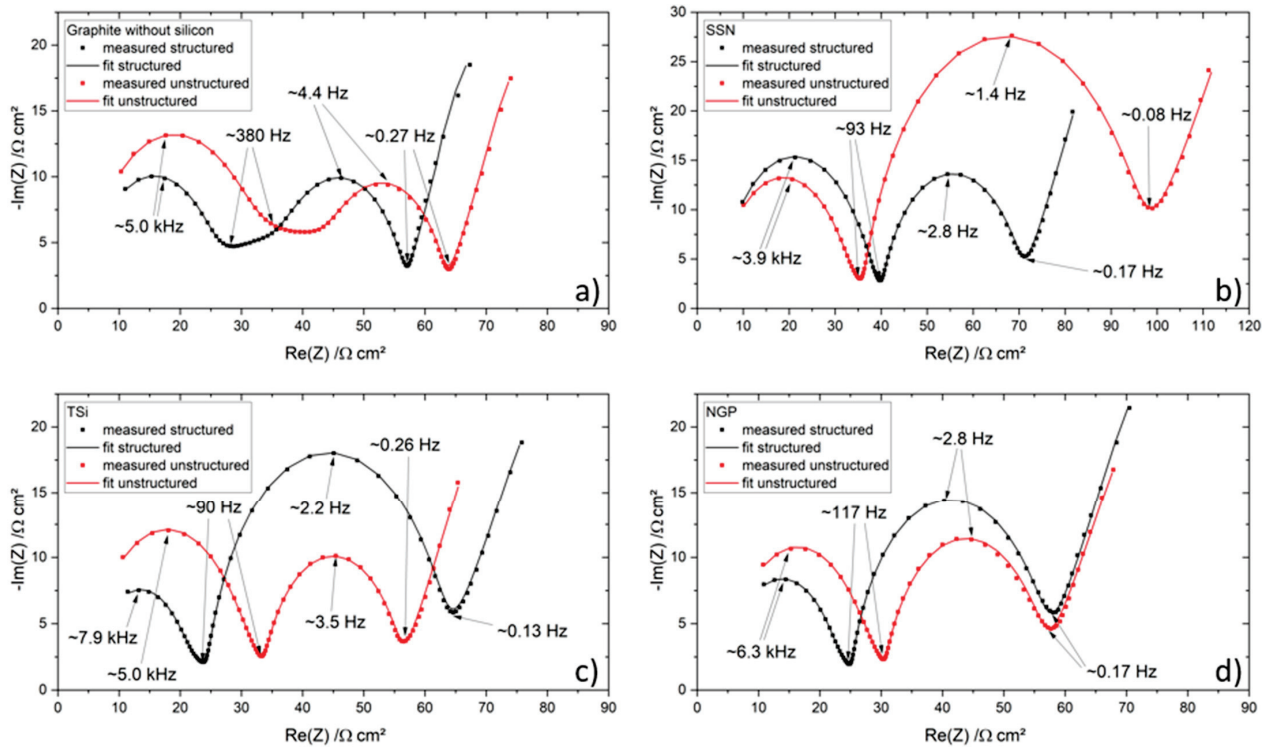


Figure 13. Electrochemical impedance spectra of the pouch cells after the rate capability test and their respective fit: (a) graphite, (b) SSN, (c) TSi, and (d) NGP anode.

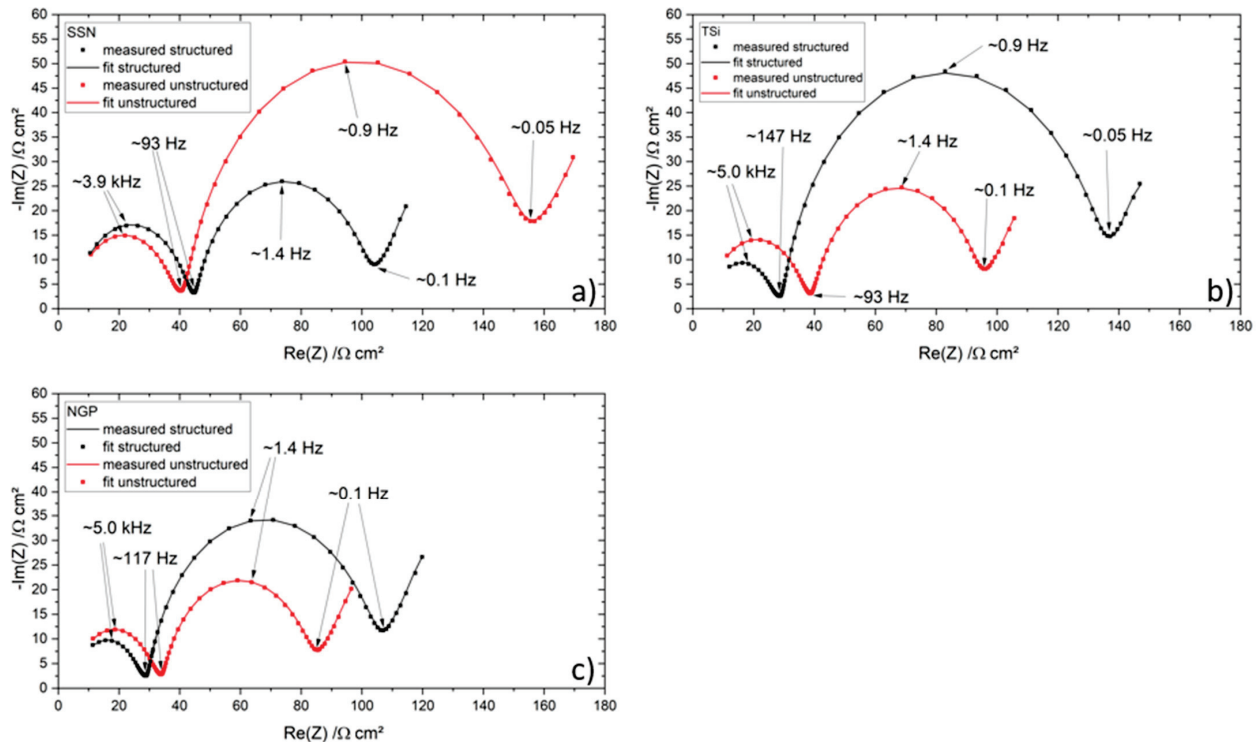


Figure 14. Electrochemical impedance spectra of the pouch cells after EoL and their respective fit: (a) SSN, (b) TSi, and (c) NGP anode.

The noticeable contrary behavior of the SSN pouch cells might be explained by the total capacity. The cell with a structured electrode showed a larger capacity for all C-rates compared to the cell with an unstructured electrode (see Figure 7), while the specific capacities were comparable for both setups. For all other cell compositions, the capacity of the unstructured cell was larger for C-rates up to 3C. A direct inclusion of the capacity values in the impedance is not expedient. Additionally, an overall inhomogeneous distribution of the silicon due to an insufficient breaking of the silicon agglomerates during mixing was observed for the SSN electrodes, and was shown by the EDX measurements (Figure A6) as well as the presence of impurities in the silicon raw material detected by the chemical analysis (see Table 3). The EIS of the SSN pouch cells after EoL was reached was measured after 100 cycles at 1C; however the state of health of the cell with an unstructured electrode was lower than that of the structured cell (Figure 8), which may have impacted the results shown in Figure 14.

In conclusion, the first/second semicircle of the Nyquist plots (except for the SSN pouch cells) was minimized when the electrodes were laser structured. This behavior was observed over the entire lifetime of the cells. The size of the semicircle at lower frequencies was increased when the electrodes were structured (with the exception of the SSN pouch cells). This behavior was more pronounced when silicon was used.

The semicircles at high frequencies are mostly associated with the lithium-ion migration through the SEI [39]. With the laser patterning, a more homogenous development of the SEI was enabled, since the wetting with liquid electrolyte is improved due to the capillary effect. This leads to a reduction of the semicircles at higher frequencies for laser structured electrodes.

The semicircle at lower frequencies is mostly associated with the double layer capacitance, the charge transfer, and the inter-particle electron transfer [38–40]. It was shown for the coin cells that the structured cells showed a reduction of the semicircle at lower frequencies, which could be associated with a decreasing charge transfer resistance due to improved lithium-ion diffusion kinetics and reduced compressive stresses. For the structured pouch cells, the semicircle at lower frequencies was larger. The most significant difference between the pouch cells and the coin cells is the amount of available lithium. In the coin cell, a large surplus of lithium is present. Therefore, the loss of lithium due to the formation of SEI can be compensated. Further studies with full cells where prelithiated anodes or overlithiated cathodes are employed might document this behavior more precisely. The voltage window that is applied may also play a significant role. The reduction of compressive stresses plays a minor role for the thin film electrodes in the pouch cells, since the strict compression by the springs and the rigid components of the coin cell are not present here. The overall increased reactance of the silicon-containing pouch cells may be associated with the increased inter-particle electron transfer [40], since the total amount of particles is increased when a nanomaterial is used.

4. Conclusions and Outlook

Three different SiNPs were used to manufacture silicon/graphite composite electrodes for lithium-ion cells. Additionally, reference cells with graphite were prepared. First, the raw materials were thoroughly characterized. After the tape casting, drying, and calendaring of the electrodes, a high repetition rate, ultrafast-laser source was utilized to implement line structures in the electrode. The chemical composition of the electrode and the spatial distribution of the materials within the electrode were examined. The cells were assembled in coin cells vs. lithium and pouch cells vs. NMC 622 electrodes, and were subsequently galvanostatically characterized to measure their rate capability and lifetime. Additionally, the electrochemical impedance data of selected cells were measured by EIS.

It was confirmed that the laser patterning process can vastly improve the lifetime and the fast charging and discharging capability of silicon/graphite and graphite electrodes

assembled in coin and pouch cells, even when the areal capacity, and therefore thickness, is low and when suboptimal raw materials and compositions are used.

The graphite reference cells showed the most stable electrochemical performance and a higher specific discharge capacity when assembled in coin cells compared to cells with electrodes containing silicon. This is not surprising since the study was carried out with thin film electrodes, which are normally used in high power applications, and excellent performance of graphite electrodes is to be expected. Nevertheless, a low areal capacity was selected in order to identify the most promising silicon nanopowder to be adapted in future silicon/graphite electrodes with high mass loading and optimized electrode architecture.

The three different silicon grades showed an immense range of performances, but electrodes containing TSi showed a stable behavior and high specific discharge capacities during the rate capability test when assembled in coin cells. When silicon/graphite electrodes are assembled in pouch cells, the difference between electrodes with and without silicon dwindle, and the cells with structured electrodes containing TSi SiNP achieve specific discharge capacities at high C-rates almost comparable to the graphite electrodes. During lifetime analysis, the electrodes containing TSi SiNP achieved up to 200 full cycles at a C-rate of 1C until EoL was reached at 80% of initial capacity. Therefore, TSi SiNP is the most promising candidate for further development.

The inherent degradation mechanisms of silicon cannot be overcome by the laser patterning, as was shown with the measurement of the electrochemical impedance spectra. Even directly after the formation, the influence of the different SEI chemistries of graphite and silicon becomes apparent, as the reactance and resistance are increased when silicon is used. With diminishing state of health, the disparity between the graphite and silicon/graphite electrodes increases. The direct comparison of EIS data of different cells with varying capacities and states of health should be treated with caution, as it was proven that the capacity in particular has a yet to be defined impact on the impedance.

The European Union targets for gravimetric and volumetric energy densities [1] could not be met with the materials and methods used; however, future research efforts will continue to pursue this goal. The use of different graphite materials will be revised, since some publications [31,43,44] showed that the use of chamfered graphite particles could increase the capacity of the cells. It was shown with EDX measurements and SEM imaging that the spatial distribution and size of the components play a role in the successful application of electrodes in Li-ion cells; therefore, the slurry preparation will be revised, and the lateral distribution of the components will be characterized with laser induced breakdown spectroscopy. It was also shown [45–48] that the use of different binders (Na-CMC, SBR, PVDF) with different molecular weights and degrees of substitution plays a major role; hence, the amount and type of binder will also be amended. An overlithiation of the cathode or prelithiation of the anode may also increase the capacity of cells with silicon/graphite composite electrodes, which was shown in [49,50], and will also be examined in future studies. It was shown by Berckmans et al. [51] that a pressurization of the cells during cycling may also be favorable. To further understand the mechanisms in the cells, EIS will also be performed at different SoCs.

Author Contributions: Conceptualization, A.M. and W.P.; methodology, A.M. and W.P.; formal analysis, A.M.; investigation, A.M., F.B.; data curation, A.M.; writing—original draft preparation, A.M.; writing—review and editing, A.M. and W.P.; visualization, A.M.; supervision, A.M. and W.P.; project administration, W.P.; funding acquisition, W.P. All authors have read and agreed to the published version of the manuscript.

Funding: This research was funded by the Federal Ministry of Education and Research (BMBF), project NextGen-3DBat, grant no. 03XP0198F. We also acknowledge support from the KIT-Publication Fund of the Karlsruhe Institute of Technology.

Data Availability Statement: Data sharing is not applicable to this article.

Acknowledgments: The authors would like to thank Alexandra Reif and Udo Geckle for the preparation of the SEM images and the EDX measurements, Joel Fels for the XRD measurements, and Thomas Bergfeldt and his team members for the chemical analysis.

Conflicts of Interest: The authors declare no conflict of interest.

Appendix A

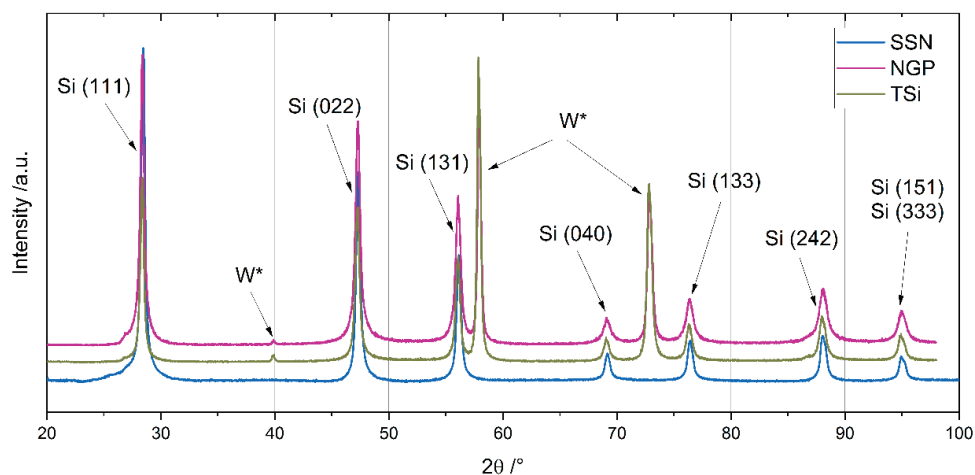


Figure A1. Reflections of the X-rays depending on the angle of incidence during XRD measurements of the Si nanoparticles; an offset was introduced for better visibility.

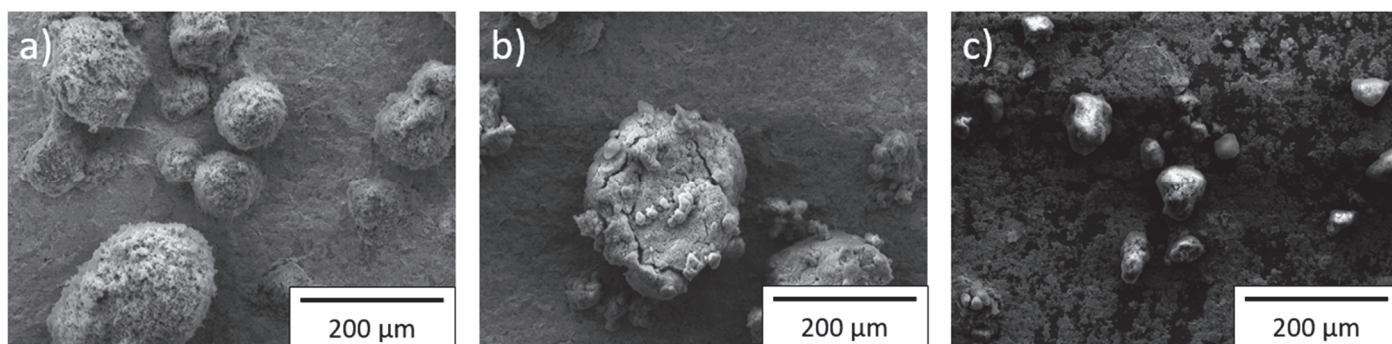


Figure A2. SEM image of the silicon particle agglomerates at 200× magnification for (a) NGP, (b) TSi, and (c) SSN.

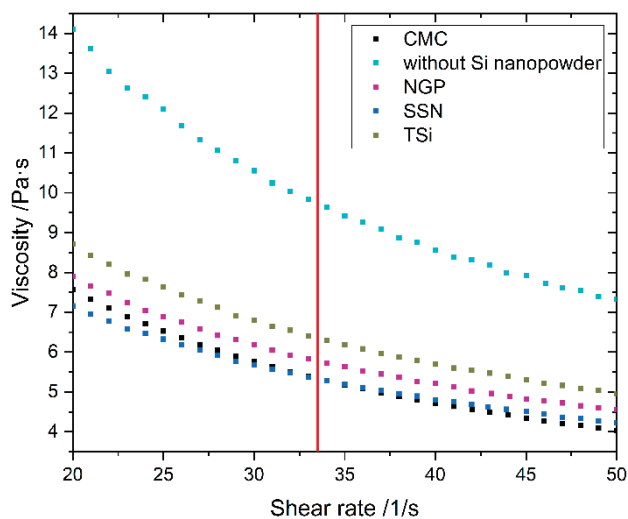


Figure A3. Viscosity of the slurries and the CMC solution for an application-oriented shear-rate range; the used shear-rate of 33.3 1/s is marked with a red line.

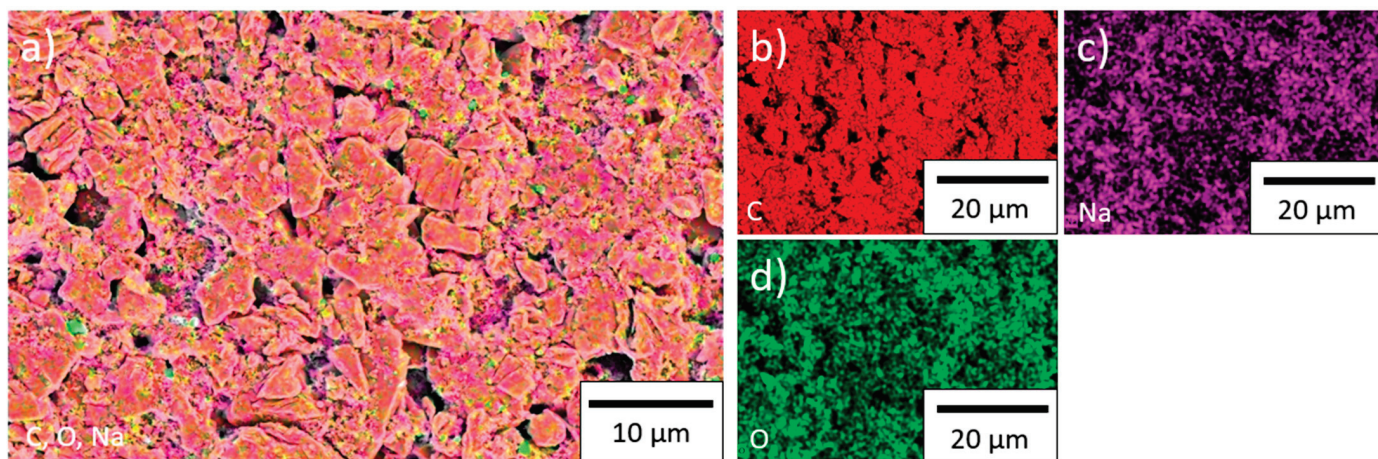


Figure A4. EDX measurements of the graphite electrode: (a) all detected elements, (b) carbon, (c) sodium, and (d) oxygen.

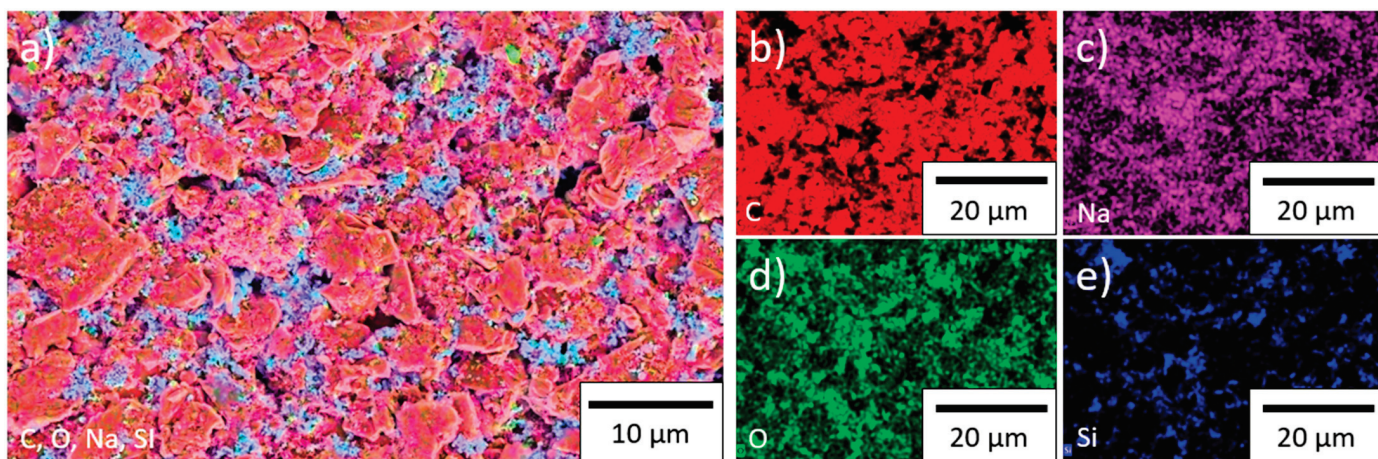


Figure A5. EDX measurements of the NGP electrode: (a) all detected elements, (b) carbon, (c) sodium, (d) oxygen, and (e) silicon.

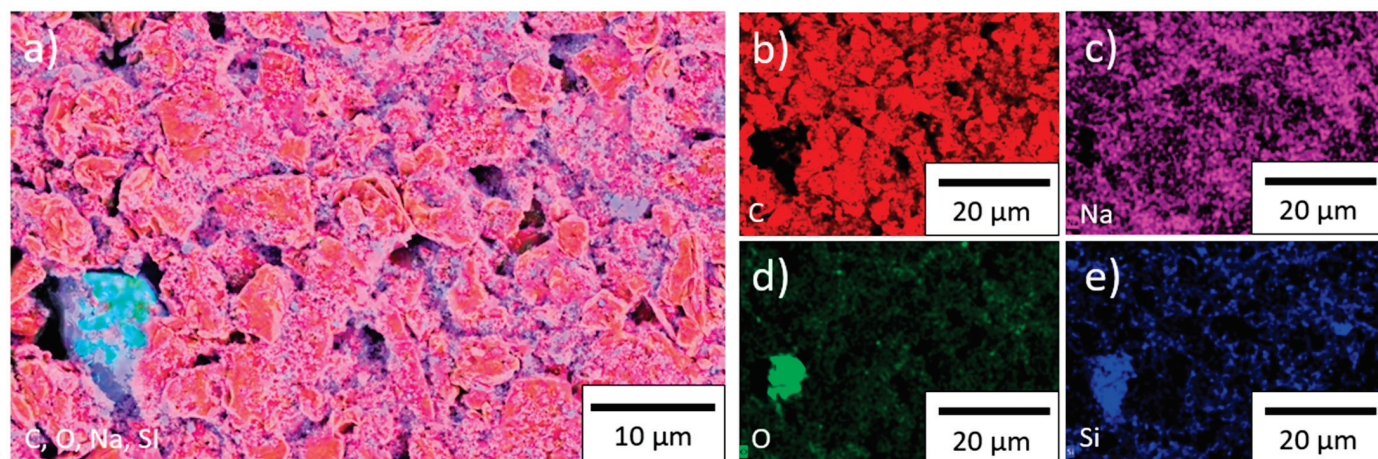


Figure A6. EDX measurements of the SSN electrode: (a) all detected elements, (b) carbon, (c) sodium, (d) oxygen, and (e) silicon.

Table A1. Measurements of the structures that were generated by a laser beam.

Material	Width Top $w_t/\mu\text{m}$	Width Middle $w_m/\mu\text{m}$	Depth $d/\mu\text{m}$	Aspect Ratio d/w_m
Graphite	25.85	19.33	34.40	1.78
SSN	28.14	17.71	30.32	1.71
TSi	22.70	16.51	35.03	2.12
NGP	27.83	18.60	38.804	2.09

Table A2. Cell balancing factor of each pouch cell.

Patterning	Without Silicon			TSi			SSN			NGP		
Unstructured	1.16	1.12	1.20	1.26	1.25	1.11	1.28	1.30	1.27	1.20	1.19	1.12
Structured	1.05	1.05	1.05	1.21	1.22	1.20	1.15	1.21	1.05	1.20	1.18	1.20

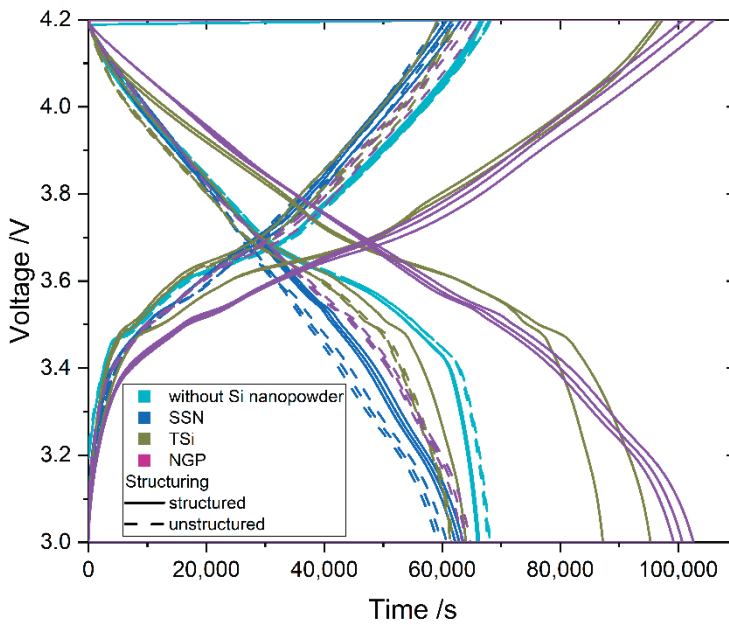


Figure A7. Voltage profiles of the pouch cells during formation at C/20.

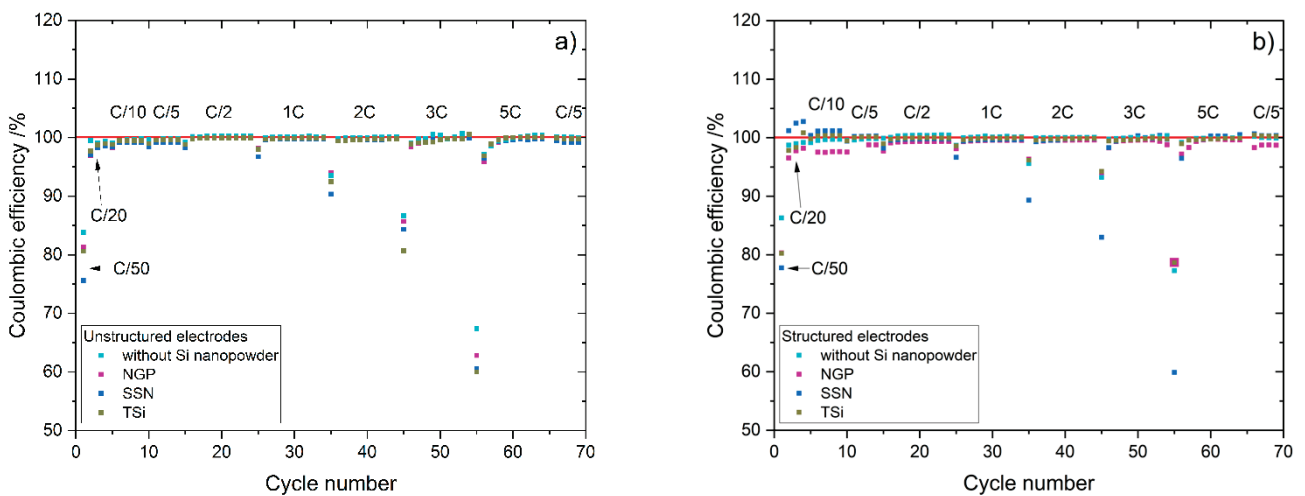


Figure A8. Coulombic efficiency of the pouch cells with (a) unstructured electrodes and (b) structured electrodes.

Table A3. Resistances of the pouch cells after formation and the rate capability test, and at EoL.

	R_1/Ω	R_2/Ω	R_3/Ω	R_4/Ω
Graphite without silicon unstructured				
Post-formation	0.126	0.296	0.886	0.714
Post-RCT	0.163	0.632	0.979	0.763
Graphite without silicon structured				
Post-formation	0.191	0.305	0.587	0.626
Post-RCT	0.189	0.665	0.756	0.661
SSN unstructured				
Post-formation	0.182	0.497	0.808	0.261
Post-RCT	0.180	2.353	0.984	0.301
EoL	0.193	4.320	1.122	0.401
SSN structured				
Post-formation	0.188	0.304	1.008	0.366
Post-RCT	0.206	1.183	1.140	0.271
EoL	0.229	0.279	1.333	2.269
TSi unstructured				
Post-formation	0.192	0.274	0.693	0.397
Post-RCT	0.203	0.865	0.862	0.298
EoL	0.213	2.128	1.067	0.341
TSi structured				
Post-formation	0.214	0.467	0.409	0.312
Post-RCT	0.226	1.510	0.485	0.284
EoL	0.231	4.162	0.590	0.395
NGP unstructured				
Post-formation	0.212	0.450	0.686	0.230
Post-RCT	0.206	1.015	0.822	0.198
EoL	0.217	1.907	0.873	0.312
NGP structured				
Post-formation	0.168	0.479	0.678	0.140
Post-RCT	0.190	1.242	0.697	0.122
EoL	0.218	2.940	0.658	0.327

References

1. European Union. *Batteries. European Battery Cell R&I Workshop*; European Union: Brussels, Belgium, 2018.
2. Zhang, N.; Li, J.; Li, H.; Liu, A.; Huang, Q.; Ma, L.; Li, Y.; Dahn, J.R. Structural, electrochemical, and thermal properties of nickel-rich $\text{LiNi}_x\text{Mn}_y\text{Co}_z\text{O}_2$ materials. *Chem. Mater.* **2018**, *30*, 8852–8860. [CrossRef]
3. Obrovac, M.N.; Krause, L.J. Reversible cycling of crystalline silicon powder. *J. Electrochem. Soc.* **2007**, *154*, A103. [CrossRef]
4. Obrovac, M.N.; Christensen, L. Structural changes in silicon anodes during lithium insertion/Extraction. *Electrochem. Solid-State Lett.* **2004**, *7*, A93–A96. [CrossRef]
5. Zheng, Y.; Seifert, H.; Shi, H.; Zhang, Y.; Kübel, C.; Pflöging, W. 3D silicon/graphite composite electrodes for high-energy lithium-ion batteries. *Electrochim. Acta* **2019**, *317*, 502–508. [CrossRef]
6. Liu, X.H.; Zhong, L.; Huang, S.; Mao, S.X.; Zhu, T.; Huang, J. Size-dependent fracture of silicon nanoparticles during lithiation. *ACS Nano* **2012**, *6*, 1522–1531. [CrossRef] [PubMed]
7. Han, N.; Li, J.; Wang, X.; Zhang, C.; Liu, G.; Li, X.; Qu, J.; Peng, Z.; Zhu, X.; Zhang, L. Flexible carbon nanotubes confined yolk-shelled silicon-based anode with superior conductivity for lithium storage. *Nanomaterials* **2021**, *11*, 699. [CrossRef]
8. Yang, J.; Wang, Y.-X.; Chou, S.; Zhang, R.; Xu, Y.; Fan, J.; Zhang, W.-X.; Liu, H.K.; Zhao, D.; Dou, S.X. Yolk-shell silicon-mesoporous carbon anode with compact solid electrolyte interphase film for superior lithium-ion batteries. *Nano Energy* **2015**, *18*, 133–142. [CrossRef]
9. Chan, C.K.; Peng, H.; Liu, G.; McIlwrath, K.; Zhang, X.F.; Huggins, R.A.; Cui, Y. High-performance lithium battery anodes using silicon nanowires. *Nat. Nanotechnol.* **2008**, *3*, 31–35. [CrossRef] [PubMed]

10. Karuppiah, S.; Keller, C.; Kumar, P.; Jouneau, P.-H.; Aldakov, D.; Ducros, J.-B.; Lapertot, G.; Chenevier, P.; Haon, C. A scalable silicon nanowires-grown-on-graphite composite for high-energy lithium batteries. *ACS Nano* **2020**, *14*, 12006–12015. [CrossRef] [PubMed]
11. Schneier, D.; Harpak, N.; Menkin, S.; Davidi, G.; Goor, M.; Mados, E.; Ardel, G.; Patolsky, F.; Golodnitsky, D.; Peled, E. Analysis of scale-up parameters in 3D silicon-nanowire lithium-battery anodes. *J. Electrochem. Soc.* **2020**, *167*, 050511. [CrossRef]
12. Liuab, X.; Shena, C.; Lua, J.; Liua, G.; Jianga, Y.; Gaoa, Y.; Liab, W.; Zhaoab, B.; Zhangb, J. Graphene bubble film encapsulated Si@C hollow spheres as a durable anode material for lithium storage. *Electrochim. Acta* **2020**, *361*, 137074. [CrossRef]
13. Yao, Y.; McDowell, M.T.; Ryu, I.; Wu, H.; Liu, N.; Hu, L.; Nix, W.D.; Cui, Y. Interconnected silicon hollow nanospheres for lithium-ion battery anodes with long cycle life. *Nano Lett.* **2011**, *11*, 2949–2954. [CrossRef] [PubMed]
14. Chen, D.; Tao, C.; Chen, T.; Liu, X.; Liu, Y.; Xu, G.; Han, G. Pomegranate-like silicon-based anodes self-assembled by hollow-structured Si/void@C nanoparticles for Li-ion batteries with high performances. *Nanotechnology* **2021**, *32*, 095402. [CrossRef]
15. Xu, K.; Liu, X.; Guan, K.; Yu, Y.; Lei, W.; Zhang, S.; Jia, Q.; Zhang, H. Research progress on coating structure of silicon anode materials for lithium-ion batteries. *ChemSusChem* **2021**, *14*, 5135–5160. [CrossRef]
16. Pflöging, W.; Kohler, R.; Pröll, J. Laser generated microstructures in tape cast electrodes for rapid electrolyte wetting: New technical approach for cost efficient battery manufacturing. In *Laser-Based Micro-and Nanoprocessing VIII*; SPIE: Bellingham, WA, USA, 2014; p. 89680B-8. [CrossRef]
17. Zheng, Y.; Smyrek, P.; Rakebrandt, J.-H.; Kübel, C.; Seifert, H.J.; Pflöging, W. Fabrication and characterization of silicon-based 3D electrodes for high-energy lithium-ion batteries. In *Laser-Based Micro-and Nanoprocessing XI*; SPIE: Bellingham, WA, USA, 2017; Volume 10092, p. 100920. [CrossRef]
18. Zheng, Y.; Smyrek, P.; Rakebrandt, J.-H.; Seifert, H.; Pflöging, W.; Kubel, C. Silicon-based 3D electrodes for high power lithium-ion battery. In Proceedings of the 2017 IEEE International Conference on Manipulation, Manufacturing and Measurement on the Nanoscale, Shanghai, China, 7–11 August 2017; pp. 61–64. [CrossRef]
19. Habedank, J.B.; Kriegler, J.; Zaeh, M.F. Enhanced fast charging and reduced lithium-plating by laser-structured anodes for lithium-ion batteries. *J. Electrochem. Soc.* **2019**, *166*, A3940–A3949. [CrossRef]
20. Habedank, J.B.; Endres, J.; Schmitz, P.; Zaeh, M.F.; Huber, H. Femtosecond laser structuring of graphite anodes for improved lithium-ion batteries: Ablation characteristics and process design. *J. Laser Appl.* **2018**, *30*, 032205. [CrossRef]
21. Smyrek, P.; Zheng, Y.; Seifert, H.J.; Pflöging, W. Post-mortem characterization of fs laser-generated micro-pillars in Li(Ni_{1/3}Mn_{1/3}Co_{1/3})O₂ electrodes by laser-induced breakdown spectroscopy. In *Laser-Based Micro- and Nanoprocessing X*; SPIE: Bellingham, WA, USA, 2016; p. 97361C. [CrossRef]
22. Smyrek, P.; Proll, J.; Rakebrandt, J.-H.; Seifert, H.J.; Pflöging, W. Manufacturing of advanced Li(NiMnCo)O₂ electrodes for lithium-ion batteries. In *Laser-Based Micro- and Nanoprocessing IX*; SPIE: Bellingham, WA, USA, 2015; p. 93511D. [CrossRef]
23. Zhu, P.; Seifert, H.J.; Pflöging, W. The ultrafast laser ablation of Li(Ni_{0.6}Mn_{0.2}Co_{0.2})O₂ electrodes with high mass loading. *Appl. Sci.* **2019**, *9*, 4067. [CrossRef]
24. Song, Z.; Zhu, P.; Pflöging, W.; Sun, J. Electrochemical performance of thick-film Li(Ni_{0.6}Mn_{0.2}Co_{0.2})O₂ cathode with hierarchic structures and laser ablation. *Nanomaterials* **2021**, *11*, 2962. [CrossRef] [PubMed]
25. Klett, M.; Gilbert, J.A.; Trask, S.; Polzin, B.J.; Jansen, A.; Dees, D.W.; Abraham, D.P. Electrode behavior RE-visited: Monitoring potential windows, capacity loss, and impedance changes in Li_{1.03}(Ni_{0.5}Co_{0.2}Mn_{0.3})_{0.97}O₂/silicon-graphite full cells. *J. Electrochem. Soc.* **2016**, *163*, A875–A887. [CrossRef]
26. Bordes, A.; Eom, K.; Fuller, T.F. The effect of fluoroethylene carbonate additive content on the formation of the solid-electrolyte interphase and capacity fade of Li-ion full-cell employing nano Si–graphene composite anodes. *J. Power Sources* **2014**, *257*, 163–169. [CrossRef]
27. Young, B.T.; Heskett, D.R.; Nguyen, C.C.; Nie, M.; Woicik, J.C.; Lucht, B.L. Hard X-ray Photoelectron Spectroscopy (HAXPES) Investigation of the Silicon Solid Electrolyte Interphase (SEI) in Lithium-Ion Batteries. *ACS Appl. Mater. Interfaces* **2015**, *36*, 20004–20011. [CrossRef] [PubMed]
28. Scherrer, P. Bestimmung der Größe und der inneren Struktur von Kolloidteilchen mittels Röntgenstrahlen. Nachrichten von der Gesellschaft der Wissenschaften zu Göttingen. *Math. Phys. Kl.* **1918**, *2*, 98–100.
29. Langford, J.I.; Wilson, A.J.C. Scherrer after sixty years: A survey and some new results in the determination of crystallite size. *J. Appl. Crystallograph.* **1978**, *11*, 102–113. [CrossRef]
30. Mourdikoudis, S.; Pallares, R.M.; Thanh, N.T.K. Characterization techniques for nanoparticles: Comparison and complementarity upon studying nanoparticle properties. *Nanoscale* **2018**, *10*, 12871–12934. [CrossRef] [PubMed]
31. Guoping, W.; Bolan, Z.; Min, Y.; Xiaolu, X.; Meizheng, Q.; Zuolong, Y. A modified graphite anode with high initial efficiency and excellent cycle life expectation. *Solid State Ion.* **2005**, *176*, 905–909. [CrossRef]
32. Hays, K.A.; Key, B.; Li, J.; Wood, D.L.; Veith, G.M. Si oxidation and H₂ gassing during aqueous slurry preparation for Li-ion battery anodes. *J. Phys. Chem. C* **2018**, *122*, 9746–9754. [CrossRef]
33. Chen, C.; Liu, J.; Amine, K. Symmetric cell approach and impedance spectroscopy of high power lithium-ion batteries. *J. Power Sources* **2001**, *96*, 321–328. [CrossRef]
34. Kalaga, K.; Shkrob, I.A.; Haasch, R.T.; Peebles, C.; Bareño, J.; Abraham, D.P. Auger electrons as probes for composite micro- and nanostructured materials: Application to solid electrolyte interphases in graphite and silicon-graphite electrodes. *J. Phys. Chem. C* **2017**, *121*, 23333–23346. [CrossRef]

35. Habte, B.T.; Jiang, F. Effect of microstructure morphology on Li-ion battery graphite anode performance: Electrochemical impedance spectroscopy modeling and analysis. *Solid State Ion.* **2018**, *314*, 81–91. [CrossRef]
36. Müller, V. *Investigation of the Influence of Mechanical Pressure on the Aging and the Expansion of Silicon-Containing Lithium-Ion Batteries*. Ph.D. Thesis; Institute of Electrical Energy Systems, University of Bayreuth: Bayreuth, Germany, 2020.
37. Westerhoff, U.; Kurbach, K.; Lienesch, F.; Kurrat, M. Analysis of lithium-ion battery models based on electrochemical impedance spectroscopy. *Energy Technol.* **2016**, *4*, 1620–1630. [CrossRef]
38. An, S.J.; Li, J.; Du, Z.; Daniel, C.; Wood, D. Fast formation cycling for lithium ion batteries. *J. Power Sources* **2017**, *342*, 846–852. [CrossRef]
39. Andre, D.; Meiler, M.; Steiner, K.; Wimmer, C.; Soczka-Guth, T.; Sauer, D.U. Characterization of high-power lithium-ion batteries by electrochemical impedance spectroscopy. I. Experimental investigation. *J. Power Sources* **2011**, *196*, 5334–5341. [CrossRef]
40. Aurbach, D.; Markovsky, B.; Weissman, I.; Levi, E.; Ein-Eli, Y. In the correlation between surface chemistry and performance of negative electrodes for Li ion batteries. *Electrochim. Acta* **1999**, *45*, 67–86. [CrossRef]
41. Heinrich, M.; Wolff, N.; Harting, N.; Laue, V.; Röder, F.; Seitz, S.; Krewer, U. Physico-chemical modeling of a lithium-ion battery: An ageing study with electrochemical impedance spectroscopy. *Batter. Supercaps* **2019**, *2*, 530–540. [CrossRef]
42. Xie, Y.; Li, J.; Yuan, C. Mathematical modeling of the electrochemical impedance spectroscopy in lithium ion battery cycling. *Electrochim. Acta* **2014**, *127*, 266–275. [CrossRef]
43. Asenbauer, J.; Eisenmann, T.; Kuenzel, M.; Kazzazi, A.; Chen, Z.; Bresser, D. The success story of graphite as a lithium-ion anode material—Fundamentals, remaining challenges, and recent developments including silicon (oxide) composites. *Sustain. Energy Fuels* **2020**, *4*, 5387–5416. [CrossRef]
44. Shi, M.; Tai, Z.; Li, N.; Zou, K.; Chen, Y.; Sun, J.; Liu, Y. Spherical graphite produced from waste semi-coke with enhanced properties as an anode material for Li-ion batteries. *Sustain. Energy Fuels* **2019**, *3*, 3116–3127. [CrossRef]
45. Huang, C. Influence of molecular structure of carboxymethyl cellulose on high performance silicon anode in lithium-ion batteries. *Int. J. Electrochem. Sci.* **2019**, *14*, 4799–4811. [CrossRef]
46. Wang, Y.; Dang, D.; Li, D.; Hu, J.; Cheng, Y.-T. Influence of polymeric binders on mechanical properties and microstructure evolution of silicon composite electrodes during electrochemical cycling. *J. Power Sources* **2019**, *425*, 170–178. [CrossRef]
47. Klamor, S.; Schröder, M.; Brunklaus, G.; Niehoff, P.; Berkemeier, F.; Schappacher, F.M.; Winter, M. On the interaction of water-soluble binders and nano silicon particles: Alternative binder towards increased cycling stability at elevated temperatures. *Phys. Chem. Chem. Phys. PCCP* **2015**, *17*, 5632–5641. [CrossRef]
48. Osinska-Broniarz, M.; Martyla, A.; Majchrzycki, L.; Nowicki, M.; Sierczynska, A. Influence of polymer binder structure on the properties of the graphite anode for lithium-ion batteries. *Eur. J. Chem.* **2016**, *7*, 182–186. [CrossRef]
49. Berhaut, C.L.; Dominguez, D.Z.; Tomasi, D.; Vincens, C.; Haon, C.; Reynier, Y.; Porcher, W.; Boudet, N.; Blanc, N.; Chahine, G.A.; et al. Prelithiation of silicon/graphite composite anodes: Benefits and mechanisms for long-lasting Li-Ion batteries. *Energy Storage Mater.* **2020**, *29*, 190–197. [CrossRef]
50. Kim, K.; Shon, J.; Jeong, H.; Park, H.; Lim, S.-J.; Heo, J. Improving the cyclability of silicon anodes for lithium-ion batteries using a simple pre-lithiation method. *J. Power Sources* **2020**, *459*, 228066. [CrossRef]
51. Berckmans, G.; De Sutter, L.; Marinaro, M.; Smekens, J.; Jaguemont, J.; Wohlfahrt-Mehrens, M.; van Mierlo, J.; Omar, N. Analysis of the effect of applying external mechanical pressure on next generation silicon alloy lithium-ion cells. *Electrochim. Acta* **2019**, *306*, 387–395. [CrossRef]



Article

Investigation of Fast-Charging and Degradation Processes in 3D Silicon–Graphite Anodes

Yijing Zheng *, Danni Yin, Hans Jürgen Seifert and Wilhelm Pfleging *

Institute for Applied Materials-Applied Materials Physics (IAM-AWP), Karlsruhe Institute of Technology (KIT), Hermann-von-Helmholtz-Platz 1, 76344 Eggenstein-Leopoldshafen, Germany; danni.yin@hotmail.com (D.Y.); hans.seifert@kit.edu (H.J.S.)

* Correspondence: yijing.zheng@kit.edu (Y.Z.); wilhelm.pfleging@kit.edu (W.P.)

Abstract: The 3D battery concept applied on silicon–graphite electrodes (Si/C) has revealed a significant improvement of battery performances, including high-rate capability, cycle stability, and cell lifetime. 3D architectures provide free spaces for volume expansion as well as additional lithium diffusion pathways into the electrodes. Therefore, the cell degradation induced by the volume change of silicon as active material can be significantly reduced, and the high-rate capability can be achieved. In order to better understand the impact of 3D electrode architectures on rate capability and degradation process of the thick film silicon–graphite electrodes, we applied laser-induced breakdown spectroscopy (LIBS). A calibration curve was established that enables the quantitative determination of the elemental concentrations in the electrodes. The structured silicon–graphite electrode, which was lithiated by 1C, revealed a homogeneous lithium distribution within the entire electrode. In contrast, a lithium concentration gradient was observed on the unstructured electrode. The lithium concentration was reduced gradually from the top to the bottom of the electrode, which indicated an inhibited diffusion kinetic at high C-rates. In addition, the LIBS applied on a model electrode with micropillars revealed that the lithium-ions principally diffused along the contour of laser-generated structures into the electrodes at elevated C-rates. The rate capability and electrochemical degradation observed in lithium-ion cells can be correlated to lithium concentration profiles in the electrodes measured by LIBS.

Keywords: fast-charging; silicon anode; graphite anode; laser structuring; LIBS; 3D battery

1. Introduction

The lithium-ion battery (LIB) was commercialized by Sony in 1991 [1]. Nowadays, the LIB has become a common and important energy storage device for mobile devices. In addition, due to its high gravimetric and volumetric energy density, the LIB has been a standard energy source for electric vehicles and drones [2]. The production cost of lithium-ion batteries (LIBs) per kilowatt-hour was USD 764 in 2009–2010 and could already be reduced to USD 111 in 2020 [3,4]. A further reduced cost of USD 92 was forecasted in 2025 [5]. The further development and establishment of hybrid and electric vehicles (xEV) are closely linked to the next generation of LIBs, which are characterized by further increased power density as well as high energy density [6]. In the current research, the main goal is to conceive cells with an energy density of about 350–500 Wh/kg at the cell level [7]. In addition, a short charging time (<15 min) and a range of over 600 km with a single battery charge have been aimed so that the electric drive system with LIBs can offer a comparable range and “fuelling time” as the combustion engine. For this purpose, there are considerable requirements for development at the cell and the material level. Thus, further development of new materials for anode and cathode with high specific capacity is necessary.

In terms of material development, silicon has been considered as a next-generation anode material due to its theoretical capacity of 3579 mAh/g, which is significantly higher

than that of the commonly used graphite (372 mAh/g) [8]. Silicon provides a moderate potential of 0.2–0.3 V (vs. Li/Li⁺), and lithiated silicon is more stable in liquid electrolytes than lithiated graphite [9]. However, the high specific capacity leads to an enormous volume change of silicon up to 300% during lithiation and delithiation, which is a well-known challenge for applications and commercialization of silicon-based anodes. The volume change causes crack formation in the silicon particles, and subsequently the solid electrolyte interphase (SEI) layer is continuously rebuilt. The internal impedance of the cells increases with increasing SEI layer thickness [10,11]. The repeated particle cracking leads to pulverization, electrical insulation of the silicon, and film delamination [12].

Therefore, the main challenges for the commercialization of silicon-based anode materials are to improve their chemical and mechanical integrity in order to achieve application-related lifetime, cycling stability, and capacity retention [13]. In the last decades, several strategies have been developed with respect to the reduction of compressive stress in silicon-based electrodes. Silicon 3D nanostructures, including nanowires [14,15], porous/hollow structures [16,17], and silicon-based composite films [18,19], as well as silicon composites with 3D structural designs [20,21], have shown improved cycling stability and rate capability compared to 2D electrode designs. However, recent research results have been successful but are still far from the practical requirements of consumer and commercial mass production. Therefore, a combined utilization of graphite and Si powders has been introduced in this work. Graphite has a low specific capacity but can provide improved volumetric energy density and cycle stability as well as a long cycle lifetime (>80% of initial capacity for more than 500 cycles). The silicon contributes to the increased specific capacity of the entire composite electrode. Graphite is a common anode material that has already been successfully commercialized. For a combination of these types of active materials, conventional battery production can be adapted quickly and cost-effectively [22,23]. 3D electrode architectures achieved by ultrafast laser structuring was successfully implemented in batteries on a laboratory scale [24,25]. Previous works [25] revealed that mechanical stress within the silicon–graphite (Si/C) electrodes can be significantly reduced by applying 3D architectures, and these cells can achieve an improvement concerning rate capability, cycle stability, and cell lifetime.

This work is focused on the investigation of lithium concentration profiles related to fast charging and discharging, as well as cell degradation mechanism in structured and unstructured Si/C electrodes. For this purpose, laser-induced breakdown spectroscopy (LIBS) was employed, and electrochemical properties of silicon and Si/C electrodes were analyzed by cyclic voltammetry (CV) and galvanostatic measurements (GM).

2. Materials and Methods

2.1. Preparation of Electrode Material

The silicon–graphite electrodes consisting of 10–20 wt% silicon were fabricated for galvanostatic measurements and subsequent laser-induced breakdown spectroscopy (LIBS). The mass of active materials, silicon, and graphite is kept to 80 wt% of the total electrode mass. The various chemical composition of electrode materials, thickness, and the corresponding application are listed in Table 1. To avoid the crack formation of silicon particles during electrochemical cycling, we applied the nano-sized silicon particles with an average particle size of 150 nm (2W iTech, LLC, San Diego, CA, USA). After exposure to the ambient air, a native oxide layer was built on the silicon surface. The chemical properties of the silicon powder were analyzed by inductively coupled plasma-optical emission spectrometry in advance. The used silicon powder contains 94 wt% silicon and 3.84 wt% oxygen. Silicon particles were mixed with flake graphite particles (D_{50} = 15.26 μ m, Targray, Kirkland, QC, Canada) and carbon black (Timcal Super C65, MTI Corporation, New York, NY, USA) in pre-prepared sodium carboxymethyl cellulose (Na-CMC, MTI Corporation, Richmond, CA, USA) solution. A planetary ball milling machine (Pulverisette 7 premium line, Fritsch GmbH, Idar-Oberstein, Germany) enables the achievement of a homogenous slurry without micro-sized silicon agglomerates. Styrene-butadiene rubber (SBR, MTI Corporation,

Richmond, CA, USA) can contribute to the improvement of the mechanical stability of electrode and film adhesion. Hence, 5 wt% styrene-butadiene rubber was added at the end of the mixing process.

Table 1. Chemical composition and theoretical capacity of the prepared silicon and Si/C electrodes.

Type	Composition (wt%)					Areal Capacity * (mAh/cm ²)	Thickness (μm)	Analytics
	Si	Graphite	Carbon	CMC	SBR			
1	40	0	30	15	15	2.42 ± 0.13	25 ± 2	CV
2	20	60	10	5	5	3.09 ± 0.20	55 ± 2	LIBS
3	10	70	10	5	5	4.03 ± 0.05	70 ± 2	Calibration LIBS and GM
4	10	70	10	5	5	6.44 ± 0.10	100 ± 2	

* related to reference electrode.

The prepared slurry was coated on a nickel-coated copper current collector (Targray, Kirkland, QC, Canada) by tape casting. The nickel layer has a thickness of 1–2 μm and serves to improve the film adhesion. Afterwards, the electrode was dried at room temperature for 2.5 h. Prior to laser structuring, the electrode was calendered using a hot rolling press machine (HR01 Hot Rolling Machine, MTI Corporation, Richmond, CA, USA). The porosity of the electrode is related to its thickness and can be calculated by the ratio of hollow volume to the total volume of the electrode using material density. The used equation for the calculation is described elsewhere [26]. The electrode was passed several times through two counter-rotating rollers with gradually reduced roller gap distance. The prepared electrodes have a porosity of about 42%.

2.2. Ultrafast Laser Processing

A processing system (PS450-TO, Optec, Frameries, Belgium) with a pulsed femtosecond laser (Tangerine, Amplitude Systèmes, Bordeaux, France) was used to create 3D structures on the surfaces of the anodes and cathodes and to cut out the electrodes. The femtosecond laser operates at a fundamental wavelength of 1030 nm with a pulse duration of 350 fs. The pulse repetition rate of 200 kHz and 500 kHz were applied for cutting and structuring, respectively. With respect to isotropic volume expansions during lithiation in the silicon–graphite electrode, grid structures with a pitch distance of 100 μm and 300 μm were generated on the electrodes.

2.3. Cell Assembly

Coin cells of type CR2032 (MTI Corporation, Richmond, CA, USA) were used to characterize the electrochemical properties of the laser-structured (“LS”) and unstructured (“reference”) electrodes. Coin cells were also used for calibration samples regarding laser-induced breakdown spectroscopy. For providing a clear type of abbreviation, the cells are denoted as “LS cells” and “reference cells”. Cell assembly was performed in a glove box filled with argon (LABmaster SP, MBraun Inertgas-Systeme GmbH, Munich, Germany) in a high-purity atmosphere (O₂ < 0.1 ppm, H₂O < 0.1 ppm). The electrodes examined have a diameter of 12 mm. Lithium foil (Sigma Aldrich, St. Louis, MO, USA) with a thickness of 250 μm and a diameter of 11 mm was used as a counter electrode. A glass fiber separator with a diameter of 15 mm (GF/A filter, thickness 260 μm, Whatman, Maidstone, UK) served as an electrical insulator between the electrodes. The electrolyte used (LP57, Merck AG, Darmstadt, Germany) consists of a 1.3 mol/L lithium hexafluorophosphate (LiPF₆) in ethylene carbonate (EC) and ethyl methyl carbonate (EMC) solution with a weight ratio of 3:7. Additionally, 5 wt% fluoroethylene carbonate (FEC) was added to the mixture, which can contribute to the formation of a more stable solid electrolyte interphase (SEI). A total of 120 μL electrolyte was added to the electrode and separator. To ensure a homogeneous wettability of the electrodes with the liquid electrolyte, the thick electrodes (thickness L > 100 μm) were previously immersed in the electrolyte bath for 30 min. The

cell components were assembled using an electric coin cell crimper (MSK-160D, MTI Corporation, Richmond, CA, USA).

2.4. Electrochemical Analyses

The galvanostatic measurements were performed at room temperature 22 °C by a battery tester (BT 2000, Arbin Instruments, College Station, TX, USA). After cell assembling, the formation was carried out. The half-cells with Si/C electrodes were discharged at a low constant current (cc) of 0.02C up to cutoff voltage (0.01 V). A constant voltage (cv) was applied just after the cell reached the cutoff voltage. The cv step was completed when the measured current at the cell was less than a specified cutoff current. Subsequently, the cells were charged at the same C-rate to upper cutoff voltage (1.5 V). The procedure was repeated for three cycles to ensure a homogenous SEI formation. After formation, the cells were prepared for the subsequent electrochemical analyses.

For rate tests, the cells were charged and discharged with increasing C-rate up to 2C and then with the lower C rate of 0.1C to investigate rate capability and cell degradation.

For a quantitative evaluation of the lithium concentration at any Si/C electrode, a calibration is necessary. Identical structured Si/C electrodes with a pitch distance of 300 µm were prepared for this purpose. After formation, the cells were discharged to the selected voltages (Table 2) using 0.1C. Subsequently the voltage was kept constant for further 3 h.

Table 2. The electrochemical titration voltages of cells prepared for LIBS calibration.

Electrochemical Titration Voltages (V)						
0.01	0.05	0.08	0.105	0.118	0.13	0.162
0.2	0.218	0.24	0.3	0.32	0.55	1.5

Cyclic voltammetry, which is applied to investigate the phase change in redox reactions, is carried out directly after cell assembling by a potentiostat VMP-3 (BioLogic Science Instruments, Seyssinet-Pariset, France). Formation of crystalline phase $\text{Li}_{15}\text{Si}_4$ (cr- $\text{Li}_{15}\text{Si}_4$) was studied with different voltage ranges of 0.01–1.5 V and 0.05–1.5 V. A sweep rate of 10 µV/s was used for recording the current response.

2.5. Laser-Induced Breakdown Spectroscopy and Creation of Calibration Data

Laser-induced plasma spectroscopy (LIBS, type: FiberLIBS SN013, SECOPTA analytics GmbH, Teltow, Germany) enables the analysis of the lithium distribution in the electrodes. A passive-mode-locked Nd:YAG laser with a wavelength of 1064 nm, pulse duration of 1.5 ns, and repetition rate of 1–100 Hz was integrated in the LIBS system. The laser beam was focused on the sample surface with a diameter of about 100 µm, which also corresponded to the lateral resolution of LIBS measurements. The measurements were performed with a maximum pulse energy of 3 mJ and a laser pulse frequency of 100 Hz. The analyzed material was ablated by laser pulses. Meanwhile, laser-induced material vapor plasmas were generated. As the plasmas decayed, the element-specific spectra were emitted. The emitted spectra were recorded by a Czerny-Turner spectrometer (FiberLIBS SN013, SECOPTA analytics GmbH, Teltow, Germany) in combination with two Hamamatsu S11155 charge-coupled detectors (CCD) (Hamamatsu Photonics K.K., Hamamatsu, Japan). By means of this setting, the emission spectra in the range of 229–498 nm and 569–792 nm can be analyzed by one single laser pulse.

The software SecViewer (version 1.9, SECOPTA analytics GmbH, Teltow, Germany) was used to evaluate the spectra. The characteristic wavelengths of the elements relevant for the Si/C electrodes can be assigned. The intensity of the characteristic wavelength allows for a qualitative analysis of the element distribution in an electrode. Due to the effect of self-absorption at the wavelength of 670.77 nm, the Li^I emission wavelength of 610.35 nm was used for the analysis of lithium [26].

For a quantitative evaluation of lithium concentration in the type of Si/C electrodes, a calibration file related to the used LIBS device is necessary. Structured Si/C electrodes with 10 wt% silicon in different lithiated states, as listed in Table 2, were prepared for this purpose. Hereby, grid structures with a pitch of 300 μm were applied to improve the reproducibility of the electrochemical titration procedure. Subsequently to titration, these prepared cells were disassembled in the glove box. The disassembled electrodes were immersed in a dimethyl carbonate (DMC) solution for 30 min and then washed up with a fresh DMC solution. This cleaning step was repeated twice to avoid contamination from the residual lithium salt by the used electrolyte. Thereafter, half of the electrode was used for the establishment of the calibration by LIBS and the other part of the electrode was used for the determination of the element concentration, e.g., lithium, silicon, and carbon, by applying inductively coupled plasma-optical emission spectrometry (ICP-OES, OPTIMA 4300 DV, PerkinElmer, Waltham, MA, USA). The calibration data were derived from LIBS and ICP-OES as described in [26]. Lithium concentration and distribution related to C-rates was systematically investigated in the structured and unstructured Si/C electrodes. The electrochemical cycling procedure for each type of electrodes is shown in Table 3.

Table 3. Electrochemical testing procedures for the investigation of lithium concentration profiles.

Samples	Cell State for LIBS	Step 1 (formation)	Step 2	Step 3
(a) Unstructured Si/C electrode	lithiated state at 0.01 V (0.05C) delithiated state at 1.5 V (0.05C)	discharging/charging: 0.02C; cycles: 1	- discharging: 0.05C	discharging: 0.05C cv at 0.01 V for 10 min charging: 0.05C, cv at 1.5 V for 10 min
(b) LS Si/C electrode	lithiated state at 0.01 V (1C) delithiated state at 1.5 V (1C)	discharging/charging: 0.05C; cycles: 2	- discharging: 0.2C	discharging: 1C, cv at 0.01 V for 10 min charging: 1C, cv at 1.5 V for 10 min

3. Results

3.1. Laser Structuring

Model electrodes with micropillars were designed for the LIBS measurements to investigate the lithium diffusion pathway in the structured electrodes. These special electrodes consist of micropillars with dimensions of $800 \times 800 \mu\text{m}^2$ (Figure 1), which are arranged at a distance of 1200 μm from each other. The microcolumns are realized by direct laser ablation of the electrode material around the micropillars. The layer thickness of the electrodes is about 100 μm . A smooth copper surface reveals a successfully selective ablation without damaging the copper current collector.

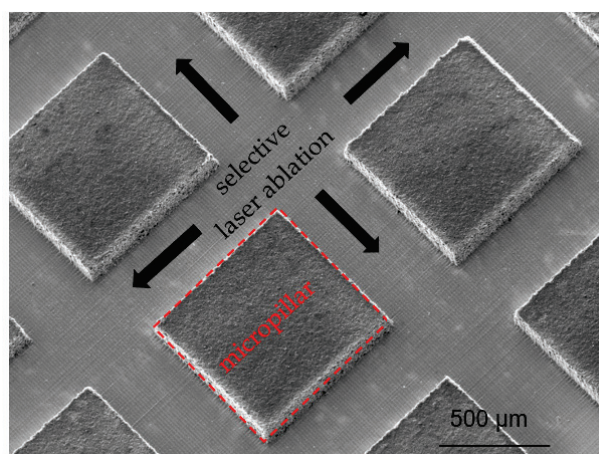


Figure 1. Scanning electron microscopy (SEM) image of a laser-generated model electrode with micropillar structures ($800 \mu\text{m} \times 800 \mu\text{m}$).

When the necessity of a small material loss after laser structuring is taken into account, narrow channels on the electrodes are typically required. The structured Si/C electrode is demonstrated in Figure 2 in the top view (a) and cross-section view (b). The structured channels in thick electrodes ($>70\ \mu\text{m}$) usually revealed a “V”-shaped contour. The channel widths on the top and in the middle were $21 \pm 2\ \mu\text{m}$ and $14.4 \pm 1\ \mu\text{m}$, respectively, and its value reduced to a few micrometers on the bottom of the channel close to the current collector.

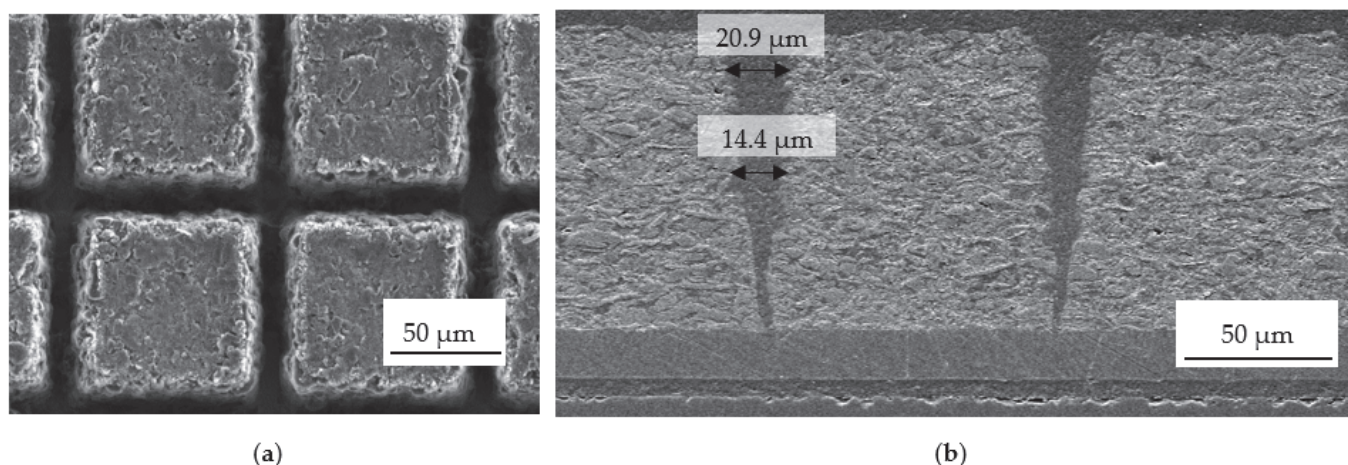


Figure 2. SEM images of laser-generated grid structures with a period of $100\ \mu\text{m}$: (a) top view and (b) cross section.

3.2. Electrochemical Properties of Silicon-Based Electrodes

3.2.1. Cyclic Voltammetry of Cells with Silicon Electrodes

The phase change of graphite has already been studied in detail [27,28] by employing (CV). Concerning the silicon–graphite composite system, it is necessary to study the material property of silicon separately. Therefore, cyclic voltammetry was performed on the cells with thin composite silicon anodes consisting of 40 wt% silicon (type 1 in Table 1) directly after the cell assembly. It is well known that the metastable crystalline phase $\text{Li}_{15}\text{Si}_4$ is only formed when the cutoff voltage is lower than a certain voltage value. Therefore, two cutoff voltages of 0.01 V and 0.05 V were set up for CV. The cyclic voltammograms of cells with the LS and reference electrodes recorded from the third cycle are shown in Figure 3 using a normalized current I_{Norm} ($I_{\text{Norm}} = \text{measured current}/\text{mass of active materials}$) as a function of the voltage. The alloying process (lithiation) of silicon occurs for voltages lower than 0.3 V. For all cells, two broad current maxima (a and b) appeared at 0.23 V and 0.075 V, respectively. A secondary maximum a' was detected at 0.28 V, as in [29], marking the formation of the P-I phase (LiSi). Finally, the phase transition from P-I to P-II ($a\text{-Li}_7\text{Si}_3$) occurred at 0.23 V. The second broad current maximum at 0.075 V can be attributed to the formation of the P-III phase ($a\text{-Li}_{3,16}\text{Si}$). Whether $a\text{-Li}_{3,5}\text{Si}$ [30] or $\text{Li}_{3,16}\text{Si}$ [29] is formed in this voltage range is still debated in the literature. Up to 0.05 V, no different current profile was observed for the LS and reference cells during lithiation. A current maximum c at 0.01 V could be detected at the LS cells, indicating the formation of $\text{cr-Li}_{15}\text{Si}_4$. However, the voltage values of the current maxima c and a slightly differed from the data from [29,31,32].

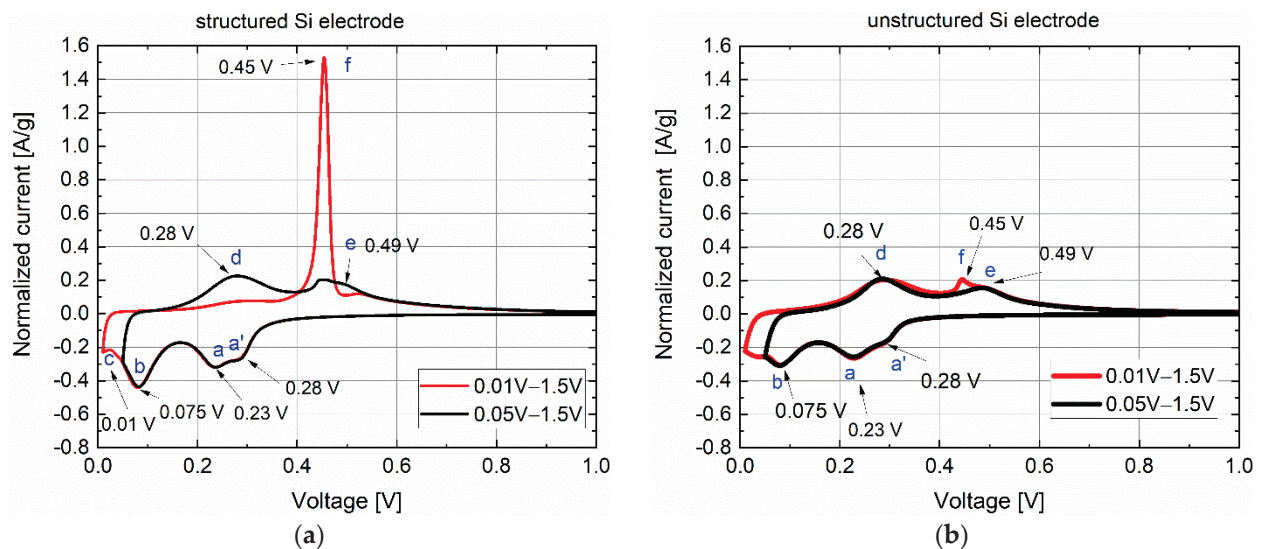


Figure 3. Cyclic voltammogram of cells with structured (a) and unstructured (b) Si electrodes recorded by a sweep rate of 10 $\mu\text{V/s}$ in a voltage window of 0.01–1.5 V and 0.05–1.5 V.

During the subsequent delithiation process in a voltage window of 0.01–1.5 V, a current maximum *f* with high current density (1.5 A/g) appeared at 0.45 V from LS cells. This current maximum and the corresponding voltage were in good agreement with data from the literature [13,31,33] and describe the delithiation of the crystalline phase $\text{cr-Li}_{15}\text{Si}_4$. Two broad current maxima *d* and *e* were observed at 0.28 V and 0.49 V, respectively, when the lower cutoff voltage was increased to 0.05 V. In this case, the current maxima *f* at 0.45 V was significantly reduced but still discernible and overlapped with the broad peak *e* at 0.49 V. This indicates that the amorphous phase Li_xSi was not completely converted to $\text{cr-Li}_{15}\text{Si}_4$ during the cathodic reaction at the lower cutoff voltage of 0.05 V. Probably due to the weak current maximum, only a small amount of $\text{cr-Li}_{15}\text{Si}_4$ was formed at 0.05 V. The current maximum at 0.28 V indicated the phase transformation from $\text{a-Li}_{3.5}\text{Si}$ to $\text{a-Li}_7\text{Si}_3$, and the peak at 0.49 V indicated the transition from Li_7Si_3 to LiSi .

Figure 3b demonstrates the cyclic voltammogram of the reference cells with unstructured Si electrodes. In comparison to LS cells, the reference cells exhibited a similar cyclic voltammogram as a function of voltage during the cathodic reaction (lithiation). No current maximum was detected at the voltage of 0.01 V. The clear difference in current peaks was observed in the anodic reaction (delithiation). A weakly pronounced current peak *f* of 0.2 A/g can be seen in comparison to the measurement with LS cells (1.5 A/g). This current maximum *f* was completely extinguished in the smaller voltage range (0.05–1.5 V). The current peak at 0.45 V recorded from reference was significantly smaller than those of the cells with LS electrodes. It was determined that the crystalline phase could not be formed effectively in the reference cells, even if the lower cutoff voltage was set to values smaller than 0.05 V.

3.2.2. Galvanostatic Measurements of Cells with Si/C-Electrodes

Rate capability and cell degradation were studied in coin cell design using high-energy silicon–graphite electrodes (type 4 in Table 1). Grid structures with a pitch distance of 100 μm (shown in Figure 2) were applied to improve rate capability. Figure 4a,b show the selected results of the discharge capacity (lithiation of the Si/C electrode) and the corresponding coulombic efficiency as a function of cycle number. The coulomb efficiency (CE) obtained from the first cycle, which describes the ratio of removed charges to previously stored charges during a charge–discharge process in a cell, was about 84% for reference and LS cells. After formation, all cells were symmetrically cycled with step-wise increased C-rate. The discharge capacity of LS cell slightly dropped with increased C-rate and the cycle number and could provide a capacity over 380 mAh/g at 2C. Subsequently, the capacity

increased to over 400 mAh/g at 0.1C, which is lower than the initial capacity of 480 mAh/g. This capacity fading can be attributed to the thickness of the electrode, the chemical degradation, side reaction with electrolyte, and quality of the used silicon depending on the supplier. In comparison to the previous research in [25], the silicon-containing high oxygen content (14 wt%) revealed a reduced initial capacity loss during electrochemical cycling. The natural SiO₂ layer on the surface of silicon particles might prevent the cracking of silicon particles and subsequent rebuilding of SEI layers. However, the coulombic efficiency of LS cell maintained about 100%. A deviation from 100% was observed at the first cycle by charging C-rate to 2C and to 0.1C, which indicated cell polarisation.

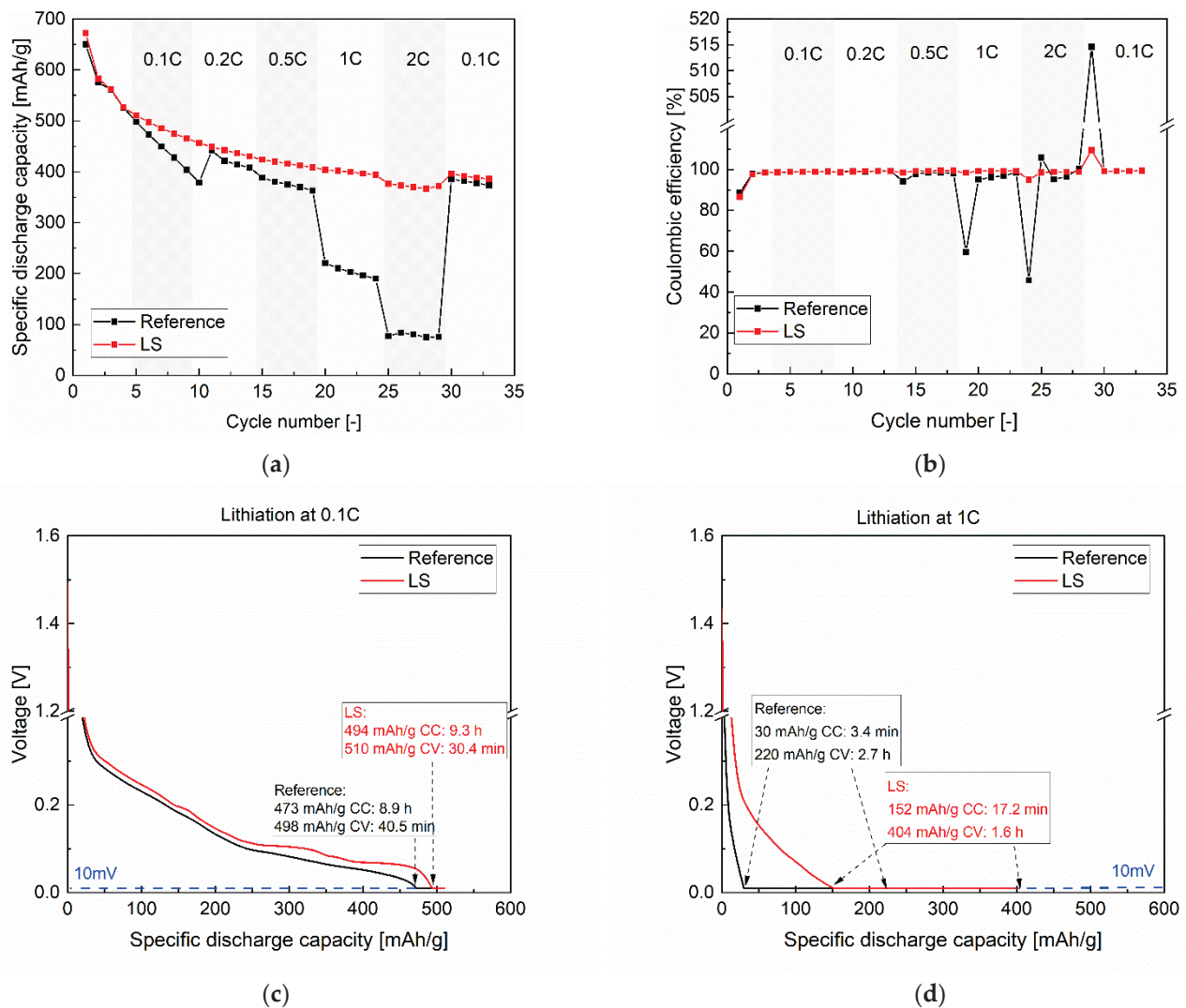


Figure 4. Results from galvanostatic measurements of cells with structured (LS) and unstructured (reference) electrodes: (a) specific discharge capacity as function of C-rate in rate capability tests, (b) corresponding coulombic efficiency, (c) voltage drop as function of specific discharge capacity by applying 0.1C, and (d) 1C (cccv-testing procedure was applied during the discharging process).

By comparison, the reference cell revealed an unstable discharge capacity and coulombic efficiency. For C-rates equal and above 1C, a significant capacity fading (from about 200 mA/g/h at 1C down to less than 100 mA/g/h at 2C) can be observed. The coulombic efficiency was reduced to less than 50% at the first cycle by charging C-rate. In this case, the inserted lithium in the Si/C electrode could not be completely removed back to the counter electrode due to the applied high C-rate and resulting polarisation. Furthermore, an extremely high value of over 515% was obtained when the reference cells cycled in the

previous step using a high C-rate (2C), and subsequently was cycling using a low C-rate (0.1C). A conclusive explanation might be that lithium remaining in the Si/C electrode during the previous cycling (from 0.5C to 2C) could be extracted at 0.1C. By laser structuring of electrodes, the stability of coulombic efficiency and capacity retention depending on the applied C-rate could be successfully improved in comparison to cells with unstructured electrodes.

In addition, the discharging process, namely, lithiation in anode material in a half-cell, is related to the charging process in a full-cell. Figure 4c,d presents the discharging capacity associated with time and voltage. This result can represent the efficiency of the charging process in real full-cells. At 0.1C, a capacity of 473 mAh/g was achieved by reference cell applying constant current (LS cell: 494 mAh/g), while the cell reached the cutoff voltage of 0.01 V. After the cccv (constant current–constant voltage)-discharging procedure, both cells delivered similar capacities of 498 mAh/h and 510 mAh/g, respectively. By applying 1C, the voltage–capacity behaviour changed dramatically. The voltage of the reference cell dropped within 3.4 min to 0.01 V with a capacity of 30 mAh/g, while the LS cell reached the cutoff voltage after 17.2 min, providing a capacity of 152 mAh/g. Eventually, the LS cell could achieve almost double capacity (404 mAh/g) in comparison to the reference cell (220 mAh/g). It can be determined on the basis of the obtained results that the lithiation process mainly took place during the constant-voltage step by applying 1C. The rapid voltage drop of the reference cell within a few minutes indicated a distinct cell polarization (also called overpotential) at high C-rates. The kinetically limited diffusion of the lithium-ions caused the cell overpotential and the lithium concentration gradient within the porous electrode, which can be demonstrated by applying laser-induced breakdown spectroscopy.

3.2.3. Lithium Distribution and Visualisation of Lithium Diffusion Pathway

The LIBS measurement was performed on the cycled Si/C electrode, and a typical spectrum is illustrated in Figure 5 with marked relevant characteristic emission wavelengths of the elements for the Si/C electrodes. The intensity of a characteristic wavelength enables qualitative analysis of the respective element and its distribution in the entire electrode. Due to the self-absorption effect for the most dominant Li^I emission wavelength at 670.77 nm, the Li^I emission wavelength at 610.35 nm was chosen for the analysis of lithium [26].

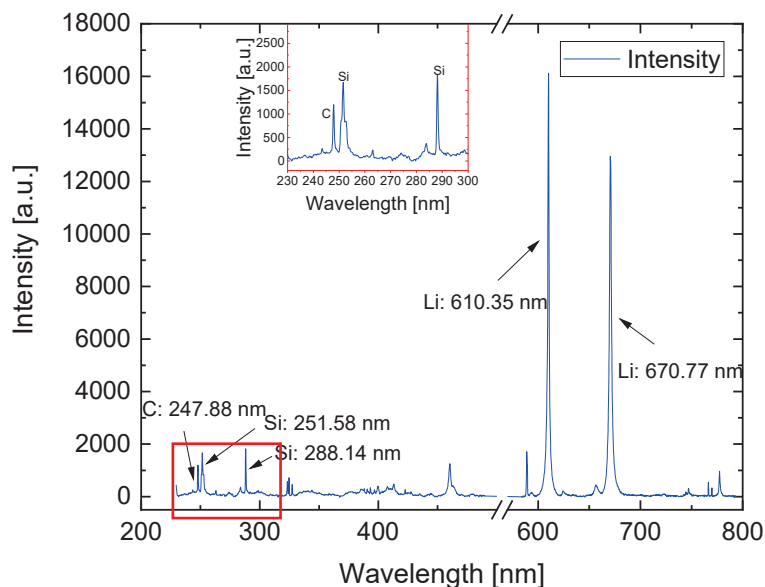


Figure 5. LIBS spectrum of a silicon–graphite electrode with the indication of the most relevant emission lines of lithium, graphite, and silicon.

The element mass ratio of Si/C calibration samples was determined by ICP-OES, and the lithium–silicon ratio ($n\text{Li}/n\text{Si}$) was calculated as a function of voltage (Figure 6). The $n\text{Li}/n\text{Si}$ ratio decreased as expected with increasing voltage. The maximum lithium–silicon ratio ($n\text{Li}/n\text{Si}$) was 7.65 ± 0.29 for the sample lithiated to 0.01 V. This value was summed up by the lithium amount in silicon, graphite, and SEI layer. In the fully delithiated sample charged to 1.5 V, the $n\text{Li}/n\text{Si}$ -ratio was 1.38 ± 0.05 . Inactive lithium remaining in SEI and irreversible alloyed Si-Li mainly contributed to this measured lithium content. LIBS measurements were subsequently performed on the calibration samples. The measured spectra were analyzed by Software Sec Analysis Tool (SECOPTA analytics GmbH, Teltow, Germany) with regard to the element mass ratio (Figure 6). A correlation between the ratios of intensities of spectra emitted by elements and the quantitative ratios of amounts of substance of elements measured by ICP-OES was established. In addition, a validation process was carried out in order to ensure the accuracy of the established calibration curve.

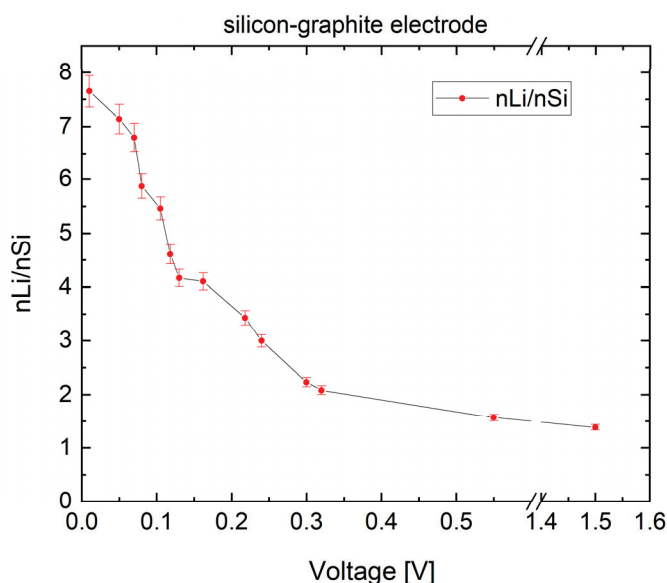


Figure 6. Relative content of lithium to silicon ($n\text{Li}/n\text{Si}$) in silicon–graphite electrodes measured by inductively coupled plasma optical emission spectroscopy (ICP-OES) as a function of depth of discharge.

Lithium concentration and homogeneity were investigated post-mortem at the reference and LS electrodes. The studying electrodes were discharged at 1C to 0.01 V, and the cell voltage was kept to 0.01 V for 10 min. As a comparison, a reference electrode without laser structuring was discharged by the same procedure but using a lower C-rate of 0.05C. The LIBS measurements were performed on the surface of the unstructured Si/C electrode by applying so-called elemental mapping with a point-to-point distance of 100 μm . The material was ablated layer by layer down to the current collector. With regard to the size of the resulting laser ablation crater profile on the electrode material (diameter > 200 μm), the grid structures with a pitch distance of 300 μm were utilized for LIBS measurements. The LIBS pulses were positioned in the center of the grid structures. The lithium concentration in this work was defined as the ratio of the amount of Li substance to that of Si ($n\text{Li}/n\text{Si}$). This value obtained from the cross section of the reference electrode was 6.34 with a standard deviation of 0.63. Figure 7 presents the elemental mapping of lithium distribution and concentration within an unstructured and structured Si/C electrode from the top of the electrode down to the current collector every four layers and the cross-sections at the position $y = 6.4$ mm within the entire electrode. An inhomogeneity of lithium distribution in the unstructured is shown in Figure 7a,b, where a lithium enrichment on the top (about 40 μm) of the electrode was detected. The average lithium concentration of the selected cross section was 3.38, with a standard deviation of 0.80, which corresponded to a measured

specific capacity of 212 mAh/g. Figure 7b exhibits the resulting lithium concentration profile as a consequence of lithium-ion diffusion through the separator and gradually diffusion from the outer electrode surface into the bulk until it reached the current collector. The lithiation process was implemented gradually and locally from the top of the electrode to the bottom. Contrary to this observation, the structured electrode revealed a higher average lithium concentration of 4.30 and a significantly enhanced homogenized lithium distribution in the entire electrode with a standard deviation of 0.42 (Figure 7c,d). This result corresponded to a higher measured specific capacity of 272 mAh/g. Laser structuring shortened the diffusion path of the lithium-ions and reduced the overall cell impedance, which led to a significant increase in diffusion kinetics at high C-rates.

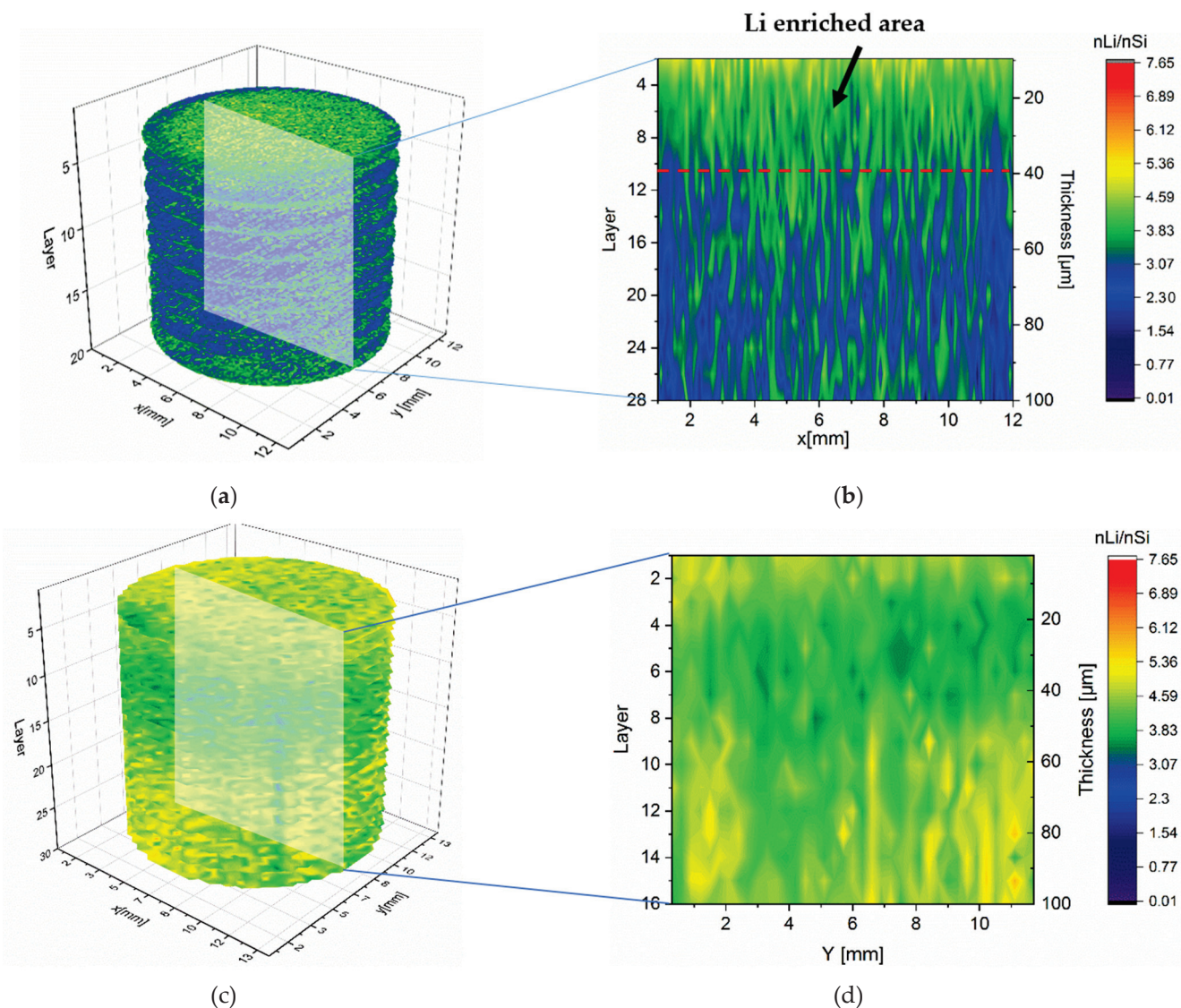


Figure 7. Lithium concentration profile in entire structured and unstructured Si/C electrodes lithiated at 1C: (a) 3D illustration of lithium concentration in a reference electrode, (b) its lithium distribution in the cross-sectional view, (c) 3D illustration of lithium concentration in a structured electrode (pitch distance: 300 μm), and (d) its lithium distribution in the cross-sectional view.

A dramatic increased coulombic efficiency was obtained in the first cycle when the operation current was changed from high C-rate (2C) to low C-rate (0.1C). The reason could be experimentally explained by means of LIBS measurements on the delithiated electrodes. The lithium concentration of the structured and unstructured electrodes after delithiation

at 1C is shown in Figure 8. The studying electrodes were lithiated with a low C-rate of 0.2C to ensure a complete lithiation and subsequently were delithiated at 1C to 1.5 V, keeping for 10 min. In the unstructured electrode, an average lithium concentration of 3.27 ± 0.75 was detected. Due to the laser-generated new diffusion pathways along the channel sidewalls, the lithium-ions could efficiently be extracted from the electrode material and revealed a lower average concentration of 2.70 ± 0.45 . The residual lithium in the electrode, which could not be completely extracted from the host material, led to the capacity fading at high C-rates. The process is particularly reversible, and the residual lithium in the electrode can be extracted by applying low C-rates, which can explain the extremely high coulombic efficiency in Figure 4b after switching to a low C-rate.

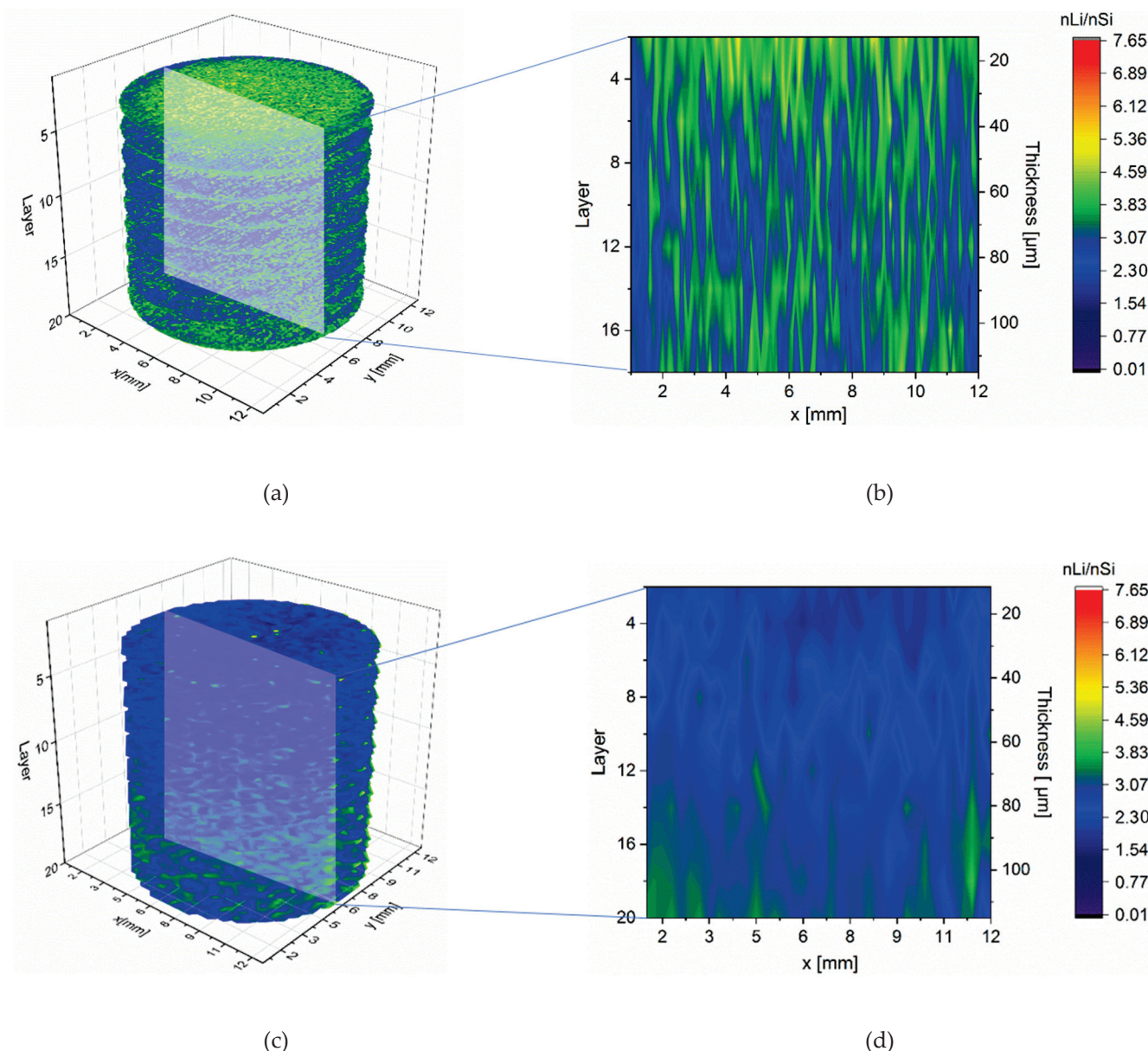


Figure 8. Lithium concentration profile in entire structured and unstructured Si/C electrodes delithiated by 1C: (a) 3D illustration of lithium concentration in a reference electrode, (b) its lithium distribution in the cross-sectional view, (c) 3D illustration of lithium concentration in a structured electrode (structure distance: 300 μm), and (d) its lithium distribution in the cross-sectional view.

The achieved results indicate that laser-generated 3D electrodes can accelerate the lithium-ion transport during the lithiation and delithiation process and thereby realize the

fast charging with reduced capacity loss. The lithium diffusion pathways established at a high C-rate (1C) were further investigated in detail using electrodes with micropillar structures. The cells with model electrodes (see Figure 1) were prepared in the identical way (Table 3). The micropillars were ablated layer-by-layer by LIBS laser pulses with 100 μm offset. The lithium distribution in a selected micropillar lithiated with 1C is presented in Figure 9. From the cross-sectional view (Figure 9a), it is obvious that a lithium enrichment with values $n\text{Li}/n\text{Si} > 6$ was located along the contour of the micropillar. Layer 6 of the horizontal cross-section (Figure 9b) revealed a minimum lithium concentration in the center of the micropillar.

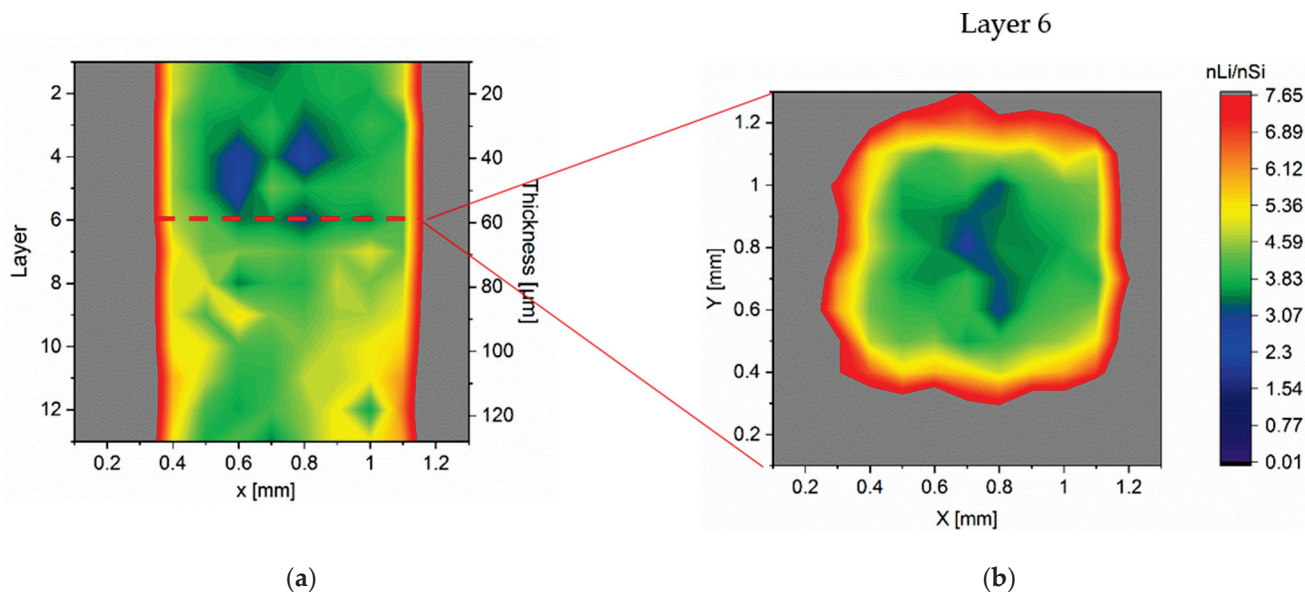


Figure 9. Lithium distribution of a Si/C micropillar lithiated at 1 C: (a) cross-sectional concentration profile of the micropillar at position $y = 0.7$; (b) horizontal layer 6 of the micropillar cross-sectional mapping.

Oumellal et al. [10] describe how lithium-ions diffuse from the separator via the pores inside the electrode filled with liquid electrolyte into the particles. The LIBS measurements indicate that at high C-rates the lithium-ions prefer to diffuse through the free electrolyte via laser-generated sidewalls of micropillars. This is mainly due to two reasons. Firstly, the lithium-ion mobility in free electrolyte is faster than in the composite electrode, which is affected by porosity and tortuosity. Secondly, the 3D topology of composite electrodes contributes to the formation of lithium-ion diffusion pathways. During intercalation, lithium-ion diffusion takes place between the basal planes of graphite. Therefore, the graphite electrodes have different tortuosity values parallel and perpendicular to the basal plane [34]. After coating, drying, and calendaring, the disc-shaped graphite particles are stacked on top of each other with a preferred orientation parallel to the current collector [35,36].

However, in contrast to the observation on graphite micropillars in our previous work [37], lower lithium concentration ($n\text{Li}/n\text{Si} \approx 3.4$) was detected on top of the electrode (layer 1–layer 6). This was attributed to the compressive pressure in the electrodes caused by the volume expansion of silicon. The compressive stress was forced on the separator and caused closure of pores inside the separator. Meanwhile, due to the volume expansion of silicon, the porosity inside the electrode was also reduced. As mentioned in Section 4.1, the lithiation process can be restricted by mechanical compressive stress. The electrode materials along the sidewalls were free from mechanical stress. Hence, lithiation, especially lithiation in silicon, was effectively promoted there.

3.2.4. Post-Mortem Analysis

Laser-generated channels can significantly reduce the overall mechanical stress inside Si/C-electrodes [25]. The cells in Figure 4 were disassembled in the delithiated state for a post-mortem SEM analysis. Figure 10 illustrates the SEM images of the cycled structured Si/C electrode, which can be geometrically divided into two parts. Due to the volume expansion, the laser-generated V-shaped channels (Figure 2b) were deformed. Only on the top half of the electrode, a small channel structure could still be detected. In the lower half of the electrode, close to the current collector, the channels were filled due to irreversible volume expansion, namely, chemical degradation [10]. Concerning the established channel geometry in Figure 2, one can state that the minimum channel width should be larger than 15 μm regarding the volume expansion. Increased capacity retention and cell lifetime of the same electrodes can be achieved by using wider channels (not shown here). The main degradation mechanism of the Si/C electrode can be described by a combination of mechanical and chemical degradation.

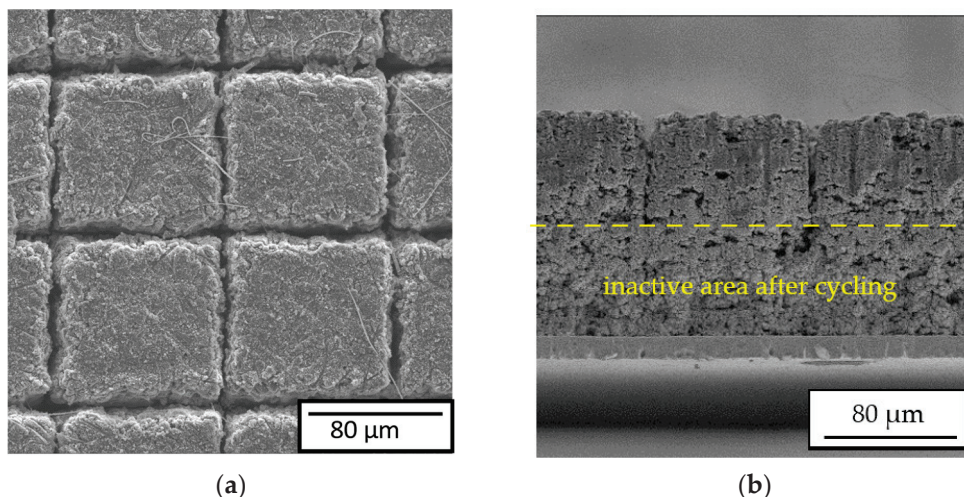


Figure 10. SEM images of cycled Si/C electrodes: (a) top view and (b) cross-sectional view.

LIBS can be used as post-mortem analysis to investigate the impact of cell degradation and to draw conclusions about the degradation mechanisms. The qualitative analysis of 3D lithium concentration of the reference electrodes without laser structuring and laser-structured electrodes was performed as described in [25] and is shown in Figure 11. A lack of film adhesion combined with the volume expansion resulted in film delamination and crack formation on the reference electrode, which can be impressively shown on the first layer in Figure 11a. A higher lithium concentration was detected in the entire reference electrode than in the LS electrode. Therefore, the reference electrode had a higher material density due to the higher Li content than the LS electrode. As a result, the reference electrode revealed a lower laser ablation rate of $\approx 5.5 \mu\text{m}$ per layer, which is defined by the ablation depth per layer and corresponds to the LIBS information depth. In contrast, the laser ablation rate of the cycled LS electrode was higher ($\approx 11 \mu\text{m}$ per layer) due to lower lithium concentration.

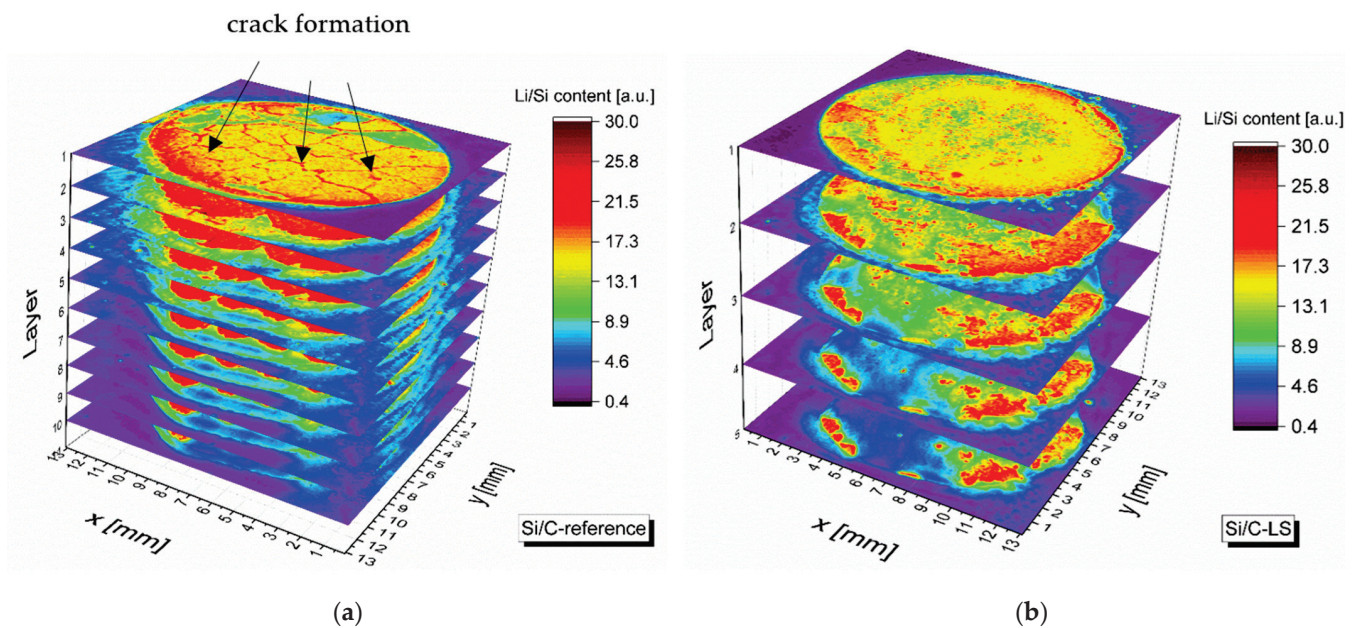


Figure 11. Post-mortem qualitative analysis of the electrochemically cycled electrodes by LIBS: (a) reference electrode without laser patterning and (b) laser patterned electrode.

The 3D mapping extracted from the qualitative analysis of the lithium concentration (Li/Si) indicates that the lithium transport was restricted due to long diffusion pathways from the current conductor to the counter electrode. The residual amount of inactive lithium inside the electrode increased cycle by cycle and led to an irreversible capacity fading and volume expansion. Finally, cell failure occurred.

Since the lithium could also reach the counter electrode via the sidewall of the free-standing structures, the lithium content in the LS electrode was found to be lower than that in the reference electrode. The reason for the cell degradation with Si-based electrodes is the lithium irreversibly stored in the electrode. Lithium-ions could not be completely extracted from the electrode materials during cycling. This correlates with the cell voltage of the cyclized cells in a delithiated state. After the long-term tests, the open-circuit voltage (OCV) of the half-cells in the delithiated state was mostly below 200 mV. The OCV of fresh cells is usually around 900 mV.

4. Discussion

4.1. Impact of Mechanical Stress on the Phase Change

The phase changes in silicon and Si/C electrodes were investigated by cyclic voltammetry. The current peak at 0.45 V in the anodic reaction (delithiation) can be regarded as a material-specific indicator for the formation of $\text{cr-Li}_{15}\text{Si}_4$. A wide range of low cutoff voltage (0.03 V–0.08 V) was reported with regard to the formation of this crystalline phase. Hatchard and Dahn [38] reported that amorphous Si films crystallize below 0.03 V, and the $\text{c-Li}_{15}\text{Si}_4$ phase does not form when the film thickness is larger than 2.5 μm . In this paper, the crystalline phase could be only detected in LS electrodes when the lower cutoff voltage was lower than 0.05 V. The LIBS studies of lithium distribution in structured and unstructured graphite and Si/C electrodes showed that lithium preferentially intercalated into the electrodes via the laser-generated sidewalls. The obtained results from CV and LIBS indicated that compressive stress affected both the electrochemical potential and the kinetics of the electrochemical reaction. The CV experiments revealed that cutoff voltage is not the only condition for crystallization. Compressive stresses within the electrode can reduce the electrochemical potential and restrict the formation of the crystalline phase, namely, full lithiation.

4.2. Degradation Mechanisms of Silicon–Graphite Electrodes

Oumellal et al. [10] investigated the silicon electrode failure mechanism using nuclear magnetic resonance (NMR) spectroscopy. This showed that most of the lithium lost during battery charging is not trapped in the Li_xSi alloys but adheres to the surface of the Si particles. Therefore, a thick SEI layer formed on the surface of the failing electrodes, which was probably produced as a degradation product of the liquid electrolyte during cycling. The groups of Peled and Aurbach [12,39] investigated the SEI-related side reactions that occur at cyclized negative electrodes of lithium batteries. These works show that lithium-ions are irreversibly trapped by oligocarbonate molecules that deposit in the electrode pores. One of the most important side reactions in a medium with high ethylene carbonate (EC) concentration could be related to a nucleophilic ring-opening of the EC molecules by the reduced Si surface [10].

Nevertheless, not only chemical degradation causes the capacity fading. Due to the trapped lithium on the silicon surface, the porosity of electrodes was also reduced. As shown schematically in Figure 12, the lithium-ions in a fresh Si/C electrode can diffuse through the pores to the silicon particles and conversely diffuse to the separator in the same way during delithiation. The degradation products are deposited in the pores and on the surface of the silicon particles during cycling. On the one hand, side products reduce the porosity and meanwhile extend the diffusion paths of the lithium-ions cycle by cycle. On the other hand, the reduced porosity leads to an increase in mechanical stress within the electrode. Crack formation in Si particles could be caused by the pressure of the surrounding materials, and new SEI layers are gradually rebuilt.

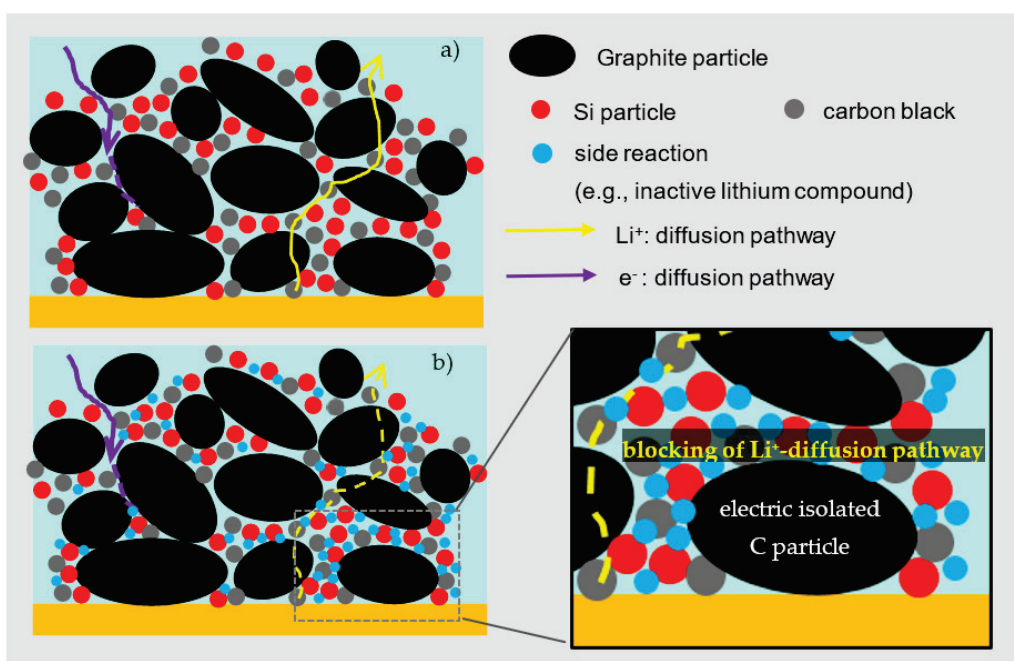


Figure 12. Schematic representation of the silicon–graphite electrode and electron diffusion pathways within the composite electrodes: (a) in a fresh state and (b) in a cycled state.

The standard graphite electrodes were able to achieve a cycle lifetime of up to 1000 cycles in the full cell format and showed capacity retention of 80% after testing. The LS silicon electrodes with 40 wt% silicon exhibited a longer cycle life than the Si/C electrode and could still deliver half of the initial capacity after 400 cycles (shown in the Appendix A). The significantly reduced capacity retention and lifetime of Si/C electrode can be attributed to the blocking of the lithium-ion access to graphite particles (Figure 12b). Since the silicon nanoparticles and conductive carbon black were homogeneously placed between the macroscale graphite particles with the help of the binder, the graphite particles were

surrounded by silicon particles. Due to the chemical degradation, the porosity of the Si/C electrode was reduced by irreversible volume expansion and side products. The lithium trapped on the silicon surface was no longer available for the electrochemical reaction, and meanwhile, the inactive materials reduced the active surface area of the surrounding graphite particles. Finally, the diffusion access on the graphite surfaces to the liquid electrolyte was blocked (Figure 12b). As a result, graphite particles were ionically and electrically isolated.

By means of LIBS measurements, less lithium was detected in the structured electrode. The chemical degradation was correlated by mechanical stress and decelerating diffusion transport due to reduced porosity and increased tortuosity. Laser structuring on Si/C electrodes can significantly reduce mechanical stress and provide new diffusion accesses to the bulk electrode material. Therefore, the lower Li content of the LS cell by a factor of about 1.5 showed that laser structuring can significantly contribute to reducing cell degradation. In addition, on the basis of the results obtained from post-mortem analysis in Figure 10, we found that the geometry of channels affected the degradation process as well. Lack of free spaces on the bottom of the structured electrode (Figure 2b) might elicit a more severe cell degradation in comparison to it occurring on the top of the electrode. The pores there might be completely blocked and result in advanced cell failure. Therefore, cells with entire channel width larger than 15 μm revealed improved capacity retention and cell lifespan.

5. Conclusions

In this work, the high-rate capability and cycle stability of cells with structured and unstructured Si/C electrodes were presented. The impact of degradation processes in Si/C electrodes was correlated in relation to the lithium concentration profiles in the entire electrodes. The lithium concentration and distribution of the structured electrodes revealed that at elevated C-rates, new lithium-ion diffusion pathways into the composite electrodes were established along the laser-generated sidewalls. The observed effect was due to low compressive stress in the active material along the sidewall and a high lithium-ion mobility in the free electrolyte in comparison to the electrolyte embedded in the porous composite electrode. The cell degradation of Si/C electrodes was attributed to the trapped lithium in the Si/C electrode. By means of post-mortem analysis of the morphology and the lithium concentration obtained from LIBS measurements, we can conclude that the mechanical stress can also accelerate chemical degradation and lead to early cell failure. 3D architectures on the Si/C electrodes enable a high rate capability, accelerate the lithium-ion transport, and can effectively reduce the mechanical stress as well as cell degradation. All those benefits can push silicon-based electrodes beyond the state of the art to become a high-energy anode material for next-generation batteries.

Author Contributions: Investigation, Y.Z. and D.Y.; supervision, H.J.S. and W.P.; writing—original draft preparation, Y.Z.; writing—review and editing, Y.Z. and W.P. All authors have read and agreed to the published version of the manuscript.

Funding: This research was funded by German Research Foundation (DFG, project no. 392322200). We acknowledge support by the KIT-Publication Fund of the Karlsruhe Institute of Technology.

Data Availability Statement: Data sharing is not applicable to this article.

Acknowledgments: We are grateful to Thomas Bergfeldt at Karlsruhe Institute of Technology for the chemical analysis by inductively coupled plasma-optical emission spectrometry and Yuanchun Huang for technical assistance and the evaluation of battery measurements.

Conflicts of Interest: The authors declare no conflict of interest.

Appendix A

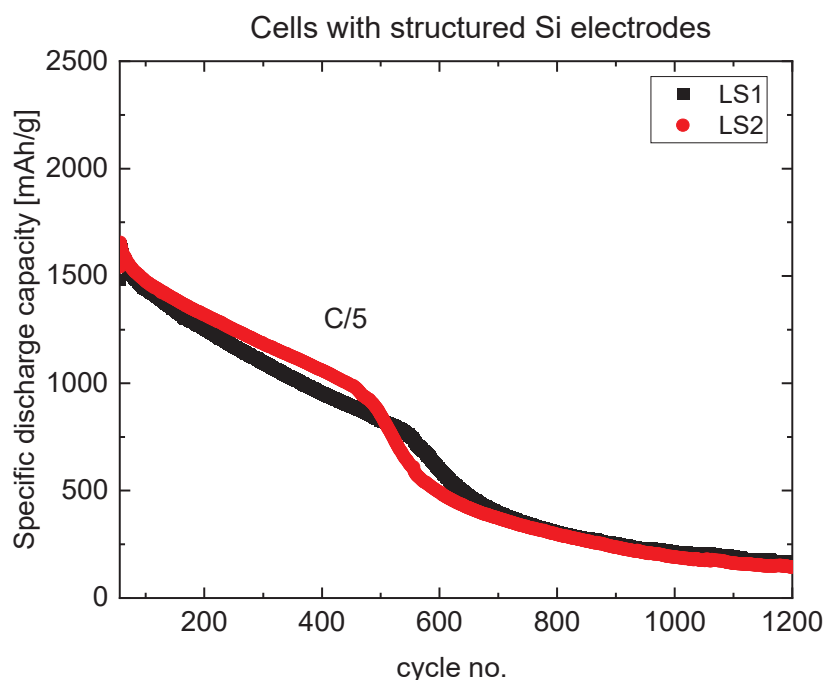


Figure A1. Galvanostatic result of cells with structured (LS) silicon electrodes (type 1 in Table 1).

References

- Nishi, Y. Lithium ion secondary batteries; past 10 years and the future. *J. Power Sources* **2001**, *100*, 101–106. [CrossRef]
- Dühnen, S.; Betz, J.; Kolek, M.; Schmich, R.; Winter, M.; Placke, T. Toward green battery cells: Perspective on materials and technologies. *Small Methods* **2020**, *4*, 2000039. [CrossRef]
- Nykvist, B.; Nilsson, M. Rapidly falling costs of battery packs for electric vehicles. *Nat. Clim. Change* **2015**, *5*, 329–332. [CrossRef]
- Wood, D.L., III; Li, J.; Daniel, C. Prospects for reducing the processing cost of lithium ion batteries. *J. Power Sources* **2015**, *275*, 234–242. [CrossRef]
- Mauler, L.; Duffner, F.; Zeier, W.G.; Leker, J. Battery cost forecasting: A review of methods and results with an outlook to 2050. *Energy Environ. Sci.* **2021**, *14*, 4712–4739. [CrossRef]
- Andre, D.; Kim, S.-J.; Lamp, P.; Lux, S.F.; Maglia, F.; Paschos, O.; Stiaszny, B. Future generations of cathode materials: An automotive industry perspective. *J. Mater. Chem. A* **2015**, *3*, 6709–6732. [CrossRef]
- Liu, J.; Bao, Z.; Cui, Y.; Dufek, E.J.; Goodenough, J.B.; Khalifah, P.; Li, Q.; Liaw, B.Y.; Liu, P.; Manthiram, A. Pathways for practical high-energy long-cycling lithium metal batteries. *Nat. Energy* **2019**, *4*, 180–186. [CrossRef]
- Tarascon, J.-M.; Armand, M. Issues and Challenges Facing Rechargeable Lithium Batteries. In *Materials for Sustainable Energy: A Collection of Peer-Reviewed Research and Review Articles from Nature Publishing Group*; Nature Publishing Group: London, UK, 2011; pp. 171–179.
- Maruyama, H.; Nakano, H.; Ogawa, M.; Nakamoto, M.; Ohta, T.; Sekiguchi, A. Improving battery safety by reducing the formation of Li dendrites with the use of amorphous silicon polymer anodes. *Sci. Rep.* **2015**, *5*, 1–9. [CrossRef] [PubMed]
- Oumellal, Y.; Delpuech, N.; Mazouzi, D.; Dupre, N.; Gaubicher, J.; Moreau, P.; Soudan, P.; Lestriez, B.; Guyomard, D. The failure mechanism of nano-sized Si-based negative electrodes for lithium ion batteries. *J. Mater. Chem.* **2011**, *21*, 6201–6208. [CrossRef]
- Yoon, T.; Nguyen, C.C.; Seo, D.M.; Lucht, B.L. Capacity fading mechanisms of silicon nanoparticle negative electrodes for lithium ion batteries. *J. Electrochem. Soc.* **2015**, *162*, A2325. [CrossRef]
- Tariq, F.; Yufit, V.; Eastwood, D.S.; Merla, Y.; Biton, M.; Wu, B.; Chen, Z.; Freedman, K.; Offer, G.; Peled, E. In-operando X-ray tomography study of lithiation induced delamination of Si based anodes for lithium-ion batteries. *ECS Electrochem. Lett.* **2014**, *3*, A76. [CrossRef]
- Obrovac, M.N.; Krause, L.J. Reversible Cycling of Crystalline Silicon Powder. *J. Electrochem. Soc.* **2007**, *154*, A103. [CrossRef]
- Leveau, L.; Laik, B.; Pereira-Ramos, J.-P.; Gohier, A.; Tran-Van, P.; Cojocar, C.-S. Silicon nano-trees as high areal capacity anodes for lithium-ion batteries. *J. Power Sources* **2016**, *316*, 1–7. [CrossRef]
- Peng, K.; Jie, J.; Zhang, W.; Lee, S.-T. Silicon nanowires for rechargeable lithium-ion battery anodes. *Appl. Phys. Lett.* **2008**, *93*, 033105. [CrossRef]
- Mishra, K.; Zheng, J.; Patel, R.; Estevez, L.; Jia, H.; Luo, L.; El-Khoury, P.Z.; Li, X.; Zhou, X.-D.; Zhang, J.-G. High performance porous Si@C anodes synthesized by low temperature aluminothermic reaction. *Electrochim. Acta* **2018**, *269*, 509–516. [CrossRef]

17. Yoon, T.; Bok, T.; Kim, C.; Na, Y.; Park, S.; Kim, K.S. Mesoporous silicon hollow nanocubes derived from metal–organic framework template for advanced lithium-ion battery anode. *ACS Nano* **2017**, *11*, 4808–4815. [CrossRef]
18. Tang, H.; Zhang, Y.; Xiong, Q.; Cheng, J.; Zhang, Q.; Wang, X.; Gu, C.; Tu, J. Self-assembly silicon/porous reduced graphene oxide composite film as a binder-free and flexible anode for lithium-ion batteries. *Electrochim. Acta* **2015**, *156*, 86–93. [CrossRef]
19. Tang, H.; Zhang, J.; Zhang, Y.; Xiong, Q.; Tong, Y.; Li, Y.; Wang, X.; Gu, C.; Tu, J. Porous reduced graphene oxide sheet wrapped silicon composite fabricated by steam etching for lithium-ion battery application. *J. Power Sources* **2015**, *286*, 431–437. [CrossRef]
20. Shen, X.; Tian, Z.; Fan, R.; Shao, L.; Zhang, D.; Cao, G.; Kou, L.; Bai, Y. Research progress on silicon/carbon composite anode materials for lithium-ion battery. *J. Energy Chem.* **2018**, *27*, 1067–1090. [CrossRef]
21. Dou, F.; Shi, L.; Chen, G.; Zhang, D. Silicon/carbon composite anode materials for lithium-ion batteries. *Electrochem. Energy Rev.* **2019**, *2*, 149–198. [CrossRef]
22. Kwade, A.; Haselrieder, W.; Leithoff, R.; Modlinger, A.; Dietrich, F.; Droeder, K. Current status and challenges for automotive battery production technologies. *Nat. Energy* **2018**, *3*, 290–300. [CrossRef]
23. Schmich, R.; Wagner, R.; Höppl, G.; Placke, T.; Winter, M. Performance and cost of materials for lithium-based rechargeable automotive batteries. *Nat. Energy* **2018**, *3*, 267–278. [CrossRef]
24. Pflüger, W. Recent Progress in Laser Texturing of Battery Materials: A Review of Tuning Electrochemical Performances, Related Material Development, and Prospects for Large-Scale Manufacturing. *Int. J. Extrem. Manuf.* **2020**, *3*, 1. [CrossRef]
25. Zheng, Y.; Seifert, H.; Shi, H.; Zhang, Y.; Kübel, C.; Pflüger, W. 3D silicon/graphite composite electrodes for high-energy lithium-ion batteries. *Electrochim. Acta* **2019**, *317*, 502–508. [CrossRef]
26. Smyrek, P.; Pröll, J.; Seifert, H.; Pflüger, W. Laser-induced breakdown spectroscopy of laser-structured Li (NiMnCo) O₂ electrodes for lithium-ion batteries. *J. Electrochem. Soc.* **2015**, *163*, A19. [CrossRef]
27. Levi, M.; Levi, E.; Aurbach, D. The mechanism of lithium intercalation in graphite film electrodes in aprotic media. Part 2. Potentiostatic intermittent titration and in situ XRD studies of the solid-state ionic diffusion. *J. Electroanal. Chem.* **1997**, *421*, 89–97. [CrossRef]
28. Levi, M.D.; Aurbach, D. The mechanism of lithium intercalation in graphite film electrodes in aprotic media. Part 1. High resolution slow scan rate cyclic voltammetric studies and modeling. *J. Electroanal. Chem.* **1997**, *421*, 79–88. [CrossRef]
29. Datta, M.K.; Kumta, P.N. In situ electrochemical synthesis of lithiated silicon–carbon based composites anode materials for lithium ion batteries. *J. Power Sources* **2009**, *194*, 1043–1052. [CrossRef]
30. Li, J.; Dahn, J. An in situ X-ray diffraction study of the reaction of Li with crystalline Si. *J. Electrochem. Soc.* **2007**, *154*, A156. [CrossRef]
31. Reyes Jiménez, A.; Klöpsch, R.; Wagner, R.; Rodehorst, U.C.; Kolek, M.; Nölle, R.; Winter, M.; Placke, T. A Step toward High-Energy Silicon-Based Thin Film Lithium Ion Batteries. *ACS Nano* **2017**, *11*, 4731–4744. [CrossRef]
32. Baggetto, L.; Niessen, R.A.H.; Roozeboom, F.; Notten, P.H.L. High Energy Density All-Solid-State Batteries: A Challenging Concept Towards 3D Integration. *Adv. Funct. Mater.* **2008**, *18*, 1057–1066. [CrossRef]
33. Obrovac, M.; Christensen, L. Structural changes in silicon anodes during lithium insertion/extraction. *Electrochem. Solid State Lett.* **2004**, *7*, A93. [CrossRef]
34. Habedank, J.B.; Kraft, L.; Rheinfeld, A.; Krezdorn, C.; Jossen, A.; Zaeh, M.F. Increasing the discharge rate capability of lithium-ion cells with laser-structured graphite anodes: Modeling and simulation. *J. Electrochem. Soc.* **2018**, *165*, A1563–A1573. [CrossRef]
35. Zhang, N.; Zheng, Y.; Trifonova, A.; Pflüger, W. Laser structured Cu foil for high-performance lithium-ion battery anodes. *J. Appl. Electrochem.* **2017**, *47*, 829–837. [CrossRef]
36. Yuan, G.; Li, X.; Dong, Z.; Westwood, A.; Cui, Z.; Cong, Y.; Du, H.; Kang, F. Graphite blocks with preferred orientation and high thermal conductivity. *Carbon* **2012**, *50*, 175–182. [CrossRef]
37. Zheng, Y.; Pfäffl, L.; Seifert, H.J.; Pflüger, W. Lithium Distribution in Structured Graphite Anodes Investigated by Laser-Induced Breakdown Spectroscopy. *Appl. Sci.* **2019**, *9*, 4218. [CrossRef]
38. Hatchard, T.; Dahn, J. In situ XRD and electrochemical study of the reaction of lithium with amorphous silicon. *J. Electrochem. Soc.* **2004**, *151*, A838. [CrossRef]
39. Markevich, E.; Salitra, G.; Aurbach, D. Fluoroethylene Carbonate as an Important Component for the Formation of an Effective Solid Electrolyte Interphase on Anodes and Cathodes for Advanced Li-Ion Batteries. *ACS Energy Lett.* **2017**, *2*, 1337–1345. [CrossRef]



Article

Gallium-Telluride-Based Composite as Promising Lithium Storage Material

Vo Pham Hoang Huy, Il Tae Kim * and Jaehyun Hur *

Department of Chemical and Biological Engineering, Gachon University, Seongnam 13120, Gyeonggi, Korea

* Correspondence: itkim@gachon.ac.kr (I.T.K.); jhhur@gachon.ac.kr (J.H.)

Abstract: Various applications of gallium telluride have been investigated, such as in optoelectronic devices, radiation detectors, solar cells, and semiconductors, owing to its unique electronic, mechanical, and structural properties. Among the various forms of gallium telluride (e.g., GaTe, Ga₃Te₄, Ga₂Te₃, and Ga₂Te₅), we propose a gallium (III) telluride (Ga₂Te₃)-based composite (Ga₂Te₃-TiO₂-C) as a prospective anode for Li-ion batteries (LIBs). The lithiation/delithiation phase change mechanism of Ga₂Te₃ was examined. The existence of the TiO₂-C hybrid buffering matrix improved the electrical conductivity as well as mechanical integrity of the composite anode for LIBs. Furthermore, the impact of the C concentration on the performance of Ga₂Te₃-TiO₂-C was comprehensively studied through cyclic voltammetry, differential capacity analysis, and electrochemical impedance spectroscopy. The Ga₂Te₃-TiO₂-C electrode showed high rate capability (capacity retention of 96% at 10 A g⁻¹ relative to 0.1 A g⁻¹) as well as high reversible specific capacity (769 mAh g⁻¹ after 300 cycles at 100 mA g⁻¹). The capacity of Ga₂Te₃-TiO₂-C was enhanced by the synergistic interaction of TiO₂ and amorphous C. It thereby outperformed the majority of the most recent Ga-based LIB electrodes. Thus, Ga₂Te₃-TiO₂-C can be thought of as a prospective anode for LIBs in the future.

Keywords: Ga₂Te₃; Ga₂Te₃-TiO₂-C; anodes; Li-ion batteries; lithiation/delithiation

1. Introduction

In recent decades, the rapidly growing desire for portable electronics, electric vehicles, and smart grids has resulted in innovative Li-ion batteries (LIBs) with high energy densities. However, the conventional carbonaceous anodes utilized in LIB systems have low capacities and rate capabilities, making LIBs unsuitable for meeting the requirements of advanced devices. This has necessitated the discovery of new high-performance electrode materials [1–7]. Li alloys containing components, for instance, Ge, Si, Sb, and Sn, have been proposed as attractive alternatives to high-performance LIBs because their theoretical capacities are considerably higher (Li-Ge: 1384 mAh g⁻¹, Li-Si: 3590 mAh g⁻¹, Li-Sn: 993.4 mAh g⁻¹, Li-Sb: 660 mAh g⁻¹) than those of commercial graphite anodes (372 mAh g⁻¹) [8–22]. However, the cycling instabilities of these alloys, which are associated with significant volume changes during Li insertion/extraction, have limited their commercialization [23–28].

With the ability to alloy with two Li-ions ((Li₂Ga), Ga is deemed a feasible anode material for LIB. This provides theoretical Li-storage specific capacities of 769 mAh g⁻¹, respectively. Furthermore, Ga anodes have high theoretical volumetric Li-storage capacities (4545 mAh cm⁻³) due to the high density of Ga (5.91 g cm⁻³ at ambient temperature) [29,30]. As a result, various Ga-based anodes have been studied; however, they generally experience liquid agglomeration during cycling because of the low melting temperature of Ga (29.8 °C), leading to low cycling performance [31–36].

Among the chalcogenide elements, S- and Se-based alloys or composite materials have been widely selected as anode materials in rechargeable LIB systems [37–48]. Te has recently been investigated as a viable electrode material for LIBs [49–51]. When utilized as an electrode material, Te has various advantages over other chalcogen group elements.

Te possesses the highest electronic conductivity among all nonmetallic materials (approximately $2 \times 10^{-2} \text{ S cm}^{-1}$), which is significantly greater than those of S (approximately $5 \times 10^{-16} \text{ S cm}^{-1}$) and Se (approximately $1 \times 10^{-4} \text{ S cm}^{-1}$). Furthermore, Te retains a high theoretical volumetric capacity (Li: 2621 mAh cm^{-3}), which is associated with its high density (6.24 g cm^{-3}) [51]. However, Te cannot overcome the capacity fading attributed to the large volume variation during cycling [52–61].

Various applications of gallium telluride, which is a binary compound of Ga and Te, have been studied, such as optoelectronic devices, radiation detectors, solar cells, and semiconductors, owing to its unique electronic, mechanical, and structural properties [62–65]. Among various gallium tellurides (GaTe , Ga_3Te_4 , Ga_2Te_3 , and Ga_2Te_5), Ga_2Te_3 is a steady compound that is odorless, black, brittle, and non-toxic. Because Ga_2Te_3 has a high melting point of 789°C , and it does not undergo Ga dissolution and agglomeration during cycling, it can be safely used as a LIB anode material [66]. In addition, the high density (5.57 cm^{-3}) of Ga_2Te_3 allows for high theoretical volumetric capacities for LIBs (2858 mAh cm^{-3}) [67]. Despite these suitable features, the application of Ga_2Te_3 as an LIB anode material has not been studied in detail. In addition, ordinary considerations such as unstable stability, irreversible capacity, and inferior Coulombic efficiency remain significant challenges due to the large volume expansion during electrochemical reactions. Thus, an efficient strategy is needed to achieve stable and high-performance anode materials. To this end, many approaches have been investigated to resolve the aforementioned issues. The employment of diverse carbonaceous materials (including graphite, carbon nanotubes, porous carbon, carbon black, carbon fiber, and graphene (or reduced graphene oxide)) to active materials has been demonstrated as an effective approach [68–73]. The carbon-based materials not only buffer the large volume change of active materials and prevent electrode pulverization but also enhance the electrical conductivity. Nevertheless, the presence of excess carbon concentration leads to a specific capacity reduction due to its low theoretical capacity. Another strategy is to create a composite or compound that contains passive metal elements (such as Ni, Cu, Fe, Co, V, and Mo) that are alloyed with the active material to improve its mechanical and electrical conductivity [74–79]. As a last effective strategy for preventing volume change, ceramic-based materials such as TiO_2 , TiC , Al_2O_3 , Si_3N_4 , and MgO are cooperated with active materials [80–84]. Although certain ceramics possess low specific capacities, they can prevent agglomeration and volume changes in the active material owing to their great mechanical properties.

In this work, we synthesized a Ga_2Te_3 -based composite electrode ($\text{Ga}_2\text{Te}_3\text{-TiO}_2\text{-C}$) using simple high-energy ball milling (HEBM) and demonstrated its suitability for LIB anodes. The feasibility of the $\text{Ga}_2\text{Te}_3\text{-TiO}_2\text{-C}$ anode for LIBs was examined by performing galvanostatic measurements, differential capacity analysis, and electrochemical impedance spectroscopy (EIS). More importantly, the Li insertion/extraction electrochemical phase-change mechanism of $\text{Ga}_2\text{Te}_3\text{-TiO}_2\text{-C}$ anodes was studied via *ex situ* X-ray diffraction (XRD) analysis. The optimal C concentration of the $\text{Ga}_2\text{Te}_3\text{-TiO}_2\text{-C}$ composite was determined through various electrochemical measurements of the as-prepared LIBs. $\text{Ga}_2\text{Te}_3\text{-TiO}_2\text{-C}$ (10%) exhibited high cycling and rate performances comparable to those of the most recent Ga-based electrodes.

2. Experimental Materials and Methods

2.1. Material Synthesis

Ga_2Te_3 was synthesized using simple HEBM, as shown in Figure 1. In the first step, a mixture of Ga_2O_3 (99.99%, Sigma Aldrich, St. Louis, MI, USA), Te powder (99.8%, Alfa Aesar, Haverhill, MA, USA), and Ti (325 mesh, 99.99%, Alfa Aesar), in a molecular ratio of 2:3:6 was placed in a bowl containing zirconium oxide balls. The ratio of the balls and powder mixture was 20:1. The powder compound was ball milled for 10 h at 300 rpm under an Ar atmosphere. In the second step, the obtained powder ($\text{Ga}_2\text{Te}_3\text{-TiO}_2$) was mixed with acetylene carbon black powder (C) (99.9+%, Alfa Aesar, bulk density: $170\text{--}230 \text{ g L}^{-1}$, S.A.: $75 \text{ m}^2 \text{ g}^{-1}$) in mass ratios of 9:1, 8:2, and 7:3 (denoted as $\text{Ga}_2\text{Te}_3\text{-TiO}_2\text{-C}$

(10%), Ga₂Te₃-TiO₂-C (20%), and Ga₂Te₃-TiO₂-C (30%), respectively). These combinations were manually ground and then subjected to a 10-h ball milling process under identical conditions as the initial milling. The following is the mechanochemical reaction route for synthesizing Ga₂Te₃-TiO₂-C:

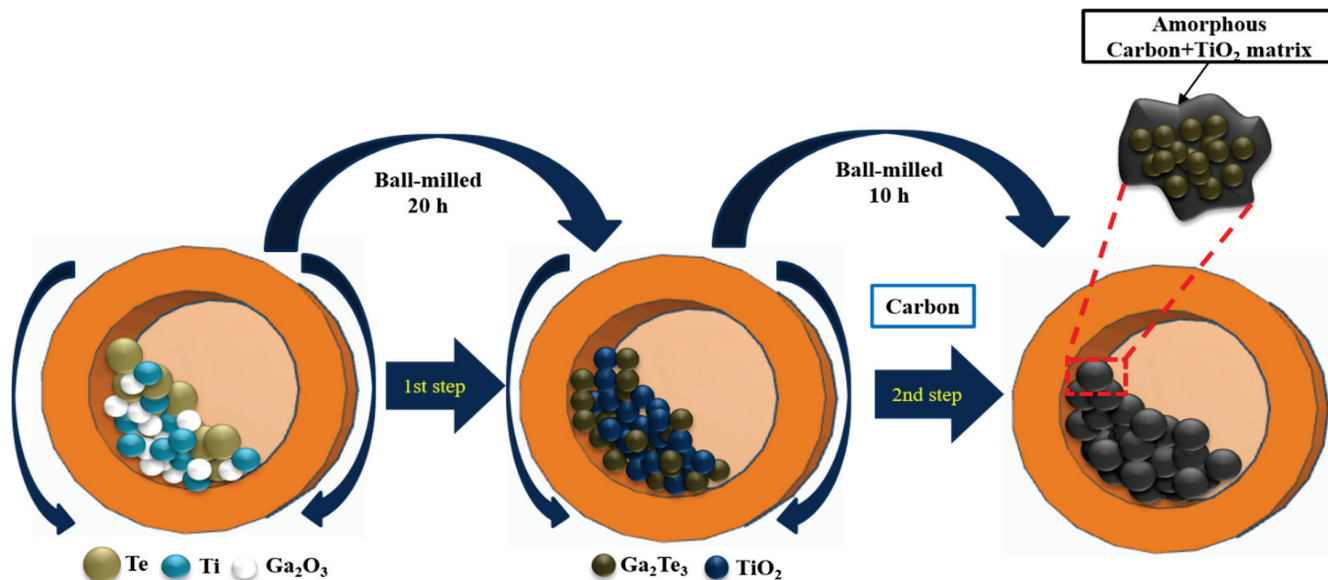


Figure 1. Schematic of Ga₂Te₃-TiO₂-C synthesis using two-step HEBM process.

First step:



Second step:



2.2. Material Characterization

Ga₂Te₃-TiO₂ and Ga₂Te₃-TiO₂-C crystal structures were determined using powder XRD (D/MAX-2200 Rigaku, Japan) with Cu K α ($\lambda = 1.54 \text{ \AA}$) radiation at a scan rate of 2° min^{-1} . High-resolution transmission electron microscopy (HRTEM, JEOL JEM-2100F), scanning electron microscopy (SEM, Hitachi S4700, Japan), and energy-dispersive X-ray spectroscopy (EDXS) were employed to examine the microscopic morphology of the as-synthesized composite materials. The chemical states of the produced materials were assessed using X-ray photoelectron (XP) spectroscopy (XPS, Kratos Axis Anova). Ga₂Te₃-TiO₂-C anode reaction process was investigated using ex situ XRD.

2.3. Electrochemical Measurements

A conventional casting technique was used to prepare all of the electrodes. Briefly, a slurry including the active material, poly (acrylic acid) (PAA, Mw 450000, Sigma Aldrich) binder, and conductive carbon (Super-P, 99.9%, Alfa Aesar) in a ratio of 7.0:1.5:1.5 (w/w) was dissolved into the N-methyl-2-pyrrolidone (NMP) solution with the solid-to-liquid ratio of 1:12.5, and then casted on a Cu foil current collector. The cast electrodes were transferred to an Ar gas-filled glove box for cell assembly after being dried in a vacuum oven overnight at 70°C to completely eliminate the solvent residue. For half-cell testing, a coin-type cell (CR2032) was utilized with Li metal foil as a counter electrode, polyethylene as a separating membrane, and 1 M LiPF₆ in diethyl carbonate/ethylene carbonate (1:1 by v/v) as an electrolyte. Using a battery-testing device (WBCS3000, WonATech, South Korea), the electrochemical performance of Ga₂Te₃-TiO₂-C was assessed. When compared to Li/Li⁺, a 0.01 to 2.5 V voltage range was applied to establish the galvanostatic charge–discharge

(GCD) profile. To describe the electrochemical responses of the electrodes with Li^+ , cyclic voltammetry (CV) analyses were conducted at a scanning rate of 0.1 mV s^{-1} . A battery cycler (WBCS3000, WonATech) was used to measure the rate capability at various current densities (0.1, 0.5, 1, 3, 5, and 10 A g^{-1}), and the current densities are calculated based on the per gram Ga_2Te_3 . The EIS was conducted using a ZIVE MP1 (WonaTech) analyzer in the frequency range of 100 kHz–100 MHz at an AC amplitude of 10 mV.

3. Results and Discussion

The XRD pattern of the as-synthesized $\text{Ga}_2\text{Te}_3\text{-TiO}_2$ obtained by HEBM is shown in Figure 2a. The XRD pattern was the same as that of monoclinic Ga_2Te_3 . The peaks at 26.2° , 30.3° , 43.4° , 51.4° , 53.8° , 63.0° , 69.4° , and 79.5° corresponded to the (111), (200), (220), (311), (222), (400), (331), and (422) planes of Ga_2Te_3 , respectively. The relatively small peaks observed at 28.6° , 33.3° , 44.5° , and 75.6° were attributed to the (002), (311), (601), and (623) planes of TiO_2 , respectively. The insignificant TiO_2 peaks below 20° are associated with the low TiO_2 content in the composite (as shown in Figure S1) [85,86]. The addition of amorphous C decreased the crystallinity of Ga_2Te_3 and TiO_2 in $\text{Ga}_2\text{Te}_3\text{-TiO}_2\text{-C}$ (Figure S2) [87]. It was clear that the target product had been completely transformed from the raw elements by a solid-state reaction because there were no impurity peaks for the precursor components (Ga, Ti, Te or Ga_2O_3). The chemical bonding of $\text{Ga}_2\text{Te}_3\text{-TiO}_2\text{-C}$ (10%) was assessed using XPS (Figure 2b–g). The presence of Ga, Te, O, Ti, and C in $\text{Ga}_2\text{Te}_3\text{-TiO}_2\text{-C}$ (10%) was shown in the XPS survey spectrum in Figure 2b, along with their specific binding energies. The Ga 3d orbital level signal in Figure 2c corresponded to Ga 3d_{3/2} (20.9 eV) and Ga 3d_{5/2} (19.8 eV), whereas the peaks in Figure 2d were ascribed to Te 3d_{3/2} (583.9 eV) and Te 3d_{5/2} (573.6 eV), which confirms the formation of Ga_2Te_3 alloy after the HEBM process. Furthermore, the existence of Te–O bonding with signals at 576.0 and 586.4 eV (Figure 2d) on the $\text{Ga}_2\text{Te}_3\text{-TiO}_2\text{-C}$ (10%) surface implied that partial surface oxidation of active Ga_2Te_3 [88,89]. Although obvious oxidation is observed for Ga_2Te_3 , the air does not seem to have too much of an effect on anode composites. Indeed, there were no impurities nor significant compositional changes for the composite anode (Figure S7) compared with the as-synthesized $\text{Ga}_2\text{Te}_3\text{-TiO}_2\text{-C}$ (10%) powder (Figure S4). In addition, oxidation was mainly observed for Te due to the Te-rich compound of Ga_2Te_3 . As shown in Figure S1, the atomic percent of Te (27%) was greater than that of Ga (17%). Therefore, Te sites seem to be more affected by the rapid oxidation in air [90]. Ga 3D hybridization was found because of the constitution of the O 2s peak at 23.7 eV [86,91]. Regarding the formation of TiO_2 , Ti–O binding was demonstrated through the detection of the orbital level signals of Ti 2p_{3/2} (458.9 eV) and Ti 2p_{1/2} (464.6 eV) (Figure 2e) along with the O 1s peak (530.9 eV) (Figure 2f). More importantly, the binding energy level in the O 1s spectrum at 532.3 eV (Figure 2f) showed the formation of hydroxide groups on the active surface of Ga_2Te_3 , implying hydrogen bond formation with functional moieties (carboxylate functional groups) of PAA binder due to its possessing high affinity. The strong binding between the PAA binder and hydroxides on Ga_2Te_3 is expected to prevent particle agglomeration and maintain good contact between the current collector and electrode [86,92]. The XPS results of C 1s in Figure 2g showed binding energies at 284.6, 285.0, and 285.9 eV, which indicate C–C, C–O–C, and C–O=C bonds, respectively. These results confirmed the constitution of the target ternary composites (Ga_2Te_3 , TiO_2 , and C for $\text{Ga}_2\text{Te}_3\text{-TiO}_2\text{-C}$ (10%)).

Morphological and structural analyses of $\text{Ga}_2\text{Te}_3\text{-TiO}_2\text{-C}$ (10%) were investigated using SEM, HRTEM, and EDXS, as shown in Figure 3. The SEM images showed that the particle size ranged from submicrometers to a few micrometers (Figure 3a,b). The HRTEM images (Figures 3c and S3) revealed crystalline lattice spacings of 0.340, 0.294, 0.208, and 0.170 nm, which corresponded to the (111), (200), (220), and (222) planes of Ga_2Te_3 , respectively, and 0.311 nm attributed to the (002) plane of TiO_2 . Additionally, amorphous C was created as a flat surface layer around Ga_2Te_3 and TiO_2 , and it was anticipated to serve as a buffering matrix for the active material. In the $\text{Ga}_2\text{Te}_3\text{-TiO}_2\text{-C}$ (10%) sample, the EDXS mapping analysis of the scanning transmission electron microscopy image (Figure 3d)

revealed a homogeneous dispersion of each element (Ga, Te, Ti, O, and C). Furthermore, the SEM–EDXS analysis results (Figure S4) of $\text{Ga}_2\text{Te}_3\text{-TiO}_2\text{-C}$ (10%) consistently showed that the component elements were uniformly scattered throughout the composite. Additionally, the quantitative examination of the EDS results demonstrated that the stoichiometric ratio of the component elements was nearly similar to the theoretical values.

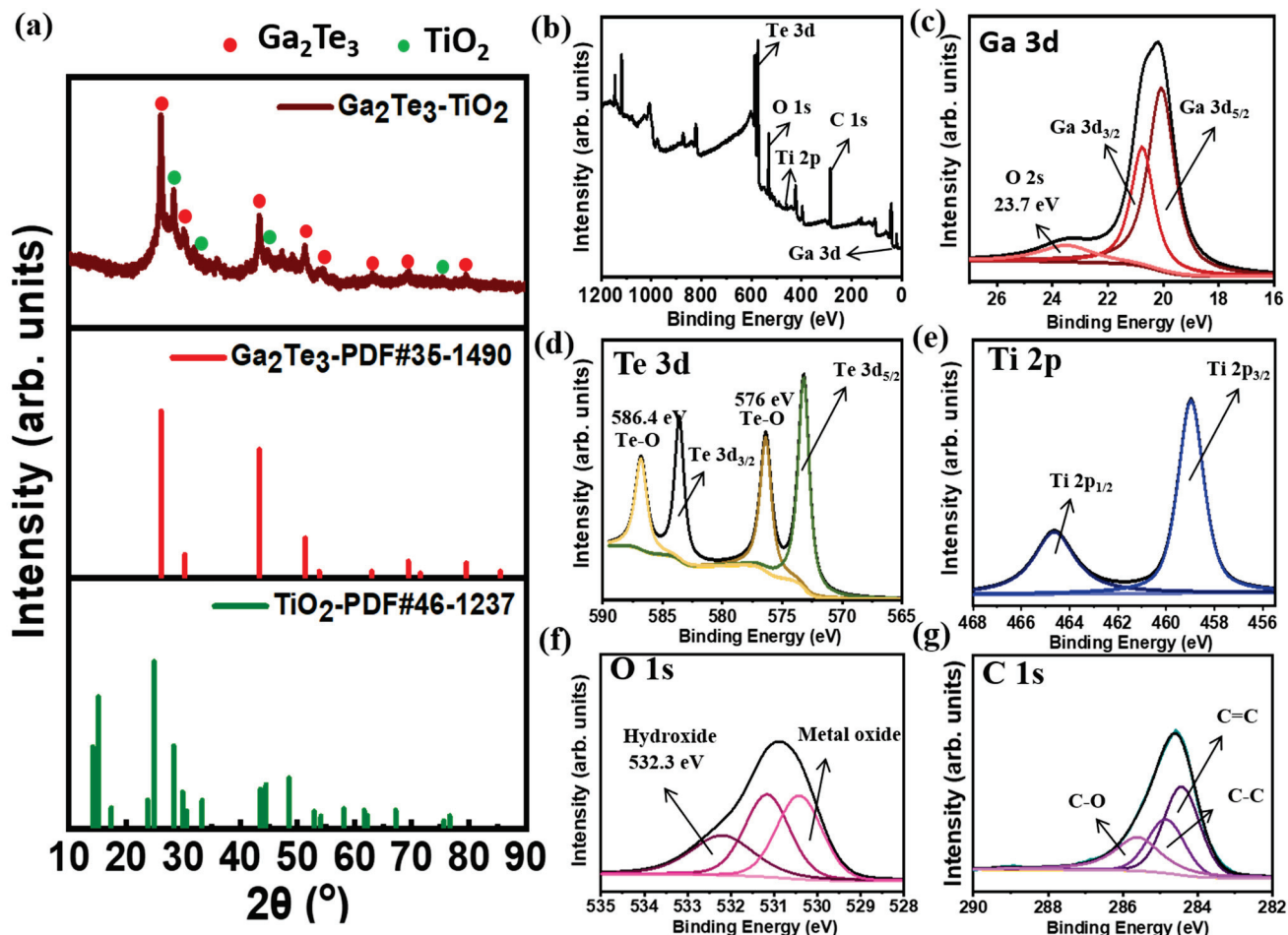


Figure 2. (a) XRD pattern of $\text{Ga}_2\text{Te}_3\text{-TiO}_2$; (b) XPS survey spectrum; (c) high-resolution XP spectra of Ga 3d; (d) Te 3d; (e) Ti 2p; (f) O 1s and (g) C 1s for $\text{Ga}_2\text{Te}_3\text{-TiO}_2\text{-C}$ (10%).

$\text{Ga}_2\text{Te}_3\text{-TiO}_2\text{-C}$ with various C content for LIBs was investigated electrochemically using half-cells electrode systems (Figure 4). The GCD voltage profiles of $\text{Ga}_2\text{Te}_3\text{-TiO}_2\text{-C}$ (10%), $\text{Ga}_2\text{Te}_3\text{-TiO}_2\text{-C}$ (20%), and $\text{Ga}_2\text{Te}_3\text{-TiO}_2\text{-C}$ (30%) are shown in Figure 4a and Figure S8. The first discharge/charge performance of $\text{Ga}_2\text{Te}_3\text{-TiO}_2\text{-C}$ (10%), $\text{Ga}_2\text{Te}_3\text{-TiO}_2\text{-C}$ (20%), and $\text{Ga}_2\text{Te}_3\text{-TiO}_2\text{-C}$ (30%) were 892/677, 837/586, and 789/568 mAh g^{-1} , respectively, which corresponded to initial Coulombic efficiencies (ICEs) of 75.9%, 70.0%, and 71.9%, respectively. The three electrodes experienced irreversible capacity losses in the initial cycle that were attributed to the development of a solid electrolyte interfacial (SEI) layer. On the basis of the EDXS results (Figure S4) and the computed theoretical capacities of the separate elements (Table S1), the capacity contributions of C and TiO_2 to $\text{Ga}_2\text{Te}_3\text{-TiO}_2\text{-C}$ (10%) were estimated to be ~9% and ~16%, respectively. Therefore, active Ga_2Te_3 (75% of the total capacity) was the principal source of the capacity of the electrode. The primary role of C and TiO_2 was as a buffering matrix (25% capacity involvement), which reduced the volume variation of the active material. Furthermore, the theoretical capacity contribution of different components in $\text{Ga}_2\text{Te}_3\text{-TiO}_2\text{-C}$ (20 and 30%) was also determined (Tables S2 and S3). Compared with $\text{Ga}_2\text{Te}_3\text{-TiO}_2\text{-C}$ (10%), increase in the C concentration results in a decrease in the capacity contribution of active material. Based on Figures S4–S6

and Tables S1–S3, the calculated capacity contribution of the active material Ga_2Te_3 was 75, 61, and 53%, resulting in the actual Ga_2Te_3 capacity of ~ 576 , ~ 401 , and ~ 314 mAh g^{-1} for the $\text{Ga}_2\text{Te}_3\text{-TiO}_2\text{-C}$ (10%), $\text{Ga}_2\text{Te}_3\text{-TiO}_2\text{-C}$ (20%), and $\text{Ga}_2\text{Te}_3\text{-TiO}_2\text{-C}$ (30%), respectively. Notably, the measured capacities of $\text{Ga}_2\text{Te}_3\text{-TiO}_2\text{-C}$ (10%) and $\text{Ga}_2\text{Te}_3\text{-TiO}_2$ (455 and 477 mAh g^{-1} , respectively, as computed in Table S4) that were higher than their theoretical capacities are most likely ascribed to the interfacial Li-ion storage and electrolyte decomposition. The specific performance of the lowest C content electrode ($\text{Ga}_2\text{Te}_3\text{-TiO}_2\text{-C}$ (10%)) was the highest in terms of stability and capacity. It reached 768.9 mAh g^{-1} with capacity retention (CR) of 99.8% after 300 cycles at 100 mA g^{-1} (Figure 4b). The specific capacities of $\text{Ga}_2\text{Te}_3\text{-TiO}_2\text{-C}$ (20%) and $\text{Ga}_2\text{Te}_3\text{-TiO}_2\text{-C}$ (30%) were 587.3 and 585.3 mAh g^{-1} after 300 cycles at 100 mA g^{-1} , respectively, which corresponded to a CR of 89.2% and 98.7%, respectively. This behavior was further explained using Coulombic efficiency (CE, Table S5) and differential capacity plot (DCP) analyses of the first 300 cycles (Figure S9). The CE increased gradually and steadily. Particularly, the CE achieved almost 99.13% after 150 cycles, with the possibility that side reactions were involved until this point. Then, the CE decreased slightly and stabilized at 98.5% after 300 cycles. The DCP analysis showed that the main reduction peaks (at ~ 1.22 and ~ 1.69 V) remained unchanged for 300 cycles. However, the oxidation peaks (at ~ 0.41 , ~ 0.98 , and ~ 1.25 V) were stable for 100 cycles, after which they became broader and shifted toward a high voltage. Nevertheless, this polarization had an almost negligible effect on the lithiation/delithiation, resulting in a stable capacity after 300 cycles. This was because the TiO_2 matrix and lowest C content (10%) effectively prevented the side reactions that could result from good electrode–electrolyte contact at 100 mA g^{-1} . At 500 mA g^{-1} , a similar trend was observed (Figure 4c). In this instance, the performance increased until 250 cycles, then slightly decreased, and finally became saturated (~ 600 mAh g^{-1}). The CE variation (Table S6) and DCP analysis both showed this tendency (Figures S10 and S11). According to Figure S10, the magnitudes of the reduction (at ~ 0.98 and ~ 1.69 V) and the oxidation (at ~ 0.41 , ~ 1.58 , and ~ 1.85 V) rose for 200 cycles with a decrease in polarization and then reduced after 200 cycles with a minor increase in polarization. This was followed by a reduction in polarization after 400 cycles (Figure S11). Therefore, although the capacity decreased from 250 cycles to 400 cycles, it saturated after 400 cycles. Under a high current density, an electrode requires demanding lithiation/delithiation conditions (500 mA g^{-1}). This makes it more difficult to achieve steady and stable cycling [93–95]. To comprehend the steady rise in the performance, the variations in the DCP curves, as a function of the cycle number, were studied at 100 and 500 mA g^{-1} (Figure S12). The DCP curves of the $\text{Ga}_2\text{Te}_3\text{-TiO}_2\text{-C}$ (10%) electrode showed that the overall intensity of the redox peaks were relatively stable as the cycle number increased at 100 mA g^{-1} , indicating a stable capacity until 300 cycles. However, at 500 mA g^{-1} , the overall magnitudes of the redox peaks rose with the cycle number until 300 cycles, reduced from 300 cycles to 400 cycles, and became saturated after 400 cycles. The CE variations at 100 and 500 mA g^{-1} of $\text{Ga}_2\text{Te}_3\text{-TiO}_2\text{-C}$ with varied C concentrations were compared in Figure S13. The detailed CE values for the $\text{Ga}_2\text{Te}_3\text{-TiO}_2\text{-C}$ (10%), $\text{Ga}_2\text{Te}_3\text{-TiO}_2\text{-C}$ (20%), and $\text{Ga}_2\text{Te}_3\text{-TiO}_2\text{-C}$ (30%) electrodes over the first ten cycles are described in Table S7 (at 100 mA g^{-1}) and Table S8 (at 500 mA g^{-1}). As displayed in Table S7, the ICE of the $\text{Ga}_2\text{Te}_3\text{-TiO}_2\text{-C}$ (10%) electrode (75.9%) were slightly higher than those of the $\text{Ga}_2\text{Te}_3\text{-TiO}_2\text{-C}$ (20%) (ICE = 69.9%) and $\text{Ga}_2\text{Te}_3\text{-TiO}_2\text{-C}$ (30%) electrodes (ICE = 72.1%). The CE of the $\text{Ga}_2\text{Te}_3\text{-TiO}_2\text{-C}$ (10%) electrode was the highest after ten cycles. At 500 mA g^{-1} , it revealed a similar tendency (Table S8). After the first cycle, the high CE of the $\text{Ga}_2\text{Te}_3\text{-TiO}_2\text{-C}$ (10%) electrode suggested that lithiation/delithiation was highly reversible. The $\text{Ga}_2\text{Te}_3\text{-TiO}_2\text{-C}$ (10%) CV curves for the first five cycles in the voltage range of 0.01–2.5 V vs. Li/Li^+ were shown in Figure 4d. Due to SEI layer formed on the electrode surface, the CV curve in the first cycle was noticeably different from that of the subsequent cycles. The intercalation of Li into Ga_2Te_3 to form Li_2Te and Ga is indicated by a substantial reduction peak at 1.37 V in the first discharge. The peak at 0.98 V was responsible for the interaction between Ga and Li to generate Li_2Ga . Thus, Li_2Te and Li_2Ga were the final

products after the discharge step was completed. The three oxidation peaks were shown at 0.92, 1.56, and 1.88 V in the charge process. The first peak was caused by the complete exclusion of Li, turning Li_2Ga into Ga. Ga began to intrude into Li_2Te to form Ga_2Te_3 when the anode was charged to 1.56 and 1.88 V. In the ex situ analyses, this phase change is examined in detail. After the second cycle, the curves nearly overlapped, indicating the excellent reversibility and stability of $\text{Ga}_2\text{Te}_3\text{-TiO}_2\text{-C}$ (10%). Compared to $\text{Ga}_2\text{Te}_3\text{-TiO}_2\text{-C}$ (10%), $\text{Ga}_2\text{Te}_3\text{-TiO}_2\text{-C}$ (20%) and $\text{Ga}_2\text{Te}_3\text{-TiO}_2\text{-C}$ (30%) showed similar stability in terms of the polarization of the reduction and oxidation peaks after the second cycle (Figure S14). The control experiments of $\text{Ga}_2\text{Te}_3\text{-TiO}_2\text{-C}$ (10%) with PVDF were conducted to better define the role of the PAA binder. The oxidation occurring on the Ga_2Te_3 surface positively affects the electrochemical performance by stabilizing the electrode structure through hydrogen bonding between hydroxyl groups in Ga_2Te_3 and carboxylate groups in the PAA binder. As shown in Figure S15, the cyclic performance of the composite with PAA binder showed significantly enhanced performance compared to the composite with PVDF. Besides, CV curves do not overlap with the increase in the cycle number for the composite with PVDF, indicating the irreversible cycling behavior. This result is consistent with the previous study in which the cycling performance of oxidized active material was enhanced with PAA binder [86]. The rate performances (Figure 4e) and normalized capacity retention values (Figure 4f) of the electrodes were studied at different current densities. In Figure 4e, the average discharge capacities of $\text{Ga}_2\text{Te}_3\text{-TiO}_2\text{-C}$ (10%) were significantly greater than those of $\text{Ga}_2\text{Te}_3\text{-TiO}_2\text{-C}$ (20%) and $\text{Ga}_2\text{Te}_3\text{-TiO}_2\text{-C}$ (30%), which were 708, 706, 687, 665, 636, and 613 mAh g^{-1} at current densities of 0.1, 0.5, 1.0, 3.0, 5.0, and 10.0 A g^{-1} , respectively. Surprisingly, even at a high current density of 10 A g^{-1} , $\text{Ga}_2\text{Te}_3\text{-TiO}_2\text{-C}$ (10%) had capacity retention of up to 96% (Figure 4f). Furthermore, $\text{Ga}_2\text{Te}_3\text{-TiO}_2\text{-C}$ (10%) showed high rate performance when the discharge rate was reduced from 10 A g^{-1} to 0.1 A g^{-1} , resulting in high-capacity retention (99%).

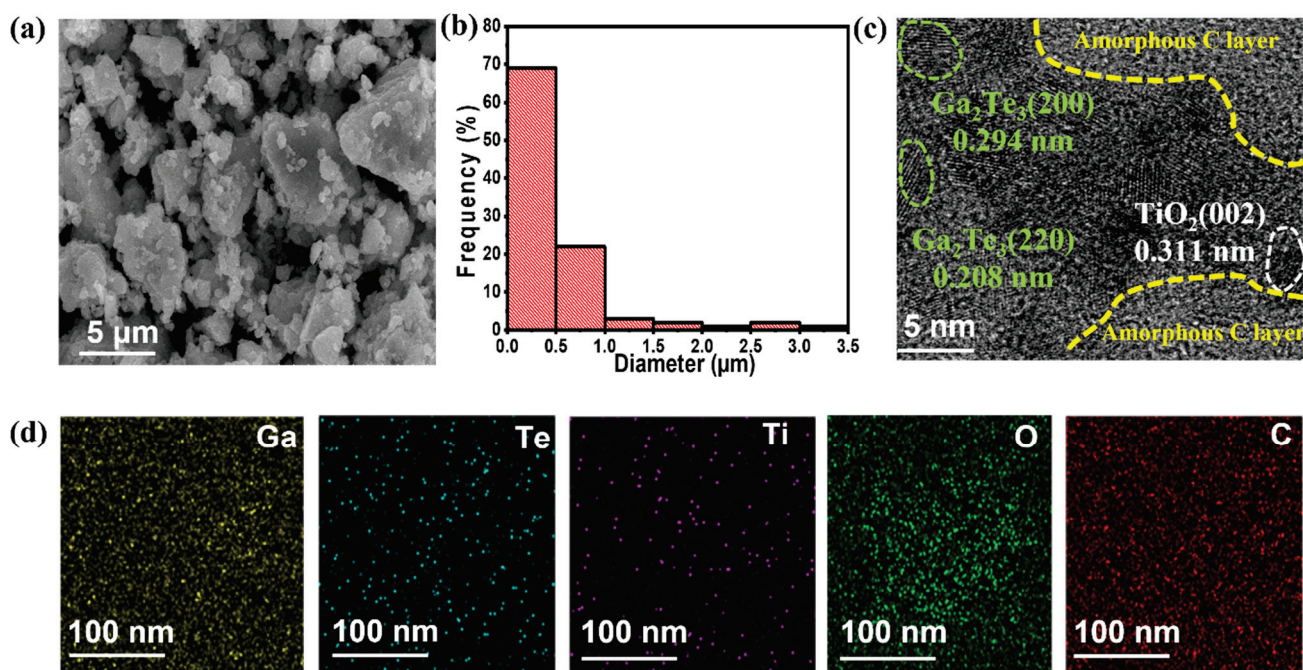


Figure 3. (a) SEM image; (b) particle size distribution; (c) HRTEM image and (d) EDXS elemental mappings of Ga, Te, Ti, O, and C for $\text{Ga}_2\text{Te}_3\text{-TiO}_2\text{-C}$ (10%).

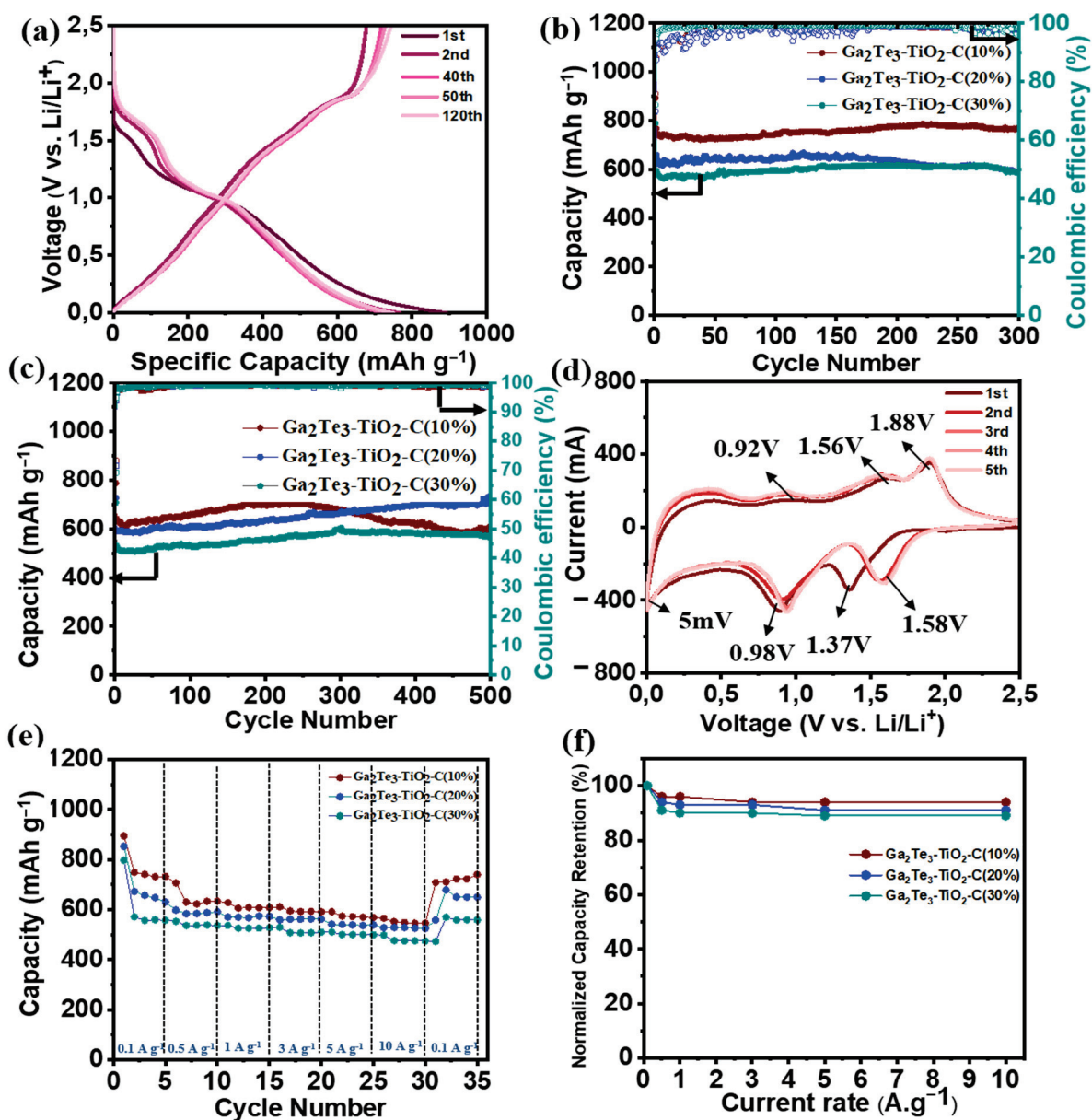


Figure 4. Electrochemical performance of $\text{Ga}_2\text{Te}_3\text{-TiO}_2\text{-C}$ composites for LIBs: (a) GCD curves of $\text{Ga}_2\text{Te}_3\text{-TiO}_2\text{-C}$ (10%) at 100 mA g^{-1} ; (b) cycling performance of $\text{Ga}_2\text{Te}_3\text{-TiO}_2\text{-C}$ composites at 100 mA g^{-1} and (c) 500 mA g^{-1} ; (d) CV curves of $\text{Ga}_2\text{Te}_3\text{-TiO}_2\text{-C}$ (10%); (e) rate capabilities of $\text{Ga}_2\text{Te}_3\text{-TiO}_2\text{-C}$ composites; and (f) capacity retention of $\text{Ga}_2\text{Te}_3\text{-TiO}_2\text{-C}$ composites from 0.1 to 10 A g^{-1} .

The phase change mechanism during the lithiation/delithiation process of the $\text{Ga}_2\text{Te}_3\text{-TiO}_2\text{-C}$ (10%) electrode was investigated using ex situ XRD (Figure 5a). Peaks corresponding to Li_2Te and Ga were observed at a discharge voltage of 1.37 V (D-1.37 V). When the electrode was completely discharged (D-5 mV), Li_2Ga peaks emerged and Li_2Te peaks remained. The Li_2Ga phase partly disappeared when the electrode was charged to 0.92 V (C-0.92 V). In the charging state at 1.56 V, the Li_2Te phase partly disappeared, Ga was observed, and Li_2Ga completely disappeared. Only the peaks corresponding to Ga_2Te_3 were observed again when the electrode was completely charged to 2.5 V (C-2.5 V). Ga_2Te_3 undergoes structural changes during first lithiation/delithiation as follows:

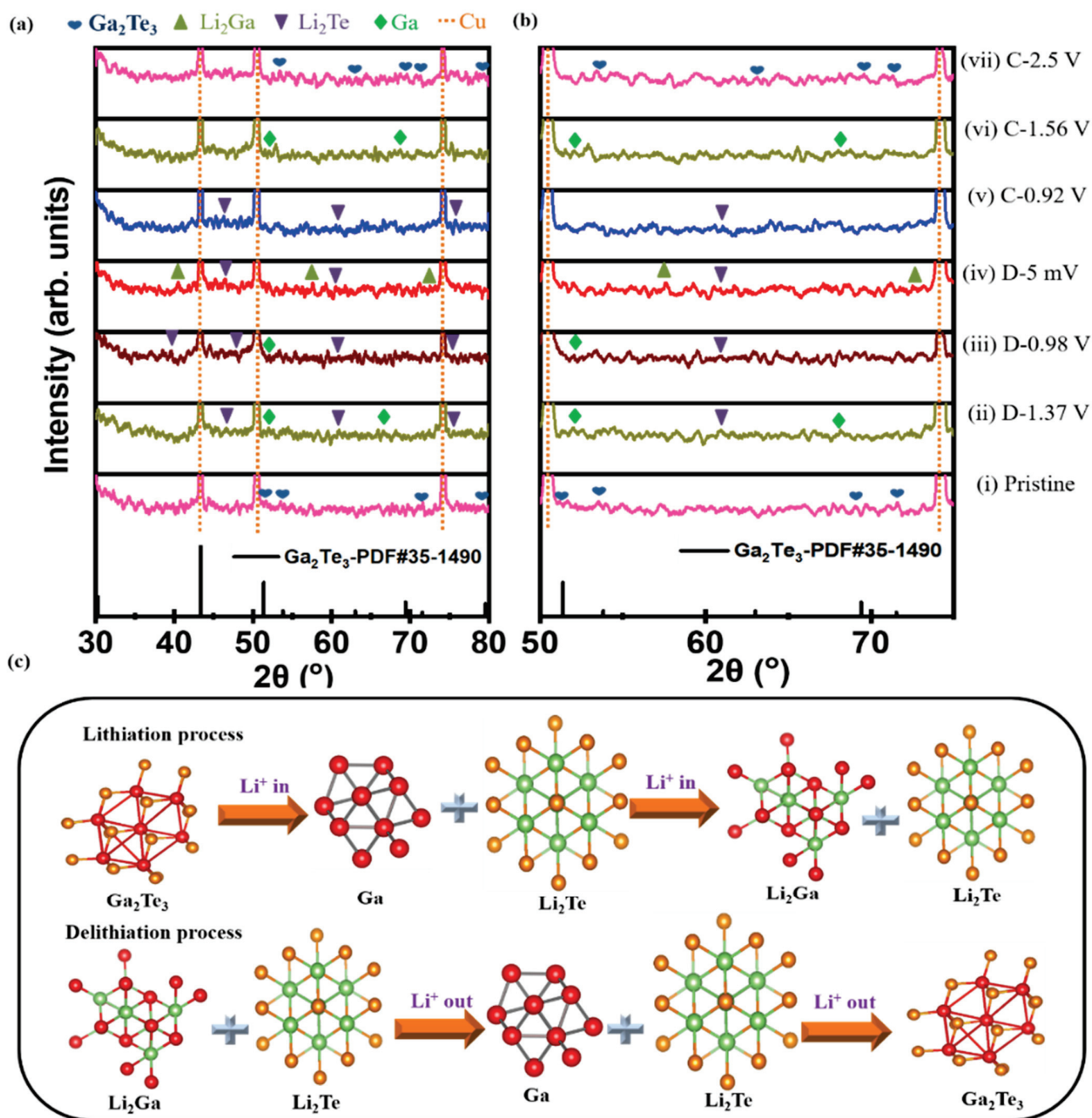
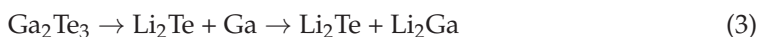


Figure 5. (a,b) Ex situ XRD patterns obtained at selected cutoff potentials in the initial discharge/charge process, and (c) schematics of phase change of Ga_2Te_3 - TiO_2 -C (10%) electrode during cycling.

Discharging:



Charging:



It is noteworthy that after the first cycle, the Ga_2Te_3 phase (major peaks at 51.4° , 53.8° , and 69.4°) was completely restored with no impurity peaks, showing the highly reversible interaction of Ga_2Te_3 with Li-ions. The active material was well shielded from pulverization and delamination because of volume expansion thanks to the strong binding between Ga_2Te_3 and TiO_2 -C. As schematically shown in Figure 5b, the ex situ XRD result

demonstrated the alloying/dealloying and conversion mechanism of the Ga_2Te_3 electrode during the first charge/discharge process.

At the 1st, 5th, and 20th cycles, the EIS profiles of the $\text{Ga}_2\text{Te}_3\text{-TiO}_2\text{-C}$ (10%), $\text{Ga}_2\text{Te}_3\text{-TiO}_2\text{-C}$ (20%), and $\text{Ga}_2\text{Te}_3\text{-TiO}_2\text{-C}$ (30%) electrodes were obtained (Figure 6). The equivalent circuit to fit EIS profile shown in Figure 6d includes the SEI layer resistance (R_{SEI}), charge-transfer resistance (R_{CT}), electrolyte resistance (R_b), interfacial double-layer capacitance (C_{dl}), constant phase element (C_{PE}), and Warburg impedance (Z_w). R_{CT} at the electrode-electrolyte interface is shown by compressed semicircles in the mid-frequency region of the Nyquist plots. As the number of cycles grew from 1 to 20, cells containing various concentrations of C displayed decreasing sizes of semicircles, suggesting that R_{CT} decreased (Figure 6a–c). $\text{Ga}_2\text{Te}_3\text{-TiO}_2\text{-C}$ (10%) showed the lowest value of R_{CT} after 20 cycles (Table S9), indicating the optimal charge transport circumstances, which resulted in the highest electrochemical performance.

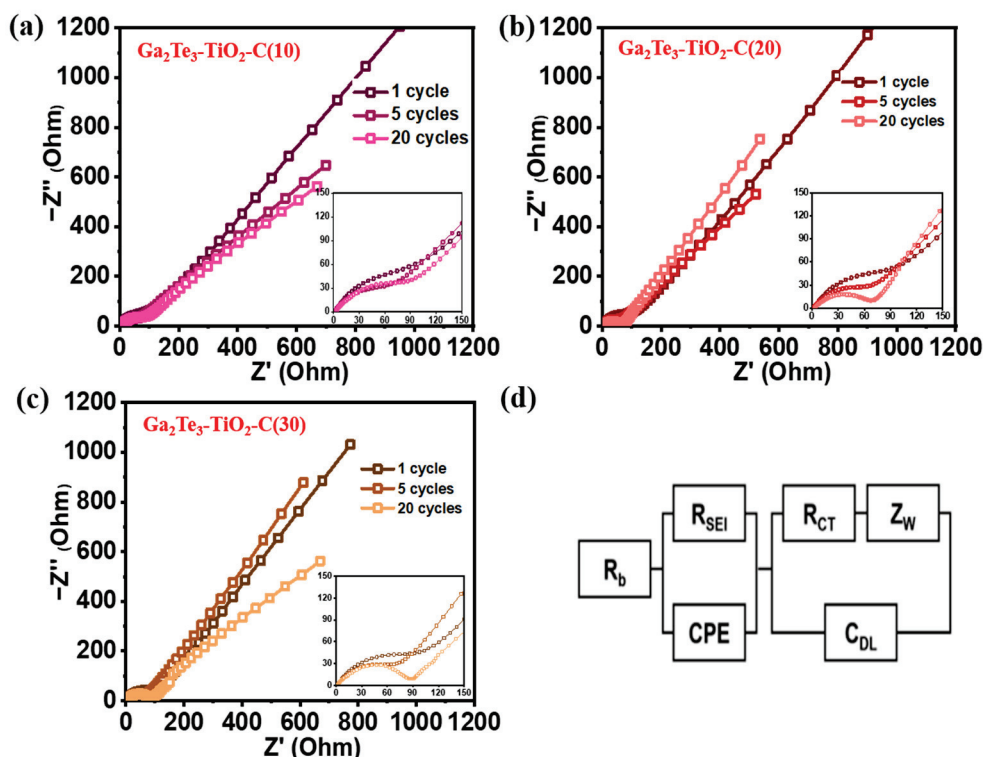


Figure 6. EIS-based Nyquist plots for (a) $\text{Ga}_2\text{Te}_3\text{-TiO}_2\text{-C}$ (10%), (b) $\text{Ga}_2\text{Te}_3\text{-TiO}_2\text{-C}$ (20%), (c) $\text{Ga}_2\text{Te}_3\text{-TiO}_2\text{-C}$ (30%) after 1, 5, and 20 cycles; and (d) equivalent circuit.

The electrochemical Li-storage behaviors were determined from the above results. Because amorphous C was delivered as a buffer to limit volume expansion during the lithiation/delithiation process, the cyclic performance was stable. Nevertheless, the regulation of the C content played an important role. A C content of 10% was sufficient to achieve high electrochemical efficiency for the LIBs. When the C content was increased, the specific capacity was rather decreased due to the reduced active material in the composite. In addition, TiO_2 synergistically prevented electrode pulverization and improved Li-ion diffusion. Therefore, the $\text{Ga}_2\text{Te}_3\text{-TiO}_2\text{-C}$ (10%) electrode showed high electrochemical performance and fast kinetics due to the cooperative impact of the $\text{TiO}_2\text{-C}$ hybrid matrix, as demonstrated in Figure 7. Accordingly, the capacity of the $\text{Ga}_2\text{Te}_3\text{-TiO}_2\text{-C}$ (10%) electrode was higher than those of recently reported Ga-based anodes for LIBs (Table 1).

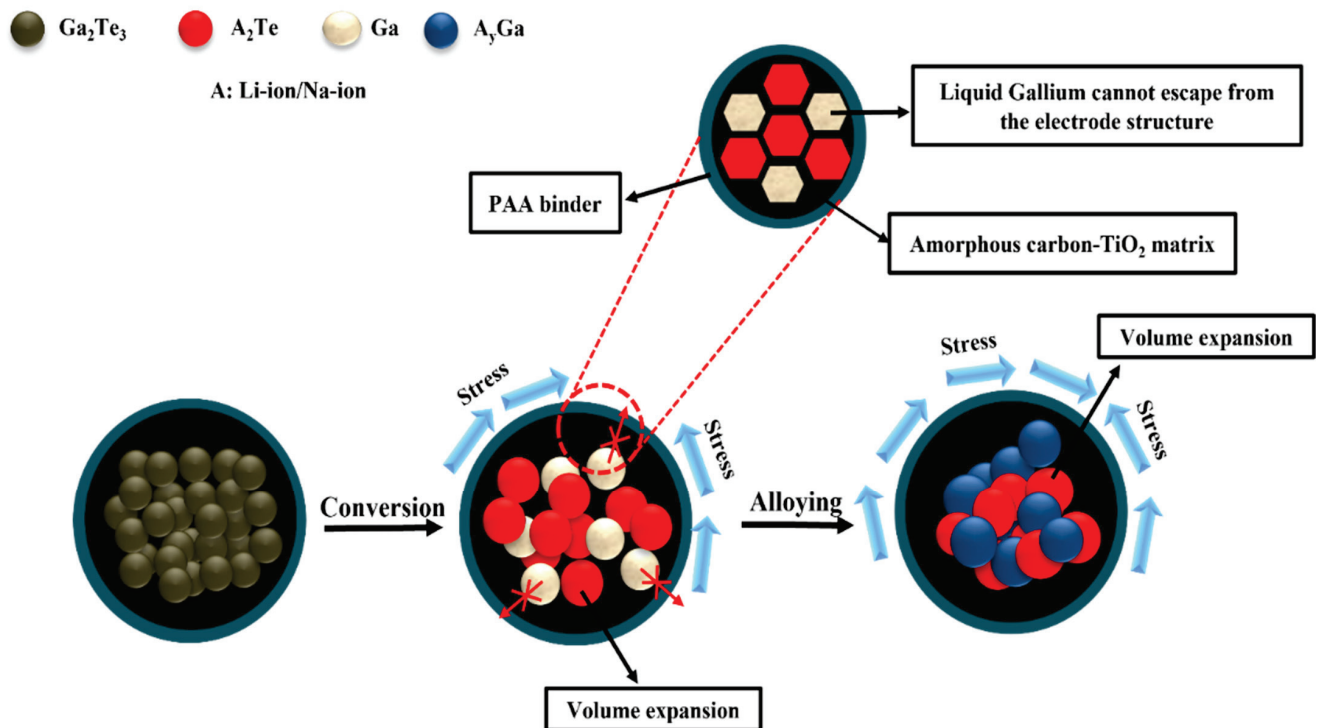


Figure 7. Schematic of reaction mechanism of $\text{Ga}_2\text{Te}_3\text{-TiO}_2\text{-C}$ (10%).

Table 1. Performances of Ga-based intermetallic electrode for LIBs.

Anode	Cycling Performance	Rate Capability	Synthesis Method	Ref.
GaN-CNFs	405 mAh g^{-1} after 1200 cycles at 3 A g^{-1}	310 mAh g^{-1} at 5 A g^{-1}	Electrospinning	[95]
$\alpha\text{-Ga}_2\text{O}_3\text{@G}$	350 mAh g^{-1} after 50 cycles at 0.15 A g^{-1}	344 mAh g^{-1} at 0.5 A g^{-1}	Hydrothermal and sintering process	[96]
$\text{Ga}_2\text{O}_3/\text{rGO}$	411 mAh g^{-1} after 600 cycles at 1 A g^{-1}	222 mAh g^{-1} at 2 A g^{-1}	Sol-gel method	[97]
$\text{Ga}_2\text{O}_3/\text{C}$	542 mAh g^{-1} after 200 cycles at 1 A g^{-1}	192 mAh g^{-1} at 5 A g^{-1}	One-step hydrogen reduction	[98]
Ga-Ni	420 mAh g^{-1} after 500 cycles at 3 C	410 mAh g^{-1} at 5C	Heating process	[99]
CuGa_2	510 mAh g^{-1} after 65 cycles at 2 A g^{-1}	440 mAh g^{-1} at 4 A g^{-1}	Painting liquid Ga onto Cu foil	[100]
GaN/G	600 mAh g^{-1} after 1000 cycles at 1 A g^{-1}	200 mAh g^{-1} at 10 A g^{-1}	Wet chemical method	[101]
Ga_2O_3 NPs	721 mAh g^{-1} after 200 cycles at 0.5 A g^{-1}	280 mAh g^{-1} at 2 A g^{-1}	Hydrothermal carbonization method	[102]
Ga_2S_3	400 mAh g^{-1} after 20 cycles at 0.1 A g^{-1}	-	Commercial material	[103,104]
SWCNT- GaS_x	590 mAh g^{-1} after 100 cycles at 0.6 A g^{-1}	-	Atomic layer deposition	[105]
GaSe	760 mAh g^{-1} after 50 cycles at 0.1 A g^{-1}	450 mAh g^{-1} at 5 A g^{-1}	Chemical reduction method	[106]
Ball-milled $\text{Ga}_2\text{Te}_3/\text{C}$	590 mAh g^{-1} after 500 cycles at 0.1 A g^{-1}	495 mAh g^{-1} at 1C	Ball milling	[107]
$\text{Ga}_2\text{Te}_3\text{-TiO}_2\text{-C}$	769 mAh g^{-1} after 300 cycles at 0.1 A g^{-1}	600 mAh g^{-1} at 10 A g^{-1}	Ball milling	This work

4. Conclusions

$\text{Ga}_2\text{Te}_3\text{-TiO}_2\text{-C}$ was successfully prepared via HEBM and investigated as a propitious anode material for LIBs. The morphology, chemical state, and crystal structure of $\text{Ga}_2\text{Te}_3\text{-TiO}_2\text{-C}$ were investigated through XRD analysis, SEM, EDXS, HRTEM, and XPS. To identify the conversion/recombination reaction mechanism of the Ga_2Te_3 anode during the lithiation/delithiation processes, ex situ XRD analysis was studied. The major strategy for achieving high capacity and long-term cycling performance for the $\text{Ga}_2\text{Te}_3\text{-TiO}_2\text{-C}$

nanocomposite was to homogeneously embed nanoconfined Ga₂Te₃ crystallites within an electronically conductive TiO₂-C matrix. This promoted Li-ion diffusion kinetics and improved the mechanical stability by accommodating the change in the volume of the Ga₂Te₃ particles and preventing the agglomeration of Ga. As a result, the Ga₂Te₃-TiO₂-C electrode showed high rate capability (CR of 96% at 10 A g⁻¹ compared to 0.1 A g⁻¹), as well as great reversible specific capacity (769 mAh g⁻¹ at 100 mA g⁻¹ after 300 cycles). It thereby outperformed the majority of the most recent Ga-based LIB electrodes. The electrochemical performance of Ga₂Te₃-TiO₂-C was enhanced by the synergistic interaction of TiO₂ and amorphous C. Thus, Ga₂Te₃-TiO₂-C can be thought of as a prospective anode material for LIBs of the future.

Supplementary Materials: The following supporting information can be downloaded at: <https://www.mdpi.com/article/10.3390/nano12193362/s1>, Figure S1: EDX spectrum of as-synthesized Ga₂Te₃-TiO₂, Figure S2: XRD pattern of Ga₂Te₃-TiO₂-C with different concentration of C, Figure S3: HRTEM image of Ga₂Te₃-TiO₂-C(10%), Figure S4: EDX spectrum of as-synthesized Ga₂Te₃-TiO₂-C(10%), Figure S5: EDX spectrum of as-synthesized Ga₂Te₃-TiO₂-C(20%), Figure S6: EDX spectrum of as-synthesized Ga₂Te₃-TiO₂-C(30%), Figure S7: EDX spectrum of Ga₂Te₃-TiO₂-C(10%) anode, Figure S8: Galvanostatic discharge-charge profiles of (a) Ga₂Te₃-TiO₂-C(20%) and (b) Ga₂Te₃-TiO₂-C(30%), Figure S9: DCP profiles of Ga₂Te₃-TiO₂-C(10%) during 300 cycles measured at 100 mA g⁻¹: (a) 1–150 cycles and (b) 150–300 cycle. Enlarged view of (c) reduction and (d) oxidation peaks, Figure S10: (a) DCP profiles of Ga₂Te₃-TiO₂-C(10%) during initial 200 cycles measured at 500 mA g⁻¹. Enlarged view of (b) oxidation and (c) reduction peaks, Figure S11: DCP profiles of Ga₂Te₃-TiO₂-C(10%) from 300 cycle to 500 cycles measured at 500 mA g⁻¹. Enlarged view of (b) oxidation and (c) reduction peaks, Figure S12: DCP profiles of Ga₂Te₃-TiO₂-C(10%) at current density (a) at 100 mA g⁻¹ and during 300 cycles and (b) at 500 mA g⁻¹ during 500 cycles, Figure S13: Coulombic efficiency of Ga₂Te₃-TiO₂ with different C content at current densities of (a) 100 and (b) 500 mA g⁻¹, Figure S14: CV curves of (a) Ga₂Te₃-TiO₂-C(20%) and (b) Ga₂Te₃-TiO₂-C(30%) for LIBs, Figure S15: (a) Cycling performance of Ga₂Te₃-TiO₂-C (10%) with PAA and PVDF binder, (b) CV curves of Ga₂Te₃-TiO₂-C(10%) with PVDF binder, Table S1: Calculation of capacity contribution of Ga₂Te₃, TiO₂ and C in the Ga₂Te₃-TiO₂-C(10%) composite in LIB, Table S2: Calculation of capacity contribution of Ga₂Te₃, TiO₂ and C in the Ga₂Te₃-TiO₂-C(20%) composite in LIB, Table S3: Calculation of capacity contribution of Ga₂Te₃, TiO₂ and C in the Ga₂Te₃-TiO₂-C(30%) composite in LIB, Table S4: Calculation of theoretical capacity of Ga₂Te₃-TiO₂-C(10%) and Ga₂Te₃-TiO₂ in LIB, Table S5: Coulombic efficiency variation of Ga₂Te₃-TiO₂-C (10%) at various cycle numbers measured at 100 mA g⁻¹ for LIB, Table S6: Coulombic efficiency variation of Ga₂Te₃-TiO₂-C(10%) at various cycle numbers measured at 500 mA g⁻¹ for LIB, Table S7: Coulombic efficiency of Ga₂Te₃-TiO₂-C at current density of 100 mA g⁻¹ during initial 10 cycles for LIB, Table S8: Coulombic efficiency of Ga₂Te₃-TiO₂-C at current density of 500 mA g⁻¹ during initial 10 cycles for LIB, Table S9: Charge-transfer resistance (R_{ct}) of Ga₂Te₃-TiO₂-C for LIB.

Author Contributions: Conceptualization, J.H. and I.T.K.; methodology, J.H. and V.P.H.H.; validation, V.P.H.H.; investigation, V.P.H.H.; data curation, V.P.H.H.; writing—original draft preparation, V.P.H.H.; writing—review and editing, J.H. and I.T.K.; supervision, J.H. and I.T.K.; funding acquisition, J.H. All authors have read and agreed to the published version of the manuscript.

Funding: This work was supported by the Gachon University research fund of 2019 (GCU-2019-0805) and the Basic Science Research Capacity Enhancement Project through a Korea Basic Science Institute (National Research Facilities and Equipment Center) grant funded by the Ministry of Education (2019R1A6C1010016).

Institutional Review Board Statement: Not applicable.

Informed Consent Statement: Not applicable.

Data Availability Statement: The data is available on reasonable request from the corresponding author.

Conflicts of Interest: The authors declare no competing interests.

References

1. Dunn, B.; Kamath, H.; Tarascon, J.M. Electrical energy storage for the grid: A battery of choices. *Science* **2011**, *334*, 928–935. [CrossRef]
2. Etacheri, V.; Marom, R.; Elazari, R.; Salitra, G.; Aurbach, D. Challenges in the development of advanced Li-ion batteries: A review. *Energy Environ. Sci.* **2011**, *4*, 3243–3262. [CrossRef]
3. Armand, M.; Tarascon, J.M. Building better batteries. *Nature* **2008**, *451*, 652–657. [CrossRef] [PubMed]
4. Huggins, R.A. *Advanced Batteries: Materials Science Aspects*; Springer Science & Business Media: Berlin, Germany, 2009; pp. 1–474.
5. Reddy, M.V.; Rao, G.V.S.; Chowdari, B.V.R. Metal Oxides and Oxysalts as Anode Materials for Li Ion Batteries. *Chem. Rev.* **2013**, *113*, 5364–5457. [CrossRef]
6. Weng, W.; Li, J.; Du, Y.; Ge, X.; Zhou, X.; Bao, J. Template-free synthesis of metal oxide hollow micro-/nanospheres via Ostwald ripening for lithium-ion batteries. *J. Mater. Chem. A* **2018**, *6*, 10168–10175. [CrossRef]
7. Zou, R.; Xu, M.; He, S.-A.; Han, X.; Lin, R.; Cui, Z.; He, G.; Brett, D.J.L.; Guo, Z.X.; Hu, J.; et al. Cobalt nickel nitride coated by a thin carbon layer anchoring on nitrogen-doped carbon nanotube anodes for high-performance lithium-ion batteries. *J. Mater. Chem. A* **2018**, *6*, 19853–19862. [CrossRef]
8. Chen, X.; Zhou, J.; Li, J.; Luo, H.; Mei, L.; Wang, T.; Zhang, Y. A germanium and zinc chalcogenide as an anode for a high-capacity and long cycle life lithium battery. *RSC Adv.* **2019**, *9*, 35045–35049. [CrossRef] [PubMed]
9. Ashuri, M.; He, Q.; Shaw, L.L. Silicon as a potential anode material for Li-ion batteries: Where size, geometry and structure matter. *Nanoscale* **2016**, *8*, 74–103. [CrossRef]
10. Mou, H.; Xiao, W.; Miao, C.; Li, R.; Yu, L. Tin and Tin Compound Materials as Anodes in Lithium-Ion and Sodium-Ion Batteries: A Review. *Front. Chem.* **2020**, *8*, 141. [CrossRef]
11. He, J.; Wei, Y.; Zhai, T.; Li, H. Antimony-based materials as promising anodes for rechargeable lithium-ion and sodium-ion batteries. *Mater. Chem. Front.* **2018**, *2*, 437–455. [CrossRef]
12. Nguyen, T.P.; Kim, I.T. Ag Nanoparticle-Decorated MoS₂ Nanosheets for Enhancing Electrochemical Performance in Lithium Storage. *Nanomaterials* **2021**, *11*, 626. [CrossRef] [PubMed]
13. Nguyen, T.P.; Kim, I.T. Self-Assembled Few-Layered MoS₂ on SnO₂ Anode for Enhancing Lithium-Ion Storage. *Nanomaterials* **2020**, *10*, 2558. [CrossRef] [PubMed]
14. Preman, A.N.; Lee, H.; Yoo, J.; Kim, I.T.; Saito, T.; Ahn, S.-K. Progress of 3D network binders in silicon anodes for lithium ion batteries. *J. Mater. Chem. A* **2020**, *8*, 25548–25570. [CrossRef]
15. Nguyen, T.P.; Kim, I.T. W₂C/WS₂ Alloy Nanoflowers as Anode Materials for Lithium-Ion Storage. *Nanomaterials* **2020**, *10*, 1336. [CrossRef]
16. Kim, W.S.; Vo, T.N.; Kim, I.T. GeTe-TiC-C Composite Anodes for Li-Ion Storage. *Materials* **2020**, *13*, 4222. [CrossRef] [PubMed]
17. Vo, T.N.; Kim, D.S.; Mun, Y.S.; Lee, H.J.; Ahn, S.-K.; Kim, I.T. Fast charging sodium-ion batteries based on Te-P-C composites and insights to low-frequency limits of four common equivalent impedance circuits. *Chem. Eng. J.* **2020**, *398*, 125703. [CrossRef]
18. Hoang Huy, V.P.; Kim, I.T.; Hur, J. The Effects of the Binder and Buffering Matrix on InSb-Based Anodes for High-Performance Rechargeable Li-Ion Batteries. *Nanomaterials* **2021**, *11*, 3420. [CrossRef]
19. Nguyen, Q.H.; Phung, V.D.; Kidanu, W.G.; Ahn, Y.N.; Nguyen, T.L.; Kim, I.T. Carbon-free Cu/Sb_xO_y/Sb nanocomposites with yolk-shell and hollow structures as high-performance anodes for lithium-ion storage. *J. Alloys Compd.* **2021**, *878*, 160447. [CrossRef]
20. Nguyen, P.T.; Kim, I.T. In Situ Growth of W₂C/WS₂ with Carbon-Nanotube Networks for Lithium-Ion Storage. *Nanomaterials* **2022**, *12*, 1003. [CrossRef]
21. Nguyen, T.P.; Kim, I.T. Boron Oxide Enhancing Stability of MoS₂ Anode Materials for Lithium-Ion Batteries. *Materials* **2022**, *15*, 2034. [CrossRef]
22. Phan Nguyen, T.; Giang, T.T.; Kim, I.T. Restructuring NiO to LiNiO₂: Ultrastable and reversible anodes for lithium-ion batteries. *Chem. Eng. J.* **2022**, *437*, 135292. [CrossRef]
23. Park, C.-M.; Kim, J.-H.; Kim, H.; Sohn, H.-J. Li-alloy based anode materials for Li secondary batteries. *Chem. Soc. Rev.* **2010**, *39*, 3115–3141. [CrossRef] [PubMed]
24. Obrovac, M.N.; Chevrier, V.L. Alloy Negative Electrodes for Li-Ion Batteries. *Chem. Rev.* **2014**, *114*, 11444–11502. [CrossRef]
25. Zhou, X.; Guo, Y.-G. A PEO-assisted electrospun silicon-graphene composite as an anode material for lithium-ion batteries. *J. Mater. Chem. A* **2013**, *1*, 9019–9023. [CrossRef]
26. Su, X.; Wu, Q.; Li, J.; Xiao, X.; Lott, A.; Lu, W.; Sheldon, B.W.; Wu, J. Silicon-Based Nanomaterials for Lithium-Ion Batteries: A Review. *Adv. Energy Mater.* **2014**, *4*, 1300882. [CrossRef]
27. Seo, J.-U.; Park, C.-M. Nanostructured SnSb/MO_x (M = Al or Mg)/C composites: Hybrid mechanochemical synthesis and excellent Li storage performances. *J. Mater. Chem. A* **2013**, *1*, 15316–15322. [CrossRef]
28. Li, H.; Yamaguchi, T.; Matsumoto, S.; Hoshikawa, H.; Kumagai, T.; Okamoto, N.L.; Ichitsubo, T. Circumventing huge volume strain in alloy anodes of lithium batteries. *Nat. Commun.* **2020**, *11*, 1584. [CrossRef] [PubMed]
29. Moskalyk, R. Gallium: The Backbone of the Electronics Industry. *Miner. Eng.* **2003**, *16*, 921–929. [CrossRef]
30. Lee, K.T.; Jung, Y.S.; Kim, T.; Kim, C.H.; Kim, J.H.; Kwon, J.Y.; Oh, S.M. Liquid Gallium Electrode Confined in Porous Carbon Matrix as Anode for Lithium Secondary Batteries. *Electrochem. Solid-State Lett.* **2008**, *11*, A21. [CrossRef]
31. Yang, W.; Zhang, X.; Tan, H.; Yang, D.; Feng, Y.; Rui, X.; Yu, Y. Gallium-based anodes for alkali metal ion batteries. *J. Energy Chem.* **2021**, *55*, 557–571. [CrossRef]
32. Deshpande, R.D.; Li, J.; Cheng, Y.-T.; Verbrugge, M.W. Liquid Metal Alloys as Self-Healing Negative Electrodes for Lithium Ion Batteries. *J. Electrochem. Soc.* **2011**, *158*, A845. [CrossRef]

33. Yarema, M.; Wörle, M.; Rossell, M.D.; Erni, R.; Caputo, R.; Protesescu, L.; Kravchyk, K.V.; Dirin, D.N.; Lienau, K.; von Rohr, F.; et al. Monodisperse Colloidal Gallium Nanoparticles: Synthesis, Low Temperature Crystallization, Surface Plasmon Resonance and Li-Ion Storage. *J. Am. Chem. Soc.* **2014**, *136*, 12422–12430. [CrossRef] [PubMed]
34. Liang, W.; Hong, L.; Yang, H.; Fan, F.; Liu, Y.; Li, H.; Li, J.; Huang, J.Y.; Chen, L.-Q.; Zhu, T.; et al. Nanovoid Formation and Annihilation in Gallium Nanodroplets under Lithiation–Delithiation Cycling. *Nano Lett.* **2013**, *13*, 5212–5217. [CrossRef]
35. Guo, X.; Zhang, L.; Ding, Y.; Goodenough, J.B.; Yu, G. Room-temperature liquid metal and alloy systems for energy storage applications. *Energy Environ. Sci.* **2019**, *12*, 2605–2619. [CrossRef]
36. Zhu, J.; Wu, Y.; Huang, X.; Huang, L.; Cao, M.; Song, G.; Guo, X.; Sui, X.; Ren, R.; Chen, J. Self-healing liquid metal nanoparticles encapsulated in hollow carbon fibers as a free-standing anode for lithium-ion batteries. *Nano Energy* **2019**, *62*, 883–889. [CrossRef]
37. Yan, Y.; Yin, Y.; Guo, Y.; Wan, L.-J. Effect of cations in ionic liquids on the electrochemical performance of lithium-sulfur batteries. *Sci. China Chem.* **2014**, *57*, 1564–1569. [CrossRef]
38. Xin, S.; Gu, L.; Zhao, N.-H.; Yin, Y.-X.; Zhou, L.-J.; Guo, Y.-G.; Wan, L.-J. Smaller Sulfur Molecules Promise Better Lithium–Sulfur Batteries. *J. Am. Chem. Soc.* **2012**, *134*, 18510–18513. [CrossRef]
39. Yang, C.-P.; Xin, S.; Yin, Y.-X.; Ye, H.; Zhang, J.; Guo, Y.-G. An Advanced Selenium–Carbon Cathode for Rechargeable Lithium–Selenium Batteries. *Angew. Chem. Int. Ed.* **2013**, *52*, 8363–8367. [CrossRef]
40. Xin, S.; Yin, Y.-X.; Guo, Y.-G.; Wan, L.-J. A High-Energy Room-Temperature Sodium-Sulfur Battery. *Adv. Mater.* **2014**, *26*, 1261–1265. [CrossRef]
41. Zeng, L.; Wei, X.; Wang, J.; Jiang, Y.; Li, W.; Yu, Y. Flexible one-dimensional carbon–selenium composite nanofibers with superior electrochemical performance for Li–Se/Na–Se batteries. *J. Power Sources* **2015**, *281*, 461–469. [CrossRef]
42. Yang, C.-P.; Yin, Y.-X.; Guo, Y.-G. Elemental Selenium for Electrochemical Energy Storage. *J. Phys. Chem. Lett.* **2015**, *6*, 256–266. [CrossRef] [PubMed]
43. Yan, J.; Huang, H.; Zhang, J.; Liu, Z.; Yang, Y. A study of novel anode material CoS₂ for lithium ion battery. *J. Power Sources* **2005**, *146*, 264–269. [CrossRef]
44. Yin, J.; Cao, H.; Zhou, Z.; Zhang, J.; Qu, M. SnS₂@reduced graphene oxide nanocomposites as anode materials with high capacity for rechargeable lithium ion batteries. *J. Mater. Chem.* **2012**, *22*, 23963–23970. [CrossRef]
45. Zhang, Z.; Zhao, X.; Li, J. SnSe/carbon nanocomposite synthesized by high energy ball milling as an anode material for sodium-ion and lithium-ion batteries. *Electrochim. Acta* **2015**, *176*, 1296–1301. [CrossRef]
46. Zhang, Z.; Zhao, X.; Li, J. Robust nanocube framework CoS₂-based composites as high-performance anodes for Li- and Na-ion batteries. *Compos. Part B Eng.* **2022**, *231*, 109592.
47. Nam, K.-H.; Park, C.-M. 2D layered Sb₂Se₃-based amorphous composite for high-performance Li- and Na-ion battery anodes. *J. Power Sources* **2019**, *433*, 126639. [CrossRef]
48. Park, A.-R.; Jeon, K.-J.; Park, C.-M. Electrochemical mechanism of Li insertion/extraction in ZnS and ZnS/C anodes for Li-ion batteries. *Electrochim. Acta* **2018**, *265*, 107–114. [CrossRef]
49. Zhang, J.; Yin, Y.-X.; You, Y.; Yan, Y.; Guo, Y.-G. A High-Capacity Tellurium@Carbon Anode Material for Lithium-Ion Batteries. *Energy Technol.* **2014**, *2*, 757–762. [CrossRef]
50. Nagulapati, V.M.; Kim, D.S.; Oh, J.; Lee, J.H.; Hur, J.; Kim, I.T.; Lee, S.G. Enhancing the Electrochemical Performance of SbTe Bimetallic Anodes for High-Performance Sodium-Ion Batteries: Roles of the Binder and Carbon Support Matrix. *Nanomaterials* **2019**, *9*, 1134. [CrossRef]
51. Zhang, J.; Yin, Y.-X.; Guo, Y.-G. High-Capacity Te Anode Confined in Microporous Carbon for Long-Life Na-Ion Batteries. *ACS Appl. Mater. Interfaces* **2015**, *7*, 27838–27844. [CrossRef]
52. Seo, J.-U.; Seong, G.-K.; Park, C.-M. Te/C nanocomposites for Li-Te Secondary Batteries. *Sci. Rep.* **2015**, *5*, 7969. [CrossRef] [PubMed]
53. Li, Y.; Wang, M.-Q.; Chen, Y.; Hu, L.; Liu, T.; Bao, S.; Xu, M. Muscle-like electrode design for Li-Te batteries. *Energy Storage Mater.* **2018**, *10*, 10–15. [CrossRef]
54. He, J.; Chen, Y.; Lv, W.; Wen, K.; Wang, Z.; Zhang, W.; Li, Y.; Qin, W.; He, W. Three-Dimensional Hierarchical Reduced Graphene Oxide/Tellurium Nanowires: A High-Performance Freestanding Cathode for Li–Te Batteries. *ACS Nano* **2016**, *10*, 8837–8842. [CrossRef] [PubMed]
55. Ding, N.; Chen, S.-F.; Geng, D.-S.; Chien, S.-W.; An, T.; Hor, T.S.A.; Liu, Z.-L.; Yu, S.-H.; Zong, Y. Tellurium@Ordered Macroporous Carbon Composite and Free-Standing Tellurium Nanowire Mat as Cathode Materials for Rechargeable Lithium–Tellurium Batteries. *Adv. Energy Mater.* **2015**, *5*, 1401999. [CrossRef]
56. Park, A.-R.; Park, C.-M. Cubic Crystal-Structured SnTe for Superior Li- and Na-Ion Battery Anodes. *ACS Nano* **2017**, *11*, 6074–6084. [CrossRef]
57. Nam, K.-H.; Park, C.-M. Layered Sb₂Te₃ and its nanocomposite: A new and outstanding electrode material for superior rechargeable Li-ion batteries. *J. Mater. Chem. A* **2016**, *4*, 8562–8565. [CrossRef]
58. Sun, D.; Liu, S.; Zhang, G.; Zhou, J. NiTe₂/N-doped graphitic carbon nanosheets derived from Ni-hexamine coordination frameworks for Na-ion storage. *Chem. Eng. J.* **2019**, *359*, 1659–1667. [CrossRef]
59. Nam, K.H.; Sung, G.K.; Choi, J.H.; Youn, J.S.; Jeon, K.J.; Park, C.M. New high-energy-density GeTe-based anodes for Li-ion batteries. *J. Mater. Chem. A* **2019**, *7*, 3278–3288. [CrossRef]
60. Seo, J.-U.; Park, C.-M. ZnTe and ZnTe/C nanocomposite: A new electrode material for high-performance rechargeable Li-ion batteries. *J. Mater. Chem. A* **2014**, *2*, 20075–20082. [CrossRef]

61. Ganesan, V.; Nam, K.-H.; Park, C.-M. Robust Polyhedral CoTe₂-C Nanocomposites as High-Performance Li- and Na-Ion Battery Anodes. *ACS Appl. Energy Mater.* **2020**, *3*, 4877–4887. [CrossRef]
62. Abed Al- Abbas, S.S.; Muhsin, M.K.; Jappor, H.R. Tunable optical and electronic properties of gallium telluride monolayer for photovoltaic absorbers and ultraviolet detectors. *Chem. Phys. Lett.* **2018**, *713*, 46–51. [CrossRef]
63. Bose, D.N.; De Purkayastha, S. Dielectric and photoconducting properties of Ga₂Te₃ and In₂Te₃ crystals. *Mater. Res. Bull.* **1981**, *16*, 635–642. [CrossRef]
64. Aydoğan, Ş.; Karacalı, T.; Yoğurtçu, Y.K. Investigation of the switching phenomena in Ga₂Te₃ single crystals. *J. Cryst. Growth* **2005**, *279*, 110–113. [CrossRef]
65. Huang, G.-Y.; Abdul-Jabbar, N.M.; Wirth, B.D. Theoretical study of Ga₂Se₃, Ga₂Te₃ and Ga₂(Se_{1-x}Te_x)₃: Band-gap engineering. *Acta Mater.* **2014**, *71*, 349–369. [CrossRef]
66. Antonopoulos, J.G.; Karakostas, T.; Bleris, G.L.; Economou, N.A. On the phase diagram of the Ga-Te system in the composition range 55 at % Te. *J. Mater. Sci.* **1981**, *16*, 733–738. [CrossRef]
67. David, R. (Ed.) *CRC Handbook of Chemistry and Physics*, 87th ed.; Lide (National Institute of Standards and Technology); CRC Press/Taylor and Francis Group: Boca Raton, FL, USA, 2006; Volume 2608, ISBN 0-8493-0487-3.
68. Gnanamuthu, R.M.; Lee, C.W. Electrochemical properties of Super P carbon black as an anode active material for lithium-ion batteries. *Mater. Chem. Phys.* **2011**, *130*, 831–834. [CrossRef]
69. Ko, M.; Chae, S.; Ma, J.; Kim, N.; Lee, H.-W.; Cui, Y.; Cho, J. Scalable synthesis of silicon-nanoparticle-embedded graphite for high-energy lithium-ion batteries. *Nat. Energy* **2016**, *1*, 16113. [CrossRef]
70. Ng, S.; Wang, J.; Guo, Z.; Chen, J.; Wang, G.; Liu, H. Single wall carbon nanotube paper as anode for lithium-ion battery. *Electrochim. Acta* **2005**, *51*, 23–28. [CrossRef]
71. Qin, S.; Liu, D.; Lei, W.; Chen, Y. Synthesis of an indium oxide nanoparticle embedded graphene three-dimensional architecture for enhanced lithium-ion storage. *J. Mater. Chem. A* **2015**, *3*, 18238–18243. [CrossRef]
72. Xu, Y.; Zhu, Y.; Liu, Y.; Wang, C. Electrochemical Performance of Porous Carbon/Tin Composite Anodes for Sodium-Ion and Lithium-Ion Batteries. *Adv. Energy Mater.* **2013**, *3*, 128–133. [CrossRef]
73. Moyer, K.; Meng, C.; Marshall, B.; Assal, O.; Eaves, J.; Perez, D.; Karkkainen, R.; Roberson, L.; Pint, C.L. Carbon fiber reinforced structural lithium-ion battery composite: Multifunctional power integration for CubeSats. *Energy Storage Mater.* **2020**, *24*, 676–681. [CrossRef]
74. Ni, S.; Li, T.; Lv, X.; Yang, X.; Zhang, L. Designed constitution of NiO/Ni nanostructured electrode for high performance lithium ion battery. *Electrochim. Acta* **2013**, *91*, 267–274. [CrossRef]
75. Taberna, P.-L.; Mitra, S.; Poizot, P.; Simon, P.; Tarascon, J.-M. High rate capabilities Fe₃O₄-based Cu nano-architected electrodes for lithium-ion battery applications. *Nat. Mater.* **2006**, *5*, 567–573. [CrossRef] [PubMed]
76. Na, Z.; Huang, G.; Liang, F.; Yin, D.; Wang, L. A Core—Shell Fe/Fe₂O₃ Nanowire as a High-Performance Anode Material for Lithium-Ion Batteries. *Chem. A Eur. J.* **2016**, *22*, 12081–12087. [CrossRef]
77. Mahmood, N.; Zhang, C.; Liu, F.; Zhu, J.; Hou, Y. Hybrid of Co₃Sn₂@Co Nanoparticles and Nitrogen-Doped Graphene as a Lithium Ion Battery Anode. *ACS Nano* **2013**, *7*, 10307–10318. [CrossRef] [PubMed]
78. Kim, K.-H.; Jung, C.-H.; Kim, W.-S.; Hong, S.-H. V₄P₇@C nanocomposite as a high performance anode material for lithium-ion batteries. *J. Power Sources* **2018**, *400*, 204–211. [CrossRef]
79. Lee, H.J.; Shim, H.W.; Kim, J.C.; Kim, D.W. Mo-MoO₃-graphene nanocomposites as anode materials for lithium-ion batteries: Scalable, facile preparation and characterization. *Electrochim. Acta* **2017**, *251*, 81–90. [CrossRef]
80. Lee, G.; Kim, S.; Kim, S.; Choi, J. SiO₂/TiO₂ Composite Film for High Capacity and Excellent Cycling Stability in Lithium-Ion Battery Anodes. *Adv. Funct. Mater.* **2017**, *27*, 1703538. [CrossRef]
81. Allcorn, E.; Manthiram, A. FeSb₂-Al₂O₃-C Nanocomposite Anodes for Lithium-Ion Batteries. *ACS Appl. Mater. Interfaces* **2014**, *6*, 10886–10891. [CrossRef] [PubMed]
82. Yao, Y.; Huo, K.; Hu, L.; Liu, N.; Cha, J.J.; McDowell, M.T.; Chu, P.K.; Cui, Y. Highly Conductive, Mechanically Robust, and Electrochemically Inactive TiC/C Nanofiber Scaffold for High-Performance Silicon Anode Batteries. *ACS Nano* **2011**, *5*, 8346–8351. [CrossRef]
83. Xu, B.; Shen, H.; Ge, J.; Tang, Q. Improved cycling performance of SiO_x/MgO/Mg₂SiO₄/C composite anode materials for lithium-ion battery. *Appl. Surf. Sci.* **2021**, *546*, 148814. [CrossRef]
84. Xiao, Z.; Lei, C.; Yu, C.; Chen, X.; Zhu, Z.; Jiang, H.; Wei, F. Si@Si₃N₄@C composite with egg-like structure as high-performance anode material for lithium ion batteries. *Energy Storage Mater.* **2020**, *24*, 565–573. [CrossRef]
85. So, S.; Ko, J.; Ahn, Y.N.; Kim, I.T.; Hur, J. Unraveling improved electrochemical kinetics of In₂Te₃-based anodes embedded in hybrid matrix for Li-ion batteries. *Chem. Eng. J.* **2022**, *429*, 132395. [CrossRef]
86. Huy, V.P.H.; So, S.; Kim, I.T.; Hur, J. Self-healing gallium phosphide embedded in a hybrid matrix for high-performance Li-ion batteries. *Energy Storage Mater.* **2021**, *34*, 669–681. [CrossRef]
87. Voevodin, A.A.; Zabinski, J.S. Load-adaptive crystalline-amorphous nanocomposites. *J. Mater. Sci.* **1998**, *33*, 319–327. [CrossRef]
88. Zhang, W.; Zhang, Q.; Shi, Q.; Xin, S.; Wu, J.; Zhang, C.; Qiu, L.; Zhang, C. Facile Synthesis of Carbon-Coated Porous Sb₂Te₃ Nanoplates with High Alkali Metal Ion Storage. *ACS Appl. Mater. Interfaces* **2019**, *11*, 29934–29940. [CrossRef] [PubMed]
89. Cho, J.S.; Ju, H.S.; Lee, J.-K.; Kang, Y.C. Carbon/two-dimensional MoTe₂ core/shell-structured microspheres as an anode material for Na-ion batteries. *Nanoscale* **2017**, *9*, 1942–1950. [CrossRef]

90. Bondino, F.; Duman, S.; Nappini, S.; D'Olimpio, G.; Ghica, C.; Menteş, T.O.; Mazzola, F.; Istrate, M.C.; Jugovac, M.; Vorokhta, M.; et al. Improving the Efficiency of Gallium Telluride for Photocatalysis, Electrocatalysis, and Chemical Sensing through Defects Engineering and Interfacing with its Native Oxide. *Adv. Funct. Mater.* **2022**, 2205923. [CrossRef]
91. Huang, C.; Mu, W.; Zhou, H.; Zhu, Y.; Xu, X.; Jia, Z.; Zheng, L.; Tao, X. Effect of OH⁻ on chemical mechanical polishing of β-Ga₂O₃ (100) substrate using an alkaline slurry. *RSC Adv.* **2018**, *8*, 6544–6550. [CrossRef]
92. Kang, W.; Tang, Y.; Li, W.; Yang, X.; Xue, H.; Yang, Q.; Lee, C.S. High interfacial storage capability of porous NiMn₂O₄/C hierarchical tremella-like nanostructures as the lithium ion battery anode. *Nanoscale* **2015**, *7*, 225–231. [CrossRef]
93. Zeng, Z.; Zhao, H.; Lv, P.; Zhang, Z.; Wang, J.; Xia, Q. Electrochemical properties of iron oxides/carbon nanotubes as anode material for lithium ion batteries. *J. Power Sources* **2015**, *274*, 1091–1099. [CrossRef]
94. Zhu, X.J.; Guo, Z.P.; Zhang, P.; Du, G.D.; Zeng, R.; Chen, Z.X.; Li, S.; Liu, H.K. Highly porous reticular tin–cobalt oxide composite thin film anodes for lithium ion batteries. *J. Mater. Chem.* **2009**, *19*, 8360–8365. [CrossRef]
95. Jung, J.-W.; Kim, C.; Cheong, J.Y.; Kim, I.-D. Gallium Nitride Nanoparticles Embedded in a Carbon Nanofiber Anode for Ultralong-Cycle-Life Lithium-Ion Batteries. *ACS Appl. Mater. Interfaces* **2019**, *11*, 44263–44269. [CrossRef]
96. Ni, S.; Chen, Q.; Liu, J.; Yang, S.; Li, T.; Yang, X.; Zhao, J. New insights into the Li-storage mechanism in α-Ga₂O₃ anode and the optimized electrode design. *J. Power Sources* **2019**, *433*, 126681. [CrossRef]
97. Wang, K.; Ye, W.; Yin, W.; Chai, W.; Rui, Y.; Tang, B. Several carbon-coated Ga₂O₃ anodes: Efficient coating of reduced graphene oxide enhanced the electrochemical performance of lithium ion batteries. *Dalton Trans.* **2021**, *50*, 3660–3670. [CrossRef] [PubMed]
98. Wang, K.; Ye, W.; Yin, W.; Chai, W.; Tang, B.; Rui, Y. One-step synthesis of MOF-derived Ga/Ga₂O₃@C dodecahedra as an anode material for high-performance lithium-ion batteries. *Dalton Trans.* **2019**, *48*, 12386–12390. [CrossRef]
99. Guo, X.; Ding, Y.; Xue, L.; Zhang, L.; Zhang, C.; Goodenough, J.B.; Yu, G. A Self-Healing Room-Temperature Liquid-Metal Anode for Alkali-Ion Batteries. *Adv. Funct. Mater.* **2018**, *28*, 1804649. [CrossRef]
100. Sun, C.; Yang, M.; Wang, T.; Shao, Y.; Wu, Y.; Hao, X. A self-healing CuGa₂ anode for high-performance Li ion batteries. *J. Power Sources* **2019**, *437*, 226889.
101. Sun, C.; Yang, M.; Wang, T.; Shao, Y.; Wu, Y.; Hao, X. Graphene-Oxide-Assisted Synthesis of GaN Nanosheets as a New Anode Material for Lithium-Ion Battery. *ACS Appl. Mater. Interfaces* **2017**, *9*, 26631–26636. [CrossRef]
102. Tang, X.; Huang, X.; Huang, Y.; Gou, Y.; Pastore, J.; Yang, Y.; Xiong, Y.; Qian, J.; Brock, J.D.; Lu, J.; et al. High-Performance Ga₂O₃ Anode for Lithium-Ion Batteries. *ACS Appl. Mater. Interfaces* **2018**, *10*, 5519–5526. [CrossRef]
103. Gómez-Cámer, J.L.; Novák, P. Polyacrylate bound TiSb₂ electrodes for Li-ion batteries. *J. Power Sources* **2015**, *273*, 174–179. [CrossRef]
104. Senoh, H.; Kageyama, H.; Takeuchi, T.; Nakanishi, K.; Ohta, T.; Sakaebe, H.; Yao, M.; Sakai, T.; Yasuda, K. Gallium (III) sulfide as an active material in lithium secondary batteries. *Lancet* **2011**, *196*, 5631–5636. [CrossRef]
105. Meng, X.; He, K.; Su, D.; Zhang, X.; Sun, C.; Ren, Y.; Wang, H.-H.; Weng, W.; Trahey, L.; Canlas, C.P.; et al. Gallium Sulfide–Single-Walled Carbon Nanotube Composites: High-Performance Anodes for Lithium-Ion Batteries. *Adv. Funct. Mater.* **2014**, *24*, 5435–5442. [CrossRef]
106. Jeong, J.-H.; Jung, D.-W.; Oh, E.-S. Lithium storage characteristics of a new promising gallium selenide anodic material. *J. Alloys Compd.* **2014**, *613*, 42–45. [CrossRef]
107. Lee, Y.-H.; Hwa, Y.; Park, C.-M. Novel high-performance Ga₂Te₃ anodes for Li-ion batteries. *J. Mater. Chem. A* **2021**, *9*, 20553–20564. [CrossRef]



Article

Effects of Nickel Impregnation on the Catalytic Removal of Nitric Oxide by Polyimide-Based Activated Carbon Fibers

Hun-Seung Jeong^{1,2} and Byung-Joo Kim^{1,3,*}

¹ Material Application Research Institute, Jeonju University, Jeonju 55069, Republic of Korea; hunseung.jeong@jj.ac.kr

² Department of Energy Science, Sungkyunkwan University, Suwon 16419, Republic of Korea

³ Department of Advanced Materials and Chemical Engineering, Jeonju University, Jeonju 55069, Republic of Korea

* Correspondence: kimbyungjoo@jj.ac.kr; Tel.: +82-63-220-3293

Abstract: Activated carbon fibers (ACFs) are beneficial for adsorbing harmful gases because of the well-developed micropores on their surface. Usually, the physical adsorption of harmful gases by ACFs is limited by their textural properties. In this study, the effect of nickel particle catalyst impregnation on the physicochemical removal of nitric oxide (NO) by polyimide (PI)-based ACFs (PI-ACFs) was investigated. Ni(NO₃)₂ was used as the precursor of nickel particle catalysts and impregnated on ACFs as a function of concentrations. The Ni(NO₃)₂/ACFs were then thermally reduced in an argon atmosphere containing 4% hydrogen (400 °C, 1 h). The gases generated during heat treatment were verified using Fourier transform infrared spectroscopy, and the impregnation amount of metallic nickel was also calculated based on the gas amount generated. The specific surface areas of the ACF and Ni-ACFs were determined to be 1010–1180 m²/g, while the nickel impregnation amount was 0.85–5.28 mg/g. The NO removal capacity of the Ni-ACF was found to be enhanced with the addition of Ni catalysts. In addition, metallic nickel particles on the ACFs maintained their chemical molecular structures before and after the NO removal tests.

Keywords: polyimide-based activated carbon fiber; catalysts; metal; nitric oxide

1. Introduction

Industrialization has led to air pollution, a severe environmental problem primarily caused by particulate emissions such as coal dust, ozone, carbon dioxide, volatile hydrocarbons, and nitrogen oxides. Among these, NO_x are considered major atmospheric pollutants, contributing to various environmental problems such as acid rain, photochemical smog, and ozone layer destruction [1,2]. Although types of NO_x include NO, NO₂, NO₃, N₂O₃, N₂O₄, and N₂O₅, the term NO_x generally refers to NO and NO₂. At room temperature, the equilibrium between NO and NO₂ is favored toward NO₂, and the NO produced by combustion is oxidized in the atmosphere to form NO₂ [3]. Therefore, removing NO before its emission into the atmosphere is crucial to reducing NO and NO₂. Previous studies have been conducted on NO_x purification technologies [4–6], and dry and wet methods have been used to remove NO_x. In the case of the dry method, selective catalytic reduction (SCR) by NH₃, selective noncatalytic reduction (SNCR) and adsorption by adsorbents have been used [7,8]. Meanwhile, in the case of the wet method, a scrubber column is used, in which NO_x is absorbed by the absorbent [9,10]. Among the aforementioned methods, the most widely used NO_x reduction technology is SCR by NH₃. However, this process is limited due to the high reaction temperature (>300 °C) and leakage of NH₃. Moreover, additional costs are incurred to reheat the desulfurization gas or replace deactivated catalysts. Therefore, an inexpensive method that removes NO_x stably at low temperatures (<150 °C) is required for NO_x removal.

Methods for removing NO_x at low temperatures include the use of activated carbons (ACs) and their fibers (ACFs) [11,12]. These porous carbons are beneficial owing to their low cost [13,14], resistance to acids and bases [15], wide specific surface area [16–18], porous structure [19,20], and high catalytic activity [21]. However, NO_x removal using only these adsorbents is limited, and much research has been conducted to introduce various metals and additives to porous carbon carriers. The commonly used metals include Cu [22], Mn [23], Ni [24,25], Fe [26], Co [27], and Ru [28], which are impregnated on the surface of porous carbon, thereby enhancing its adsorption capacity by acting as catalysts. Khristova et al. [29] prepared nickel-impregnated AC (Ni-AC) by impregnating AC in a solution of Ni(NO₃)₂, followed by heat treatment at 200–300 °C; the content of nickel was 2.9–8.3%. The produced Ni-AC was reported to have an approximately fourfold enhanced NO conversion capacity in an air atmosphere, ranging from 80 to 350 °C. Yamashita et al. [30] prepared nickel-impregnated carbon samples by impregnating coal particles in a solution of nickel (II) acetate, followed by heat treatment at 650 °C. The reported nickel content was approximately 4.0%, and the samples exhibited approximately twice the NO conversion capacity in an air atmosphere at 300 °C. Santiago Veiga et al. [31] prepared nickel-impregnated carbon samples by impregnating coal particles in a solution of nickel (II) acetate and maintaining the suspension with stirring for 5 h. Then, the solvent was removed by rotary evaporation, and the obtained solid was dried in an oven at 110 °C for 24 h, followed by heat treatment at 700 °C under argon flow (20 mL/min) for 6 h. The reported nickel content was approximately 10%. Numerous studies [29–31] have used AC as a porous carrier, primarily impregnated with more than 3% nickel. It has been reported that the specific surface area of nickel-impregnated carbon materials decreases by up to 30%. However, studies utilizing ACFs as porous carriers have not been exhaustively conducted. Compared with ACs, ACFs have well-developed micropores on their surfaces. Furthermore, the porous characteristics of the ACFs enable fast adsorption and desorption, resulting in excellent adsorption even at low concentrations [32,33]. Thus, ACFs can serve as better porous carriers than ACs. However, the micropores distributed on their surfaces can be filled or blocked by metals and additives [34,35].

ACFs are typically manufactured using various precursors [36–39], including polyacrylonitrile, cellulose, and pitch. The characteristics of the precursor influence several fundamental properties of ACFs, including specific surface area, pore structure, surface characteristics, adsorption properties, and yields [35–39]. Recently, ACFs utilizing polyimide (PI) are gaining attention for their economic advantages owing to a process characteristic that can skip a stabilization step [40]. However, no studies have been conducted on metal impregnation and harmful gas removal using PI-based ACFs (PI-ACFs).

This study investigated the metallic nickel impregnation of the PI-based ACFs within a range that did not significantly reduce the specific surface area and their effects on the NO removal. The amount of nickel on the ACFs was controlled to be <1 wt.% to minimize the impact on the pore structure with varying nickel content. Changes in the surface functional groups and NO-removing ability corresponding to the nickel content were evaluated. Additionally, changes in the chemical molecular structure of metallic nickel were observed by comparing the results before and after NO adsorption.

2. Experimental

2.1. Materials

The PI fibers used in this study were supplied by Dissol Co., Ltd. (Jeonju, Republic of Korea). The PI fibers (7.5 g) were placed in an alumina crucible and carbonized using a custom quartz tube furnace (SiC heater, 1000 mm × 90 mm) under an atmosphere of ultrahigh-purity nitrogen (N₂, 99.999%, 200 cc/min). Carbonization was maintained at 800 °C (heating rate 10 °C/min) for 60 min, following which the fibers were allowed to cool to room temperature (25 °C). The carbonized fibers (CFs) were weighed (3.7 g), which confirmed a carbonization yield of 49.3%.

For activation, the CFs (3.5 g) were placed in a boat-type alumina crucible and loaded into a tubular furnace (Inconel, 1200 mm × 80 mm). An ultrahigh-purity nitrogen at-

mosphere (99.999%, 200 cc/min) was maintained until the activation temperature was reached (900 °C, heating rate 10 °C/min), following which it was replaced with steam (0.5 mL/min) upon reaching the activation temperature; activation was performed for 30 min. Subsequently, the atmosphere was maintained under ultrahigh-purity nitrogen during the natural cooling phase. The resultant ACF was named PI-ACF.

For nickel impregnation, the PI-ACFs (1.0 g) were placed in a square dish, and impregnation solutions of 0.10, 0.50, 1.00, 5.0, and 9.0 mol of $\text{Ni}(\text{NO}_3)_2 \cdot 6\text{H}_2\text{O}$ were used. Each concentration of the solution was sprayed onto the PI-ACF using a spray bottle, with 0.2 mL of the $\text{Ni}(\text{NO}_3)_2 \cdot 6\text{H}_2\text{O}$ solution being sprayed per 1.0 g of the PI-ACF. The impregnated PI-ACF was dried at 110 °C for 24 h and then heat-treated at 400 °C for 1 h under an argon atmosphere (200 cc/min) with 4% hydrogen to obtain the reduced metallic catalyst. After heat treatment, all samples were stored in a vacuum oven (0.1 Pa). The gases generated during the heat treatment were examined using Fourier transform infrared spectroscopy (FT-IR, I4001-E, MIDAC Corp., Westfield, NJ, USA). The content of nickel-impregnated on the ACF was determined through Inductively Coupled Plasma Optical Emission Spectroscopy (ICP-OES, Spectro ARCOS, SPECTRO Analytical Instruments LTD., Kleve, Germany). The prepared PI-ACFs were named 0.1, 0.5, 1.0, 5.0, and 9.0-Ni-ACF.

2.2. Characterization

The surface metal of the ACFs was identified using X-ray diffractometry (XRD; Smart-Lab SE, Rigaku Co., Tokyo, Japan) within the range of 10–60° at a scan speed of 2°/min using $\text{Cu-K}\alpha$ as the light source ($\lambda = 1.54 \text{ \AA}$). The presence and distribution of specific elements in the ACFs were confirmed using X-ray photoelectron spectroscopy (XPS; Nexsa XPS system, Thermo Fisher Scientific Inc., Waltham, MA, USA). The X-ray anode was operated in a vacuum chamber at 2.0×10^{-7} torr over the binding energy range of 0–1300 eV. $\text{O}_{1\text{S}}$ and $\text{Ni}_{2\text{P}}$ data were obtained to observe the chemical binding states of oxygen and nickel present on the surface of the ACFs.

The pore characteristics of the ACFs were measured using an isothermal adsorption analyzer (BELSORP-Max II, Microtrac BEL, Osaka, Japan) and analyzed using the obtained $\text{N}_2/77\text{K}$ adsorption-desorption isotherm. The specific surface area of the ACF was calculated using the Brunauer-Emmett-Teller (BET) equation [41], and the volume of the micropores and pore size distribution were calculated using the t-plot [42] and non-local density functional theory (NLDFT) methods [43], respectively. The mesopore volume was obtained by subtracting the micropore volume from the total pore volume.

2.3. NO Removal (Adsorption)

Before the adsorption analysis of NO, all samples were dried in a vacuum oven (0.1 Pa) at 110 °C for 24 h and then filled to a certain volume of 0.4 g in a reaction tube (quartz column). The NO removal experiment was conducted by introducing 30 ppm NO (200 cc/min, N_2 balance) after purging with N_2 for 1 h. The adsorption capacity is expressed relative to the initial concentration ($C/C_0 = 1.0$ (30 ppm)). The experiment was terminated when the outlet concentration reached 30 ppm. The concentration of NO was detected by FT-IR, which is capable of gas analysis, and the chemical composition changes in the Ni-ACF before and after the adsorption were confirmed using XRD.

3. Results and Discussion

3.1. Preparation of Nickel-Impregnated ACF Samples

The $\text{Ni}(\text{NO}_3)_2$ -impregnated ACF was reduced by heat treatment, and the gases generated during the heat treatment process were confirmed by FT-IR. Figure 1a illustrates the gases generated by heat treatment, and the detected curve represents NO, which is the decomposition gas of $\text{Ni}(\text{NO}_3)_2$. All ACFs detected NO near 200 °C, and the detected amount was observed to have increased with the impregnated amount of $\text{Ni}(\text{NO}_3)_2$. Figure 1b shows the amount of impregnated Ni calculated from the detected amount of NO. The amount of impregnated Ni (Ni_{imp} mg/g) was calculated using Equations (1) and (2).

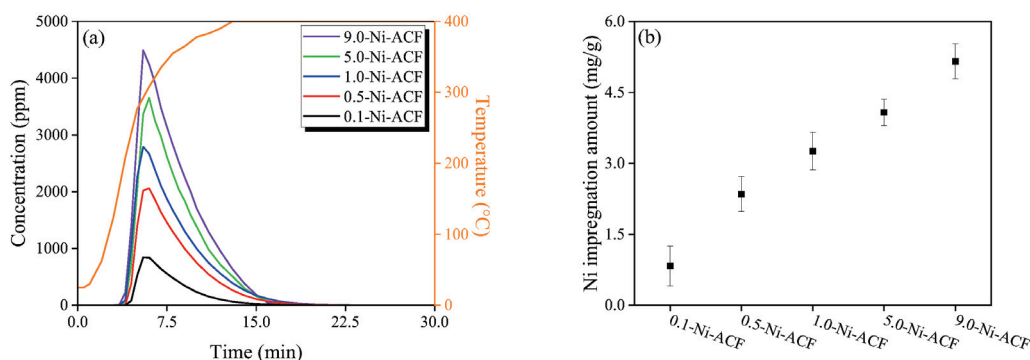
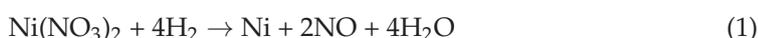


Figure 1. (a) NO generation amount from Ni-impregnated activated carbon fiber as a function of $\text{Ni}(\text{NO}_3)_2$ concentration with reduction temperature and (b) calculated Ni amount based on the result of (a).



$$Ni_{imp} = \frac{Ni_{weight}}{2NO_{weight}} \times NO_{det} \quad (2)$$

where Ni_{weight} is the atomic weight of nickel (g/mol), NO_{weight} is the molecular weight of NO (g/mol), and NO_{det} is the amount of NO (mg/g) generated by thermal decomposition. The results confirmed that the impregnated nickel amounts of 0.1-, 0.5-, 1.0-, 5.0-, and 9.0-Ni-ACF were 0.83, 2.35, 3.25, 4.08, and 5.16 mg/g, respectively.

Table 1 presents the nickel content of Ni-impregnated ACF, which was determined through ICP-OES analysis, providing the actual amount of nickel adsorbed. The nickel content for 0.1-, 0.5-, 1.0-, 5.0-, and 9.0-Ni-ACF was found to be 0.56, 2.10, 2.89, 3.88, and 5.41 mg/g, respectively. Notably, the calculated nickel content from FT-IR and the confirmed nickel content from ICP-OES exhibit remarkably similar trends, validating the accuracy of the measurements. However, it is essential to note that there is a slight difference in nickel content between FT-IR and ICP-OES, which can be attributed to the method of nickel ($\text{Ni}(\text{NO}_3)_2$) impregnation via spray. This variation is considered the influencing factor responsible for the minor discrepancy observed between the two measurements. Overall, both FT-IR and ICP-OES analyses served as valuable tools in confirming the nickel content of Ni-impregnated ACF in this study.

Table 1. Amount of Ni-Impregnated by Reduction of $\text{Ni}(\text{NO}_3)_2$ using FT-IR and Amount of Ni-Impregnated by ICP-OES.

Sample Name	FT-IR (mg/g)	ICP-OES (mg/g)
PI-ACF	-	-
0.1-Ni-ACF	0.83	0.56
0.5-Ni-ACF	2.35	2.10
1.0-Ni-ACF	3.26	2.89
5.0-Ni-ACF	4.08	3.88
9.0-Ni-ACF	5.16	5.41

3.2. XRD and XPS Analyses

Figure 2 exhibits the XRD patterns of the Ni-impregnated ACFs. XRD analysis is a helpful method for analyzing the crystal structure of ACF and confirming the chemical structure of impregnated Ni [44]. In the untreated ACF, a wide non-crystalline carbon structure was observed at $20\text{--}25^\circ$, resulting from the diffraction from the (002) plane owing to the irregularly stacked structure of graphite. A significantly broad peak was found around 43° , composed of not clearly separated (100) and (101) planes due to the incomplete graphite molecular layers. After nickel impregnation and subsequent thermal

reduction, a leftward bias of the (002) plane was observed, which was similar to the increase in the interlayer spacing due to the oxidation of the fine crystal structure by oxygen molecules generated during $\text{Ni}(\text{NO}_3)_2$ decomposition. Moreover, as the amount of impregnation increased, the peak intensities of 44.6° and 51.9° increased. The peaks at 44.6° and 51.9° correspond to the (111) and (200) planes of the FCC crystal structure of pure nickel [45]. Thus, the impregnated material was primarily composed of metallic nickel. Peaks corresponding to the reference NiO and $\text{Ni}(\text{NO}_3)_2$ were not observed in any samples.

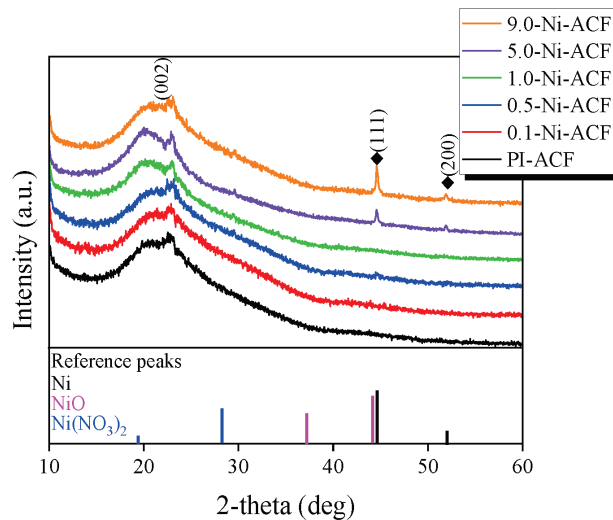


Figure 2. XRD patterns of nickel-impregnated activated carbon fibers as a function of $\text{Ni}(\text{NO}_3)_2$ impregnation concentration.

XPS is a non-destructive (or weak) surface technique that utilizes the electron binding energy of atoms present on the sample surface to determine elemental composition and chemical state. Figure 3 illustrates the change in oxygen content in Ni-ACF following nickel impregnation and subsequent thermal reduction treatment. Although all Ni-ACF samples were treated at the same temperature and time, the oxygen content tended to decrease as the nickel content increased. It is believed that the deposited nickel acted as a catalyst for the reduction reaction, enhancing the activation energy and reaction rate, and thus, more vigorous reduction occurred as the nickel content increased.

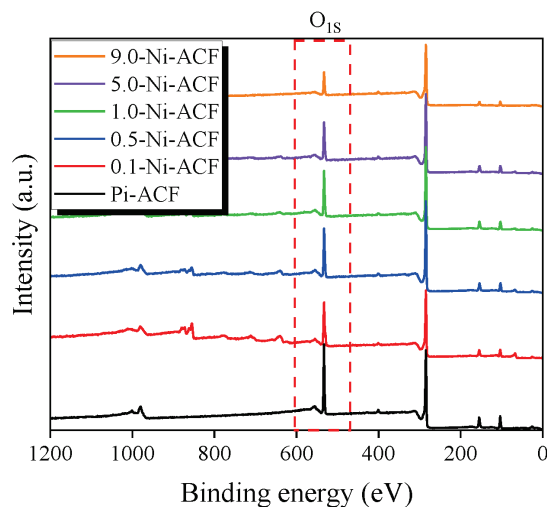


Figure 3. XPS survey spectra of nickel-impregnated activated carbon fibers as a function of $\text{Ni}(\text{NO}_3)_2$ impregnation concentration at room temperature.

Figure 4 presents the O_{1s} and Ni_{2p} spectra of the Ni-ACFs obtained using XPS. Figure 4a,b show the Ni_{2p} peaks of the untreated PI-ACF and 1.0-Ni-ACF, respectively, where Ni_{2p} and O_{1s} are compared on the same y-axis scale. While no Ni peak was discernible in the untreated PI-ACF, Ni metal and NiO peaks in the 850–868 eV range were detected in the 1.0-Ni-ACF due to the impregnation and reduction processes [46]. Figure 4c,d show the O_{1s} peaks of the untreated PI-ACF and 1.0-Ni-ACF, respectively. For the PI-ACF, peaks for C-O, C=O, and COOH were observed at 9.0%, 72.1%, and 18.9%, respectively, while those for the 1.0-Ni-ACF were observed at 6.1%, 66.2%, and 21.6%, with an additional Ni-O peak at 6.0%. All the oxygen functional groups decreased after reduction, with the decrease in C-O being the most obvious. XPS and XRD verified the impregnation state of nickel on the ACF, and most of the nickel was confirmed to be pure metallic nickel by XRD. Furthermore, the XPS results confirmed that some of the nickel on the surface was formed as NiO.

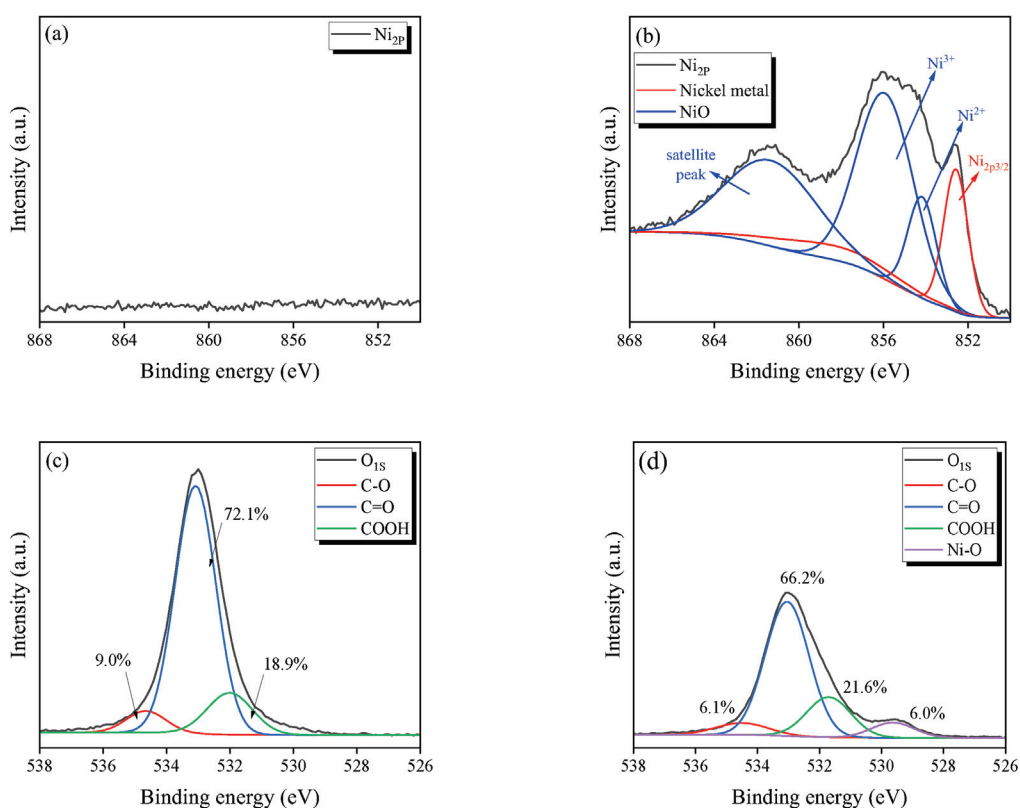


Figure 4. High-resolution Ni_{2p} and O_{1s} deconvolution peaks of nickel-impregnated activated carbon fibers; (a) Ni_{2p} of PI-ACF, (b) Ni_{2p} of 1.0-Ni-ACF, (c) O_{1s} of PI-ACF, and (d) O_{1s} of 1.0-Ni-ACF.

3.3. $N_2/77K$ Adsorption-Desorption Isotherm Curve

Figure 5 exhibits the $N_2/77K$ adsorption-desorption isotherms of the ACF. All ACFs were classified as Type I according to the IUPAC classification [47], and their N_2 adsorption was predominantly observed at a relative pressure (P/P_0) of <0.1 . This indicates monolayer adsorption owing to the strong interaction between the pore walls of the ACF and N_2 , suggesting that the ACFs are primarily microporous. The decrease in adsorption at a relative pressure (P/P_0) of <0.1 with increased impregnated nickel was confirmed. However, despite impregnation, increased N_2 adsorption was observed at a relative pressure (P/P_0) of <0.1 in the 0.1-Ni-ACF, and a subsequent decrease was confirmed with an increase in the amount of impregnated nickel. This may be because the amount of pore opening due to (1) the decomposition of oxygen functional groups and (2) the oxidation of ultrafine crystallites by additionally generated oxygen molecules, as confirmed by XRD, was more significant than the reduction in adsorption caused by pore blocking due to

nickel impregnation. However, an increase in additional impregnation led to the dominant occurrence of typical pore blocking.

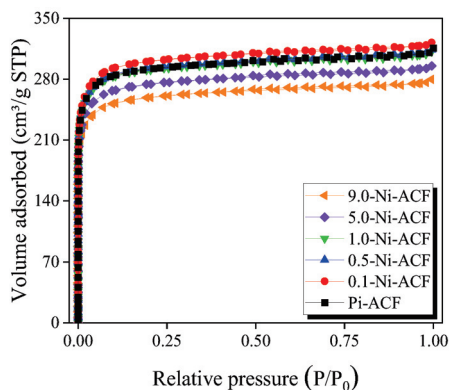


Figure 5. N₂/77K adsorption-desorption isotherm curves of nickel-impregnated activated carbon fibers as a function of Ni(NO₃)₂ impregnation concentration.

The shape of the hysteresis loop correlates with specific pore characteristics [47]. The N₂/77K adsorption-desorption isotherms of all the ACF samples exhibited type H4 hysteresis according to the IUPAC classification. Even with increased impregnation, the area of the hysteresis loop did not change significantly. This indicates that the untreated ACF possessed slit-shaped pores and that the impregnation and thermal reduction treatments did not significantly alter the pore shape.

Figure 6 illustrates the pore size distribution (PSD) curves for Ni-ACF, which were obtained using the NLDFT equation. In Figure 6, the PSD curves for Ni-ACFs display a gradual decrease in pore volume for sizes below 1.0 nm as the amount of nickel impregnation increases. However, in the range of 1.0–2.0 nm, the pore volume shows an increase from Pi-ACF to 0.5-Ni-ACF, followed by a subsequent decrease up to 9.00-Ni-ACF. Notably, there are no significant changes in pore volume observed for mesopores with sizes of 2.0 nm and above. These changes in pore volume are attributed to the influence of (1) the decomposition of oxygen functional groups and (2) the oxidation of ultrafine crystallites by additionally generated oxygen molecules. This has resulted in an increase in pore volume at certain pore sizes and a decrease in pore volume in the range of 1.0–2.0 nm as the nickel impregnation amount increases.

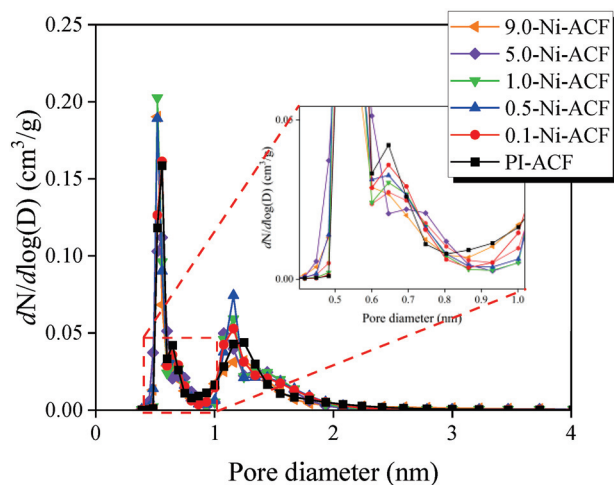


Figure 6. Pore size distribution of the nickel-impregnated activated carbon fibers as a function of Ni(NO₃)₂ impregnation concentration.

3.4. Textural Properties

Table 2 presents the pore characteristics of the ACF as a function of nickel impregnation. The specific surface area and total pore volume of the ACF were 1010–1180 m²/g and 0.43–0.50 cm³/g, respectively. The micropore volume of the ACF was 0.41–0.47 cm³/g, while its fractional micropore volume was 94.0–94.7%. Compared to the untreated ACF, the nickel impregnated ACF exhibited a gradual decrease in specific surface area. However, in the case of 0.1 and 0.5-Ni-ACF, the oxygen functional groups were observed to have been removed, and additional mesopores were opened because of the thermal reduction treatment, thus increasing the specific surface area. As the amount of impregnation increased, the specific surface area decreased. The micropore volume exhibits a trend similar to that of the specific surface area. The mesopore volume was 0.03 cm³/g for all samples except 9.0-Ni-ACF.

Table 2. Textural Properties of Ni-impregnated Polyimide-based Activated Carbon Fibers as a Function of Ni(NO₃)₂ Concentration.

Sample Name	S _{BET} ^a (m ² /g)	V _{Total} ^b (cm ³ /g)	V _{Micro} ^c (cm ³ /g)	V _{Meso} ^d (cm ³ /g)	R _{Micro} ^e (%)	D _{avg} ^f (nm)
PI-ACF	1150	0.48	0.45	0.03	93.8	1.69
0.1-Ni-ACF	1180	0.50	0.47	0.03	94.0	1.68
0.5-Ni-ACF	1160	0.49	0.46	0.03	93.9	1.71
1.0-Ni-ACF	1130	0.48	0.45	0.03	93.8	1.71
5.0-Ni-ACF	1070	0.46	0.43	0.03	93.5	1.73
9.0-Ni-ACF	1010	0.43	0.41	0.02	95.3	1.74

^a S_{BET}: Specific surface area: BET method $\frac{p}{v(p_0-p)} = \frac{1}{v_m} + \frac{c-1}{v_m c} \cdot \frac{p}{p_0}$. ^b V_{Total}: Total pore volume; The amount adsorbed P/P₀ = 0.99. ^c V_{Micro}: Micropore volume: t-plot methods. ^d V_{Meso}: ^b V_{Total} - ^c V_{Micro}. ^e R_{Micro}: Micropore volume ratio; $\frac{V_{Micro}}{V_{Total}} \times 100$ ^f D_{avg}: Average pore diameter.

3.5. NO Adsorption Behavior

Figure 7a illustrates the NO adsorption behavior of the ACF, where C/C₀ = 1.0 (30 ppm) is the saturation point. The adsorption capacity up to saturation was in the order of 0.1-Ni-ACF < 0.5-Ni-ACF < PI-ACF < 1.0-Ni-ACF < 5.0-Ni-ACF < 9.0-Ni-ACF. The specific surface area of the ACF was in the order of 9.0-Ni-ACF < 5.0-Ni-ACF < 1.0-Ni-ACF < PI-ACF < 0.5-Ni-ACF < 0.1-Ni-ACF; NO adsorption showed a completely opposite behavior to the specific surface area. Although the nickel content followed the order 0.1-Ni-ACF < 0.5-Ni-ACF < 1.0-Ni-ACF < 5.0-Ni-ACF < 9.0-Ni-ACF, it did not correlate directly with the NO adsorption capacity. Therefore, the NO adsorption behavior was influenced by a combination of the specific surface area (physical adsorption) and nickel content (chemical adsorption), along with other potential variables.

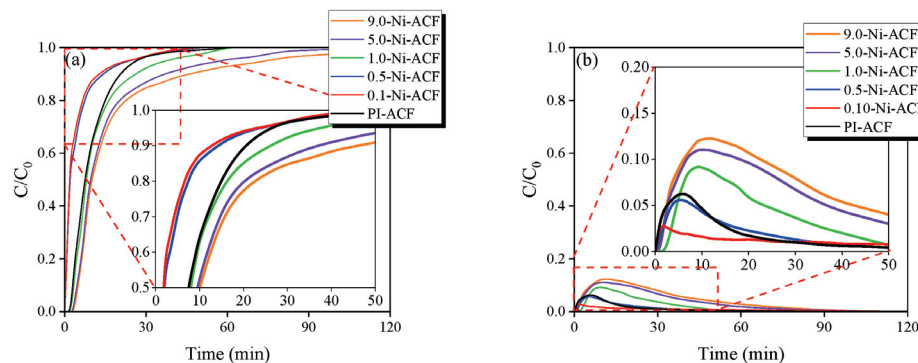


Figure 7. (a) NO adsorption curves and (b) CO₂ generation curves of nickel-impregnated activated carbon fibers as a function of Ni(NO₃)₂ impregnation concentration at room temperature.

Figure 7b shows the CO₂ detection curve according to NO adsorption. CO₂ was detected in all ACF samples in the order of 0.1-Ni-ACF < 0.5-Ni-ACF < PI-ACF < 1.0-Ni-ACF < 5.0-Ni-ACF < 9.0-Ni-ACF. The behavior of CO₂ detection was parallel to the trend observed for the NO adsorption capacity. This similarity in the behavior of NO adsorption and CO₂ detection suggests the emission of CO₂ during the adsorption of NO on carbonaceous materials. The following equation represents the NO adsorption mechanism on carbonaceous surfaces [48,49].

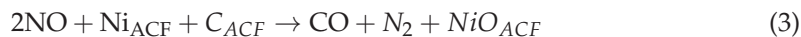


Figure 8 presents the XPS O_{1s} spectra before and after NO adsorption for the 9.0-Ni-ACF sample and the XRD results before and after adsorption for the untreated PI-ACF and 9.0-Ni-ACF samples. As shown in Figure 8b, no NO peak associated with physical adsorption was observed. The percentages of C-O, C=O, COOH, and Ni-O before adsorption were 6.1%, 66.2%, 21.6%, and 6.0%, and after adsorption were 6.4%, 64.2%, 23.2%, and 6.2%. Interestingly, only the quantity of C=O decreased, whereas those of the others increased. This can be attributed to the higher initial proportion of C=O in the PI-ACF, where a higher probability of conversion to COOH rather than C=O occurs during the oxidation of the carbon surface. Although the increase in Ni-O after the adsorption treatment was 0.2%, it was assumed to be within the range of experimental error. This suggests that impregnated nickel primarily plays a catalytic role. Furthermore, Figure 8c illustrates the XRD patterns before and after adsorption, which show no evident differences, confirming the presence of pure Ni peaks at 44.6° and 51.9°. These results indicate that the nickel-impregnated on ACF undergoes only catalytic interactions without significant chemical transformations during NO adsorption.

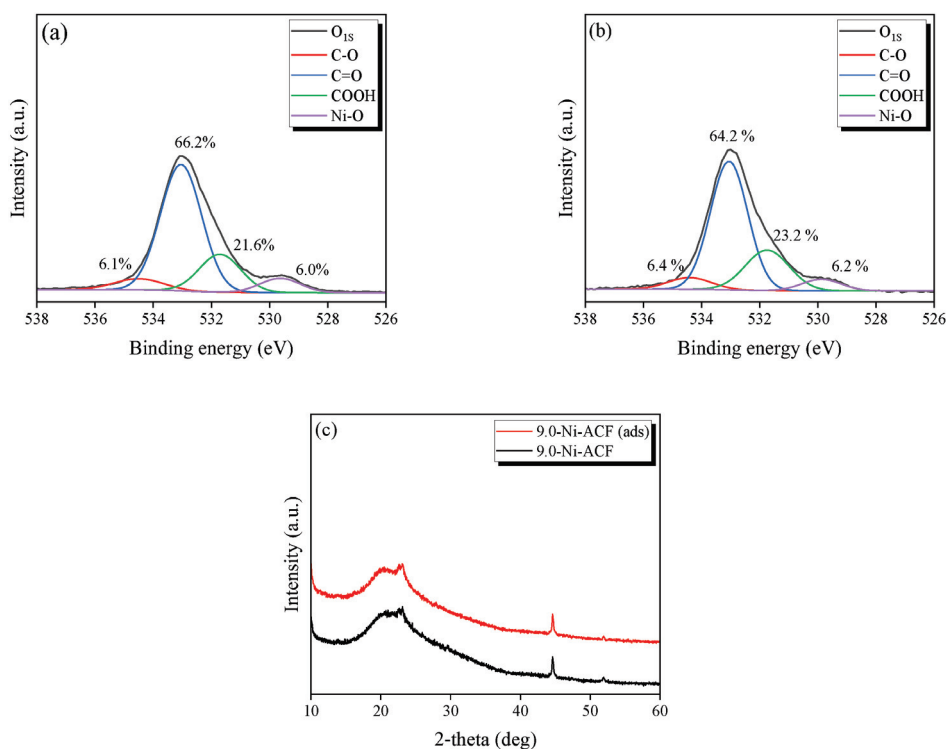


Figure 8. High-resolution O_{1s} deconvolution peaks of nickel-impregnated activated carbon fibers before and after NO adsorption: (a) 9.0-Ni-ACF before NO adsorption, (b) 9.0-Ni-ACF. (c) XRD pattern comparison of 9.0-Ni-ACF before and after NO adsorption.

We illustrate the NO adsorption capacity and CO₂ emission in Figure 9, which shows similar trends. Compared to PI-ACF, the NO adsorption capacity and CO₂ emissions decreased for 0.1-Ni-ACF and 0.5-Ni-ACF and then increased with higher nickel loadings. Notably, despite nickel impregnation, the NO adsorption capacity and CO₂ emission decreased for these samples, which have higher specific surface areas than the untreated PI-ACF. This suggests that factors other than nickel impregnation contributed to the reduction in the adsorption capacity. This decrease in NO adsorption capacity and CO₂ emission, despite the impregnation of nickel, suggests that factors other than nickel loading led to a decrease in the adsorption capacity. These specific samples exhibited a higher surface area than the untreated PI-ACF, indicating that other factors contributed to the observed reduction in adsorption capacity.

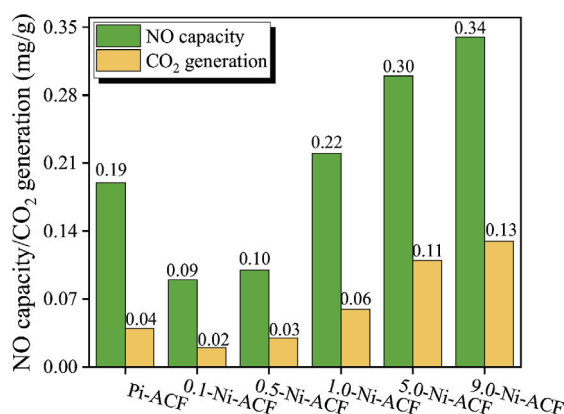


Figure 9. NO removal and CO₂ generation capacity of nickel-impregnated activated carbon fibers as a function of Ni(NO₃)₂ impregnation concentration at room temperature.

Figure 3 shows the oxygen content based on the XPS analysis for all ACF samples, indicating a decreasing trend for all heat-reduced samples compared with the untreated sample. In the NO adsorption behavior of the adsorbent, physical adsorption is initially performed, and then chemical/catalytic adsorption is performed. Therefore, the decrease in surface oxygen functional groups can lead to a decrease in the amount of physical adsorption in the initial stage, which can directly cause a decrease in the amount of chemical/catalytic adsorption in the later stage. In particular, the observed decrease in NO adsorption for the 0.1-Ni-ACF and 0.5-Ni-ACF samples, despite the presence of nickel as a catalyst and their high surface areas, can be attributed to the reduction of oxygen functional groups during the thermal reduction process [50,51]. This reduction in oxygen functional groups can weaken the dipole-dipole interaction between the ACF surface and NO molecules, thus decreasing the adsorption of polar NO molecules. For samples with higher nickel content, starting from 1.0-Ni-ACF, the catalytic reaction of nickel became more active, resulting in increased adsorption capacity compared to the untreated PI-ACF. However, as the adsorption capacity continued to increase, the blockage of the pore structure intensified, leading to a further decrease in the initial material adsorption and ultimately decreasing the overall NO adsorption removal characteristics.

4. Conclusions

In this study, we investigated the NO adsorption removal behavior of nickel-impregnated PI-based ACFs and found that it was influenced by the amount of impregnated nickel and surface oxygen functional groups. The impregnated metallic nickel played a catalytic role without undergoing significant chemical structure changes in composition, whereas the adsorption removal of NO increased with increasing nickel impregnation within a range in which the specific surface area did not decrease significantly. Furthermore, due to the reduction treatment, the surface oxygen content decreased, and samples with lower nickel loadings exhibited lower NO adsorption removal than the untreated ACF. However, compared to the

untreated sample, a distinct increase in NO adsorption was observed with a nickel loading of 0.3 wt.% or higher. Nevertheless, excessive nickel impregnation is expected to further block the pore structure and negatively affect NO adsorption removal. The unchanged pore diameter due to this impregnation is in the nanoscale range, indicating that the impregnated metal particles are expected to be in the nanoscale or even smaller size, as the pore structure remains unaltered after impregnation. In addition, a minor metal impregnation method that does not significantly affect the pore structure could offer various contributions to future nanomaterial research. This approach can be applied not only to metals other than nickel but also to diverse research fields, such as energy storage technologies (e.g., activated carbon in supercapacitors), beyond the field of adsorption. Therefore, we will conduct further research to investigate the optimal impregnation loading, focusing on nanoscale impregnation studies for our future investigations.

Author Contributions: Conceptualization, B.-J.K.; Data curation, H.-S.J. and B.-J.K.; Formal analysis, H.-S.J.; Funding acquisition, B.-J.K.; Investigation, H.-S.J.; Methodology, B.-J.K.; Project administration, B.-J.K.; Resources, B.-J.K.; Software, H.-S.J.; Supervision, B.-J.K.; Validation, H.-S.J. and B.-J.K.; Visualization, H.-S.J.; Writing—original draft, H.-S.J.; Writing—review and editing, H.-S.J. and B.-J.K. All authors have read and agreed to the published version of the manuscript.

Funding: This research was supported by the Nano-Material Technology Development Program through the National Research Foundation of Korea (NRF-2019M3A7B9071501), funded by the Ministry of Science and ICT of the Republic of Korea.

Data Availability Statement: Not applicable.

Conflicts of Interest: The authors declare no conflict of interest.

References

- Boningari, T.; Smirniotis, P.G. Impact of nitrogen oxides on the environment and human health: Mn-based materials for the NO_x abatement. *Curr. Opin. Chem. Eng.* **2016**, *13*, 133–141. [CrossRef]
- Chin, T.; Tam, I.C.; Yin, C.-Y. Comparison of various chemical compounds for the removal of SO₂ and NO_x with wet scrubbing for marine diesel engines. *Environ. Sci. Pollut. Res.* **2021**, *29*, 8873–8891. [CrossRef]
- Fang, Z.; Yu, X.; Tu, S.-T. Catalytic oxidation of NO on activated carbons. *Energy Procedia* **2019**, *158*, 2366–2371. [CrossRef]
- Pârvulescu, V.I.; Grange, P.; Delmon, B. Catalytic removal of NO. *Catal. Today* **1998**, *46*, 233–316. [CrossRef]
- Zhu, J.; Thomas, A. Perovskite-type mixed oxides as catalytic material for NO removal. *Appl. Catal. B Environ.* **2009**, *92*, 225–233. [CrossRef]
- Nakamura, I.; Negishi, N.; Kutsuna, S.; Ihara, T.; Sugihara, S.; Takeuchi, K. Role of oxygen vacancy in the plasma-treated TiO₂ photocatalyst with visible light activity for NO removal. *J. Mol. Catal. A Chem.* **2000**, *161*, 205–212. [CrossRef]
- Hong, Z.; Wang, Z.; Li, X. Catalytic oxidation of nitric oxide (NO) over different catalysts: An overview. *Catal. Sci. Technol.* **2017**, *7*, 3440–3452. [CrossRef]
- Wang, T.; Zhu, C.; Liu, H.; Xu, Y.; Zou, X.; Xu, B.; Chen, T. Performance of selective catalytic reduction of NO with NH₃ over natural manganese ore catalysts at low temperature. *Environ. Technol.* **2017**, *39*, 317–326. [CrossRef]
- Wei, J.; Luo, Y.; Yu, P.; Cai, B.; Tan, H. Removal of NO from flue gas by wet scrubbing with NaClO₂/(NH₂)₂CO solutions. *J. Ind. Eng. Chem.* **2009**, *15*, 16–22. [CrossRef]
- Fang, P.; Cen, C.; Wang, X.; Tang, Z.; Tang, Z.; Chen, D. Simultaneous removal of SO₂, NO and Hg₀ by wet scrubbing using urea+KMnO₄ solution. *Fuel Process. Technol.* **2013**, *106*, 645–653. [CrossRef]
- Nikolov, P.; Khristova, M.; Mehandjiev, D. Low-temperature NO removal over copper-containing activated carbon. *Colloids Surf. A Physicochem. Eng. Asp.* **2007**, *295*, 239–245. [CrossRef]
- Wang, M.-X.; Guo, Z.; Huang, Z.-H.; Kang, F. NH₃-activated carbon nanofibers for low-concentration NO removal at room temperature. *Catal. Commun.* **2015**, *62*, 83–88. [CrossRef]
- Mohan, D.; Pittman, C.U., Jr. Activated carbons and low cost adsorbents for remediation of tri- and hexavalent chromium from water. *J. Hazard. Mater.* **2006**, *137*, 762–811. [CrossRef] [PubMed]
- Neolaka, Y.A.B.; Riwo, A.A.P.; Aigbe, U.O.; Ukhurebor, K.E.; Onyancha, R.B.; Darmokoeseomo, H.; Kusuma, H.S. Potential of activated carbon from various sources as a low-cost adsorbent to remove heavy metals and synthetic dyes. *Results Chem.* **2023**, *5*, 100711. [CrossRef]
- Kang, K.C.; Kim, S.S.; Choi, J.W.; Kwon, S.H. Sorption of Cu²⁺ and Cd²⁺ onto acid- and base-pretreated granular activated carbon and activated carbon fiber samples. *J. Ind. Eng. Chem.* **2008**, *14*, 131–135. [CrossRef]
- Kim, B.-J.; Lee, H.-M.; Kim, H.-G.; An, K.-H.; Kang, H.-R. Comparative studies of porous carbon nanofibers by various activation methods. *Carbon Lett.* **2013**, *14*, 180–185.

17. Lee, B.-H.; Lee, H.-M.; Chung, D.C.; Kim, B.-J. Effect of Mesopore Development on Butane Working Capacity of Bio-mass-Derived Activated Carbon for Automobile Canister. *Nanomaterials* **2021**, *11*, 673. [CrossRef]
18. Lee, H.-M.; Lee, B.-H.; An, K.-H.; Park, S.-J.; Kim, B.-J. Facile preparation of activated carbon with optimal pore range for high butane working capacity. *Carbon Lett.* **2020**, *30*, 297–305. [CrossRef]
19. Lozano-Castelló, D.; Cazorla-Amorós, D.; Linares-Solano, A.; Quinn, D.F. Influence of pore size distribution on methane storage at relatively low pressure: Preparation of activated carbon with optimum pore size. *Carbon* **2002**, *40*, 989–1002. [CrossRef]
20. Hao, Y.; Leng, Z.; Yu, C.; Xie, P.; Meng, S.; Zhou, L.; Li, Y.; Liang, G.; Li, X.; Liu, C. Ultra-lightweight hollow bowl-like carbon as microwave absorber owning broad band and low filler loading. *Carbon* **2023**, *212*, 118156. [CrossRef]
21. Mochida, I.; Kawabuchi, Y.; Kawano, S.; Matsumura, Y.; Yoshikawa, M. High catalytic activity of pitch-based activated carbon fibres of moderate surface area for oxidation of NO to NO₂ at room temperature. *Fuel* **1997**, *76*, 543–548. [CrossRef]
22. Chang, S.; Han, Z.; Yang, J.; Chen, X.; Liu, J.; Liu, Y.; Li, J. Nitrogen-Doped Pitch-Based Activated Carbon Fibers with Multi-Dimensional Metal Nanoparticle Distribution for the Effective Removal of NO. *Catalysts* **2022**, *12*, 1192. [CrossRef]
23. Qu, Y.-F.; Guo, J.-X.; Chu, Y.-H.; Sun, M.-C.; Yin, H.-Q. The influence of Mn species on the SO₂ removal of Mn-based activated carbon catalysts. *Appl. Surf. Sci.* **2013**, *282*, 425–431. [CrossRef]
24. Moosavi, E.S.; Dastgheib, S.A.; Karimzadeh, R. Adsorption of Thiophenic Compounds from Model Diesel Fuel Using Copper and Nickel Impregnated Activated Carbons. *Energies* **2012**, *5*, 4233–4250. [CrossRef]
25. Jiménez-Marín, E.; Villalpando, I.; Trejo-Valdez, M.; Cervantes-Sodi, F.; Vargas-García, J.R.; Torres-Torres, C. Coexistence of positive and negative photoconductivity in nickel oxide decorated multiwall carbon nanotubes. *Mater. Sci. Eng. B* **2017**, *220*, 22–29. [CrossRef]
26. Yang, J.-K.; Park, H.-J.; Lee, H.-D.; Lee, S.-M. Removal of Cu(II) by activated carbon impregnated with iron(III). *Colloids Surf. A Physicochem. Eng. Asp.* **2009**, *337*, 154–158. [CrossRef]
27. Wang, J.; Zhao, F.; Hu, Y.; Zhao, R.; Liu, R. Modification of Activated Carbon Fiber by Loading Metals and Their Performance on SO₂ Removal. *Chin. J. Chem. Eng.* **2006**, *14*, 478–485. [CrossRef]
28. Xu, S.; Niu, M.; Zhao, G.; Ming, S.; Li, X.; Zhu, Q.; Ding, L.-X.; Kim, M.; Allothman, A.A.; Mushab, M.S.S.; et al. Size control and electronic manipulation of Ru catalyst over B, N co-doped carbon network for high-performance hydrogen evolution reaction. *Nano Res.* **2022**, *16*, 6212–6219. [CrossRef]
29. Khristova, M.; Mehandjiev, D. Conversion of NO on a Ni impregnated-active carbon catalyst in the presence of oxygen. *Carbon* **1998**, *36*, 1379–1385. [CrossRef]
30. Yamashita, H.; Yamada, H.; Tomita, A. Reaction of nitric oxide with metal-loaded carbon in the presence of oxygen. *Appl. Catal.* **1991**, *78*, L1–L6. [CrossRef]
31. Veiga, S.; Bussi, J. Steam reforming of crude glycerol over nickel supported on activated carbon. *Energy Convers. Manag.* **2017**, *141*, 79–84. [CrossRef]
32. Lee, H.-M.; Lee, B.-H.; Park, S.-J.; An, K.-H.; Kim, B.-J. Pitch-Derived Activated Carbon Fibers for Emission Control of Low-Concentration Hydrocarbon. *Nanomaterials* **2019**, *9*, 1313. [CrossRef] [PubMed]
33. Lee, H.-M.; Lee, B.-H.; Kim, J.-H.; An, K.-H.; Park, S.-J.; Kim, B.-J. Determination of the optimum porosity for 2-CEES adsorption by activated carbon fiber from various precursors. *Carbon Lett.* **2019**, *29*, 649–654. [CrossRef]
34. Liu, H.-S.; Chen, J.-Y.; Peng, Y.-H. Activated carbon fibers impregnated with Pd and Pt catalysts for toluene removal. *J. Hazard. Mater.* **2013**, *256–257*, 49–55. [CrossRef]
35. Lin, C.-L.; Cheng, Y.-H.; Liu, Z.-S.; Chen, J.-Y. Metal catalysts supported on activated carbon fibers for removal of polycyclic aromatic hydrocarbons from incineration flue gas. *J. Hazard. Mater.* **2011**, *197*, 254–263. [CrossRef] [PubMed]
36. Wang, C.; Bai, L.; Zhao, F.; Bai, L. Activated carbon fibers derived from natural cattail fibers for supercapacitors. *Carbon Lett.* **2022**, *32*, 907–915. [CrossRef]
37. Hassan, M.F.; Sabri, M.A.; Fazal, H.; Hafeez, A.; Shezad, N.; Hussain, M. Recent trends in activated carbon fibers production from various precursors and applications—A comparative review. *J. Anal. Appl. Pyrolysis* **2020**, *145*, 104715. [CrossRef]
38. Kim, J.-H.; Jung, S.-C.; Lee, H.-M.; Kim, B.-J. Comparison of Pore Structures of Cellulose-Based Activated Carbon Fibers and Their Applications for Electrode Materials. *Int. J. Mol. Sci.* **2022**, *23*, 3680. [CrossRef]
39. Lee, H.-M.; An, K.-H.; Kim, B.-J. Effects of carbonization temperature on pore development in polyacrylonitrile-based activated carbon nanofibers. *Carbon Lett.* **2014**, *15*, 146–150. [CrossRef]
40. Zhang, M.Y.; Niu, H.Q.; Qi, S.L.; Tian, G.F.; Wang, X.D.; Wu, D.Z. Structure evolutions involved in the carbonization of polyimide fibers with different chemical constitution. *Mater. Today Commun.* **2014**, *1*, 1–8. [CrossRef]
41. Brunauer, S.; Emmett, P.H.; Teller, E. Adsorption of Gases in Multimolecular Layers. *J. Am. Chem. Soc.* **1938**, *60*, 309–319. [CrossRef]
42. Lippens, B. Studies on pore systems in catalysts V. The t method. *J. Catal.* **1965**, *4*, 319–323. [CrossRef]
43. Barrett, E.P.; Joyner, L.G.; Halenda, P.P. The Determination of Pore Volume and Area Distributions in Porous Substances. I. Computations from Nitrogen Isotherms. *J. Am. Chem. Soc.* **1951**, *73*, 373–380. [CrossRef]
44. Aboud, M.; AlOthman, Z.; Habila, M.; Zlotea, C.; Latroche, M.; Cuevas, F. Hydrogen Storage in Pristine and d10-Block Metal-Anchored Activated Carbon Made from Local Wastes. *Energies* **2015**, *8*, 3578–3590. [CrossRef]
45. Jayaseelan, C.; Rahuman, A.A.; Ramkumar, R.; Perumal, P.; Rajakumar, G.; Kirthi, A.V.; Santhoshkumar, T.; Marimuthu, S. Effect of sub-acute exposure to nickel nanoparticles on oxidative stress and histopathological changes in Mozambique tilapia, *Oreochromis mossambicus*. *Ecotoxicol. Environ. Saf.* **2014**, *107*, 220–228. [CrossRef]

46. Biesinger, M.C.; Payne, B.P.; Lau, L.W.M.; Gerson, A.; Smart, R.S.C. X-ray photoelectron spectroscopic chemical state quantification of mixed nickel metal, oxide and hydroxide systems. *Surf. Interface Anal.* **2009**, *41*, 324–332. [CrossRef]
47. Thommes, M.; Kaneko, K.; Neimark, A.V.; Olivier, J.P.; Rodriguez-Reinoso, F.; Rouquerol, J.; Sing, K.S.W. Physisorption of gases, with special reference to the evaluation of surface area and pore size distribution (IUPAC Technical Report). *Pure Appl. Chem.* **2015**, *87*, 1051–1069. [CrossRef]
48. Chen, Z.; Lin, M.; Ignowski, J.; Kelly, B.; Linjewile, T.M.; Agarwal, P.K. Mathematical modeling of fluidized bed combustion. 4: N₂O and NO_x emissions from the combustion of char. *Fuel* **2001**, *80*, 1259–1272. [CrossRef]
49. Swartz, W.E., Jr.; Youssefi, M. The reactions of nitric oxide with nickel films as studied by X-ray photoelectron spectroscopy. *J. Electron Spectrosc. Relat. Phenom.* **1976**, *8*, 61–70. [CrossRef]
50. Liu, X.; Sun, F.; Qu, Z.; Gao, J.; Wu, S. The effect of functional groups on the SO₂ adsorption on carbon surface I: A new insight into noncovalent interaction between SO₂ molecule and acidic oxygen-containing groups. *Appl. Surf. Sci.* **2016**, *369*, 552–557. [CrossRef]
51. Liu, H.; Yu, Y.; Shao, Q.; Long, C. Porous polymeric resin for adsorbing low concentration of VOCs: Unveiling adsorption mechanism and effect of VOCs' molecular properties. *Sep. Purif. Technol.* **2019**, *228*, 115755. [CrossRef]

Disclaimer/Publisher's Note: The statements, opinions and data contained in all publications are solely those of the individual author(s) and contributor(s) and not of MDPI and/or the editor(s). MDPI and/or the editor(s) disclaim responsibility for any injury to people or property resulting from any ideas, methods, instructions or products referred to in the content.



Article

Effect of Solvent on Fluorescence Emission from Polyethylene Glycol-Coated Graphene Quantum Dots under Blue Light Illumination

Po-Chih Yang ^{1,*}, Yu-Xuan Ting ¹, Siyong Gu ², Yasser Ashraf Gandomi ³, Jianlin Li ⁴ and Chien-Te Hsieh ^{1,*}

¹ Department of Chemical Engineering and Materials Science, Yuan Ze University, Taoyuan 32003, Taiwan; danny0935331003@gmail.com

² Fujian Provincial Key Laboratory of Functional Materials and Applications, School of Materials Science and Engineering, Xiamen University of Technology, Xiamen 361024, China; gu-siyong@163.com

³ Department of Chemical Engineering, Massachusetts Institute of Technology, Cambridge, MA 02142, USA; ygandomi@mit.edu

⁴ Oak Ridge National Laboratory, Electrification and Energy Infrastructure Division, Oak Ridge, TN 37831, USA; lij4@ornl.gov

* Correspondence: pcyang@saturn.yzu.edu.tw (P.-C.Y.); cthsieh@saturn.yzu.edu.tw (C.-T.H.)

Abstract: To explore aggregate-induced emission (AIE) properties, this study adopts a one-pot hydrothermal route for synthesizing polyethylene glycol (PEG)-coated graphene quantum dot (GQD) clusters, enabling the emission of highly intense photoluminescence under blue light illumination. The hydrothermal synthesis was performed at 300 °C using o-phenylenediamine as the nitrogen and carbon sources in the presence of PEG. Three different solvents, propylene glycol methyl ether acetate (PGMEA), ethanol, and water, were used for dispersing the PEG-coated GQDs, where extremely high fluorescent emission was achieved at 530–550 nm. It was shown that the quantum yield (QY) of PEG-coated GQD suspensions is strongly dependent on the solvent type. The pristine GQD suspension tends to be quenched (i.e., QY: ~1%) when dispersed in PGMEA (aggregation-caused quenching). However, coating GQD nanoparticles with polyethylene glycol results in substantial enhancement of the quantum yield. When investigating the photoluminescence emission from PEG-coated GQD clusters, the surface tension of the solvents was within the range of from 26.9 to 46.0 mN/m. This critical index can be tuned for assessing the transition point needed to activate the AIE mechanism which ultimately boosts the fluorescence intensity. The one-pot hydrothermal route established in this study can be adopted to engineer PEG-coated GQD clusters with solid-state PL emission capabilities, which are needed for next-generation optical, bio-sensing, and energy storage/conversion devices.

Keywords: nitrogen functionalization; graphene quantum dots; photoluminescence; hydrothermal synthesis

1. Introduction

Graphene quantum dots (GQDs) have experienced a surge in attention compared to other nanomaterials thanks to their superior physicochemical properties including excellent solubility, high stability, and low toxicity [1]. In particular, due to their stable photoluminescence and ultra-high resistance to photobleaching, GQDs have been widely used in the architecture of various devices such as bio-imaging instruments [2], high-precision sensors [3], electrochemical energy devices [4–10], light-emitting apparatus [11], and solar reactors [12]. It is well established that GQDs with an average particle size of <10 nm exhibit quantum confinement, and as a result, photoluminescence (PL) with variable wavelength and photobleaching impedance can be designed and engineered [13]. Compared to conventional semiconducting quantum dots, GQDs have superior properties

such as remarkable biocompatibility, very robust interfacial structure, high solubility (aqueous), and a tunable band gap [11,14].

Despite these remarkable attributes, the widespread adoption of GQDs faces several critical challenges. Low quantum yield (QY), wide full width at half maximum (FWHM), and solvent-dependent PL behavior are among the major issues yet to be addressed. The latter plays a crucial role in affecting the PL behavior of GQD suspensions such as red/blue shift, FWHM, and QY, mainly originating from its dispersion extent and storage period in various solvents. One important PL mechanism, aggregation-caused quenching (ACQ), has recently been discovered, where the molecules are aggregated due to the intense intermolecular π - π interactions [15,16]. The conventional organic dyes commonly demonstrate ACQ behavior; thus, their implementation within the organic light emitting diodes as well as the bio-imaging devices has been significantly limited since the emission is easily quenched when an organic dye is employed as a solid film and in the aggregate state [15]. On the other hand, aggregate-induced emission (AIE) is intense for the solid state, as well as the aggregated mode, and is insignificant in dilute solutions. Most commonly, restricting the intramolecular motions (RIM) is considered a key control for modulating the AIE operation [17]. To further explore the RIM structures, several prior efforts have focused on developing hydrothermal synthesis routes for preparing polyethylene glycol (PEG)-passivated carbon nanostructures in the form of carbon nanodots [18]. It has been shown that the QY associated with the PEG-passivated composite nanostructures is almost two-fold higher compared to the pristine case with no passivation [18]. Recently, our group adopted a one-pot solvothermal method for synthesizing PEG-coated GQD clusters, capable of emitting green (QY: 85.3%) and red (14.6%) fluorescence under blue light illumination [19]. Such an ultrahigh QY for the PEG-coated GQD suspensions was primarily due to the formation of a structurally robust, two-dimensional framework on the exterior surface of the GQDs (i.e., a PEG-coated aggregate).

In our previous work, we demonstrated the capability of the PEG-coated GQD clusters of emitting green and red fluorescence under blue light illumination; however, an in-depth analysis of the AIE-enhanced luminescent process in PEG-coated GQD nanostructures is yet to be conducted. Therefore, this study aims to explore the influence of solvent on the PL performance of PEG-coated GQD clusters. Herein, we report a facile and green hydrothermal technique to produce PEG-coated GQD clusters using *o*-phenylenediamine (*o*-PD), as both the nitrogen and carbon sources in the presence of PEG. Pioneering studies have proved the efficacy of *o*-PD precursors for synthesizing carbon nanodots using hydrothermal [20,21], solvothermal [22], microwave-assisted [23], and electrochemical bottom-up synthesis techniques [24]. The PEG chains enable the in-situ formation of a two-dimensional network covering the GQDs during the hydrothermal molecular fusion process. The effect of the molecular weight of PEG on the PL emission from the PEG-coated GQD clusters was explored in water, ethanol, and propylene glycol methyl ether acetate (PGMEA). Finally, we have proposed a single-step hydrothermal synthesis route that can be employed for preparing immensely luminescent PEG-coated GQD clusters. Thus, this work has been dedicated to establishing the ACQ/AIE cycle through exploring the relationship between the solvent type and cluster structure, based on the RIM fluorescence mechanism.

2. Materials and Methods

2.1. Hydrothermal Synthesis of PEG-Coated GQD Clusters

To synthesize the PEG-coated GQD clusters, first, the *o*-PD (1.5 g, Alfa Aesar, Ward Hill, MA, USA, purity: 98%) and PEG (1.5 g, purity: 99.5% Sigma Aldrich, St. Louis, MO, USA) were homogeneously dispersed in 50 mL deionized water, then thoroughly stirred to prepare a well-mixed solution. Second, the suspension was placed into a poly(tetrafluoroethylene) (Teflon)-lined autoclave (75 mL, Macro Fortunate Co., Ltd., Taipei, Taiwan). The hydrothermal synthesis procedure was conducted at 300 °C for

~120 min. Upon cooling down to the ambient temperature, the as-prepared suspension with PEG-coated GQD samples was freeze-dried at $-30\text{ }^{\circ}\text{C}$ for 72 h. The PEG-coated GQD samples were filtered using a microporous separator with the average pore size of $\sim 0.02\text{ }\mu\text{m}$ in order to remove any insoluble residuals. Finally, the as-purified CNDs were dispersed in ultrapure water before conducting any experiment. Schematic illustration of synthesis procedure for the pristine and PEG-coated GQD clusters is provided in Figure 1. Throughout this paper, the pristine GQD samples with no PEG polymer additives have been labeled as “GQD-P”. In addition, the “GQD-100k”, and “GQD-6k” symbols have been used referring to the as-prepared PEG powders with higher molecular weight (i.e., 100,000 and 6000, respectively).

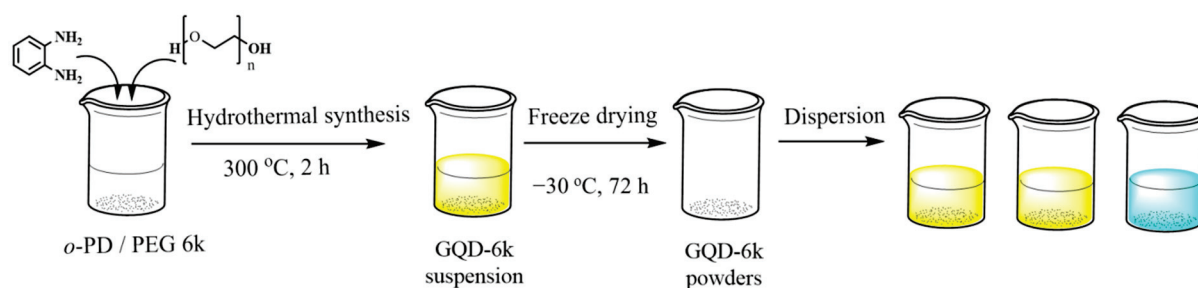


Figure 1. Schematic of PEG-coated GQD clusters (GQD-6k) through one-pot hydrothermal route.

2.2. Materials Characterization of PEG-Coated GQD Clusters

To characterize the as-prepared PEG-coated GQD clusters, several characterization methods and apparatus were employed, including a transmission electron microscopy (HR-TEM, model: F200s/Talos/FEI, Middlesex County, MA, USA), X-ray photoelectron spectroscopy (XPS, model: ESCA210/Fison VG, AZ, USA), Fourier-transform infrared (FT-IR, Varian, 1000-FTIR, Palo Alto, CA, USA), and ultraviolet-visible (UV-vis, Jasco, v650, Tokyo, Japan) absorption spectroscopy. To conduct the HR-TEM spectroscopy, the FEI Talos F200s electron microscope was used at 200 kV. The XPS spectra were recorded with the Fison VG ESCA210 machine and the corresponding C1s, N1s, and O1s peaks were fitted using an optimization algorithm developed in-house.

In order to prepare the GQD suspensions, the GQD powder (50 mg) was uniformly dispersed in different solvents (500 mL) including deionized water, PGMEA (Sigma Aldrich, St. Louis, MO, USA, purity: 99.5%), and ethanol (ECHO Chem., Miaoli, Taiwan, purity: 85 vol%). Next, a fluorescence spectrometer (Hitachi F-7000 FLS920P, Taipei, Taiwan) was utilized (at 450 and 360 nm) for acquiring the PL emission spectra. Finally, the quantum yield for each solution was assessed with respect to the Coumarin ($\text{C}_9\text{H}_6\text{O}_2$) reference (i.e., quantum yield $\sim 73\%$ at 373 nm) using Equation (1) [11]

$$\text{QY} = \text{QY}_r \times [(\text{PL}_a/\text{OD})_s / (\text{PL}_a/\text{OD})_r] \times F_s^2 / F_r^2 \quad (1)$$

where the subscripts “r” and “s” are used for the reference and the GQD sample, respectively. Furthermore, F represents the reflective index of the solvent, “ PL_a ” refers to the PL emission spectral surface, and “OD” is the absorbance magnitude.

3. Results and Discussion

HR-TEM micrographs of the GQD samples are provided in Figure 2. The GQD-P sample, as shown in Figure 2a, displays a spherical shape with an average diameter of $\sim 3\text{ nm}$. According to Figure 2a, a well-resolved lattice spacing of 0.21 nm, corresponding to the (100) facet of graphite [19,25], can be identified, indicating the formation of polycrystalline or amorphous carbon nanodots. The selected area diffraction (SAD) pattern (see the inset of Figure 2a reveals that the single GQD-P powder is of polycrystalline domain due to the presence of circular rings in the SAD pattern [19]. Figure 2b,c includes

the HR-TEM micrographs of PEG-coated GQD samples, confirming the presence of GQD clusters induced by the PEG bonding. It is critical to mention that the GQD nanoparticles have a high tendency to be confined together; however, being well-dispersed within the solution enables the formation of the PEG-coated clusters. The GQD nanoparticles formed demonstrate a relatively uniform particle size distribution where the diameter of the nanoparticles was in the range of 3–5 nm. Additionally, the cluster size increases with increased PEG molecular weight, i.e., 310 nm (PEG-100k) > 28 nm (PEG-6k). The SAD patterns, as illustrated in the inset of Figure 2a–c, also confirm the hydrothermal synthesis of polycrystalline structure of the GQD nanoparticles within the clusters. To further explore this observation, a dynamic laser-scattering (DLS) technique was used to characterize the cluster size of the PEG-coated composites, as depicted in the electronic supporting information (see Figure S1). According to Figure S1, the cluster size dependence on the PEG molecular weight can be identified (i.e., a trend of increasing cluster size with increasing molecular weight). This result confirms that the in-situ hydrothermal process provides a straightforward pathway for engineering the spherical carbon nanodots along with the PEG-coated clusters during the one-pot synthesis process [19].

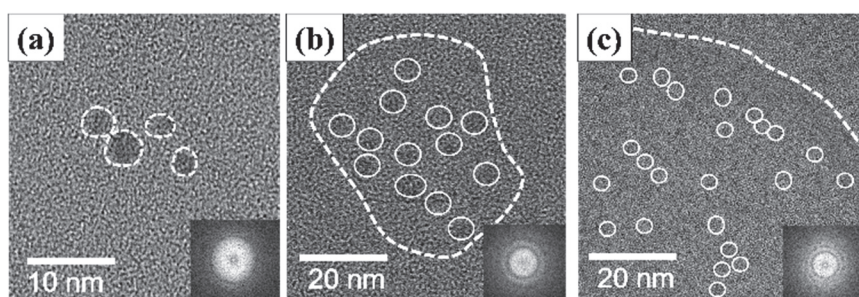


Figure 2. HR-TEM micrographs of (a) GQD-P, (b) GQD-6k, and (c) GQD-100k samples, where the inset shows their corresponding SAD patterns.

The XPS measurement was carried out to explore the surface chemistry and the distribution of functionalities imparted by the PEG coating layer. As shown in the survey-scan XPS spectra (see Figure S2), all the GQD samples were comprised of three main elements including C1s (ca. 282–292 eV), N1s (ca. 396–405 eV), and O1s (ca. 530–535 eV) [26,27]. The pristine GQD sample contained oxidation and amidation levels of 53.6 (O/C ratio) and 20.2 at.% (N/C ratio), respectively. Upon being modified by PEG bonding, the oxidation extent of PEG-coated GQD clusters decreased to 48.4 (GQD-6k) and 39.1 at.% (GQD-100k), while the amidation extent drastically reduced to 4.6 (GQD-6k) and 3.3 at.% (GQD-100k), as depicted in Figure S2. The changes in oxidation/amidation levels were mainly due to the formation of the PEG skin layer that covers the GQD particles and constructs a stereo framework of $\text{H}-(\text{O}-\text{CH}_2-\text{CH}_2)_n-\text{OH}$ chains. The decreased O/C ratio after the PEG coating is presumably due to polymer chains containing a large number of alkyl groups that tend to totally cover O-rich GQD surfaces (i.e., GQD-P (O/C ratio: 53.6 at.%)). We also observed that the O/C ratio is a decreasing function of PEG content. Thus, the construction of such a polymeric framework results in a lower amidation level within the molecular structure. It is worth mentioning that the GQD-100k sample imparts the lowest N/C atomic ratio among the GQD samples, attributed to the fact that high-molecular-weight PEG acts as a protective layer covering the GQD clusters, as confirmed by the HR-TEM and DLS analyses.

The distribution of oxygen functionalities on the pristine and PEG-coated GQD nanoparticles was investigated through decomposing the C1s and N1s peaks with an algorithm developed in-house (see Figure 3). First, the C1s spectra were extracted into five peaks at C=C/C-C (ca. 284.5 eV), C-N (ca. 285.8 eV), C-O (ca. 286.2 eV), and C=O (ca. 287.2 eV) [27,28]. It is very clear that the oxygen functionalities decrease upon the introduction of PEG chains into the GQD clusters. Indeed, the PEG framework provides a large amount of $\text{H}-(\text{O}-\text{CH}_2-\text{CH}_2)_n-\text{OH}$ chains, covering the GQD solid state. Due to

the PEG skin layer, the C-O/C=O ratio shows an increasing trend with the PEG content, i.e., GQD-P (0.59) < GQD-6k (1.63) < GQD-100k (1.86). Figure 4 illustrates the N1s peaks deconvoluted into three major peaks located at 399.6 eV (pyrrolic or pyridinic N), 400.4 eV (quaternary N), and 401.5 eV (N-oxides) [29,30]. The first and second components are due to the presence of aromatic C=N–C and tertiary N-(C)₃ bonds, respectively [31,32]. The presence of these two N doping types, commonly called “lattice-N”, confirms that the N-doping onto the GQD lattices was successful. As shown in Figure 5, the O1s spectra are composed of two major peaks at ca. 531.8 and ca. 532.5 eV, which mainly originated from the presence of C=O and C–O bonds, respectively [33].

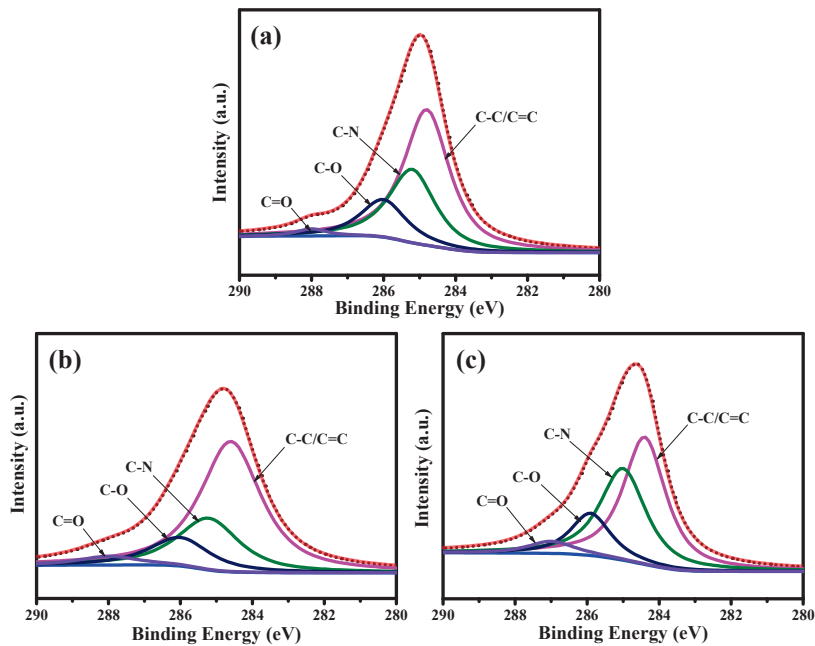


Figure 3. XPS C1s spectra of (a) GQD-P, (b) GQD-6k, and (c) GQD-100k samples, decomposed by a multiple Gaussian function.

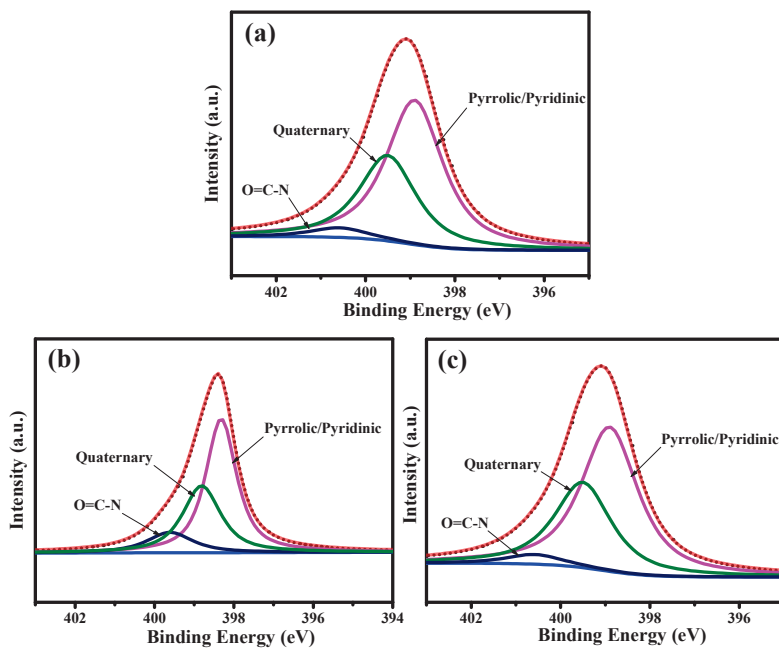


Figure 4. XPS N1s spectra of (a) GQD-P, (b) GQD-6k, and (c) GQD-100k samples, decomposed by a multiple Gaussian function.

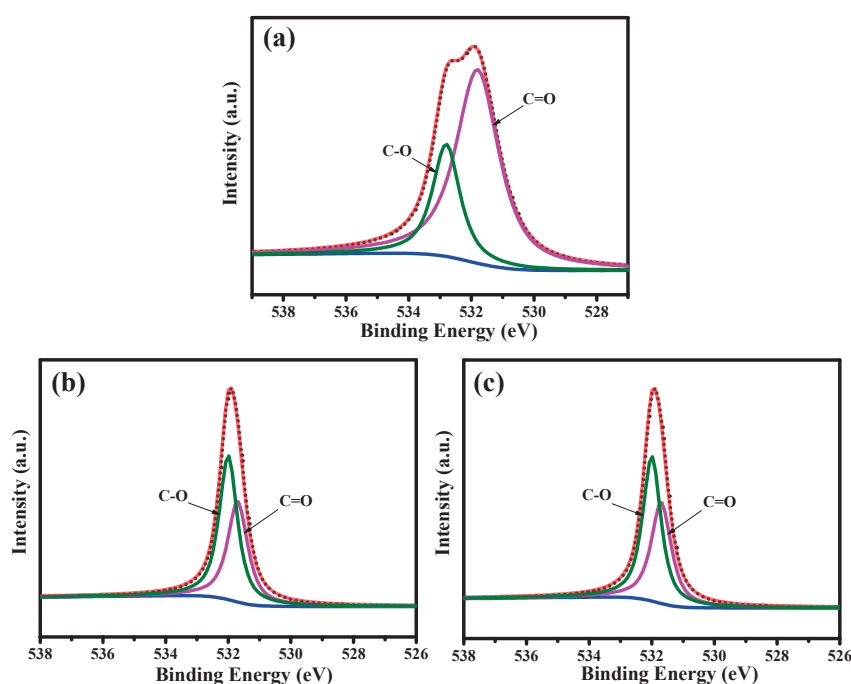


Figure 5. XPS O1s spectra of (a) GQD-P, (b) GQD-6k, and (c) GQD-100k samples, decomposed by a multiple Gaussian function.

FT-IR spectra were also recorded to examine the functional groups formed on the surface of the GQD samples (see Figure S3). We observed that one transmittance peak in the range of $1200\text{--}1300\text{ cm}^{-1}$ corresponded to the C-O stretch of -COOH , revealing the appearance of hydroxyl and carboxyl functional groups [34–36] attached to the GQD clusters. The transmittance band appearing at $\sim 1710\text{ cm}^{-1}$ is primarily due to the presence of C=N or C=O surface functionalities [37,38]. Furthermore, a single band at ca. $3250\text{--}3400\text{ cm}^{-1}$ was observed due to the adsorption of water molecules or N-H groups on the surface of GQD clusters [39]. Due to the hydrophilic PEG skin layer, the transmittance band becomes more evident on the PEG-coated GQD clusters compared to the pristine GQD sample, indicating the presence of a water-adsorbed layer onto the PEG-coated GQD clusters. The analysis of FT-IR spectra is consistent with the insight gained through the XPS measurements.

Figure 6a–c includes the UV-vis absorbance spectra of various GQD suspensions in DI water, PGMEA, and ethanol. The UV-vis spectra contain three major absorption bands with wavelengths ranging from 200 to 500 nm. The absorption bands at 200–250 nm are usually due to the $\pi\text{-}\pi^*$ transition of C=C of the sp^2 domain and the absorption bands within 280–450 nm can be attributed to the $\text{n}\text{-}\pi^*$ transition of C=N and C=O bonds [39–41]. Compared to the GQD-P suspension, both PEG-coated GQD clusters (i.e., GQD-6k and GQD-100k) exhibit an obvious shift in the C=C absorption band ($\pi\text{-}\pi^*$) and an intense absorption band associated with the $\text{n}\text{-}\pi^*$ transition. This confirms that the C-containing bonds in the molecular structure (C=N/C=O, C–O, and C–N) promote the $\text{n}\text{-}\pi^*$ transitions within solid or aggregate states [42]. Indeed, the PEG layer covers the GQD core, leading to a substantial absorbance throughout the entire domain. It is important to mention that the absorbance edge ($\text{n}\text{-}\pi^*$) in PGMEA demonstrates a different absorbance pattern compared to that in water and ethanol. Indeed, it can be inferred that the polarity of the solvent influences the absorbance of the GQD clusters [11, 43]. This trend is mainly due to partial dissolution of hydrophilic PEG nanolayer in high-polarity solvents (i.e., water), whereas the PEG layer constructs a protective layer against PGMEA molecules, creating a robust framework of PEG-coated GQD clusters. Therefore, the formation of the PEG layer is influenced by the solvent type and is capable of altering the edge morphology at multiple band gap structures.

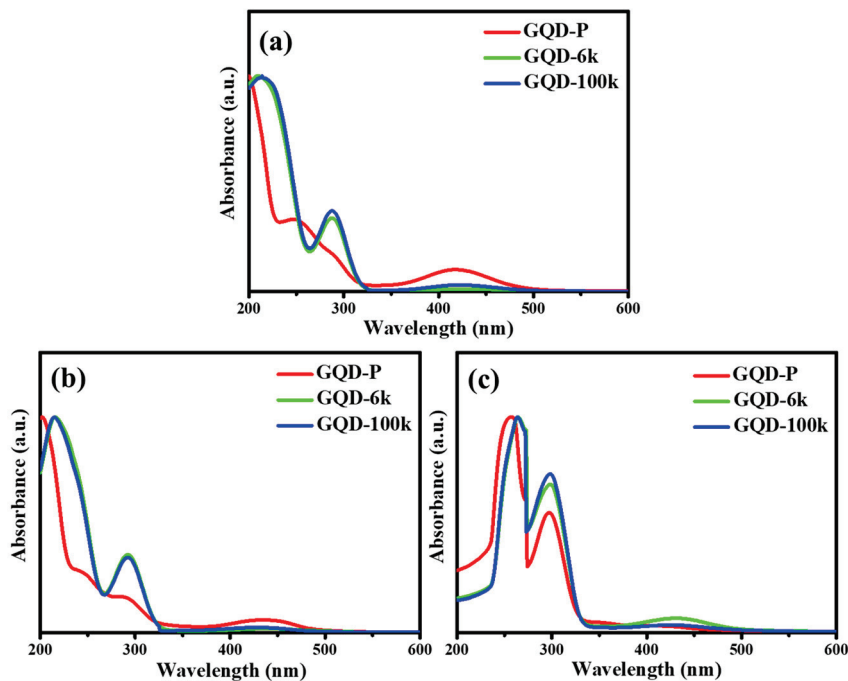


Figure 6. UV-vis absorbance spectra of pristine GQD and PEG-coated GQD cluster suspensions in (a) water, (b) ethanol, and (c) PGMEA.

Figure 7 depicts PL emission spectra of the as-prepared and PEG-coated GQD clusters recorded within the range of 360–450 nm in water, ethanol, and PGMEA. As shown in Figure 7, the GQD suspensions in water (see Figure 7a,d) display a quasi-symmetric peak in the range of 650–700 nm. The PL spectrum includes a single band at ca. 570 nm with a FWHM of ca. 90 nm under 360 and 450 nm. Compared to the emission spectra associated with the GQD suspensions in ethanol (see Figure 6b,e), the GQD-P suspension exhibits an asymmetric lump at 450 nm, while both GQD-6k and GQD-100k samples demonstrate a quasi-symmetric peak with a small FWHM of 95 nm. Since the PEG skin layer covers over the GQD samples, the maximal PL emission shows a slight red-shift from 540 to 550 nm. For the GQD suspensions in PGMEA (as shown in Figure 7c,f), the GQD-P sample displays a very weak fluorescence, being quenched at 360 and 450 nm. In contrast, the GQD-6k and GQD-100k suspensions still emit ~530-nm light under 360 and 450 nm. Accordingly, the solvent type significantly alters the PL emission (e.g., fluorescence intensity) from the PEG-coated GQD clusters, while the influence of solvent type on the maximal wavelength (i.e., blue/red shift) is insignificant. This finding also demonstrates that the PEG-coated GQD clusters are capable of emitting intense fluorescence under blue light illumination (i.e., 450 nm).

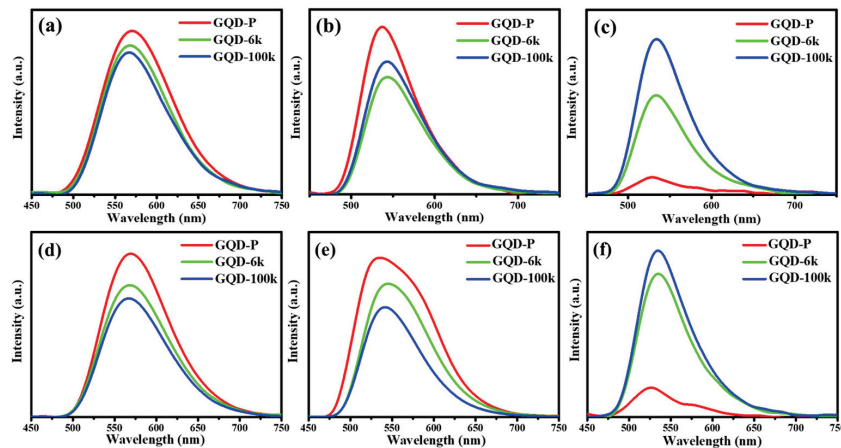


Figure 7. PL emission spectra of pristine GQD and PEG-coated GQD cluster suspensions in (a) water, (b) ethanol, and (c) PGMEA under an excitation of 360 nm. PL emission spectra of pristine GQD and PEG-coated GQD cluster suspensions in (d) water, (e) ethanol, and (f) PGMEA under an excitation of 450 nm.

To further explore the effect of solvent type on the PL emissions, QY was assessed as a crucial index in evaluating the PL performance from the pristine GQD and PEG-coated GQD clusters. Figure 8a–c includes the QY values (see Equation (1)) as a function of different GQD structures under UV light illumination. Analyzing the GQD suspensions in water and ethanol, the QY values ranged from 15.2% to 21.6%. Notably, the GQD-P suspension in PGMEA was substantially quenched with an ultralow quantum yield (QY < 2.5%). However, the magnitude of QY in PGMEA was significantly enhanced after the introduction of PEG coating. A similar trend was observed when the GQD suspensions were placed under blue light illumination (i.e., 450 nm), as illustrated in Figure 8d–f. According to Figure 8, the QY values were ultra-high (60–95%) for the GQD suspensions in water and ethanol. Nonetheless, the QY values drastically decreased when the GQD-P suspension was placed in PGMEA. Implementing the PEG coating, the QY values were significantly enhanced for the GQD suspensions in PGMEA.

This enhanced QY associated with the PEG-coated GQD clusters is mainly due to the formation of robust PEG-coated GQD aggregates that severely restrict the intermolecular rotational motion and subsequently boost the PL intensity [44]. It is important to note that the PGMEA is frequently used in the structure of various optical devices (e.g., micro-light-emitting diode display). Therefore, the PEG-coated GQD clusters can potentially enable solid-state fluorescence feasibility for next-generation optical instruments if the recipe for RIE clusters is optimized.

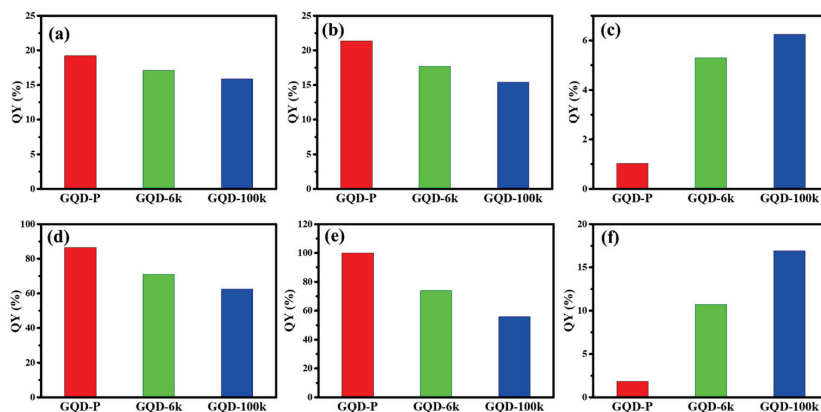


Figure 8. The QY values of pristine GQD and PEG-coated GQD cluster suspensions in (a) water, (b) ethanol, and (c) PGMEA under an excitation of 360 nm. The QY values of pristine GQD and PEG-coated GQD cluster suspensions in (d) water, (e) ethanol, and (f) PGMEA under an excitation of 450 nm.

The PL emission from the GQD suspensions demonstrates a significant effect of the solvent type on the PL performance. Optical photographs of all GQD suspensions in different solvents under blue-light illumination (450 nm) were also collected, as shown in Figure S4. This implies that the selection of the solvent type not only alters the PL behavior but also affects the AIE fluorescence through the RIE mechanism. Considering the solvents used in this work (deionized water (surface tension: ~ 72.3 mN/m, pH = 5.8), ethanol (surface tension: ~ 46.0 mN/m, pH = 7.1), and PGMEA (surface tension: ~ 26.9 mN/m, pH = 7.5)), a large number of oxygen and nitrogen functional groups are formed on the edge of GQD-P nanoparticles serving as the electron donor groups [45,46]. Indeed, the formation of hydrophilic edges on the functionalized GQDs facilitates the adsorption of polar molecules onto the surface by providing emissive traps within the molecular structure [47]. This analysis is consistent with the PL emission mechanism where the GQD-P suspension in high-polar solvents, i.e., water and ethanol, displays a highly luminescent green emission with increased QY values. In contrast, the remarkable PL emission recorded for the PEG-coated GQD clusters in PGMEA is primarily due to the decreased solvent polarity [43] (i.e., polarity index: $\text{H}_2\text{O} \gg \text{PGMEA}$) along with reduced solubility, resulting in the rigid confinement of GQDs within the PEG framework. This solvent-dependent mechanism is similar to the “solvatochromism” behavior that organic dyes commonly exhibit [48–50]. Since the surface tension of the solvent ranges from 26.9 to 46.0 mN/m, the transition point can be reached for activating the AIE mechanism, which ultimately results in an improved fluorescence intensity.

A schematic diagram illustrating the PL emission from the GQD-P and GQD-100k suspensions in water and PGMEA is illustrated in Figure 9. Decorating the O atoms, along with doping the N atoms within the GQD-P sample, enables the formation of a superhydrophilic carbon surface and provides strong affinity to the water molecules. Considering the illumination at 450 nm, upon electron transition, an electron–hole pair is generated when the photons are absorbed by the double bonds within the molecular structure [19]. The transition of the excited electrons from a higher energy level (i.e., orbital) to a lower state results in substantial PL emission where various excited electronic states are observed (i.e., N_{π^*} , O_{π^*} and C_{π^*}) [19,26]. As shown in Figure 8a, the GQD-P suspension in water enables a strong fluorescence due to being well dispersed in water, whereas the suspension in PGMEA tends to be quenched owing to the formation of GQD aggregates (i.e., the π - π stacking interaction (ACQ mechanism)) [42]. Considering the GQD-100k suspension, the PEG framework tends to partially dissolve in high-polarity water molecules, causing the loss of GQDs from the cluster. Such a partial dissolution imparts a heterogeneous dispersion which disturbs the RIE structure and causes an unstable and weak PL emission under blue-light illumination. This undesired performance can be improved when the GQD-100k suspension is placed in low-polarity solvents, as shown in Figure 8b. The GQD-100k suspension in PGMEA maintains a well-developed framework in the solid state, where the rotational motion around the single bonds along with the partial energy relaxation (i.e., rotational and vibrational) promote the non-radiative decay pathways in the HOMO-LUMO multiple band structures [1]. Within the PEG-coated GQD cluster, an aggregated solid state can be confined by the PEG nanostructure where intense intermolecular interactions occur between the GQDs and the PEG framework inside the aggregate that ultimately populates the radiative decay pathways, leading to the AIE fluorescence.

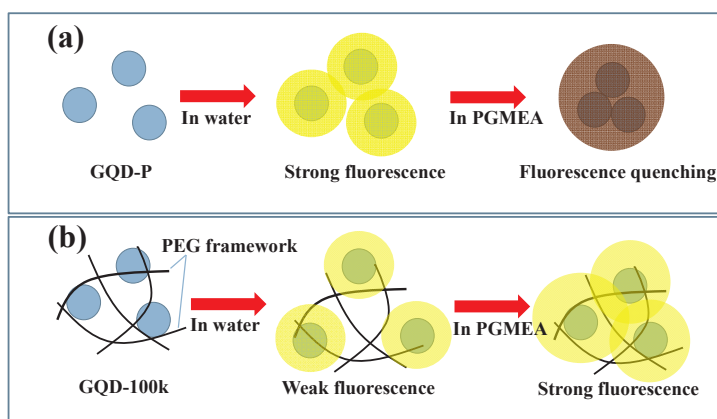


Figure 9. Schematic diagram for the PL emission from (a) GQD-P and (b) GQD-100k suspensions in different solvents under blue-light illumination.

4. Conclusions

In this work, we have assessed the critical role of the solvent on the PL emission from PEG-coated GQD clusters under blue light and UV illumination. The one-pot hydrothermal method enabled the creation of PEG-coated GQD clusters using o-PD as the carbon and nitrogen sources in the presence of PEG with different molecular weights. Through analyzing various solvents, the AIE/ACQ behavior was determined for a series of as-prepared GQD structures. The PEG-coated GQD particles were suspended in ethanol, water, and PGMEA, enabling PL emission within the range of 530–550 nm. The pristine GQD suspension was quenched (i.e., QY: ~1%) when dispersed in PGMEA, resembling the ACQ mechanism. In contrast, the quantum yield was significantly intensified upon implementing the PEG nanocoating since the PEG layer promotes the AIE fluorescence process. Therefore, the one-pot hydrothermal route introduced in this work provides the initial framework for designing efficient ACQ/AIE cycles through modulating the interaction between the solvent's molecular structure and GQD clusters. The findings of this study can be employed to synthesize finely tuned PEG-coated GQD clusters with numerous applications in optical, sensing, energy conversion/storage, and biological devices.

Supplementary Materials: The following are available online at <https://www.mdpi.com/2079-4991/11/6/1383/s1>, Figure S1: Particle size distributions of different GQD samples determined from DLS technique. Figure S2: Survey-scan XPS spectra of pristine GQD and PEG-coated GQD cluster samples, Figure S3: FT-IR spectra of pristine GQD and PEG-coated GQD cluster samples. Figure S4.: Photographs of different GQD suspensions at 450 nm: (a) water, (b) ethanol, and (c) PGMEA.

Author Contributions: Conceptualization, C.-T.H. and P.-C.Y.; methodology, Y.-X.T.; resources, S.G., C.-T.H. and P.-C.Y.; data curation, Y.-X.T., P.-C.Y. and C.-T.H.; software: Y.-X.T. and C.-T.H.; validation, C.-T.H. and P.-C.Y.; writing—original draft preparation, C.-T.H., J.L. and Y.A.G.; writing—review, validation and editing, C.-T.H. and Y.A.G.; visualization, Y.-X.T. and C.-T.H.; supervision, C.-T.H. and P.-C.Y.; project administration, C.-T.H.; funding acquisition, S.G., C.-T.H. and P.-C.Y. All authors have read and agreed to the published version of the manuscript.

Funding: The major financial support for this work was provided by the Ministry of Science and Technology of Taiwan (Contact # MOST 108-2221-E-155-036-MY3 and MOST 109-2221-E-155-053). S.G. also thanks the partial support received from the Natural Science Foundation of Fujian Province (No. 2020J01288).

Institutional Review Board Statement: The study did not require ethical approval.

Informed Consent Statement: Not applicable.

Data Availability Statement: Data is contained within the article or Supplementary Material.

Conflicts of Interest: The authors declare no conflict of interest.

References

1. Pathan, S.; Jalal, M.; Prasad, S.; Bose, S. Aggregation-induced enhanced photoluminescence in magnetic graphene oxide quantum dots as a fluorescence probe for As(III) sensing. *J. Mater. Chem. A* **2019**, *7*, 8510–8520. [CrossRef]
2. Fu, C.-C.; Wu, C.-Y.; Chien, C.-C.; Hsu, T.-H.; Ou, S.-F.; Chen, S.-T.; Wu, C.-H.; Hsieh, C.-T.; Juang, R.-S.; Hsueh, Y.-H. Polyethylene Glycol6000/carbon Nanodots as Fluorescent Bioimaging Agents. *Nanomaterials* **2020**, *10*, 677. [CrossRef]
3. Fu, C.-C.; Hsieh, C.-T.; Juang, R.-S.; Gu, S.; Gandomi, Y.A.; Kelly, R.E.; Kihm, K.D. Electrochemical sensing of mercury ions in electrolyte solutions by nitrogen-doped graphene quantum dot electrodes at ultralow concentrations. *J. Mol. Liq.* **2020**, *302*, 112593. [CrossRef]
4. Zhou, S.; Xu, H.; Gan, W.; Yuan, Q. Graphene quantum dots: Recent progress in preparation and fluorescence sensing applications. *RSC Adv.* **2016**, *6*, 110775–110788. [CrossRef]
5. Shteplyuk, I.; Caffrey, N.M.; Iakimov, T.; Khranovskyy, V.; Abrikosov, I.A.; Yakimova, R. On the interaction of toxic Heavy Metals (Cd, Hg, Pb) with graphene quantum dots and infinite graphene. *Sci. Rep.* **2017**, *7*, 1–17. [CrossRef]
6. Gu, S.; Hsieh, C.-T.; Tsai, Y.-Y.; Gandomi, Y.A.; Yeom, S.; Kihm, K.D.; Fu, C.-C.; Juang, R.-S. Sulfur and Nitrogen Co-Doped Graphene Quantum Dots as a Fluorescent Quenching Probe for Highly Sensitive Detection toward Mercury Ions. *ACS Appl. Nano Mater.* **2019**, *2*, 790–798. [CrossRef]
7. Fu, C.-C.; Hsieh, C.-T.; Juang, R.-S.; Yang, J.-W.; Gu, S.; Gandomi, Y.A. Highly efficient carbon quantum dot suspensions and membranes for sensitive/selective detection and adsorption/recovery of mercury ions from aqueous solutions. *J. Taiwan Inst. Chem. Eng.* **2019**, *100*, 127–136. [CrossRef]
8. Fei, H.; Ye, R.; Ye, G.; Gong, Y.; Peng, Z.; Fan, X.; Samuel, E.L.G.; Ajayan, P.M.; Tour, J.M. Boron- and Nitrogen-Doped Graphene Quantum Dots/Graphene Hybrid Nanoplatelets as Efficient Electrocatalysts for Oxygen Reduction. *ACS Nano* **2014**, *8*, 10837–10843. [CrossRef]
9. Li, Q.; Zhang, S.; Dai, L.; Li, L.-S. Nitrogen-Doped Colloidal Graphene Quantum Dots and Their Size-Dependent Electrocatalytic Activity for the Oxygen Reduction Reaction. *J. Am. Chem. Soc.* **2012**, *134*, 18932–18935. [CrossRef]
10. Gu, S.; Hsieh, C.-T.; Mallick, B.C.; Ashraf, Y.G. Infrared-assisted synthesis of highly amidized graphene quantum dots as metal-free electrochemical catalysts. *Electrochim. Acta* **2020**, *360*, 137009. [CrossRef]
11. Gu, S.; Hsieh, C.-T.; Gandomi, Y.A.; Li, J.; Yue, X.X.; Chang, J.-K. Tailoring fluorescence emissions, quantum yields, and white light emitting from nitrogen-doped graphene and carbon nitride quantum dots. *Nanoscale* **2019**, *11*, 16553–16561. [CrossRef]
12. Zhang, Z.; Zhang, J.; Chen, N.; Qu, L. Graphene quantum dots: An emerging material for energy-related applications and beyond. *Energy Environ. Sci.* **2012**, *5*, 8869–8890. [CrossRef]
13. Wang, Y.; Zhang, L.; Liang, R.-P.; Bai, J.-M.; Qiu, J.-D. Using Graphene Quantum Dots as Photoluminescent Probes for Protein Kinase Sensing. *Anal. Chem.* **2013**, *85*, 9148–9155. [CrossRef]
14. Shen, J.H.; Zhu, Y.H.; Yang, X.L.; Li, C.Z. Graphene quantum dots: Emergent nanolights for bioimaging, sensors, catalysis and photovoltaic device. *Chem. Commun.* **2012**, *48*, 3686–3699. [CrossRef]
15. Chen, Y.; Lam, J.W.Y.; Kwok, R.T.K.; Liu, B.; Tang, B.Z. Aggregation-induced emission: Fundamental understanding and future developments. *Mater. Horiz.* **2019**, *6*, 428–433. [CrossRef]
16. Wang, L.; Wang, Y.; Xu, T.; Liao, H.; Yao, C.; Liu, Y.; Li, Z.; Chen, Z.; Pan, D.; Sun, L.; et al. Gram-scale synthesis of single-crystalline graphene quantum dots with superior optical properties. *Nat. Commun.* **2014**, *5*, 5357. [CrossRef] [PubMed]
17. Luo, J.; Xie, Z.; Lam, J.W.Y.; Cheng, L.; Chen, H.; Qiu, C.; Kwok, H.S.; Zhan, X.; Liu, Y.; Zhu, D.; et al. Aggregation-induced emission of 1-methyl-1,2,3,4,5-pentaphenylsilole. *Chem. Commun.* **2001**, *18*, 1740–1741. [CrossRef]
18. Shen, J.; Zhu, Y.; Yang, X.; Zong, J.; Zhang, J.; Li, C. One-pot hydrothermal synthesis of graphene quantum dots surface-passivated by polyethylene glycol and their photoelectric conversion under near-infrared light. *New J. Chem.* **2012**, *36*, 97–101. [CrossRef]
19. Juang, R.-S.; Fu, C.-C.; Hsieh, C.-T.; Gu, S.; Gandomi, Y.A.; Liu, S.-H. Highly luminescent aggregate-induced emission from polyethylene glycol-coated carbon quantum dot clusters under blue light illumination. *J. Mater. Chem. C* **2020**, *8*, 16569–16576. [CrossRef]
20. Vedamalai, M.; Periasamy, A.P.; Wang, C.W.; Tseng, Y.U.; Ho, L.C.; Shih, C.C.; Chang, H.T. Carbon nanodots prepared from o-phenylene-diamine for sensing of Cu²⁺ ions in cell. *Nanoscale* **2014**, *6*, 13119–13125. [CrossRef] [PubMed]
21. Ding, H.; Yu, S.-B.; Wei, J.-S.; Xiong, H.-M. Full-Color Light-Emitting Carbon Dots with a Surface-State-Controlled Luminescence Mechanism. *ACS Nano* **2016**, *10*, 484–491. [CrossRef]
22. Jiang, K.; Sun, S.; Zhang, L.; Lu, Y.; Wu, A.; Cai, C.; Lin, H. Red, Green, and Blue Luminescence by Carbon Dots: Full-Color Emission Tuning and Multicolor Cellular Imaging. *Angew. Chem.* **2015**, *127*, 5450–5453. [CrossRef]
23. Song, L.; Cui, Y.; Zhang, C.; Hu, Z.; Liu, X. Microwave-assisted facile synthesis of yellow fluorescent carbon dots from o-phenylenediamine for cell imaging and sensitive detection of Fe³⁺ and H₂O₂. *RSC Adv.* **2016**, *6*, 17704–17712. [CrossRef]
24. Tian, L.; Yang, S.; Yang, Y.; Li, J.; Deng, Y.; Tian, S.; He, P.; Ding, G.; Xie, X.; Wang, Z. Green, simple and large scale synthesis of N-doped graphene quantum dots with uniform edge groups by electrochemical bottom-up synthesis. *RSC Adv.* **2016**, *6*, 82648–82653. [CrossRef]
25. Lu, S.; Xiao, G.; Sui, L.; Feng, T.; Yong, X.; Zhu, S.; Li, B.; Liu, Z.; Zou, B.; Jin, M.; et al. Piezochromic Carbon Dots with Two-photon Fluorescence. *Angew. Chem. Int. Ed.* **2017**, *56*, 6187–6191. [CrossRef] [PubMed]
26. Jin, Z.; Yao, J.; Kittrell, C.; Tour, J.M. Large-Scale Growth and Characterizations of Nitrogen-Doped Monolayer Graphene Sheets. *ACS Nano* **2011**, *5*, 4112–4117. [CrossRef]

27. Tang, L.; Ji, R.; Li, X.; Bai, G.; Liu, C.P.; Hao, J.; Lin, J.; Jiang, H.; Teng, K.S.; Yang, Z.; et al. Deep Ultraviolet to Near-Infrared Emission and Photoresponse in Layered N-Doped Graphene Quantum Dots. *ACS Nano* **2014**, *8*, 6312–6320. [CrossRef] [PubMed]
28. Chen, C.-M.; Zhang, Q.; Zhao, X.-C.; Zhang, B.; Kong, Q.-Q.; Yang, M.-G.; Yang, Q.-H.; Wang, M.-Z.; Yang, Y.-G.; Schlögl, R.; et al. Hierarchically aminated graphene honeycombs for electrochemical capacitive energy storage. *J. Mater. Chem.* **2012**, *22*, 14076–14084. [CrossRef]
29. Dai, Y.; Long, H.; Wang, X.; Wang, Y.; Gu, Q.; Jiang, W.; Wang, Y.; Li, C.; Zeng, T.H.; Sun, Y. Doping: Versatile graphene quantum dots with tunable nitrogen doping. *Part. Part. Syst. Char.* **2014**, *31*, 597. [CrossRef]
30. Barman, S.; Sadhukhan, M. Facile bulk production of highly blue fluorescent graphitic carbon nitride quantum dots and their application as highly selective and sensitive sensors for the detection of mercuric and iodide ions in aqueous media. *J. Mater. Chem.* **2012**, *22*, 21832–21837. [CrossRef]
31. Wang, A.; Wang, C.; Fu, L.; Wong-Ng, W.; Lan, Y. Recent advances of graphitic carbon nitride-based structures and applications in catalyst, sensing, imaging, and LEDs. *Nano Micro Lett.* **2017**, *9*, 47. [CrossRef] [PubMed]
32. Chen, K.; Chai, Z.; Li, C.; Shi, L.; Liu, M.; Xie, Q.; Zhang, Y.; Xu, D.; Manivannan, A.; Liu, Z. Catalyst-Free Growth of Three-Dimensional Graphene Flakes and Graphene/g-C₃N₄ Composite for Hydrocarbon Oxidation. *ACS Nano* **2016**, *10*, 3665–3673. [CrossRef] [PubMed]
33. Dillip, G.; Sreekanth, T.; Joo, S. Tailoring the bandgap of N-rich graphitic carbon nitride for enhanced photocatalytic activity. *Ceram. Int.* **2017**, *43*, 6437–6445. [CrossRef]
34. Russo, P.; Hu, A.; Compagnini, G.; Duley, W.W.; Zhou, N.Y. Femtosecond laser ablation of highly oriented pyrolytic graphite: A green route for large-scale production of porous graphene and graphene quantum dots. *Nanoscale* **2014**, *6*, 2381–2389. [CrossRef]
35. Vinayan, B.P.; Zhao-Karger, Z.; Diemant, T.; Chakravadhanula, V.S.K.; Schwarzburger, N.I.; Cambaz, M.A.; Behm, R.J.; Kübel, C.; Fichtner, M. Performance study of magnesium-sulfur battery using a graphene based sulfur composite cathode electrode and a non-nucleophilic Mg electrolyte. *Nanoscale* **2016**, *8*, 3296–3306. [CrossRef]
36. Yang, Z.; Yao, Z.; Li, G.; Fang, G.; Nie, H.; Liu, Z.; Zhou, X.; Chen, X.; Huang, S. Sulfur-Doped Graphene as an Efficient Metal-free Cathode Catalyst for Oxygen Reduction. *ACS Nano* **2012**, *6*, 205–211. [CrossRef]
37. Kharangarh, P.R.; Umamathy, S.; Singh, G. Thermal Effect of Sulfur Doping for Luminescent Graphene Quantum Dots. *ECS J. Solid State Sci. Technol.* **2018**, *7*, M29–M34. [CrossRef]
38. Gu, S.; Hsieh, C.-T.; Yuan, C.-Y.; Gandomi, Y.A.; Chang, J.-K.; Fu, C.-C.; Yang, J.-W.; Juang, R.-S. Fluorescence of functionalized graphene quantum dots prepared from infrared-assisted pyrolysis of citric acid and urea. *J. Lumin.* **2020**, *217*, 116774. [CrossRef]
39. Yeh, T.-F.; Huang, W.-L.; Chung, C.-J.; Chiang, I.-T.; Chen, L.-C.; Chang, H.-Y.; Su, W.-C.; Cheng, C.; Chen, S.-J.; Teng, H. Elucidating Quantum Confinement in Graphene Oxide Dots Based on Excitation-Wavelength-Independent Photoluminescence. *J. Phys. Chem. Lett.* **2016**, *7*, 2087–2092. [CrossRef]
40. Eda, G.; Lin, Y.-Y.; Mattevi, C.; Yamaguchi, H.; Chen, H.-A.; Chen, I.-S.; Chen, C.-W.; Chhowalla, M. Blue Photoluminescence from Chemically Derived Graphene Oxide. *Adv. Mater.* **2010**, *22*, 505–509. [CrossRef]
41. Liu, F.; Jang, M.H.; Ha, H.D.; Kim, J.H.; Cho, Y.H.; Seo, T.S. Facile synthetic method for pristine graphene quantum dots and graphene oxide quantum dots: Origin of blue and green luminescence. *Adv. Mater.* **2013**, *25*, 3657. [CrossRef]
42. Yang, H.; Liu, Y.; Guo, Z.; Lei, B.; Zhuang, J.; Zhang, X.; Liu, Z.; Hu, C. Hydrophobic carbon dots with blue dispersed emission and red aggregation-induced emission. *Nat. Commun.* **2019**, *10*, 1–11. [CrossRef] [PubMed]
43. Wu, M.; Zhan, J.; Geng, B.; He, P.; Wu, K.; Wang, L.; Xu, G.; Li, Z.; Yin, L.; Pan, D. Scalable synthesis of organic-soluble carbon quantum dots: Superior optical properties in solvents, solids, and LEDs. *Nanoscale* **2017**, *9*, 13195–13202. [CrossRef] [PubMed]
44. Zhang, L.; Zhang, Z.-Y.; Liang, R.-P.; Li, Y.-H.; Qiu, J.-D. Boron-Doped Graphene Quantum Dots for Selective Glucose Sensing Based on the “Abnormal” Aggregation-Induced Photoluminescence Enhancement. *Anal. Chem.* **2014**, *86*, 4423–4430. [CrossRef] [PubMed]
45. Lakowicz, J.R.; Masters, B.R. *Principles of Fluorescence Spectroscopy*, 3rd ed.; Kluwer-Plenum: New York, NY, USA, 2008; p. 029901. [CrossRef]
46. Zhou, X.; Zhang, Y.; Wang, C.; Wu, X.; Yang, Y.; Zheng, B.; Wu, H.; Guo, S.; Zhang, J. Photo-Fenton Reaction of Graphene Oxide: A New Strategy to Prepare Graphene Quantum Dots for DNA Cleavage. *ACS Nano* **2012**, *6*, 6592–6599. [CrossRef]
47. Zhu, S.; Zhang, J.; Tang, S.; Qiao, C.; Wang, L.; Wang, H.; Liu, X.; Li, B.; Li, Y.W.; Yu, W.; et al. Surface chemistry routes to modulate the photoluminescence of graphene quantum dots: From fluorescence mechanism to pp-conversion bioimaging applications. *Adv. Funct. Mater.* **2012**, *22*, 4732–4740. [CrossRef]
48. Wang, H.; Sun, C.; Chen, X.; Zhang, Y.; Colvin, V.L.; Rice, Q.; Seo, J.; Feng, S.; Wang, S.; Yu, W.W. Excitation wavelength independent visible color emission of carbon dots. *Nanoscale* **2017**, *9*, 1909–1915. [CrossRef]
49. Pan, D.; Zhang, J.; Li, Z.; Wu, C.; Yan, X.; Wu, M. Observation of pH-, solvent-, spin-, and excitation-dependent blue photoluminescence from carbon nanoparticles. *Chem. Commun.* **2010**, *46*, 3681–3683. [CrossRef]
50. Jiang, K.; Zhang, L.; Lu, J.; Xu, C.; Cai, C.; Lin, H. Triple-mode emission of carbon dots: Applications for advanced anticounterfeiting. *Angew. Chem. Int. Ed.* **2016**, *55*, 7231–7235. [CrossRef]

MDPI AG
Grosspeteranlage 5
4052 Basel
Switzerland
Tel.: +41 61 683 77 34

Nanomaterials Editorial Office
E-mail: nanomaterials@mdpi.com
www.mdpi.com/journal/nanomaterials



Disclaimer/Publisher's Note: The title and front matter of this reprint are at the discretion of the Guest Editor. The publisher is not responsible for their content or any associated concerns. The statements, opinions and data contained in all individual articles are solely those of the individual Editor and contributors and not of MDPI. MDPI disclaims responsibility for any injury to people or property resulting from any ideas, methods, instructions or products referred to in the content.



Academic Open
Access Publishing

mdpi.com

ISBN 978-3-7258-4570-5